Filtering of interstellar dust in the heliosphere

Von der Fakultät für Elektrotechnik, Informationstechnik, Physik

der Technischen Universität Carolo-Wilhelmina

zu Braunschweig

zur Erlangung des Grades einer

Doktorin der Naturwissenschaften

(Dr.rer.nat.)

genehmigte

Dissertation

von Veerle Jasmin Sterken
aus Gent, Belgien

1. Referentin oder Referent: Prof. Dr. Jürgen Blum
2. Referentin oder Referent: Prof. Dr. Eberhard Grün
eingereicht am: 10.07.2012
mündliche Prüfung (Disputation) am: 27.08.2012

2012
(Druckjahr)

Vorveröffentlichungen der Dissertation

Teilergebnisse aus dieser Arbeit wurden mit Genehmigung der Fakultät für Elektrotechnik, Informationstechnik, Physik, vertreten durch die Mentorin oder den entor/die Betreuerin oder den Betreuer der Arbeit, in folgenden Beiträgen vorab veröffentlicht:

Publikationen (Referiert)

Sterken V. J., Westphal A. J., Altobelli N., Grün E., Postberg F., Srama R. et al.: Impact speeds and directions of interstellar grains on the Stardust dust collector. Meteoritics and Planetary Science (planned submission in July 2012).

Sterken, V. J., Altobelli, N., Kempf, S., Krüger H., Srama, R., Strub P. & Grün, E.: The filtering of interstellar dust in the solar system. Astronomy & Astrophysics (submitted).

Sterken, V. J., Altobelli, N., Kempf, S., Krüger H., Postberg F., Soja, R. H., Srama, R. & Grün, E.: An optimum opportunity for interstellar dust measurements by the JUICE mission. Planetary and Space Science; in press (2012).

Soja, R. H., Altobelli N., Krüger H., Sterken V. J.: Dust environment predictions for the ESA L-class mission candidate JUICE. Planetary and Space Science (submitted).

Sterken, V. J., Altobelli, N., Kempf, S., Schwehm, G., Srama, R. & Grün, E.: The flow of interstellar dust into the solar system. Astronomy & Astrophysics Vol. 538: A102 (2012).

Srama, R., et al.: SARIM PLUS–sample return of comet 67P/CG and of interstellar matter. Experimental Astronomy Vol. 33, Issue 2-3: pp. 723-751 (2012).

Srama R., et al: The cosmic dust analyser onboard cassini: ten years of discoveries. CEAS Space Journal Vol. 2, Issue 1-4: pp. 3-16 (2011).

Publikationen (Nicht referiert)

Sterken V.J., Altobelli N., Kempf S., Schwehm G., Srama R., Strub P. & Grün: The flow of interstellar dust through the solar system: the role of dust charging. Proceedings of the ICPDP Conference pp.179-182 (2011).

Strub P., Sterken V. J., Krüger H., Grün E. & Horanyi M.: Interstellar Dust Flow through the Solar System. Proceedings of the ICPDP Conference (2011) pp.385-386 (2011).

Sterken V. J., Altobelli A., Kempf S., Grün E., Srama R.: Characterizing the Interstellar Dust flow through the solar system. Contribution to the MPIK year report (2010).

Tagungsbeiträge

Sterken V., Altobelli N., Kempf S., Srama R., Grün E. & Schwehm G.: Adapting Cassini-CDA observation strategy to ISD detection in the Saturnian System. (Poster) European Planetary Science Congress, Potsdam, Germany (2009).

Sterken V., Kempf S., Altobelli N., Grün E., Srama R. & Schwehm G.: Simulations of interstellar dust particle trajectories in our Solar System. (Vortrag) Deutsche Physikalische Gesellschaft Frühjahrstagung, Bonn, Germany (2009).

Sterken V., Kempf S., Altobelli N., Grün E., Srama R. & Schwehm G.: Simulations of interstellar dust particle trajectories in our Solar System. (Vortrag) General Assembly of the European Geosciences Union Conference, Vienna, Austria (2010).

Sterken V., Kempf S., Altobelli N., Grün E., Srama R. & Schwehm G.: Modelling interstellar dust in the solar system. (Poster) Dusty Visions Workshop, Göttingen, Germany (2010).

Sterken V., Altobelli N., Kempf S., Krüger H., Grün E., Srama R. & Schwehm G.: Constraining interstellar dust properties from dynamical studies and observations. (Vortrag) European Planetary Science Congress, Rome, Italy (2010).

Sterken, V., Altobelli N., Kempf, S., Postberg F., Westphal A., Ogliore R., Srama R., Schwehm G. & Grün E.: Modeling the interstellar dust flow through the solar system, implications for Stardust Mission. (Poster) General Assembly of the European Geosciences Union Conference, Vienna, Austria (2011).

Sterken V., Altobelli N., Kempf S., Schwehm G., Srama R., Strub P. & Grün E.: The flow of interstellar dust through the solar system: the role of dust charging. (Vortrag) 6th International Conference on the Physics of Dusty Plasmas, Garmisch-Partenkirchen, Germany (2011).

Sterken V., Altobelli N., Kempf S., Postberg F., Schwehm G., Srama R. & Grün E.: Modeling interstellar dust dynamics in the solar system: application to Stardust. (Vortrag) Annual meeting of the Meteoritical Society, Greenwich, UK (2011).

Sterken V., Altobelli N., Kempf S., Strub P., Srama R., Schwehm G. & Grün E.: Modeling interstellar dust dynamics in the solar system: applications to Stardust, Ulysses and Cassini. (Vortrag) European Planetary Science Congress, Nantes, France (2011).

Sterken V., Strub P., Altobelli N., Krüger H., Kempf S., Srama R., Schwehm G. & Grün E.: Heliospheric filtering effects on the size distribution of interstellar grains in the solar system. (Poster) American Geophysical Union Fall meeting, San Francisco, USA (2011).

Sterken, V.: Cosmic dust research within the solar system. (Vortrag) 33th. Extreme Atomic Systems Tagung, Riezlern, Austria (2012).

Sterken V., Altobelli N., Kempf S., Srama R. & Grün E.: Modeling the interstellar dust flow in the solar system: application to the JUICE and Galileo missions. (Vortrag) Deutsche Physikalische Gesellschaft Frühjahrstagung, Stuttgart, Germany (2012).

Sterken V., Altobelli N., Strub P., Krüger H., Kempf S., Srama R., Schwehm G. & Grün E.: Modeling the local size distribution of interstellar dust in the solar system. (Poster) General Assembly of the European Geosciences Union Conference, Vienna, Austria (2012).

Sterken V., Westphal A., Altobelli N., Postberg F., Srama R. & Grün E.: Interstellaar dust simulations for the Stardust mission. (Vortrag) 43th Lunar and Planetary Science Conference, The Woodlands, Texas, USA (2012).

Sterken V., Altobelli N., Strub P., Krüger H., Kempf S., Srama R., Schwehm G. & Grün E.: Fluffy interstellar dust? (Vortrag) Dust and grains in low gravity and space environment, ESTEC, Noordwijk, The Netherlands (2012).

Abstract (Deutsch)

Der Raum zwischen den Sternen ist mit Gas und Interstellarem Staub (IS) gefüllt. Die Staubkörner verursachen eine Abschwächung des Sternenlichts, die wir beobachten können, und spielen eine wichtige Rolle bei der Entwicklung von Galaxien und bei der Entstehung von Sternen und Planetensystemen. Der IS wird seit langem mit astronomischen Methoden beobachtet, die Teilchen sind durch in-situ Messungen von Raumsonden im Sonnensystem identifiziert worden und es wurden sogar von der Stardust-Mission im Jahr 2006 Proben des interstellaren Materials auf die Erde zurück gebracht. Jedoch existieren noch viele Fragen über die Zusammensetzung, die Morphologie und die Grössenverteilung des IS, welche mehr und verbesserte Messungen erfordern. Um diese Beobachtungen zu interpretieren, und um die Informationen über die Staubteilchen von diesen Messungen zu extrahieren, wird ein besseres Verständnis des IS-Flusses durch das Sonnensystem benötigt. Auch ist die Modellierung für die Gestaltung und Optimierung zukünftiger Missionen mit IS Messungen notwendig.

Diese Arbeit modelliert den Fluss des IS durch das Sonnensystem unter Berücksichtigung der drei wichtigsten Kräfte: die solare Gravitation, der Strahlungsdruck der Sonne und die Lorentz-Kraft, die aus der Bewegung der geladenen Körner durch das interplanetare Magnetfeld (IMF) entsteht. Simulationen von Staubtrajektorien wurden über einen großen Bereich von IS Parametern β und Q/m durchgeführt. β ist das Verhältnis von Strahlungsdruck und Gravitation und hängt von der Korngröße, der Morphologie und dem Material des Kornes ab. Q/m ist das Ladungs-Masse-Verhältnis. Der Einfluss des Strahlungsdrucks und der Lorentz-Kraft auf die Teilchenbahnen, Dichten und Flüsse wurden systematisch erforscht.

Der Strahlungsdruck reduziert die Anziehung der Gravitationskraft und kann diese für Teilchen von etwa 0.2 μm Radius übertreffen ($\beta > 1$), was zu einem Fehlen dieser Staubteilchen, stromabwärts von der Sonne (dem β-Kegel) führt. Wenn man nur den Strahlungsdruck und die Schwerkraft der Sonne berücksichtigt, ist der IS-Fluss axialsymmetrisch, stationär und kann sogar analytisch berechnet werden. Die Lorentz-Kraft wird stärker für kleinere Körner mit höherem Q/m-Wert und dominiert für Körner < 0.15–0.2 μm. Die azimuthale Komponente des IMF führt dazu, dass die Teilchen zur oder weg von der Äquatorialebene der Sonne abgelenkt werden, abhängig von der Polarität des IMF. Diese Fokussierungs- oder Defokussierungs-Effekte folgen einem 22-Jahrigen Zyklus, sodass der IS Strom nicht-stationär und das Strömungsbild wesentlich komplizierter werden. Wenn kleine IS Körner von 0.1 bis 0.15 μm nicht schon am heliosphärischen "Termination Shock" ausgefiltert werden, dann können sie das Planetensystem in günstigen Zeiten erreichen und wieder stromaufwärts abgelenkt werden (dies wird in dieser Arbeit "Spiegelung" genannt) und so eine lokale Erhöhung der Konzentration verursachen. Da die kleinen Körner in grösserer Menge in der Grössenverteilung vorkommen, können diese immer noch eine wichtige Rolle in zukunftige Beobachtungen spielen; wie z.B. bei Cassini zwischen 2010 und 2017. Eine solche Beobachtung kann uns Aufschluß über den Filterungsprozess am "Termination Shock" geben.

Die Grössenverteilung der IS Teilchen im Sonnensystem weicht stark von der ursprüngliche IS Grössenverteilung ab und hängt von den Staubeigenschaften, der Position im Sonnensystem und der Zeit im solaren Zyklus ab. Solche modifizierten Grössenverteilungen werden für feste Positionen entlang der IS Strömungsachse und für sich bewegende Objekte wie Saturn, Jupiter und den Main-Asteroid Ceres diskutiert. Implikationen für die spezifischen Missionen (Cassini, JUICE und Stardust) werden untersucht.

Die Vorhersage des IS-Flusses für Cassini zeigen, dass im Jahr 2010 der Fluss von 0.25 μm Staubteilchen maximal ist, und zwischen 2010 und dem Ende der Mission (2017) für kleinere andere Teilchen zu anderen Zeiten maximal ist. Für die Jupiter Icy Moons Explorer Mission (JUICE) zeigen die Simulationen, dass es eine optimale Gelegenheit für ISD Beobachtungen kurz vor und bei der Ankunft der Raumsonde am Jupiter im Jahr 2030 gibt. Schließlich werden die IS Bedingungen während der Stardust "Sample Return" Mission untersucht und die Simulationen mit den Ergebnissen (IS Proben) des Stardust Teams verglichen. Die Simulationen zeigen, dass die Beobachtungen zwar kompatibel mit einem interstellaren Ursprung der identifizierten IS Kandidaten sind, dass sie aber nicht als Beweis dafür genommen werden können.

Einsichten und Techniken dieser Arbeit können die Tür für die zukünftige Erforschung des IS öffnen. Die Kombination von astronomischen Beobachtungen mit Ergebnissen von in-situ-Messungen und Sample Return Missionen, und ihr Vergleich mit IS-Modellierungen wird die Staubeigenschaften einschränken und uns Inforamtionen über ihre Grössenverteilung vor und nach der Filterung auf ihrem Weg durch das Sonnensystem verschaffen. Daraus können wir Schlüsse über die unmittelbare galaktische Umgebung der Sonne und der Heliosphäre ziehen.

Abstract (English)

The space between the stars is filled with gas and interstellar dust (ISD). The dust grains cause extinction of the starlight that we observe and they play an important role in the evolution of galaxies and in the formation of stellar and planetary systems. The ISD has been long observed by astronomical methods, the grains were measured by in-situ measurements of spacecraft in the solar system and even samples of interstellar material have been brought back to Earth by the Stardust mission in 2006. Many questions on the composition, morphology and size distribution of ISD still exist today which require more and improved measurements. Modeling and understanding the ISD flow through the solar system is needed to interpret these observations and to fully extract the information on ISD grains carried by these measurements. Also, the modelling is necessary for designing and optimizing future ISD missions.

The modeling in this thesis follows this flow of ISD through the solar system taking into account three main forces: solar gravity, solar radiation pressure force and Lorentz force resulting from the motion of the charged grains through the interplanetary magnetic field (IMF). Simulations of dust trajectories over a large range of grain parameters β and Q/m were performed. β is the ratio of solar radiation pressure force to gravity and depends on the grain size, morphology and material. Q/m is the charge to mass ratio. The influence of solar radiation pressure force and Lorentz force on the trajectories, densities and fluxes were systematically studied.

Radiation pressure reduces gravitational attraction and can become even dominant ($\beta > 1$) for particles of about 0.2 μm radius, leading to a void region downstream from the Sun: the β-cone. The ISD flow under the influence of solar radiation pressure and gravity only is axi-symmetric, stationary and can even be calculated analytically. Lorentz force becomes stronger for smaller grains having higher Q/m and dominates for grains < 0.15–0.2μm. The azimuthal component of the IMF causes the grains to deflect towards or away from the solar equatorial plane depending on the polarity of the IMF. This focusing and defocusing effect occurs in a 22-year cycle, which makes the stream non-stationary and the flow pattern much more complicated. If not filtered at the termination shock, then very small grains of 0.1–0.15 μm would still reach the solar system at favorable times and would be reflected back upstream (called 'mirroring' in this thesis) causing locally enhanced concentrations. Since small grains are more abundant in the size distribution of the ISD, this may still play an important role in future observations like for Cassini between 2010 and 2017 and may teach us about filtering processes at the termination shock.

The size distribution of ISD in the solar system is strongly modified from the incoming ISD size distribution and varies with grain properties, location in the solar system and time in the solar cycle. These modified size distributions are discussed for a fixed position along the ISD flow axis and for moving objects like Saturn, Jupiter and the main-belt asteroid Ceres. Implications for specific missions (Cassini, JUICE and Stardust) are studied too.

The ISD flux predicted for Cassini at Saturn reveals that in 2010, the flux of 0.25 μm grains is maximum and that between 2010 and the end of the mission (2017) the flux of different smaller sizes of the grains is maximum at different times. For the JUpiter ICy moons Explorer (JUICE) the simulations showed that there is an optimum opportunity for ISD observations just before and at arrival of the spacecraft at Jupiter in 2030. Finally, the ISD conditions during the Stardust sample return mission are studied and the results of the simulations are compared to the preliminary findings (ISD samples) of the Stardust Team. The simulations indicate that the observations are compatible with an interstellar origin of the identified ISD candidates but cannot be taken as a proof.

Insights and techniques acquired and used in this thesis will open doors for future ISD research. Combining the knowledge derived from astronomical observations, sample return missions, and from comparing the ISD modeling to in-situ spacecraft measurements will constrain the grain properties and teach us about their size distributions before and after filtering on their way through the solar system. From this, we can learn about the immediate galactic environment of the Sun and the heliosphere.

Contents

1

Introduction

1.1 Dust in the Local Interstellar Cloud

The solar system is currently passing through a small cloud of low density weakly ionized gas and dust: the *Local Interstellar Cloud* (LIC, 0.1 - 0.3 H/cm^3, Frisch et al. (1999)). The LIC and the other surrounding clouds of the InterStellar Medium (ISM) are part of a larger structure containing hot and low density gas: the *Local Bubble* (Frisch et al., 2009). The solar system is located at the edge of the LIC, and moves in the direction of the neighboring *G-cloud*. The transition from the LIC to the G-cloud could happen in one of the next 10000 years or later.

Interstellar dust (ISD) is embedded in the gas of the LIC. Therefore the dust and the gas are assumed to have the same dynamical properties. The speed and direction of the ISD entering the solar system results from the relative motion of the Sun with respect to the LIC. The assumed dust upstream direction in this thesis was determined from in-situ dust detections with Ulysses and is equal to 259° longitude and 8° latitude (Frisch et al., 1999), with a relative velocity of 26 km/s. The upstream direction of the interstellar helium gas (254° longitude, 5.6° latitude) that was also detected by Ulysses (Witte et al., 1993) lies within the 1σ range of the determined dust direction (Baguhl et al., 1995b, 1996; Landgraf, 1998). Also astronomical (radial velocity) observations confirmed the results of Ulysses (Redfield and Linsky, 2008).

Levy and Jokipii (1976) predicted that ISD grains carry a net charge causing the particles to interact with the interplanetary magnetic field (IMF) through the Lorentz force. They predicted that this would exclude ISD grains with a high charge-to-mass-ratio from the (inner) solar system. Gustafson and Misconi (1979) and Morfill and Grün (1979) calculated the trajectories of these charged ISD particles, and concluded that there are phases during the solar cycle where ISD will be focused towards the solar equatorial plane and phases where the ISD will be defocused from the solar equatorial plane. Linde and Gombosi (2000) postulated that ISD smaller than about 0.2 μm would be filtered at the heliopause, so there is a filtering of particles at entry into the solar system.

In 1993, the first ISD particles were identified in the Ulysses dust data (Grün et al., 1993). Later, data from Galileo, Helios, and the early mission phase of Cassini were also analyzed for ISD (Altobelli et al., 2003, 2005, 2006). An overview of related papers is given in Section 1.2, Table 1.1.

Landgraf (2000) simulated the trajectories of ISD moving through the solar system, derived time-variable relative densities and fluxes of the dust, and compared these simulations to the observations of Ulysses between 1992 and 1999. From this, he estimated the mass distribution of ISD in our solar system. A bulk particle size of 0.3 μm was found, assuming that they are 'astronomical silicates' as described in Gustafson (1994). The observed flux of ISD fluctuated between $5 \cdot 10^{-5}$ and $2 \cdot 10^{-4}$ m^{-2}s^{-1} (Landgraf et al., 2003).

A review of the current state of knowledge of ISD and the in-situ measurements with spacecraft are given in Mann (2010), while Draine (2009) gives a synthesis of the current ISD models.

1.2 Interstellar dust observations

1.2.1 Astronomical observations

Astronomical observations of the extinction and polarization of starlight as well as infrared emission of the interstellar dust led to models of the size distribution and composition of interstellar dust (Weingartner and Draine, 2001; Zubko et al., 2004). Also the abundances of the materials in the gas phase of the interstellar medium constrained the abundances and materials of the dust that should be present in the ISM, assuming a Sun-like star as a reference. All of these models are using different details of the observations such as local features in the absorption spectra, but they have in common that silicates and carbons are used as constituents and that their size distribution is roughly described by a power-law. A commonly used model is the so-called "MRN-distribution" (Mathis et al., 1977) that has a power-law with slope -3.5 and a cut-off for silicate grains with radius larger than 0.25 μm and 1 μm for carbon grains. The MRN-distribution is drawn in Figure 1.1 from Krüger (2012) as straight lines for different density assumptions of Hydrogen. In this thesis, we assume the MRN-distribution as the size distribution in the LIC. Section 3.3 in this thesis describes the ISD size distribution in the LIC in more detail.

1.2.2 In-situ dust observations

The first in-situ observations of ISD in the solar system were made by Ulysses in 1993 using an impact ionization dust detector (Grün et al., 1993). Impact ionization dust instruments are based on the following principle: when dust grains impact on a target, the grain as well as part of the target material vaporizes and ionizes. This material expands from the "target" towards the "collector" of the instrument, on which an electrostatic potential is applied. The total charge on target and collector is measured as well as a rise-time of the charge signal. The rise-time depends on the particle impact speed whereas the total charge depends on the mass of the grain, impact speed, particle composition and density. The velocity can be determined within a factor of 2 for Ulysses (between 2 and 70 km s^{-1}) which causes the mass to be determined within a factor 6 (Grün et al., 1995). Similar dust instruments were flown on the Galileo mission to Jupiter (Grün et al., 1992) and the Geostationary Orbit Impact Detector (GORID) on the Russian Express-2 telecommunications satellite. Cassini also has an impact ionization dust detector, but includes also a time-of-flight mass spectrometer from which mass spectra and thus composition of the grains can be revealed (Srama et al., 2004a).

Although the directionality of the ISD grains was conform to the Helium upstream direction and the simulations of Landgraf (2000) explained the fluctuations of the observed flux between 1992 and 1999 very well, some questions remained unresolved. The size distribution of ISD in the solar system obtained from the Ulysses, Galileo and Helios measurements showed too many large grains in comparison to the ISD models obtained from astronomical observations and from cosmic abundances. Also the smaller grains were underrepresented in the in-situ data (see Figure 1.1, from Krüger (2012)) and in 2005 Ulysses observed a shift of the ISD upstream direction (Krüger et al., 2007; Strub et al., 2011) that is not yet understood. Part of the reduction of small grains is due to the filtering of the dust at the termination shock of the heliosphere (Linde and Gombosi, 2000; Slavin et al., 2010) and in the inner solar system (Landgraf, 2000). The larger grains are invisible to astronomical observations because they are too sparse (their total surface density[1] is too low). However, even when taking into account these arguments, there are still too many large grains in the in-situ data compared to what can be expected from cosmic abundances. What concerns the smaller grains, the filtering was not yet completely analyzed for the whole dataset of Ulysses and improvements in modeling (especially at the termination shock) are needed (see Section 6). The shift of dust in 2005 could possibly be explained by the forces acting on the dust grains on their trajectories in the inner solar system, although this has not been proven yet and has to be consistent with the observations of the filtering of the smaller dust grains in the solar system.

---

[1] the spatial density multiplied by the grain surface

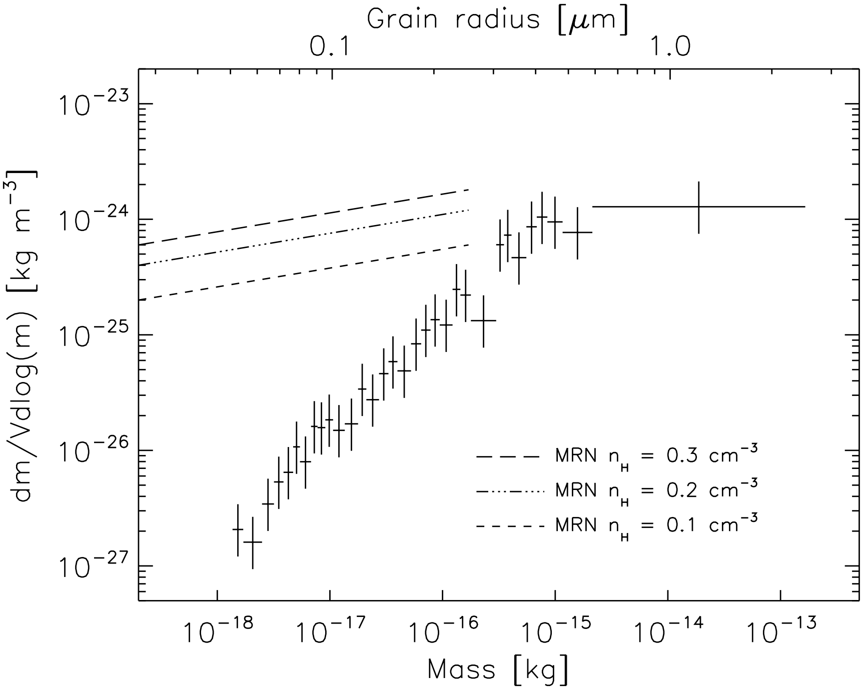

Figure 1.1: The MRN mass distribution for a Hydrogen density of 0.1, 0.2 and 0.3 cm^{-3} (dashed lines) from Mathis et al. (1977) and the ISD mass distribution from Ulysses data (crosses) between 1992 and 2008. The mass bins are chosen to contain equal amounts of dust counts. This graph is similar to Fig. 2 in Frisch et al. (1999) but uses an updated Ulysses dataset. Source: H. Krüger.

Meanwhile, the Cassini mission at Saturn keeps on recording dust impacts until 2017. These are inteplanetary as well as interstellar of origin. Altobelli et al. (2003) analyzed the interstellar dust impacts during the cruise phase of Cassini between Venus and Earth. Dedicated interstellar dust observation campaigns were fixed for Cassini in 2010, 2011 and 2012 using an optimal spacecraft pointing, and an on-going effort is currently taken in the CDA-team to extract the ISD grains from the data and to obtain their composition via their mass spectrum. For both mission planning as well as extraction of the ISD from the data, simulations of the relative flux and directionality are a helpful tool. Especially the question whether the dust trajectories can be approached by the radiation-pressure-only case or by simple straight trajectories can be answered by such analysis. Similar questions need to be answered when designing future missions like the JUpiter ICy moons Explorer (JUICE), SAmple Return of Interstellar Matter (Srama et al., 2009, 2012, SARIM and SARIM+) or the Cosmic DUst Near Earth (Srama et al., 2006, Cosmic DUNE) missions.

The data collected by all these missions (Ulysses, Galileo, Helios, Cassini) can be compared with simulations using different material assumptions and as such it is possible to find best fits of the filtered size distributions at different times and places in the solar cycle with these simulations and so the material properties of the grains can be constrained (Altobelli, 2004, 'β-spectroscopy'). Therefore a thorough understanding and analysis of the time and spatial variability of the flux of dust in the solar system is a prerequistite.

1.2.3 Sample-return missions

A third method to reveal information about the ISD grain properties is sample return of interstellar grains. The Stardust mission returned cometary and interstellar grains to Earth in 2006 using a collector

Mission	Period	Distance interval (AU)	Reference
Helios	1974 - 1980	0.3 - 1	1
Ulysses	1992 - 2007	2.5 - 5.4	2, 3, 4, 5
Galileo	1989 - 1996	0.7 - 5.4	6, 7
Cassini	1999	0.7 - 1.2	8
Stardust	1999 - 2003	1 - 2.7	9

Table 1.1: Overview of missions with ISD measurements, period and distance to the Sun. References. (1) Altobelli et al. (2006); (2) Grün et al. (1994); (3) Baguhl et al. (1996); (4) Landgraf et al. (2000); (5) Krüger et al. (2007); (6) Baguhl et al. (1996), (7) Altobelli et al. (2005); (8) Altobelli et al. (2003); (9) Krüger et al. (2004). Source: E. Grün.

of aerogel, and aluminum foils between the aerogel tiles. Up to now 3 candidate ISD grains were found in the aerogel, which is less than expected. In Section 4.3.1 in this thesis, the Stardust case is analyzed shedding light on how many grains could have been expected. Other mission proposals have been made for sample return of ISD like the SARIM and SARIM+ missions (Srama et al., 2009, 2012). Cosmic dust samples were taken in the 70s with high-altitude balloons and aircraft, but only grains $> 3\mu$m of interplanetary dust were found in the samples (Brownlee et al., 1977).

1.3 Goals of the thesis

This thesis explains the mechanism and demonstrates the modulation of the flow of ISD passing through the solar system by using numerical simulations of the dust trajectories. This is done at different locations in the solar system, at different times in the solar cycle and for different parameters of the grains. Apart from the variations in densities, fluxes and flow directions we also analyze how this affects the size distribution of the ISD in the inner solar system. The mechanism, the flow and the filterig of dust in the solar system are explained in Chapters 2 and 3 of this thesis.

Insight in the flow and filtering of ISD is a prerequisite to identify optimal observing conditions for present and future missions like Cassini, JUICE and SARIM. Simulating ISD fluxes, filtering and flow patterns for these specific missions helps to optimize the mission design and pointing profile for ISD measurements. Also, applying these simulations to past missions like Ulysses and Stardust benefits to the analysis of the in-situ data that are available now. The ISD filtering at Saturn, Jupiter and the Asteroid belt are explained in Chapter 4 as well as specific implications for the Cassini, JUICE and Stardust missions.

Finally, this thesis also aims at opening doors for future ISD research focused on expanding our knowledge on the ISD grain properties, size distribution in the LIC, and on explaining the discrepancies between in-situ and astronomical observations or specific features like the shift of ISD direction in 2005 as measured by Ulysses. How this thesis contributes to this is explained in Chapter 6.

In this thesis I made use of own contributions to published and unpublished papers, except if explicitely mentioned differently. Sections 1.1, 2, 3.1 and 4.1.1 and Appendices A are extracts from Sterken et al. (2012c) that has been published in February 2012. Sections 3.2, 3.3, 3.4, and the first parts of 4.1, 4.2, 4.3 and Appendix B are adapted from Sterken et al. (2012b) that has been submitted in May 2012. Section 4.2.1 is based on Sterken et al. (2012a), which is in press at the time of writing of this thesis. Section 4.3.1 is based on Sterken et al. (2012d) and will be submitted shortly after thesis submission (July 2012).

Throughout the thesis, the *size* of a particle denotes particle radius.

2

Modeling ISD dynamics

Simulations of the ISD grain trajectories were performed to study the motion of the ISD in the solar system. This chapter explains the modeling and dynamics of the ISD in the inner solar system, which is determined by three main forces: gravity, solar radiation pressure force and Lorentz force due to the relative motion of the charged ISD particles through the IMF. The forces on the grains, the equations of motion, the modeling of the IMF and assumptions on the grain properties are described in Section 2.1. At first, the ISD trajectories, velocities and densities resulting from gravity and radiation pressure force only are discussed in Section 2.1.1. Then Section 2.1.2 introduces the Lorentz force acting on a charged ISD grain. The modeling of the interplanetary magnetic field (IMF) is described in Section 2.1.3. A discussion on the grain parameters that were assumed is given in Section 2.1.4 and a description of the simulation tool, reference frames and further assumptions made for the simulation are given in Section 2.2. The model on which the simulation tool is based is similar to the Landgraf (2000) and Gustafson and Misconi (1979) models, but some extra options are included to be able to optimize the tool for various applications (see Section 2.1.3). Also, we preserve a wider grain parameter space which is useful for a broader analysis of the in-situ ISD observations as will be discussed at the end of this thesis in Chapter 6.

2.1 Dust dynamics in the heliosphere

The ISD dynamics are governed by solar gravity, radiation pressure force, and Lorentz forces due to the interaction of the charged particles with the IMF. Other forces like Poynting-Robertson drag, the Yarkowski effect, solar wind drag and Coulomb drag are not taken into account because of their low significance for the passage of the interstellar grains through the solar system (Altobelli, 2004). Gravitational forces of the planets in the solar system are not implemented in the simulations, but if necessary for a certain planetary mission, a correction factor can be applied to the resulting densities for the gravitational focusing and shielding of a planet (Jones and Poole, 2007; Staubach et al., 1997).

2.1.1 Radiation pressure force

The gravitational force of the Sun on a dust particle is

$$\mathbf{F_G} = -\frac{GM_\odot m_p}{|\mathbf{r}|^3}\mathbf{r}, \tag{2.1}$$

where G is the gravitational constant, $M_\odot$ the mass of the Sun, m_p the dust particle mass, and $\mathbf{r}$ the position vector of the dust particle with respect to the Sun.

The solar radiation pressure force exerted on a particle can be expressed as

$$\mathbf{F_{rad}} = \frac{A_p r_0^2}{c}\frac{\mathbf{r}}{|\mathbf{r}|^3}\int_0^\infty q_{pr}\, S_\lambda\, d\lambda \;=\; \frac{A_p\, Q_{pr}\, S_0}{c}\frac{\mathbf{r}}{|\mathbf{r}|^3} \tag{2.2}$$

(Schwehm, 1976) where A_p is the projected surface of a particle ($A_p = \pi\ a^2$ for a spherical particle, with a its radius), S_λ the solar flux per unit area and wavelength range at Earth distance from the Sun (r_0 = 1 AU), c the speed of light, q_{pr} and Q_{pr} are the efficiency factor of the radiation pressure, but Q_{pr} is weighted for the solar spectrum. Also, S_0 is the solar flux, weighted for the distance to the Sun.

Because both the gravitational and solar radiation pressure forces act radially and decrease with the squared distance to the Sun, it is common practice to express these two forces as one combined effective force

$$\mathbf{F} = \mathbf{F}_{(\mathbf{G+rad})} = -\frac{(1-\beta)GM_\odot m_p}{|\mathbf{r}^3|}\mathbf{r}, \tag{2.3}$$

where β is the ratio of the radiation pressure force to gravitational force, for a specific particle type.

$$\beta = \frac{|\mathbf{F_{rad}}|}{|\mathbf{F_G}|} = \frac{A_p\ Q_{pr}\ S_0}{c\ GM_\odot m_p}, \tag{2.4}$$

where β depends on the material and surface properties of the particle (e.g. morphology, color, particle mass, size). We assume in the simulations that the solar irradiance and the particle surface and material properties do not change during the time the particle flies through the heliosphere, so β is a constant. The parameter β is discussed in more detail in Section 2.1.4

Gravity and radiation pressure: trajectories

The effect of the combined gravitation and radiation pressure forces on the ISD trajectories is illustrated in Fig. 2.1. Particles of different β values are shown that initially move parallel to the X-axis with an impact parameter b = 1 AU. For particles with $\beta = 1$, the gravity and solar radiation pressure force cancel each other out, and the particle will move on a straight trajectory. In the case of $\beta < 1$, gravity dominates and pulls the particle into a hyperbolic trajectory, in the direction of the Sun. In the case of $\beta > 1$, the opposite occurs: the ISD particle will move on a hyperbolic trajectory away from the Sun.

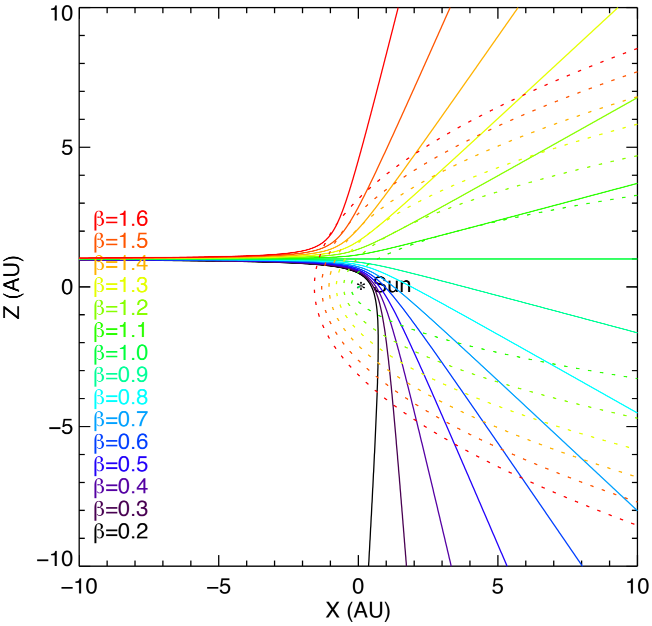

Figure 2.1: Trajectories of interstellar dust coming into the solar system, having the same impact parameter b, but different β-values. The dotted lines show the (analytically calculated) β-cones. The dust is assumed to initially move parallel to the X-axis, for simplification.

Assuming that the particle comes in parallel to the X-axis of a polar coordinate frame where $\theta = 0$ corresponds to the downstream dust direction, its equation of motion written in polar coordinates is

$$r = \frac{b^2 V_\infty^2}{GM_\odot(1-\beta)} \frac{1}{1+e\ \cos(\theta - \arccos(e^{-1}))} \quad \text{(for } \beta < 1\text{)} \tag{2.5}$$

$$r = \frac{b^2 V_\infty^2}{GM_\odot(1-\beta)} \frac{1}{1-e\ \cos(\theta - \pi + \arccos(e^{-1}))} \quad \text{(for } \beta > 1\text{)} \tag{2.6}$$

where r is the heliocentric distance of the particle with respect to the Sun, b the particle impact parameter, V_∞ the speed of the particle at entrance to the solar sytem, and θ the angle in polar coordinates corresponding to r. The eccentricity e of the hyperbolic trajectory is equal to

$$e = \sqrt{1 + \frac{V_\infty^4 b^2}{(GM_\odot(1-\beta))^2}}. \tag{2.7}$$

The radial and tangential velocity components of the particles at position r is given by

$\beta < 1$

$$V_r = \frac{GM_\odot(1-\beta)\ e\ \sin(\theta - \arccos(e^{-1}))}{bV_\infty} \tag{2.8}$$

$$V_\theta = \frac{GM_\odot(1-\beta)}{bV_\infty}\left(1 + e\cos(\theta - \arccos(e^{-1}))\right) \tag{2.9}$$

$\beta > 1$

$$V_r = \frac{GM_\odot(1-\beta)\ e\ \sin(\theta + \pi/2 - \arcsin(e^{-1}))}{bV_\infty} \tag{2.10}$$

$$V_\theta = \frac{GM_\odot(1-\beta)}{bV_\infty}\left(1 + e\cos(\theta + \pi/2 - \arcsin(e^{-1}))\right). \tag{2.11}$$

For $\beta < 1$ all trajectories with equal impact parameter b will cross each other at one point behind the Sun (focus) and a region of enhanced dust densities will be generated by a beam of initially parallel moving particles (Fig. 2.2). Since the trajectories are rotationally symmetric about the beam axis, only trajectories in one plane containing the beam axis are shown.

The focal distance d_f downstream from the Sun for particles with equal β and b-values is given by

$$d_f = \frac{b^2 V_\infty^2}{GM_\odot(1-\beta)} \frac{1}{2}. \tag{2.12}$$

For $\beta > 1$ particles are deflected away from the Sun and paraboloid-shaped regions are generated, which particles with a given β-value cannot enter. These are the so-called "β-cones" (dotted lines in Figs. 2.1 and 2.2).

The polar equation of the exclusion zones is expressed as

$$r = -\frac{4GM_\odot(1-\beta)}{V_\infty^2(1+\cos(\theta))} \tag{2.13}$$

(Altobelli, 2004). The upstream apex distance of the β-cone is given by

$$r_{\beta-cone,min} = -\frac{2GM_\odot(1-\beta)}{V_\infty^2}. \tag{2.14}$$

The deflections from straight line trajectories are shown in Figs. 2.3 and 2.4 for particles with $\beta = 0.5$ and $\beta = 1.6$, respectively. Upstream of the Sun, the deflection (in distance and angle) and acceleration

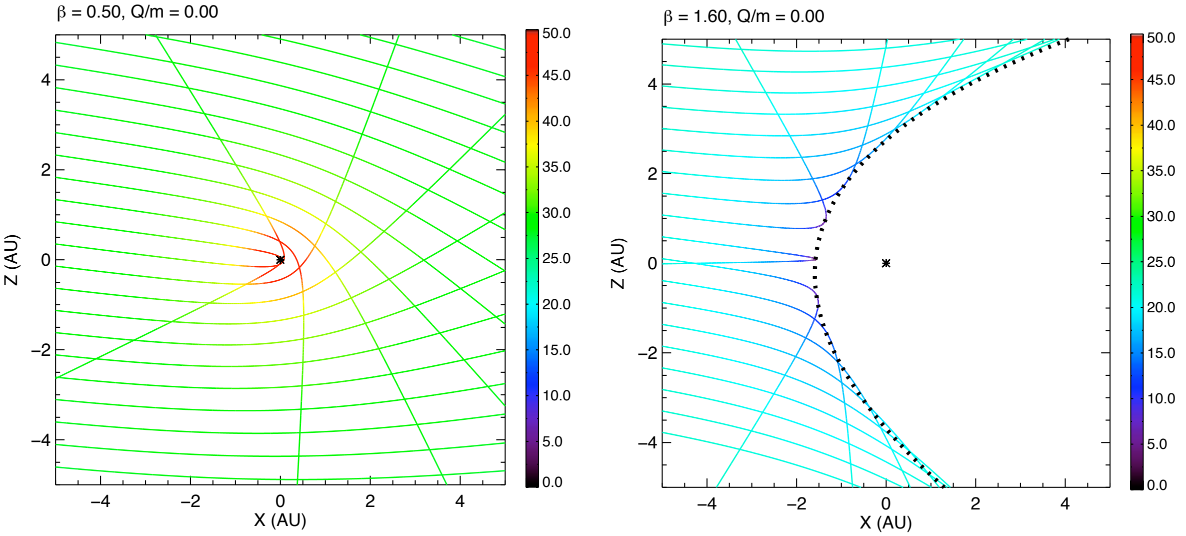

Figure 2.2: Numerically calculated trajectories of particles with $\beta = 0.5$ (left) and $\beta = 0.5$ (right), but with different impact parameters b, in the ISD frame. For $\beta < 1$ (left), the dust is concentrated downstream from the Sun, the particles accelerate near the Sun and decelerate afterwards again to their original speed. Particles with $\beta > 1$ (right) and no charge will decelerate near the Sun, and then accelerate again to their original speed. The β-cone where particles with $\beta > 1.6$ cannot enter, is visible. The colorbar shows the scale of the absolute particle speed with a maximum of 50 km/s. The particles are started at -50 AU from the Sun in 1997, and reach the region of the Sun about 9.5 years later.

(in speed) are small, and higher deflections are concentrated on trajectories close to the beam axis. Downstream from the Sun, the scattering by solar gravitation and radiation pressure forces becomes strong and straight line trajectories can no longer be used as proxies for interstellar particle trajectories.

The existence of the β-cones may help us restrict ISD particle properties by comparing the observations of the flux, density, direction, and speed of the particles, with the theoretically calculated values (Landgraf et al., 1999a). Such particle-dynamics studies can constrain the β-value of the ISD, and thereby providing some information about particle properties such as its composition or surface roughness. This study is referred to as β-*spectroscopy* (Altobelli, 2004). However, the distribution of ISD in the heliosphere is much more complex than presented here, because it is modified by the Lorentz force due to the interaction of the IMF with the charged ISD particles. For β-spectroscopy, care has to be taken in the selection of the timeperiods of the observations, as well as the locations, to avoid mixing up the effects of eventual Lorentz forces with the β-cones.

Gravity and radiation pressure: densities

The density can be analytically expressed in polar coordinates as

$$n(r,\theta) = n_\infty \frac{b^2}{r\sin(\theta)\ |2b - r\sin(\theta)|} \quad (\theta > 0) \tag{2.15}$$

where

$$b = \left| \frac{r sin(\theta)}{2} \pm \sqrt{\left(\frac{r\sin(\theta)}{2}\right)^2 + r\frac{GM_\odot(1-\beta)}{V_\infty^2}(1+\cos(\theta))} \right| \tag{2.16}$$

(Landgraf et al., 1999b) with n the local density, n_∞ the undisturbed density of the ISD at entrance to the solar system, b the impact parameter and r and θ the polar coordinates of the dust particle, with respect to the Sun. For $\beta > 1$ every position outside the β-cone is reached by two different trajectories.

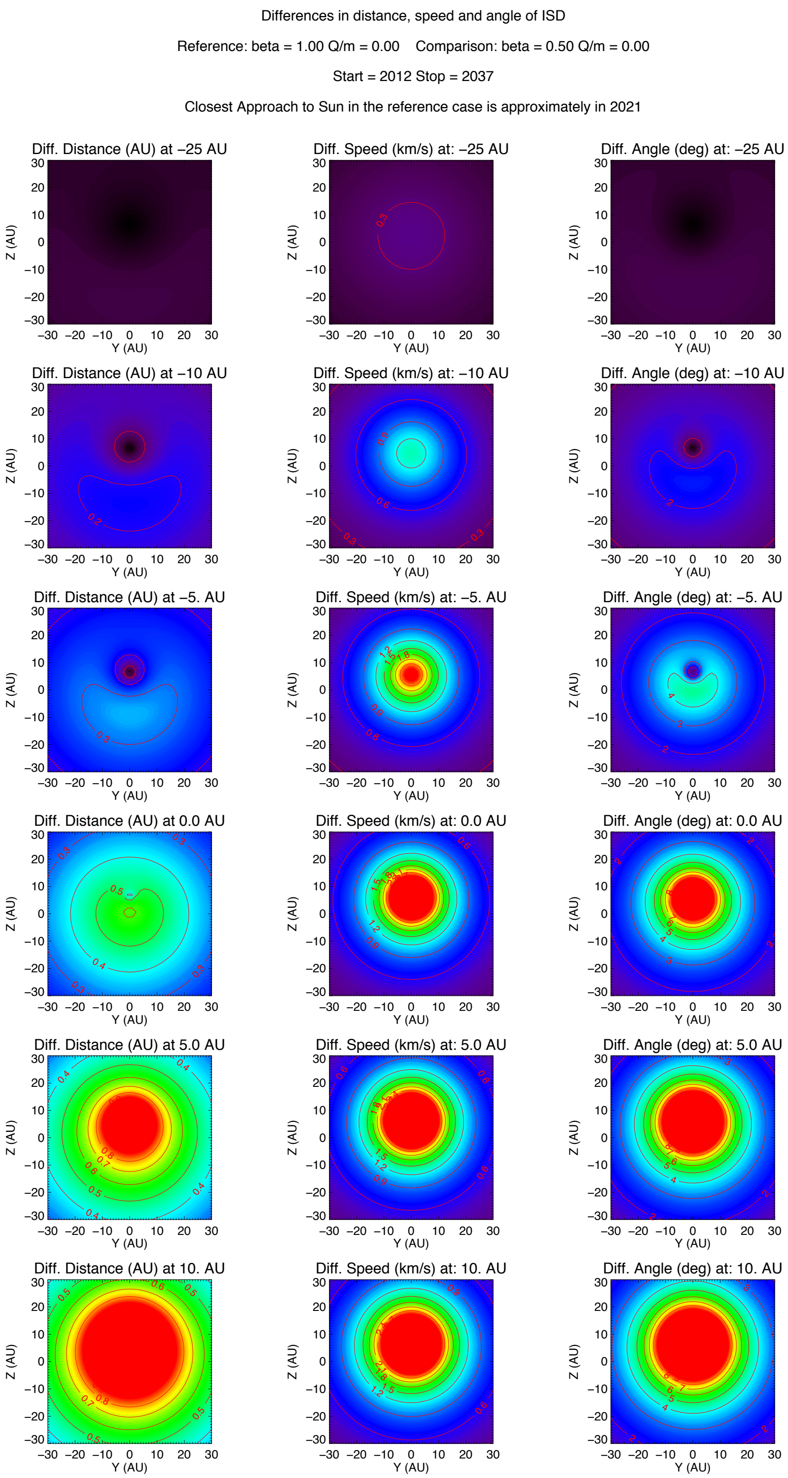

Figure 2.3: Absolute differences in position, velocity, and direction, in "sliced" planes at different positions from the Sun along the X-axis of the ISD-frame. The difference between the case for $\beta = 1$, Q/m $= 0$, and $\beta = 0.5$, Q/m $= 0$ is shown. The red regions denote trajectory differences of more than 1 AU (left), velocity differences of more than 5 km/s (middle), and angular differences of more than 5 degrees (right). The plot illustrates in what extent the straight-line approximation can be used.

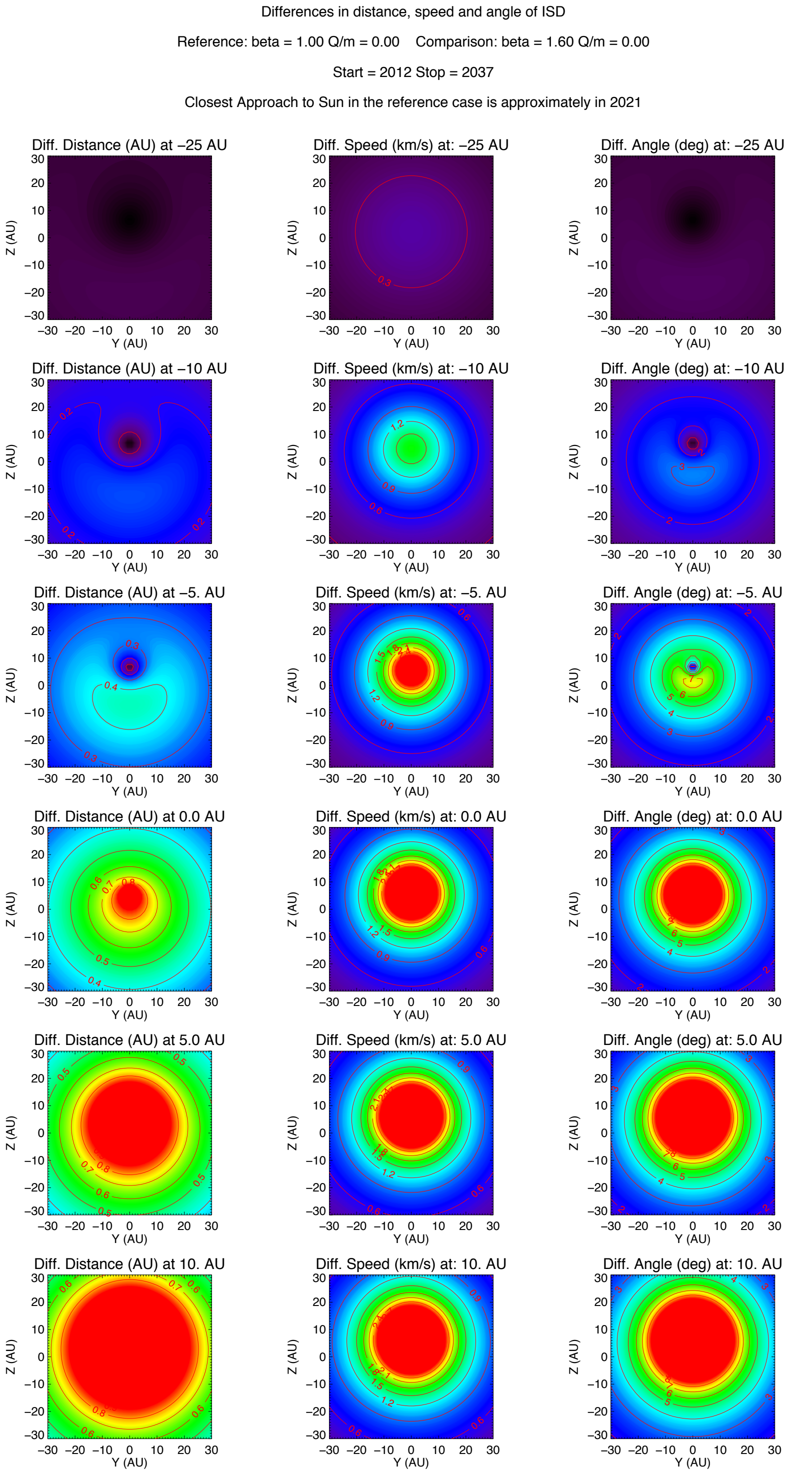

Figure 2.4: Absolute differences in position, velocity, and direction, in "sliced" planes at different positions from the Sun along the X-axis of the ISD-frame. The difference between the case for $\beta = 1$, Q/m $= 0$, and $\beta = 1.6$, Q/m $= 0$ is shown. The red regions denote trajectory differences of more than 1 AU (left), velocity differences of more than 5 km/s (middle), and angular differences of more than 5 degrees (right).

Since Eq. 2.15 only gives the contribution to the number density of one solution, the contributions from the different solutions that reach a point have to be added up to calculate the total number density at a point (Landgraf et al., 1999b). The distribution of ISD in the heliosphere due to solar gravity and radiation pressure force is axisymmetric around the axis along the inflow vector of the dust. In Fig. 2.5 scatter plots of the densities at different slices perpendicular to the particle beam are displayed at different distances to the Sun. Downstream from the Sun the dust concentrations along the beam axis are visible for the $\beta < 1$ case. Close to the Sun, higher speeds can be seen thanks to the solar acceleration. In case of $\beta > 1$, the deceleration close to the Sun and the formation of the β-cone becomes apparent with some density enhancements just outside of the β-cone.

Besides the scatter plots shown in Fig. 2.5, 3-D density maps have also been calculated from numerically integrated trajectories. The β-cones are visible in the ISD density map of the solar system (see Fig. 2.6): for particles with $\beta > 1$, there is a depletion of particles downstream of the Sun. When $\beta < 1$, the density of ISD downstream of the Sun increases (gravitational focusing of the Sun). Figures 2.6 are derived from the numerical trajectory simulations by counting the number of grains in the grid cells per time bin. They are drawn in the ecliptic reference frame. The graphical representation was developed by Sascha Kempf. The density plots are fixed at one single observation time. The trajectory plots have a fixed starting time for the particles, but time evolves along the plotted trajectory. Since the ISD flow with only radiation pressure force and solar gravity is stationary, the density plots and trajectory plots will match each other. However, when Lorentz forces are taken into account, this is no longer the case.

Gravity and radiation pressure: closest distance to the Sun

The closest approach distance to the Sun (perihelion distance r_{CA}) of the hyperbolic trajectories of interstellar grains through the planetary system is given by

$$r_{CA} = \frac{b^2 V_\infty^2}{GM_\odot(1-\beta)} \frac{1}{(1+e)} \quad (\text{for } \beta < 1) \tag{2.17}$$

$$r_{CA} = -\frac{b^2 V_\infty^2}{GM_\odot(1-\beta)} \quad (\text{for } \beta > 1). \tag{2.18}$$

To gain insight into the way that particles are spread or focused with respect to their starting position, we plot the closest distance to the Sun of the ISD. The resulting plot can be used to define the minimum size of the area where particles are started from in the simulation. As an example, we plot the *closest approaches* for particles with $\beta = 0.5$ and $\beta = 1.6$ in Fig. 2.7. The plots are drawn in the ISD frame. The dotted lines are the closest approaches to the Sun for a reference case with $\beta = 1$ and no charge, so the reference particles move in straight lines towards the Sun. Their closest distance to the Sun is equal to the distance of the particle on the starting grid to the center of the starting grid (the contour lines in Fig. 2.7 are thus circular). The offset in the Z direction is a result of the obliqueness of the incoming dust vector with respect to the solar equatorial plane.

Particles with $\beta < 1$ are attracted near the Sun. Therefore, in order to get the total ISD density in a radius of 10 AU around the Sun, one needs to start the particles from a wider range than 10 AU in the start plane. How wide this range should be can be estimated from the plots. The plots show how much the particles are focused and defocused with respect to the Sun, in comparison with the case for straight trajectory lines.

2.1.2 Lorentz forces

ISD particles moving through the heliosphere collect ions and electrons from the ambient solar wind plasma. They also emit electrons, mainly owing to the photo-ionionization effect of the solar UV radiation. The electron fluxes are much higher than the ion fluxes, and the amount of electrons emitted through the photo-ionization effect is more than electron collection through the solar wind plasma. Therefore the particle will get a positive charge, which brings the emission and collection currents into equilibrium. Since the solar UV radiation intensity and the solar wind plasma density both decrease quadratically with

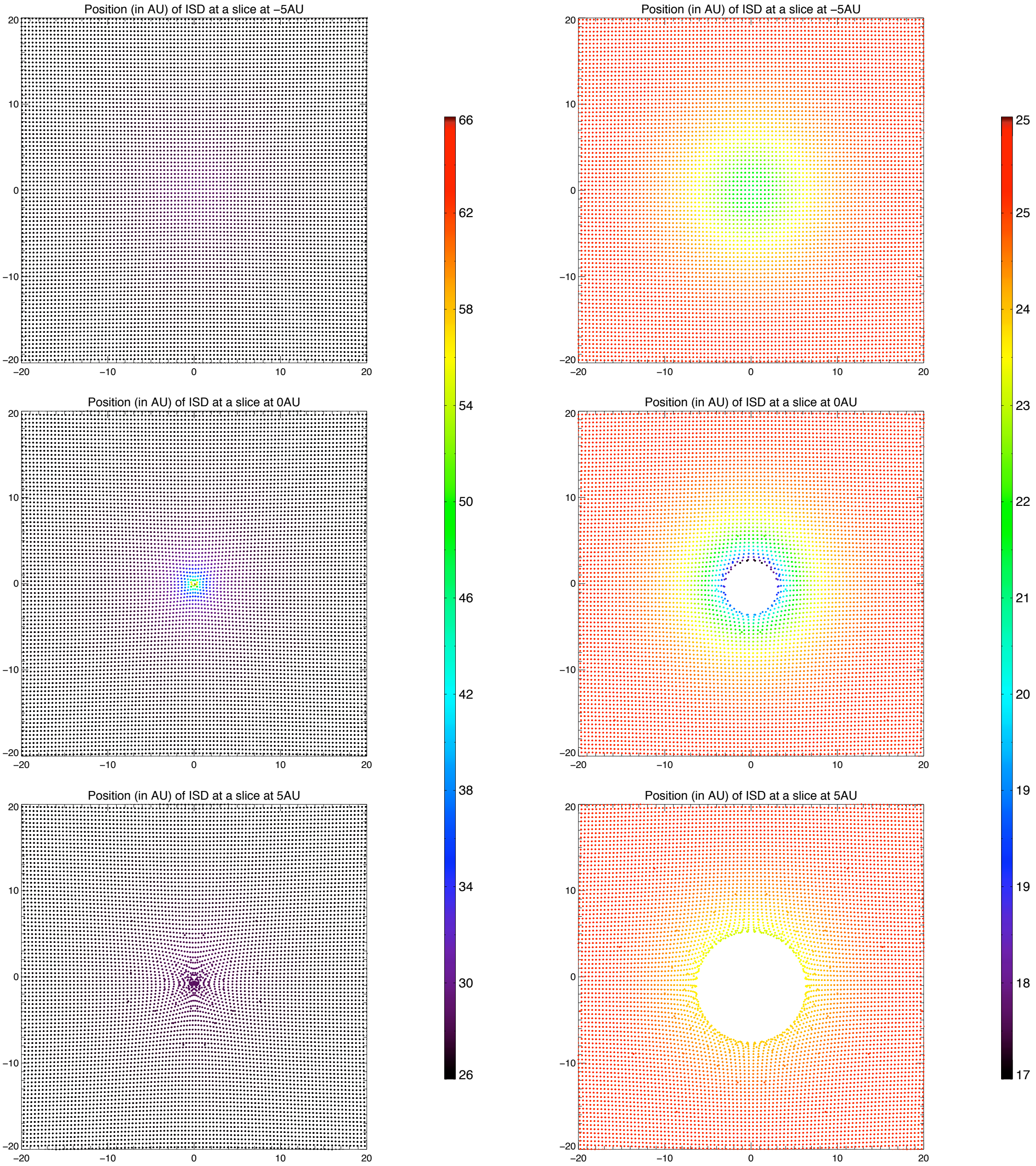

Figure 2.5: Cross-section of the trajectories for $\beta = 0.5$ (left) and $\beta = 1.6$ (right), through different YZ-planes in the ISD frame. The color denotes the particle speed in km/s. The particles are started at 50 AU distance from the Sun. The speed of the particles is higher near the Sun for grains with $\beta < 1$ and slower near the Sun for grains with $\beta > 1$. Farther away from the Sun, they slow down to their original starting speed (left) or accelerate again towards their original speed (right). The density is enhanced downstream from the Sun for $\beta < 1$ and the β-cone is visible for $\beta > 1.6$.

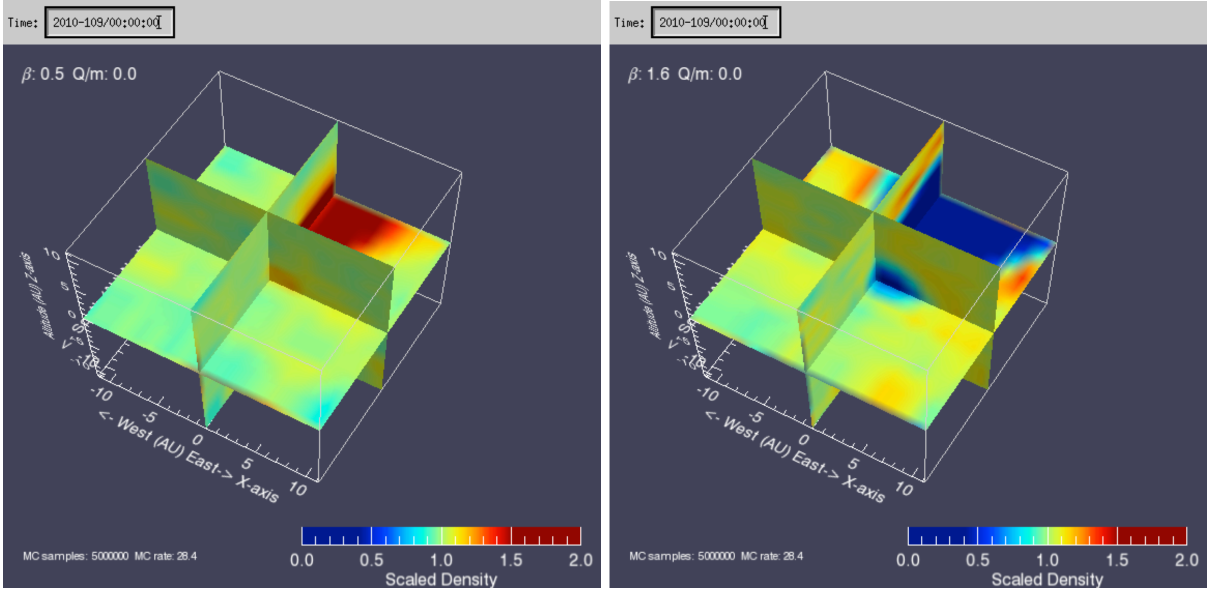

Figure 2.6: Relative density map of ISD in the solar system up to 10 AU from the Sun, for particles with $\beta = 0.5$ (left) and $\beta = 1.6$ (right). The density is shown with respect to the undisturbed ISD density at infinity, and the color scale is limited to an upper relative density of 2. The graphical representation was developed by Sascha Kempf. For grains with $\beta = 0.5$, the relative density downstream of the Sun is enhanced thanks to the gravitational focusing (left). The β-cone for $\beta = 1.6$ is visible as a conically-shaped volume of depletion (right).

increasing distance to the Sun, this charge stays in equilibrium (Horányi, 1996). It has been estimated that the surface potential on graphite grains at 1 AU from the Sun is between +0.5 V and +6 V (depending on solar wind conditions), while the surface potential on silicate grains at 1 AU is about +4 V and +14 V (Mukai, 1981). With changing solar wind conditions, the potential of the grains will fluctuate too, but these fluctuations are only small and temporary. For the ISD simulations, we assume spherical unfluffy grains, with an equilibrium potential of +5V, which is compatible with the Cassini measurements (Kempf et al., 2004) of charged grains. These measurements confirm the theoretical predictions of the charges on ISD grains. The net charge on the dust grain is then

$$q = 4\pi\epsilon_0 \, a \, U \tag{2.19}$$

where ϵ_0 is the electric permittivity of the vacuum ($8.85\,10^{-12}$ F/m), a the radius of the grain, and U the surface potential. Assuming a spherical grain with density ρ and mass m, the charge to mass ratio becomes

$$\frac{Q}{m} = \frac{3\epsilon_0 U}{\rho a^2}. \tag{2.20}$$

When the charged particles move through the IMF, they experience Lorentz forces. The Lorentz force exerted on ISD depends on the particles charge to mass ratio (Q/m), its velocity with respect to the solar wind velocity ($\dot{\mathbf{r}}_{p,sw}$) and on the field strength of the IMF ($\mathbf{B}_{sw}$) at the location of the particle. The equation of motion of the ISD becomes

$$\ddot{\mathbf{r}} = -\frac{(1-\beta)GM_\odot}{|\mathbf{r}^3|}\mathbf{r} + \frac{Q}{m}\left(\dot{\mathbf{r}}_{p,sw} \times \mathbf{B}_{sw}\right). \tag{2.21}$$

At large distances from the Sun, the main IMF component is the azimuthal component of the IMF (see Section 2.1.3), so the main effect of the Lorentz force is to deflect the ISD particles towards or away from the solar equatorial plane (Morfill and Grün, 1979; Gustafson and Misconi, 1979). Whether particles will be focused or defocused depends on the phase of the solar cycle. The Lorentz forces can narrow down

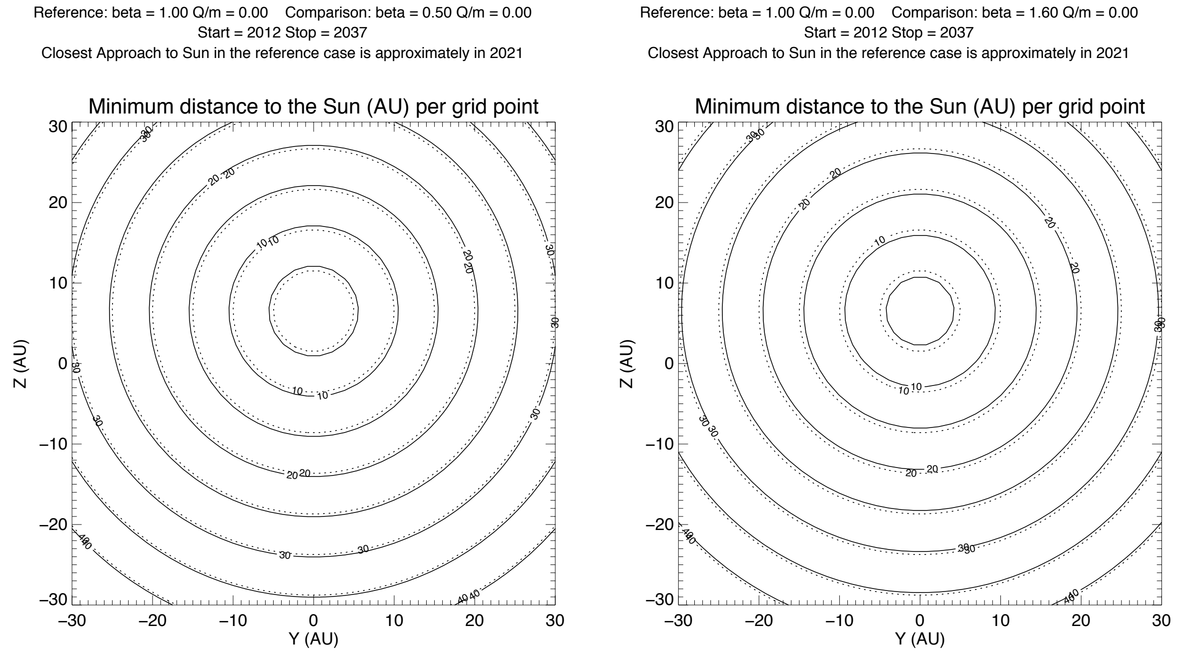

Figure 2.7: Distance to the Sun during the *closest approach* for ISD particles with $\beta = 0.5$ (left), $\beta = 1.6$ (right) and Q/m = 0, i.e. their closest distance to the Sun projected on a plane. The axes show the original position of the ISD particles in AU, in the ISD frame, while the numbers in the contour lines show their closest approach distances. The dotted lines are the reference case where $\beta = 1$ and Q/m = 0 (particles fly in straight lines, thus the dotted contour lines are circles). The contour lines for $\beta = 0.5$ are outside of the dotted contour lines, because the ISD is focused towards the Sun (so that a larger starting area is needed to investigate the ISD in an area of e.g. 10 AU around the Sun). The particles are 'pushed away' by solar radiation pressure force for $\beta = 1.6$, so less space is needed on the starting grid to investigate a certain area in the solar system.

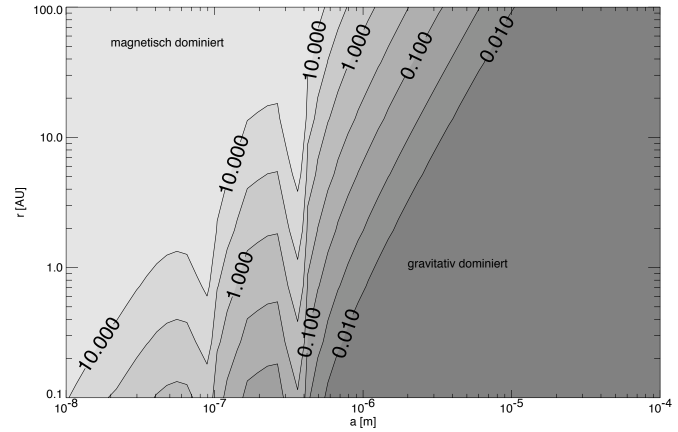

Figure 2.8: Ratio of Lorentz force to "effective gravitation" for several particle sizes and at different distances from the Sun, from Landgraf (1998).

the β-cones, or the opposite, enhance the β-cones. The importance of the Lorentz force with respect to solar gravity increases linearly with the distance to the Sun:

$$\left.\begin{array}{lcl} F_L & \propto & r^{-1} \\ F_G & \propto & r^{-2} \end{array}\right\} \Rightarrow \frac{F_L}{F_G} \propto r. \tag{2.22}$$

Only closer to the Sun ($<\sim$ 2 AU) will the radial component of the magnetic field play a larger role and the Lorentz force and gravity are not linearly related, but relate as

$$\frac{F_L}{F_G} \propto \frac{\sqrt{r^2+1}}{r^2} \tag{2.23}$$

where r is given in AU; i.e., for distances less than 1 AU, $F_L \propto F_G$. At 1 AU, $F_L = 1.4\ F_G$ and at 2 AU, $F_L = 2.23\ F_G$. The effects of the Lorentz forces are discussed in detail in Section 3.

Figure 2.8 gives an overview of the relative importance of the Lorentz force, solar gravitation, and solar radiation pressure force, from Landgraf (1998). Solar gravitation and solar radiation pressure force were combined into one "effective gravitation" term (see Eq. 2.3, Section 2.1.1). The ratio of the Lorentz force to the effective gravitation is given as function of particle size a and distance to the Sun r. Assumed is a β-particle-size dependency (β-curve) for astronomical silicates, from Gustafson (1994). The ratio of gravity and radiation pressure force is 1 for particles of sizes of approximately 0.1 μm and 0.35 μm, which can be seen in Fig. 2.8 from Landgraf (1998): gravity and radiation pressure cancel, and the Lorentz force takes over entirely. The plot shows

$$\frac{|\mathbf{F_{G+rad}}|}{|\mathbf{F_L}|} = \frac{|1-\beta(a)|\,\frac{Gm_p(a^3)M_\odot}{r^2}}{\frac{3\epsilon_0 U}{\rho a^2}\,|\mathbf{v_{p,sw}} \times \mathbf{B(r)}|}. \tag{2.24}$$

2.1.3 Modeling the interplanetary magnetic field

The Sun expels a vast amount of plasma into the heliosphere: the solar wind. This plasma, streaming radially outward, convects the magnetic field of the Sun along on its way into interplanetary space. Because the Sun is rotating, the field lines are winding up, forming a spiral - the so-called *Parker spiral* - parallel to the solar equatorial plane (Parker, 1958). In the Parker model, the radial component of the IMF field strength B_r decreases with the square of the distance to the Sun, while the azimuthal component B_ϕ decreases only linearly. The equations describing the IMF are

$$B_r = \pm B_0 \cdot \left(\frac{r_0}{r}\right)^2 \tag{2.25}$$

$$B_\phi = \pm\frac{B_0 \cdot \Omega_{Sun}}{V_{SW}} \cdot (r - r_0) \cdot \left(\frac{r_0}{r}\right)^2 \cdot \sin(90^\circ - \theta) \tag{2.26}$$

$$B_\theta = 0 \tag{2.27}$$

(Parker, 1958) where r, ϕ, and θ are the radial distance, the longitude and latitude of the position of the dust particle in the solar wind, respectively (in a coordinate system that has its XY-plane in the solar equatorial plane). In this model we assume one rotation every $\simeq 25.38$ days (sidereal period) for both the poles and the equator of the Sun. Here, $B_0 = 2300$ nT is the magnetic field strength at a reference distance r_0 from the Sun, which is the distance from the center of the Sun where the field lines are assumed to go radially outward. The reference distance in the simulation model is 10 solar radii (Parker, 1958). The field strength at the Earth is 5 nT.

Equations 2.25 and 2.26 show that, at large distances, the IMF is dominated by its azimuthal component. During solar minimum, the solar wind speed varies between about 400 km/s at the solar equator, and 800 km/s at higher latitudes. At solar maximum, the speeds are more moderate and more uniformly divided over the Sun. For the model, we adapted a constant solar wind speed at all latitudes of 400 km/s. Since the azimuthal component of the IMF is inversely linear to the solar wind speed, and since we assume that the solar wind blows radially outward of the Sun, the Lorentz force becomes independent of the solar wind speed (Gustafson and Misconi, 1979)[1]:

$$F_L = \frac{Q}{m} \begin{pmatrix} \dot{r}^{ecl}_{p,r} - \dot{r}^{ecl}_{sw,r} \\ \dot{r}^{ecl}_{p,\phi} - 0 \\ \dot{r}^{ecl}_{p,\theta} - 0 \end{pmatrix} \times \begin{pmatrix} B_0 \cdot \left(\frac{r_0}{r}\right)^2 \\ \frac{B_0 \cdot \Omega_{Sun}}{V_{SW}} \cdot (r - r_0) \cdot \left(\frac{r_0}{r}\right)^2 \cdot \sin(90^\circ - \theta) \\ 0 \end{pmatrix} \tag{2.28}$$

with F_L the Lorentz force, $\frac{Q}{m}$ the charge to mass ratio of the particle, $\dot{r}^{ecl}_{p,r}$ the radial velocity of the particle in the ecliptic coordinate frame, $\dot{r}^{ecl}_{sw,r}$ the radial solar wind velocity in the ecliptic coordinate frame, and $\dot{r}^{ecl}_{p,\phi}$ and $\dot{r}^{ecl}_{p,\theta}$ are the azimuthal and elevation components of the particle velocity in the ecliptic coordinate frame.

The solar magnetic field is modeled as a dipole, where the magnetic field lines extend into interplanetary space. The Parker model determines the direction (shape) and strength of the IMF, but the polarity of the field (positive when field lines are directed "outward" from the Sun, negative when they are directed "inward" towards the Sun) depends on the position of the dust particle with respect to the *Heliospheric Current Sheet* (HCS). The HCS divides the regions of positive polarity from the regions of negative polarity and is modeled as a flat sheet in the simulations. The modeled HCS is aligned with the solar equatorial plane during solar minimum, while at solar maximum, the 'sheet' is rotated by 90° and is aligned with the solar rotation axis. As a result, the modeled HCS turns 360°, at a steady rate of 22 years around a reference axis[2] in the solar equatorial plane. In the meantime, the HCS turns around the solar rotation axis in 25.38 days. At solar maximum, an observer in the solar equatorial plane, would thus see 50% of the time a negative polarity, and the other 50% of the time a positive polarity. Because the equatorial plane of the Sun is tilted with respect to the ecliptic frame, an observer at the Earth will observe two 'sectors' of opposite polarity during one solar rotation. In reality, the HCS is not flat but slightly warped at solar minimum (hence, an observer at the Earth would observe more (e.g. four) sectors of opposite polarity during one solar rotation), and during solar maximum there is no longer any clear dipolar structure. However, the flat sheet model is a good approximation for our purposes.

---

[1] We assume that the particle charge does not change significantly because of the different solar wind plasma conditions.

[2] Axis in the solar equatorial plane that points to vernal equinox at time t_0

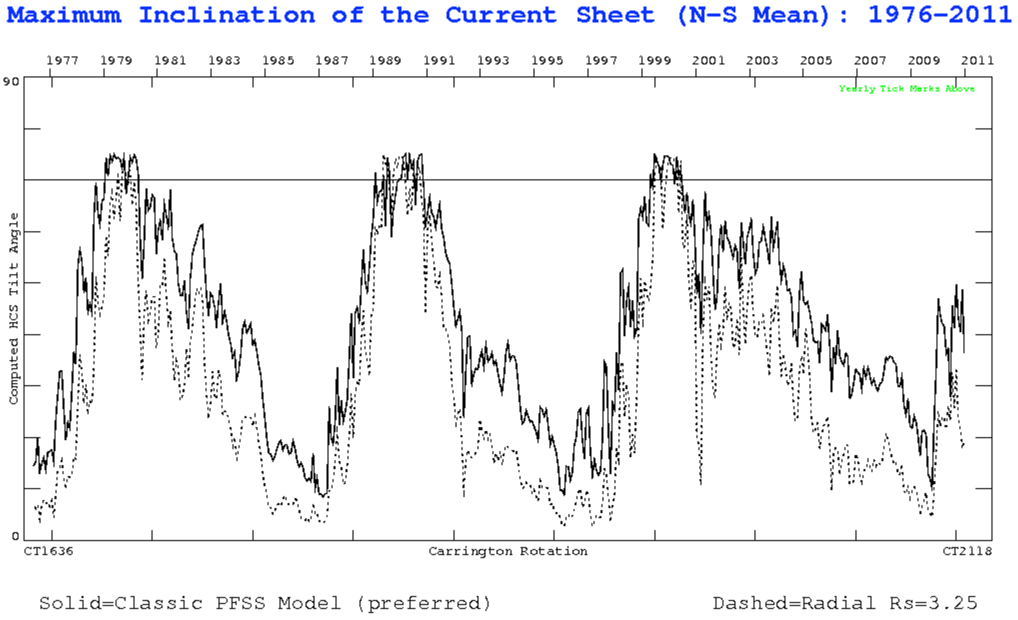

Figure 2.9: Computed tilt of the heliospheric current sheet, from Solar Wilcox Observatory (Hoeksema, 2011).

The field polarity in the model is thus determined by the phase of the solar cycle and the latitude and longitude of the observer. Three different models of the IMF are included in the simulations, and the choice of model to use depends on the particle location:

1. The HCS is modeled to turn at a steady rate of 22 years around a reference axis in the solar equatorial plane, and the magnetic field strength at the location of a dust particle is averaged over one solar rotation. The solar cycle reference time, t_0, is July 1974, where the Sun was modeled to be in solar minimum (HCS is aligned with solar equatorial plane, the northern solar hemisphere has a positive polarity, and the southern solar hemisphere has negative polarity.
   This model can be used when the speed of the particles is not too fast with respect to the rotation of the Sun, which is the case for ISD. Since we average the IMF over one solar rotation, the results are also only applicable to situations where shorter timescales are unimportant, i.e. outside 1-2 AU. Landgraf (2000) has used these assumptions for the IMF modeling.

2. The HCS is modeled to turn at a steady rate of 22 years around a reference axis in the solar equatorial plane, and the true local magnetic field is calculated at each location of the dust particles, instead of averaging out over one solar rotation. This model is useful for calculations closer to the Sun, for high time-resolution calculations, or for fast particles like nanodust with velocities of 100 to 200 km/s.

3. The HCS angle is determined by the modeling from solar data between 1976 and 2009 from the Wilcox Solar Observatory (Hoeksema, 2011). The HCS angle is thus slightly different from the angles of the steady-state rotation of the previously described model. The magnetic field is averaged over one solar rotation. The HCS angle is shown in Fig. 2.9, from 1976 until 2009.

An overview of solar maxima and minima are given in Table 2.1. In model 1, the heliospheric current sheet (HCS) turns at a steady rate during 22 years. In the WSO model, the angle of the HCS is derived from solar magnetic field data from the Wilcox Solar Observatory (WSO) (Hoeksema, 2011).

Year (model 1)	Year (model WSO)	Min / Max	Cycle
1974.5	1976	Min	defocus
1980		Max	defocus → focus
1985.5	1987	Min	focus
1991		Max	focus → defocus
1996.5		Min	defocus
2002	2000	Max	defocus → focus
2007.5	2009	Min	focus
2013	2013	Max	focus → defocus
2018.5	2018.5	Min	defocus
2024	2024	Max	defocus → focus
2029.5	2029.5	Min	focus

Table 2.1: An overview of the modeled solar cycle.

2.1.4 Particle properties, β and Q/m

The study of the ISD dynamics is governed by three parameters that determine the path of the dust through the solar system: β, Q/m, and time. The β determines the solar radiation pressure force to gravity ratio, which reduces the number of parameters from four to the stated three. The ratio Q/m and time (related to the phase of the solar cycle) determine the Lorentz force. Both β and Q/m are fairly unknown, since we do not know the exact composition, mineralogy, structure, and material properties of ISD. Realistic boundaries are set for these parameters through previous laboratory studies of dust and astronomical observations of the ISD (Draine, 2009). We perform the dust simulations for a wide range of parameters.

Discussion of parameter β

Dust particles are characterized by their mass, size, composition, and shape which affect the dynamics of interstellar grains within the solar system. All of these parameters are not, or only weakly, constrained for local interstellar grains. Astronomical observations of UV extinction and infrared emissions indicate carbonaceous particles (polycyclic aromatic hydrocarbons, PAHs, or graphite grains) and amorphous silicate grains. Analysis of in-situ Ulysses data by Landgraf et al. (1999a) suggests absorbing silicates for the particles penetrating the planetary system. Compositional analyses of collected interstellar grains by the Stardust mission are not available yet.

The interactions of dust with solar radiation are determined by the optical properties of the particle that are a function of the particle parameters size, composition, and shape. In Eq. 2.4 the cross section A_p and the efficiency factor Q_{pr} for radiation pressure describe this interaction. For particles $>> 1$ μm, Q_{pr} is roughly constant and depends only on the absorption efficiency of the particle material at visible wavelengths. Since absorption occurs at the surface of the particles, surface composition is important rather than bulk composition, which may be different. The size dependency of β is proportional to $\frac{A_p}{m} \sim \frac{1}{a\rho}$.

For particles $< 1\mu$m, scattering of sunlight also becomes important. The scattering efficiency can be calculated for spherical particles by Mie-scattering theory and for particles that are much smaller than the wavelength, Rayleigh scattering can be applied (Burns et al., 1979). For nonspherical particles, elaborate scattering algorithms have often been applied, and even laboratory simulations are used to obtain relevant Q_{pr} values for determining relevant β values (see Gustafson et al. (2001) for a review). Kimura and Mann (1999) calculated β-curves for fluffy carbon and silicate particles (Fig. 2.10). Very fluffy fractal particles are not likely to survive the harsh interstellar environment for long; therefore, we consider compact particles to be nominal.

The β-curve for astronomical silicates (Gustafson, 1994) is adapted to the Ulysses observations to have

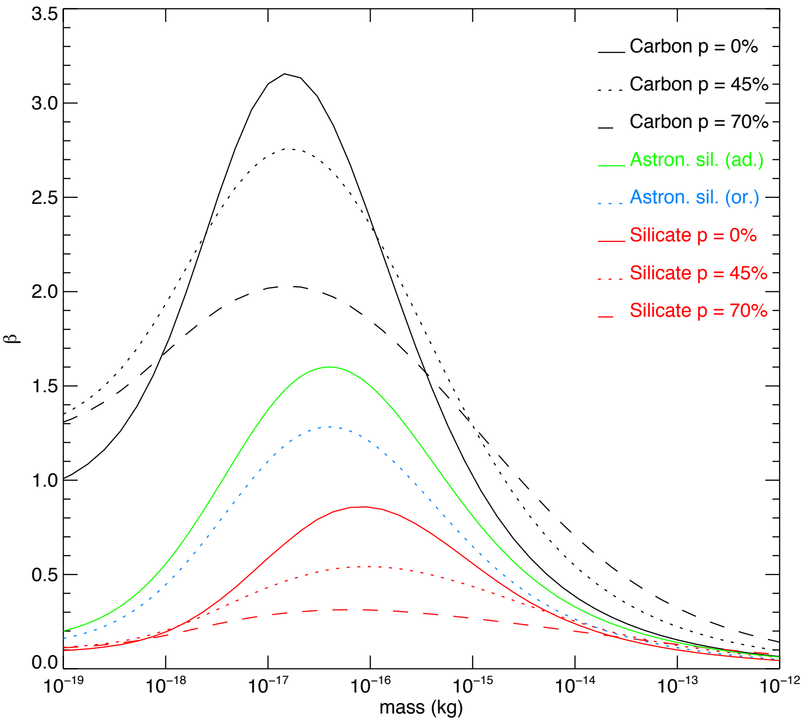

Figure 2.10: β-curves from Kimura and Mann (1999) showing the influence of porosity on the β-value of the dust, namely a flattening of the curve.

a maximum β-value of $\beta_{max} = 1.6$ (Landgraf et al., 1999a). This curve (see Fig. 2.11) is used to produce 7 nominal cases as defined in Table 2.2, which illustrates a few realistic sets of parameters and particle sizes. However, since the properties of interstellar particles and their respective β-values are not strongly constrained, we simulated dust trajectories for a wide range of β and Q/m values instead of following only one curve.

Discussion of parameter Q/m

The electrical surface potential on dust particles in interplanetary space depends mostly on the ambient solar wind parameters, density and flux, whereas the solar UV flux, hence the photo electron emission, are not that variable. Photo electron emission yields have been determined experimentally for dielectric and absorbing materials (Feuerbacher and Fitton, 1972). Dielectric materials have an electron yield of about 0.1 times the yield of absorbing materials. Since the grain potential is determined by the balance of plasma and photo electron currents, the equilibrium potential of dielectric grains is only slightly reduced. For both materials we use a surface potential of $+5$ V, which is compatible with measurements of dust charges on interplanetary particles (Kempf et al., 2004). There is a dependence on the shape of the particle. Elongated or flat particles carry higher charges than spherical particles at the same surface potential (Hill and Mendis, 1981). Very fluffy particles carry even higher charges than spherical particles (Auer et al., 2007), however, these particles are also more susceptible to electrostatic disruption. We conclude that the charge on interstellar grains deviates by less than a factor 2 from that of a spherical particle.

Overview of used β and Q/m-values

State-of-the-art in-situ dust telescopes (Srama et al., 2004b; Sternovsky et al., 2010) will provide the magnitude and direction of the interstellar dust flux at various times and positions in the planetary system, in addition to the masses and speeds of individual particles. Recent measurements of interstellar

Mass (kg)	β (...)	Q/m (C/kg)	Radius (μm)	closest β-value in simulations
3.2E-15	0.5	0.125	0.73	0.5
4.1E-16	1.1	0.5	0.36	1.1
1.4E-16	1.4	1.	0.26	1.3
7.8E-17	1.5	1.5	0.21	1.5
2.8E-17	1.6	3.	0.15	1.5
9.6E-18	1.4	6.	0.11	1.3
3.5E-18	1.	12	0.07	1

Table 2.2: The mass, β, Q/m and radius used for the calculations of the size distribution. A density $\rho = 2$ g/cm^3, grain potential U = +5 V and the adapted astrosilicates β-curve is assumed. The radii and Q/m-values correspond to the crosses in Figure 2.11.

grains by the dust detector onboard Ulysses (Krüger et al., 2007) provided the magnitude, direction, and mass distribution of the interstellar dust flux between Earth's and Jupiter's orbits. To interpret these measurements in terms of optical and physical properties of interstellar grains, we calculated dust trajectories through the planetary system for a wide range of β and Q/m values, along with the starting times over a complete solar cycle of 22 years (Fig. 2.11). Any measurement of the interstellar particle flux (direction, speed) of a given particle mass at a given position and time can be compared with possible trajectories that have the similar characteristics. Therefore, a set of measurements at different positions, times, and/or particle masses will constrain the β and Q/m values for these particles, so it will constrain the physical and compositional properties of interstellar grains. Previously Landgraf et al. (1999a) succeeded at such an analysis using the effect of β on the mass distribution. Figure 2.11 gives an overview of the parameters of the performed simulations.

2.2 Simulation tool

Monte Carlo simulations are performed for the trajectories of individual ISD particles through the heliosphere using the modeling as described in Sections 2.1 and 2.1.3. Hereby, the starting conditions for these trajectories were varied arbitrarily in starting position and time. From these trajectories we derived ISD density maps and fluxes throughout the solar system, by counting the amount of particles per grid cell and per time bin. The dust dynamics follow the description of Section 2.1, which are largely the same assumptions (except for the β and Q/m parameters) as in Landgraf (1998, 2000) since we used the averaged magnetic field model for the simulations. Two other models of the IMF are implemented (see Section 2.1.3) whose use depends on the speed for the dust and the distance to the Sun of the region we are interested in. The simulations we ran have a statistical uncertainty of about 20%.

The simulations contain two possible coordinate systems: the J2000 ecliptic frame, and the "ISD simulation frame". The frames are depicted in Fig. 2.12. Quaternions were used to transfer the grain state vector from the one to the other frame and vice versa.

Ecliptic frame
In the ecliptic frame, the dust flow is directed towards 79° longitude, -8° latitude (downstream) (Frisch et al., 1999). The flow is thus roughly along the Y-axis (11° offset in the XY-plane, -8° offset in the YZ-plane).

ISD frame
The Z-axis of the ISD frame is equal to the solar rotation axis, and the XY-plane is equal to the solar equatorial plane. The X-axis is perpendicular to the Z-axis, and the XZ-plane is defined by the direction of the velocity vector of the dust. In the XZ-plane, the dust flows mainly along the X-axis, with an offset of about 7.5° in the -Z direction. The Y-component of the initial dust velocity vector is zero in this frame.

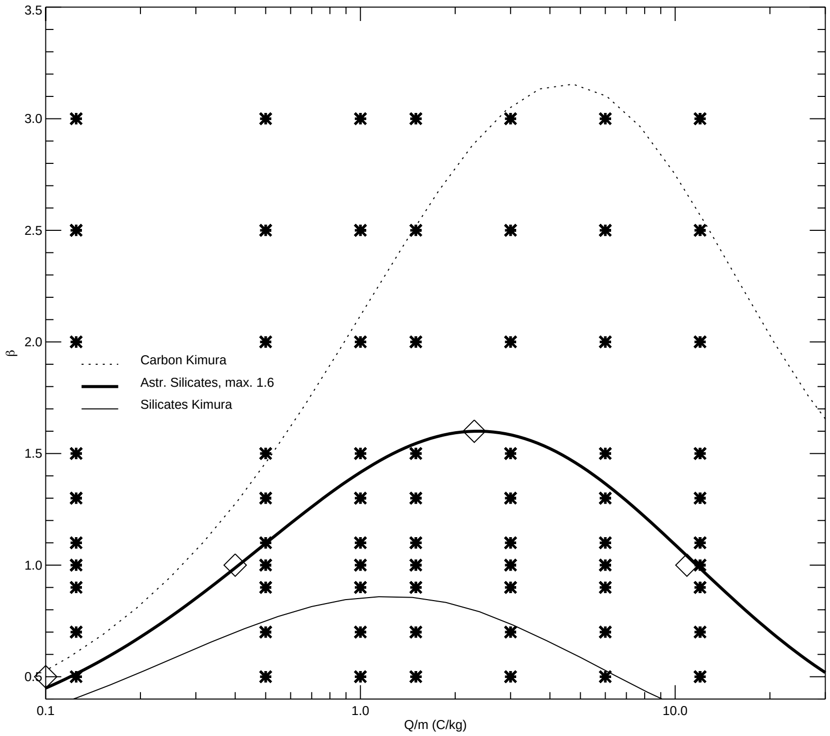

Figure 2.11: Overview of the simulations performed with various β and Q/m values. All simulations are done between 2010 and 2030, where densities and fluxes are binned per 100 days, and in a region of the solar system in a box of 22AU around the Sun. The crosses denote these simulations (β and Q/m range), while the curves are three examples of β-curves: two from Kimura and Mann (1999) and one 'adapted' astronomical silicates curve (Gustafson, 1994). The β-curves relate the β-parameter of a material to its size. The sizes are consequently converted in corresponding charge-to-mass ratio, assuming a surface potential of +5V and the material density according to the corresponding material (see Eq. 2.20).

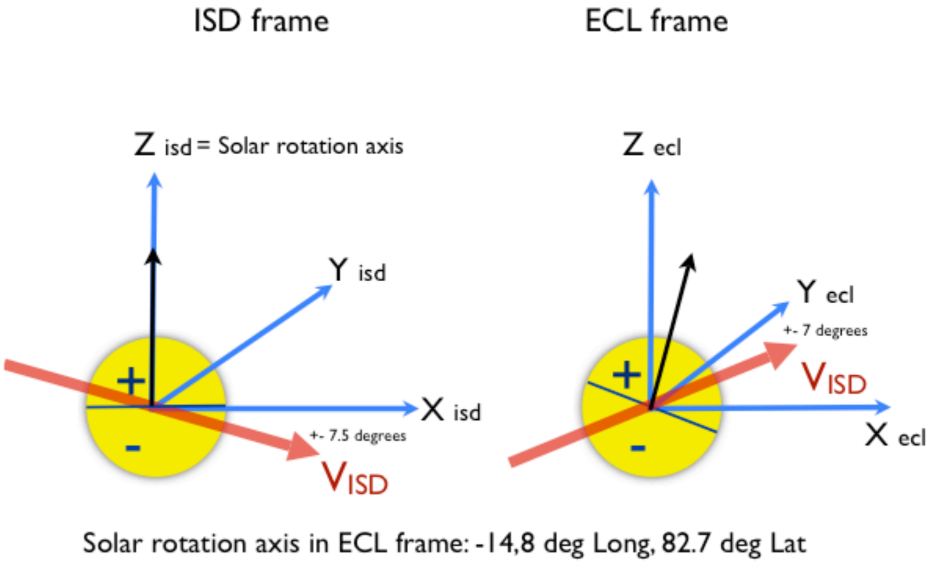

Figure 2.12: The ISD frame and the ECL frame.

2.2.1 Assumptions of the model

Several assumptions were made for modeling the dust dynamics of ISD in the solar system.

- The solar wind speed is constant.
- The potential of the dust grain is constant with the influence of solar wind speed and density variations. The influence of grain shape/fractality is not considered.
- Differential rotation of the Sun is not taken into account, but is assumed to have nearly no influence anyway.
- No assumptions are made yet about the *incoming* mass distribution of the particles. All results are relative to the density, velocity and flux before entering the solar system.
- Filtering at the heliopause is not yet taken into account.
- The incoming submicrometer sized grain flux is modeled as monodirectional and homogeneous, since it is coupled to the gas in the LIC.

With the dust dynamics, model description and assumptions in mind we are ready to discuss the resulting ISD flow patterns and filtering of ISD size distribution in the solar system in the next chapter.

3

The flow of interstellar dust into the solar system

The prime focus of this chapter is to show and explain the general flow patterns of ISD particles moving through the solar system, to illustrate how they are affected by the three main forces and to describe the filtering of ISD in the solar system by these forces. By doing this, we build upon the known and simple cases (approximation of the ISD trajectories by a straight line, ISD trajectories affected only by solar gravity and radiation pressure force, see Section 2.1.1) and expand to include now the influence of the IMF on the flow patterns. This chapter aims at clarifying where in the solar system the simplified dust trajectories can be used for spacecraft predictions or planetary science studies and where a full analysis including time-dependent Lorentz forces is needed. Getting insight in the general flow patterns of the ISD will also show us where and when to look for the ISD in the solar system with in-situ instruments.

Section 3.1 describes quantitatively the resulting dust trajectories and variations in densities from the simulations, first for grains that are influenced by the Lorentz force only ($\beta = 1$ grains, Section 3.1.1) and then for solar radiation pressure, gravity and Lorentz forces alltogether (Section 3.1.2). This gives insight in the complexity of the variations of the trajectories, and provides an answer to the question where and when the straight-line approximation or solar-radiation-only approximation can be used. The ISD density maps and fluxes throughout the solar system and throughout time were derived from a Monte Carlo run where the time and starting locations of the trajectories were randomly varied. Because the solar wind magnetic field was averaged over one solar rotation (25.38 days), the simulation results are only appropriate for larger distances to the Sun, e.g. > 2 AU. Any conclusions concerning the interstellar flux at 1 AU should be taken with caution. All particles are started at a distance of about 50 AU from the Sun. For $\beta = 1$, Q/m $= 0$, they would reach the Sun about nine years later.

The filtering at the termination shock is discussed in Section 3.2 but is not further taken into account for the calculations in this thesis.

Section 3.3 introduces a possible ISD size distribution in the LIC, the ‘MRN-distribution’, which is taken as a reference in this thesis. Starting from this MRN-distribution and ignoring the filtering at the termination shock we then study the dust size distribution for a fixed material (the ‘adapted astrosilicates’) in Section 3.4. We do this first for the gravity and radiation pressure only case (Section 3.4.1) and then illustrate the influence of an additional Lorentz force along a line parallel to the nominal ISD flow, upstream and downstream from the Sun (Section 3.4.2). This background knowledge is a preparation for understanding Chapter 4 with applications of the modeling to the Saturn, Jupiter and asteroid belt orbits and the Cassini, JUICE and Stardust missions.

3.1 Trajectory simulations of ISD in the solar system

3.1.1 Hypothetical dust flow for Lorentz force ‘only’ ($\beta = 1$)

To show the influence of the Lorentz force clearly, we studied the trajectories for a particle with $\beta = 1$ and Q/m = 0.5 C/kg. To understand the effects of the Lorentz force on the ISD trajectories, we varied Q/m up to 12 C/kg, keeping $\beta = 1$.

Q/m = 0.5 C/kg

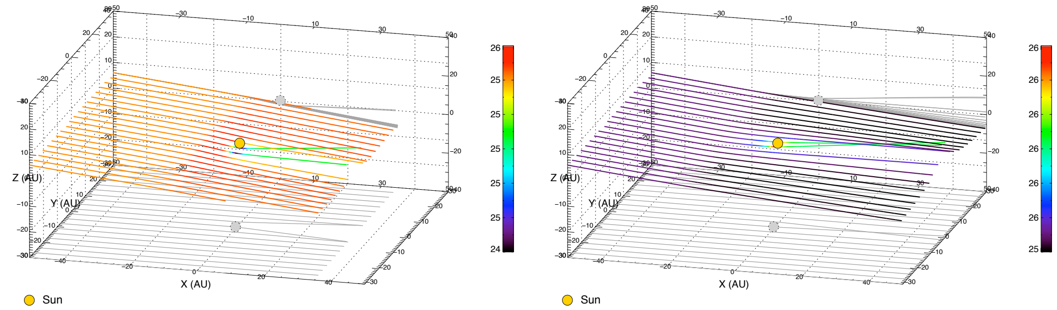

Figure 3.1: 3D-representation of a ‘sheet’ of particle trajectories with $\beta = 1.0$ and Q/m = 0.5 C/kg, during the focusing phase of the solar cycle (left) and the defocusing phase of the solar cycle (right). The start year is 2000 (left) and 1990 (right). The ‘sheet’ of particles is started along the Y-axis of the ISD frame. The focusing towards the solar ecliptic plane is visible (left), but at the same time there is a ‘defocusing’ in the XY-plane (see projection), downstream of the Sun. For the defocusing case (right plot), the particles are defocused with respect to the solar equatorial plane, but they are focused in the XY-plane (see projection) downstream of the Sun.

The special configuration of the interstellar flow (close to the solar rotation equator) and the dominant azimuthal component of the magnetic field at low latitudes (in the outer solar system), are the reasons that Lorentz force acts mostly normal to the equatorial plane. The axial symmetry of the radiation-pressure-only case is therefore broken. We demonstrate this effect by showing dust trajectories in two sheets: one close to and parallel to the solar rotational equator (Figs. 3.1)[1] and another sheet perpendicular to the equatorial plane (Figs. 3.2, 3.3). The dominant deflection of trajectories occurs close to the Sun in a direction perpendicular to the equatorial plane. The varying magnetic field configuration during the 22-year solar cycle has a focusing and defocusing effect roughly 11 years later (Morfill and Grün, 1979). The maximum defocusing effect occurs for particles launched 50 AU from the Sun in ~1990 (Fig. 3.2, right) followed by almost no deflection in 1995 (Fig. 3.3) while the maximum focusing effect occurs for particles launched in ~2000 (Fig. 3.2, left). For particles launched in 2006, already significant defocusing can be observed when they reach the region of the Sun. In the focusing period, particles get decelerated by the solar wind magnetic field, while their trajectories are bent towards the current sheet. The opposite occurs during the defocusing period when the particles are accelerated away from the current sheet.

While upstream at Kuiper belt distance (> 30 AU), the ISD trajectories can be considered straight lines (Fig. 3.4, 3.5), strong deflections, both in distance, angle, and modifications in speed already occur at the (upstream) distance of Saturn (10 AU). At Jupiter’s distance (5 AU), only trajectories close to the solar equatorial plane can be approximated with straight lines. The solar equatorial plane is tilted with ~7° from the ecliptic plane, so at the distance of Saturn, this is as much as 1.2 AU above or below the

---

[1] Figs. 3.1, left and right, look very alike, but are actually very different. In Fig. 3.1 (left), the grains are focused upstream towards the Sun, pass the solar equatorial plane (‘southward’ from the Sun), and are then bent again towards the north, from the focusing effect of the solar cycle. In Fig. 3.1 (right), the particles remain in the northern solar hemisphere because they are repelled by the Lorentz forces (defocusing phase), and are further repelled after having passed the Sun.

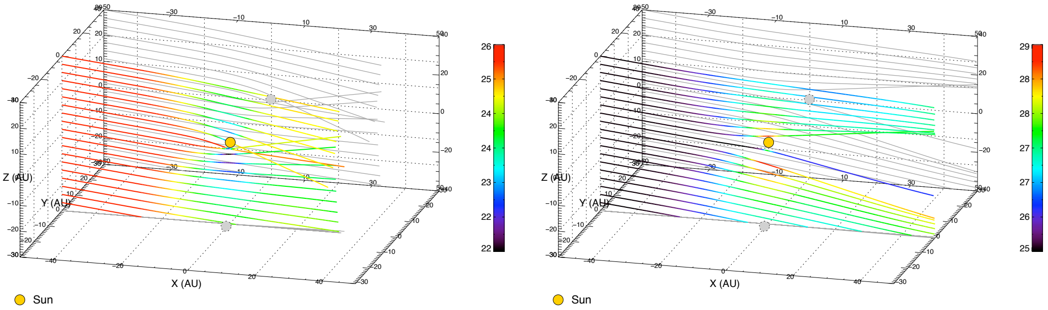

Figure 3.2: 3D-representation of a ‘sheet’ of particle trajectories with $\beta = 1.0$ and Q/m = 0.5 C/kg during the focusing phase of the solar cycle (left) and the defocusing phase of the solar cycle (right). The start year is 2000 (left) and 1990 (right). The particles are started in a ‘sheet’ along the Z-axis to illustrate the focusing and defocusing effect of the Lorentz force with respect to the solar equator. In general, during the focusing phase of the solar cycle, the particles are decelerated in the neighborhood of the Sun whereas during the defocusing phase the particles are accelerated in the neighborhood of the Sun. Since $\beta = 1$, we only see the influence of the Lorentz forces (not the radiation pressure force or gravity).

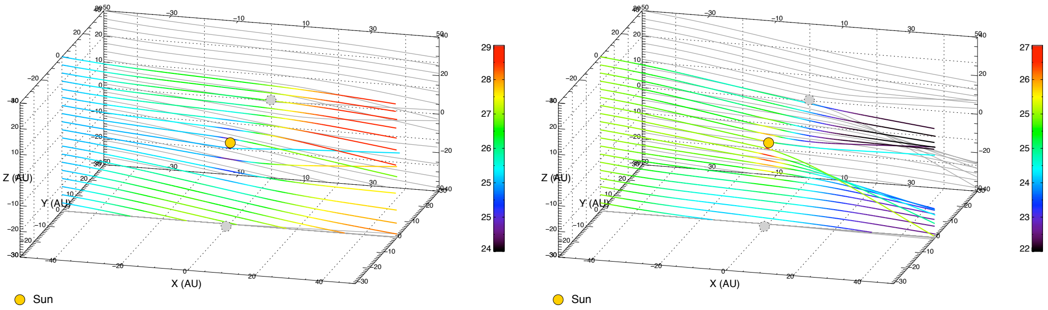

Figure 3.3: $\beta = 1.0$, Q/m = 0.5 C/kg. Start year is 1995 (left) and 2006 (right). The phase of the solar cycle is just after the solar maximum from the defocusing to focusing cycle (left) and just after the solar maximum from the focusing to defocusing cycle, resulting both in only moderate deflections.

ecliptic plane.

The ‘closest approach’ distances of trajectories (Fig. 3.6) show the effect of focusing and defocusing due to the Lorentz force. In Fig. 3.6 (left), the areas where particles reach a certain minimum distance to the Sun (solid lines) is extended in the polar direction indicating that particles that were initially farther away from the beam axis get closer to the Sun than particles on straight line trajectories. So in Fig. 3.6 (left), the particles are focused towards the Sun along the Z-direction. In the Y-direction, there is little or no focusing or defocusing at the closest distance to the Sun, with respect to the straight line case ($\beta = 1$, $Q/m = 0$). In defocusing periods, the range where particles reach a certain minimum distance is shrunk in the polar direction (Fig. 3.6, right). The particles are defocused from the solar equatorial plane. In the Y-direction, there is little or no focusing or defocusing at the time the particle is closest to the Sun, with respect to the straight line case ($\beta = 1$, $Q/m = 0$).

The dust density enhancements and depletions near the solar equator are best seen in the scatter plots (Figs. 3.7). Although density variations can be seen upstream of the Sun (-5 AU), the effects are strongest downstream of the Sun. While the dust densities decrease close to the solar equator during the defocusing period, density enhancements at higher latitudes can be observed. Also the deceleration during focusing periods and acceleration during defocusing periods are visible.

The ISD densities inside a cube of 22 AU width are displayed in Figs. 3.8. At 50 AU from the Sun, dust particles were continuously launched at random times within a time range of about 45 years. The dust densities in the inner solar system at different times from 1996 to 2018 show strong density variations. From 1996 to about 2006 the dust densities were generally lower than the initial densities, whereas the densities were higher afterwards (2000–2018). The solar minimum of the defocusing cycle is in mid-1996. The maximum effect of this on the density is about three years later. Solar maximum is in 2002 and the solar minimum of the focusing cycle is in mid-2007 (see Table 2.1). Again the effect of this on the density occurs about three years later in 2010. This time lag of several years is caused by the long travel time (about 9-10 years) in the region where the solar wind magnetic field significantly affects the dust trajectories. The focusing and defocusing effects are most prominent near the ecliptic, while the dust densities display a more complex variation at higher latitudes.

$Q/m = 1.5$ C/kg

Trajectories of dust particles with $Q/m = 1.5$ C/kg are strongly scattered by the solar wind magnetic field (Figs. 3.9). Again the strongest deflection occurs in the vertical sheet of trajectories. A strong defocusing effect can be observed for grains started in 1990, whereas for 2000 particles are strongly bent towards the equatorial plane. Some trajectories that approach close to the Sun during the focusing cycle even cross the equatorial plane in front of the Sun. Again particles’ speed are accelerated and decelerated at even stronger levels than at lower Q/m values. Only at Kuiper belt distances is the deflection upstream from the Sun is small and the trajectory can be approximated by straight lines. Everywhere else trajectories have to be calculated more accurately.

During the focusing cycle dust densities are strongly enhanced 5 AU upstream of the Sun in the equatorial plane (Fig. 3.10, right). Close to the Sun and downstream from the Sun in the central part of the beam, the dust slows down and the dust densities decrease, while the enhancements move outward in the equatorial plane. During the defocusing cycle, the dust densities are strongly depleted near the equatorial plane whereas at high latitudes dust concentrations develop downstream from the Sun (Fig. 3.10, left).

The contrast between dust concentrations during the focusing cycle and density depletions during defocusing periods (Figs. 3.11) becomes even stronger than for $Q/m = 0.5$. The depletions are stronger and the concentrations are higher.

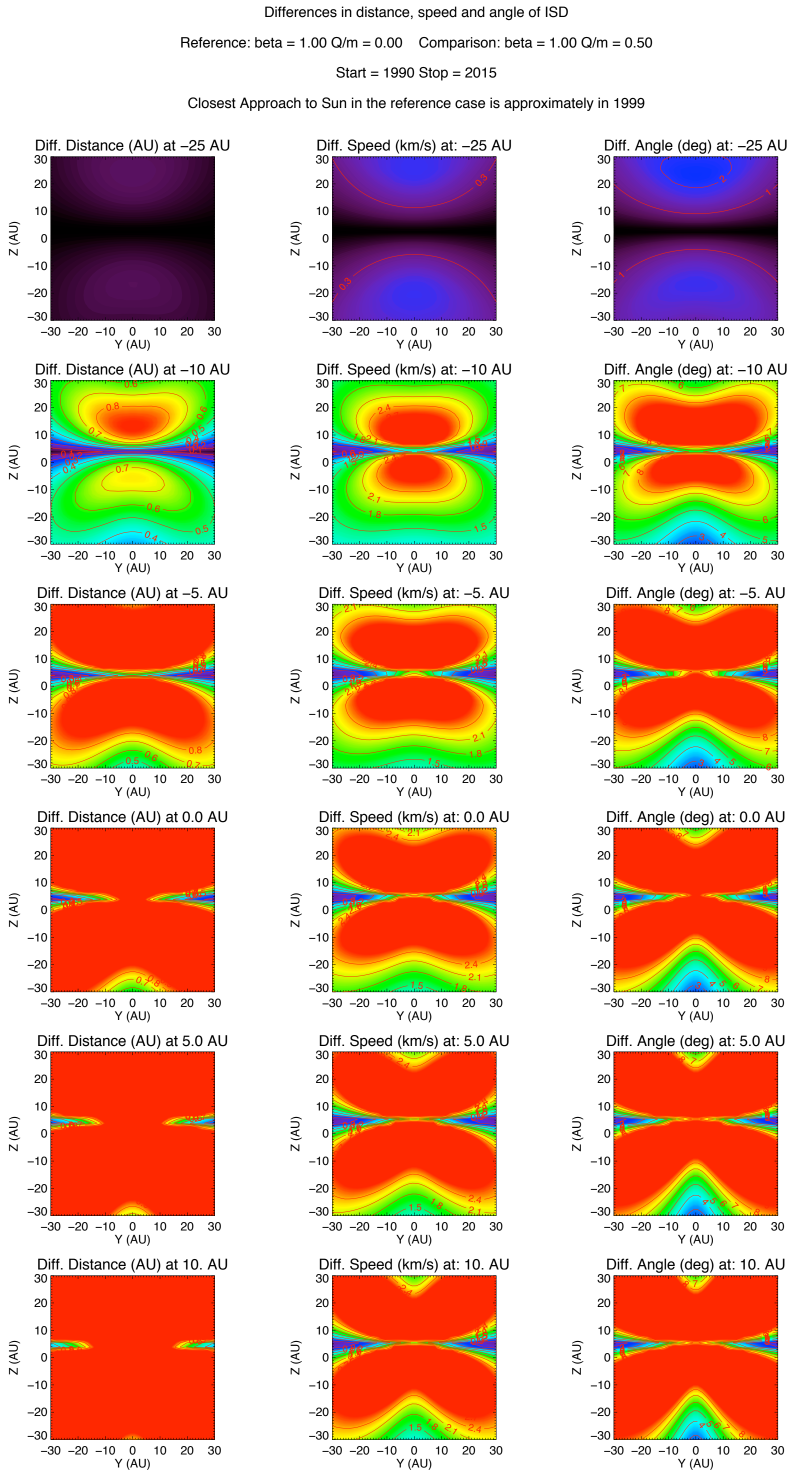

Figure 3.4: Absolute differences in position (red = difference $d > 1$ AU), velocity ($d > 5$ km/s) and direction ($d > 5°$) in different 'sliced' planes at different distances from the Sun. The case for $\beta = 1$, Q/m = 0.5 C/kg is compared to the straight-line approximation ($\beta = 1$, Q/m =0). Start year is 1990 at -50 AU from the Sun. The phase of the solar cycle is the defocusing phase.

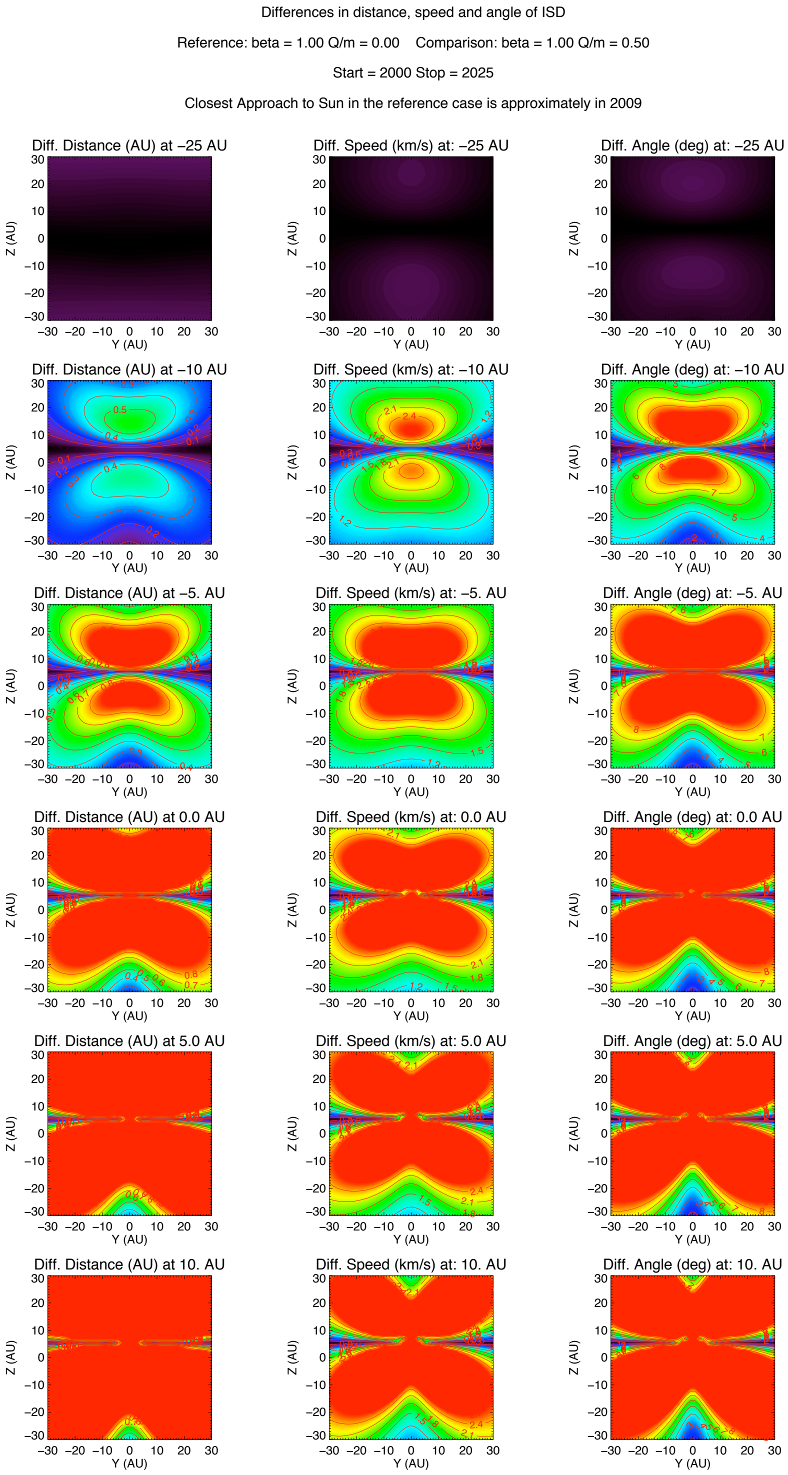

Differences in distance, speed and angle of ISD

Reference: beta = 1.00 Q/m = 0.00 Comparison: beta = 1.00 Q/m = 0.50

Start = 2000 Stop = 2025

Closest Approach to Sun in the reference case is approximately in 2009

Diff. Distance (AU) at −25 AU
Diff. Speed (km/s) at: −25 AU
Diff. Angle (deg) at: −25 AU

Diff. Distance (AU) at −10 AU
Diff. Speed (km/s) at: −10 AU
Diff. Angle (deg) at: −10 AU

Diff. Distance (AU) at −5. AU
Diff. Speed (km/s) at: −5. AU
Diff. Angle (deg) at: −5. AU

Diff. Distance (AU) at 0.0 AU
Diff. Speed (km/s) at: 0.0 AU
Diff. Angle (deg) at: 0.0 AU

Diff. Distance (AU) at 5.0 AU
Diff. Speed (km/s) at: 5.0 AU
Diff. Angle (deg) at: 5.0 AU

Diff. Distance (AU) at 10. AU
Diff. Speed (km/s) at: 10. AU
Diff. Angle (deg) at: 10. AU

Figure 3.5: Absolute differences in position (red color = difference $d > 1$ AU), velocity ($d > 5$ km/s) and direction ($d > 5°$) in different 'sliced' planes at different distances from the Sun. The case for $\beta = 1$, Q/m = 0.5 C/kg is compared to the straight-line approximation ($\beta = 1$, Q/m =0). Start year is 2000 at -50 AU from the Sun. The phase of the solar cycle is the focusing phase.

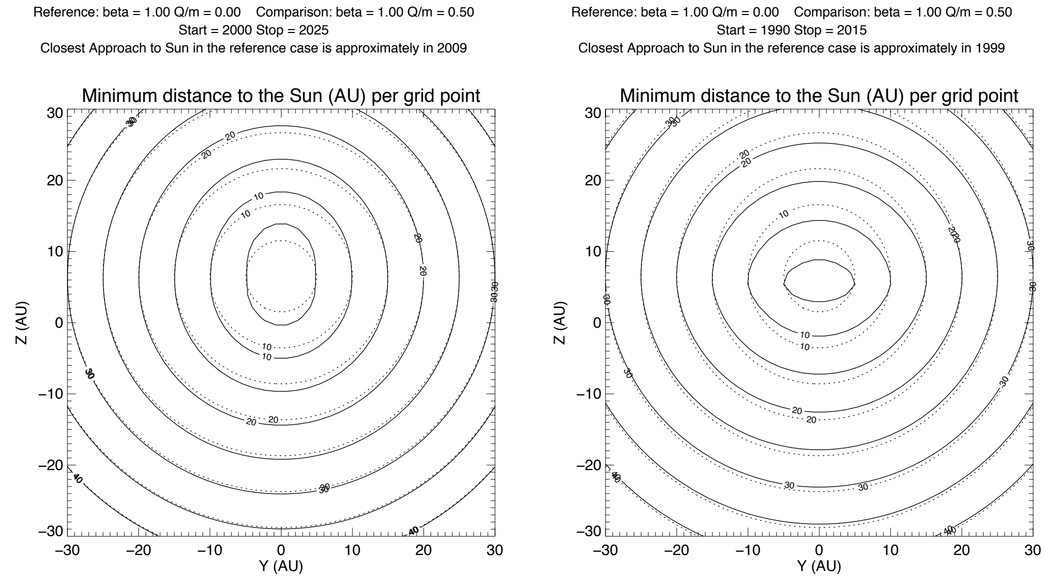

Figure 3.6: Closest distances of the particles to the Sun, projected on a plane, during their trajectory for $\beta = 1$, Q/m = 0.5 C/kg, during the focusing phase of the solar cycle (left) and the defocusing phase of the solar cycle (right). The axes show the original position of the ISD particles in AU, in the ISD frame, while the numbers in the contour lines show their closest approach distances. The dotted lines are the reference case where $\beta = 1$ and Q/m = 0. (Particles fly in straight lines, thus the dotted contour lines are circles.)

Q/m = 3 to 12 C/kg

Trajectories of interstellar grains of 1.5 C/kg during the focusing cycle (Fig. 3.9, right) already displayed significant deflection upstream of the Sun. To study this effect we increased Q/m to 3 C/kg (Fig. 3.12, left). Trajectories in the horizontal sheet displayed minimum deflections, whereas trajectories with impact parameters < 20 AU in the vertical sheet were completely reflected upstream of the Sun. Only trajectories with impact parameters > 20 AU were able to pass the Sun.

Even more bizarre are trajectories of Q/m = 12 C/kg particles in the vertical sheet (Fig. 3.12, right). Here, all particles with impact parameters < 30 AU are reflected onto trajectories with high elevation angles. However, trajectories with impact parameters < 10 AU can reach close proximity to the Sun before they are reflected. Their motion resembles trajectories of charged particles bouncing back in the high field region of a magnetic mirror. The motion of dust particles towards the Sun is coupled with a strong deceleration, while particles retreating from the Sun are initially strongly accelerated. During the defocusing cycle they are strongly diverted away from the Sun but maintain their general downstream motion (Fig. 3.13). During this deflection the particles are strongly accelerated and reach speeds twice their initial speed. At high latitudes (10-15 AU above the equatorial plane), higher concentrations of particles are found during defocusing periods.

The densities of these particles in the inner planetary system are rather low (Figs. 3.14). These particles cannot reach the inner planetary system most of the 22-year solar cycle. Only for a short period after the maximum focusing configuration particles are concentrated close to the ecliptic plane. Upstream at 10 AU these particles are more abundant.

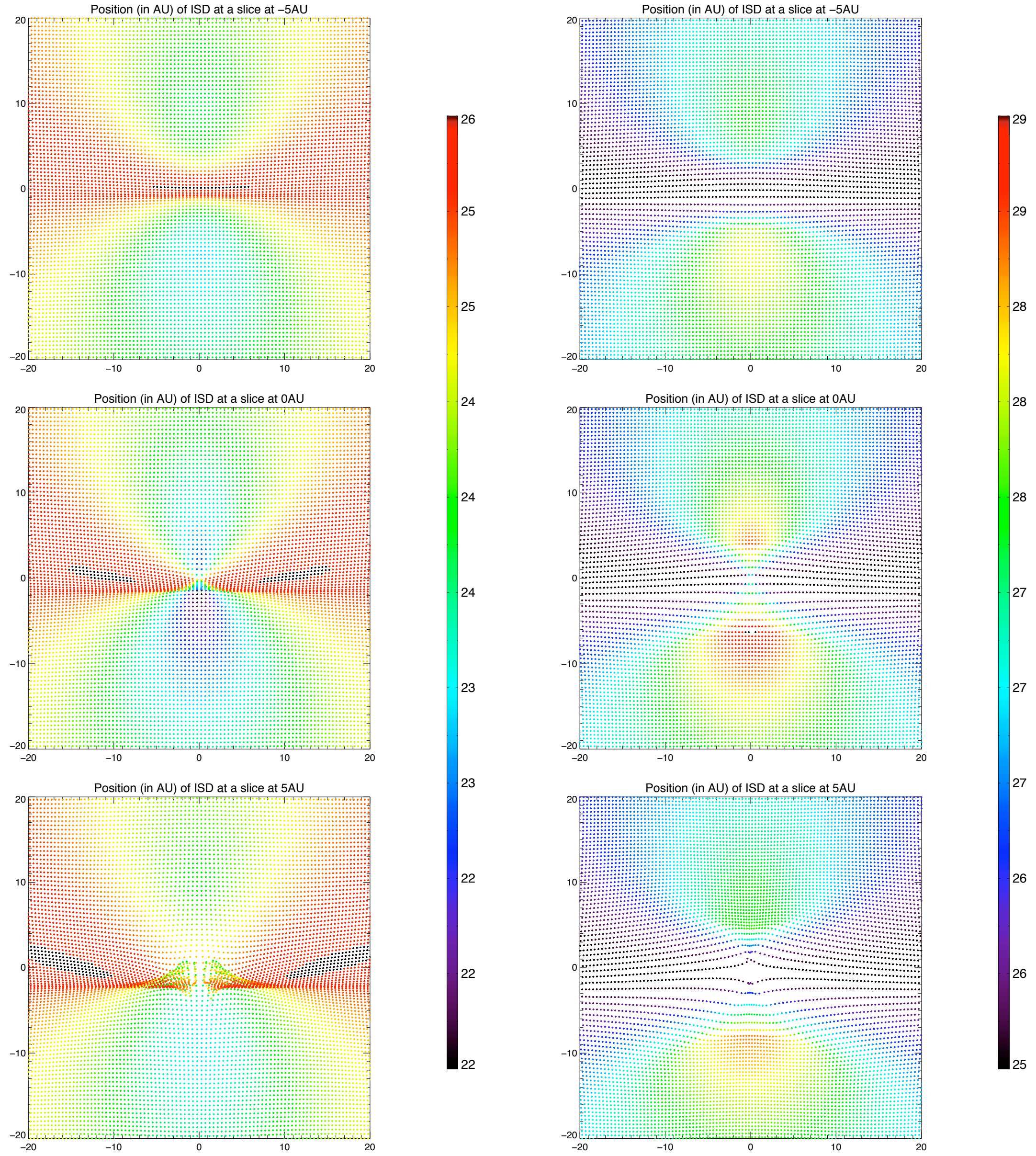

Figure 3.7: Several cross-sections through the trajectories at different distances from the Sun (-5 AU, 0 AU, and 5 AU) in the ISD-frame. The trajectories shown are for particles with $\beta = 1.0$ and Q/m = 0.5, started in 2000 at -50 AU from the Sun. The focusing effect of the Lorentz force is visible (left) and the defocusing effect is visible (right) that results in a void downstream from the Sun. This plot is directly comparable to the two corresponding trajectory plots (Figs. 3.1 and 3.2) for the left plot, and Figs. 3.1 and 3.2 for the right plot.

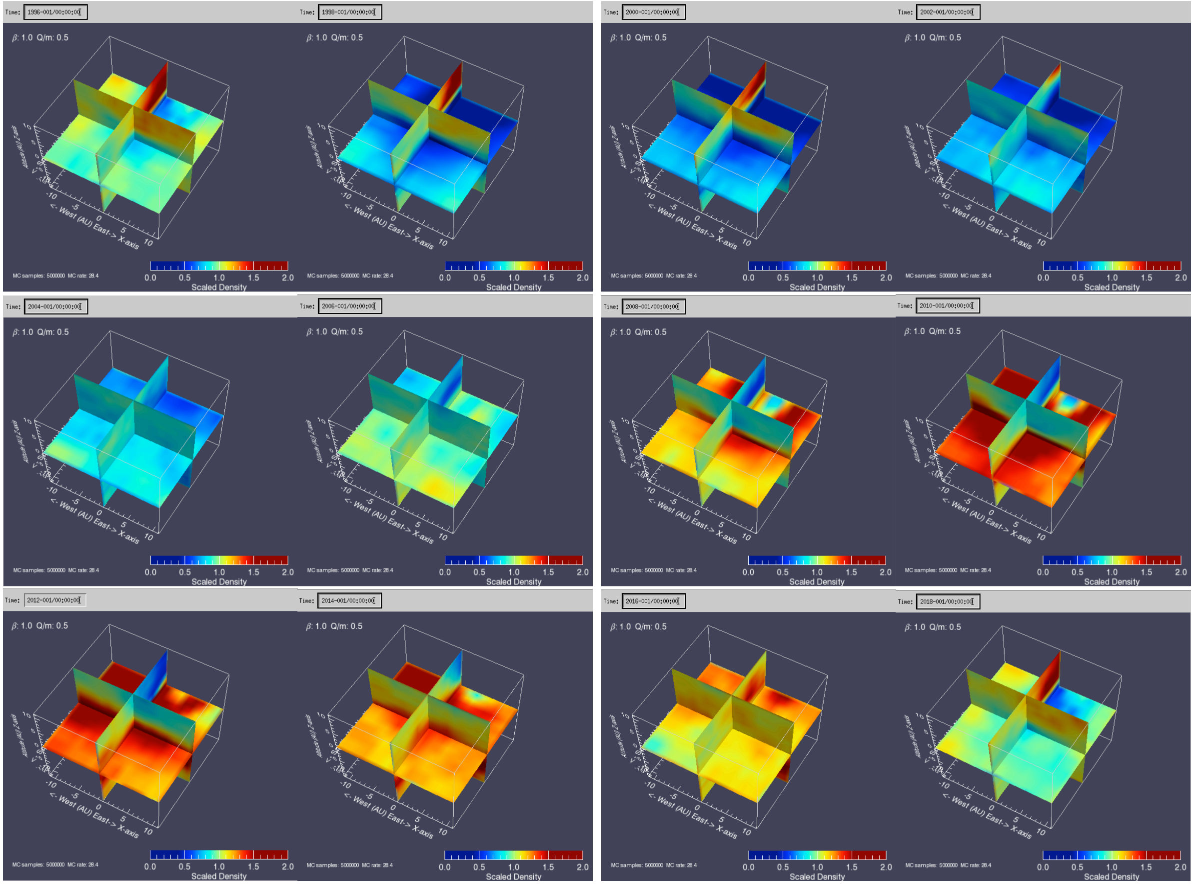

Figure 3.8: Variation in relative densities in the solar system, due to the Lorentz force ($\beta = 1$, $Q/m = 0.5$ C/kg). Observing times are from left to right and top to bottom: 1996, 1998, 2000, 2002, 2004, 2006, 2008, 2010, 2012, 2014, 2016, 2018. The solar minimum of the defocusing cycle is in mid-1996. The solar minimum of the focusing cycle is in mid-2007. The maximum effect of this on the density is about 3 years later. Solar maximum is in 2002, and the solar minimum of the focusing cycle is in mid-2007. Solar maximum is in 2013, and the solar minimum of the next defocusing cycle is in mid-2018.

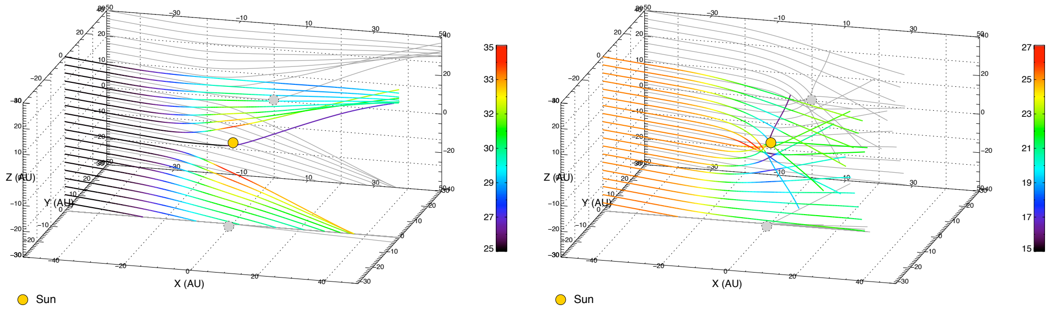

Figure 3.9: $\beta = 1.0$, $Q/m = 1.5$ C/kg. Start year 1990 (left) and 2000 (right), at -50 AU from the Sun. The main effect is defocusing (left) and focusing (right). Particles are even already clearly focused upstream of the Sun (right plot).

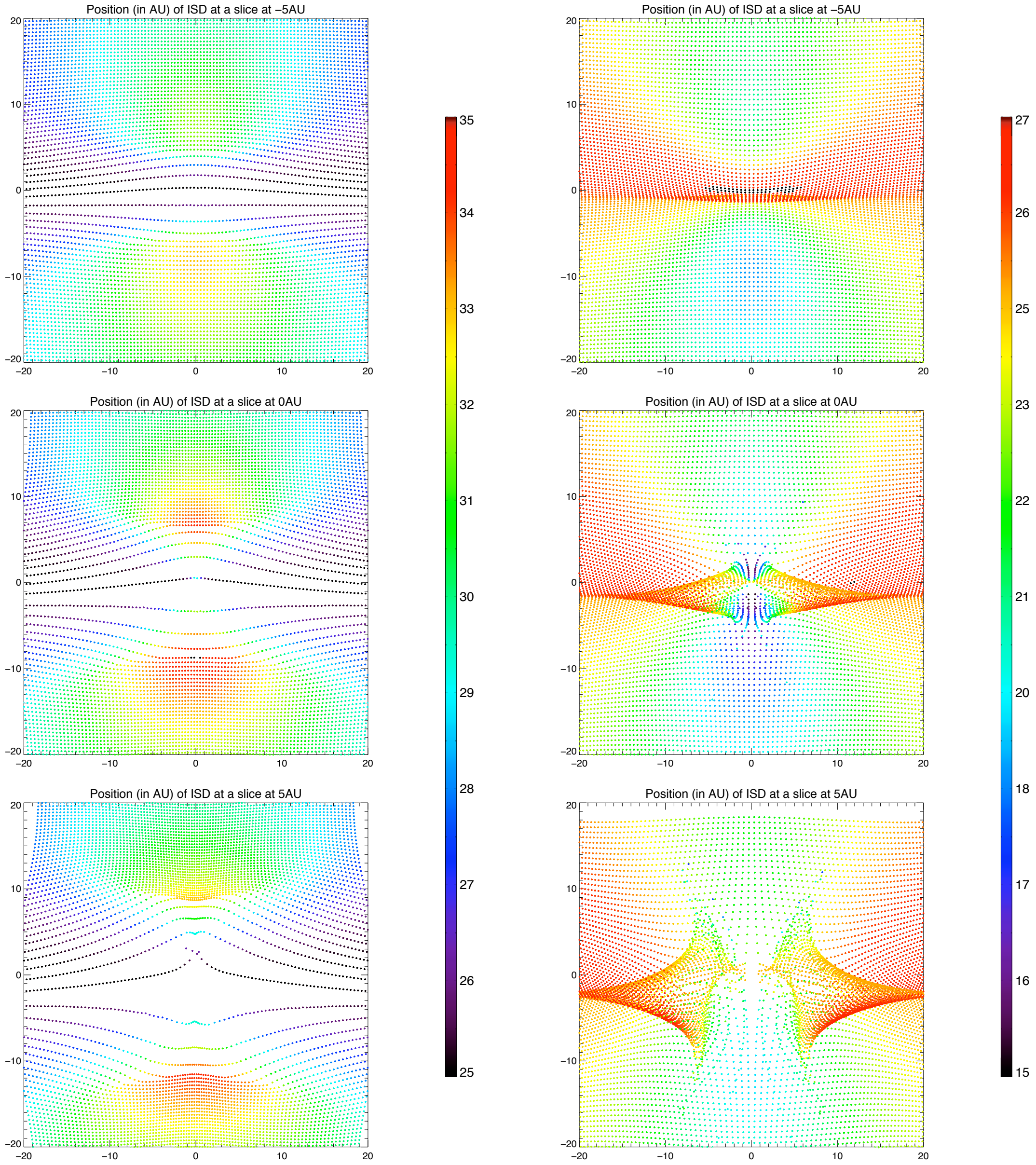

Figure 3.10: Cross-section of the trajectories during the defocusing phase of the solar cycle (left) and the focusing phase of the solar cycle (right). Start year was 1990 (left) and 2000 (right), $\beta = 1$, Q/m = 1.5 C/kg.

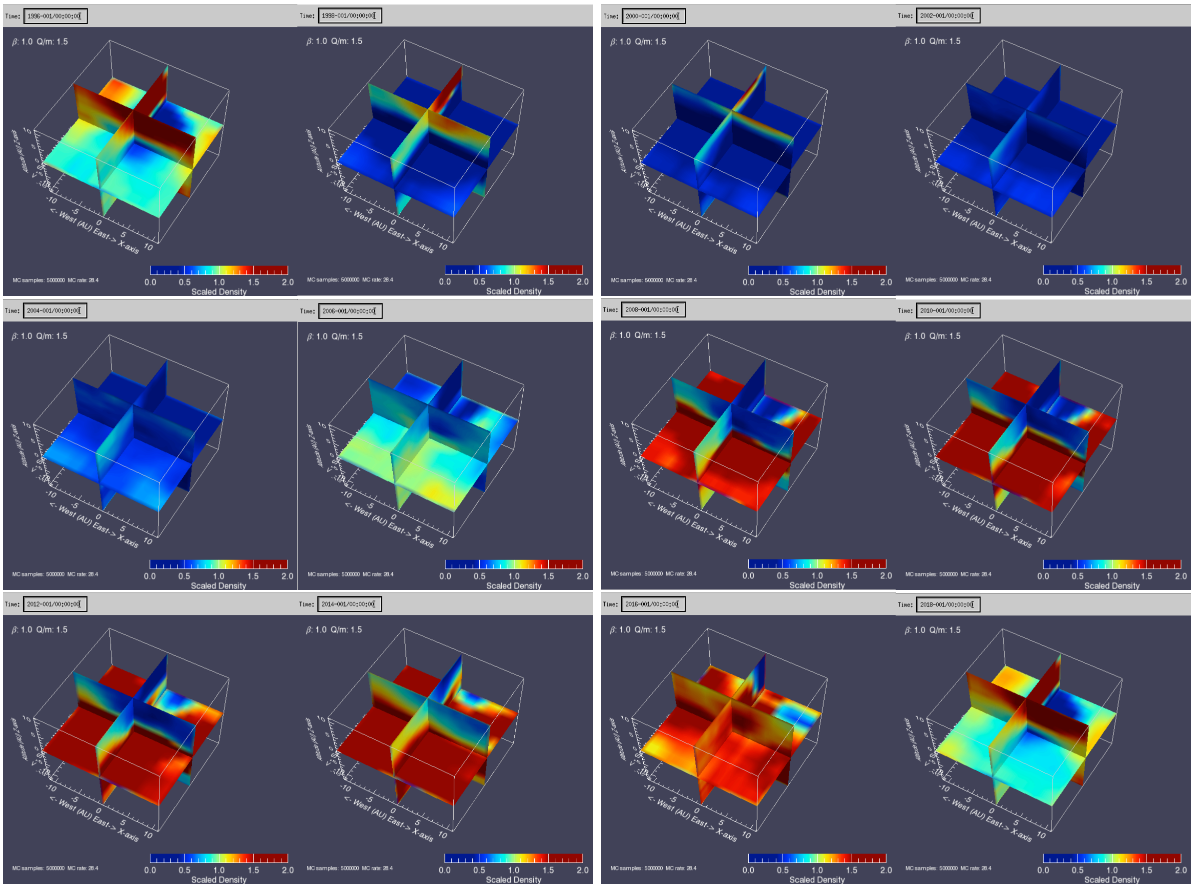

Figure 3.11: Variation in relative densities in the solar system, due to the Lorentz force ($\beta = 1$, Q/m $= 1.5$ C/kg). Observing times are from left to right and top to bottom: 1996, 1998, 2000, 2002, 2004, 2006, 2008, 2010, 2012, 2014, 2016, 2018. The solar minimum of the defocusing cycle is in mid-1996. The solar minimum of the focusing cycle is in mid-2007. The maximum effect of this on the density is about 3 years later. Solar maximum is in 2002, and the solar minimum of the focusing cycle is in mid-2007. Solar maximum is in 2013, and the solar minimum of the next defocusing cycle is in mid-2018.

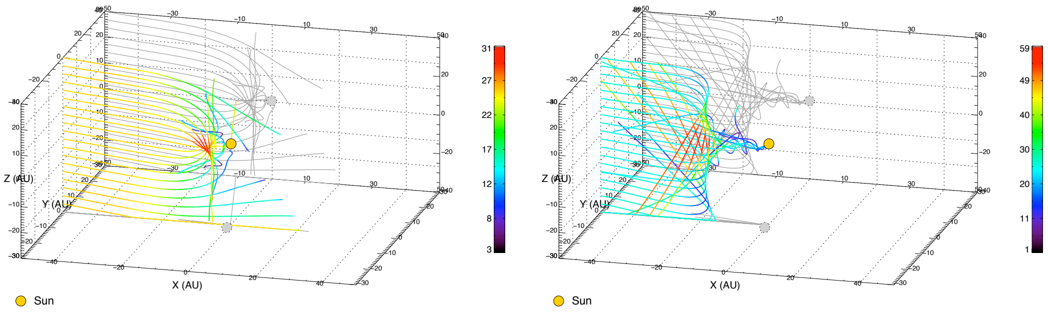

Figure 3.12: $\beta = 1.0$, Q/m $= 3$ C/kg (left) and Q/m $= 12$ C/kg (right). Start year 2000, at -50 AU of the Sun. In the left plot, the particles are strongly focused, even upstream from the Sun. Particles with a low impact factor are reflected, while particles with an impact factor greater than about 20 AU are seen to pass downstream from the Sun. In the right plot, the particles are reflected upstream of the Sun and accelerated to high speeds. Particles with a low impact factor get far into the inner solar system (hypothetically assumed they are not already filtered at the heliosphere) and are reflected upstream of the Sun.

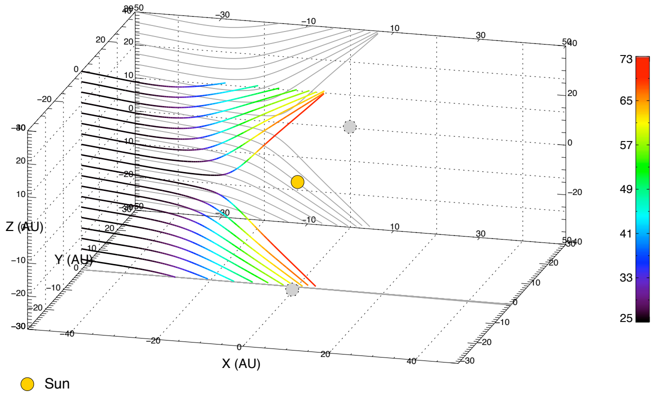

Figure 3.13: $\beta = 1.0$, Q/m = 12 C/kg. Start year 1990, at -50 AU from the Sun. The particles are strongly deflected away from the solar equatorial plane, and are accelerated to high speeds on their way out of the solar system.

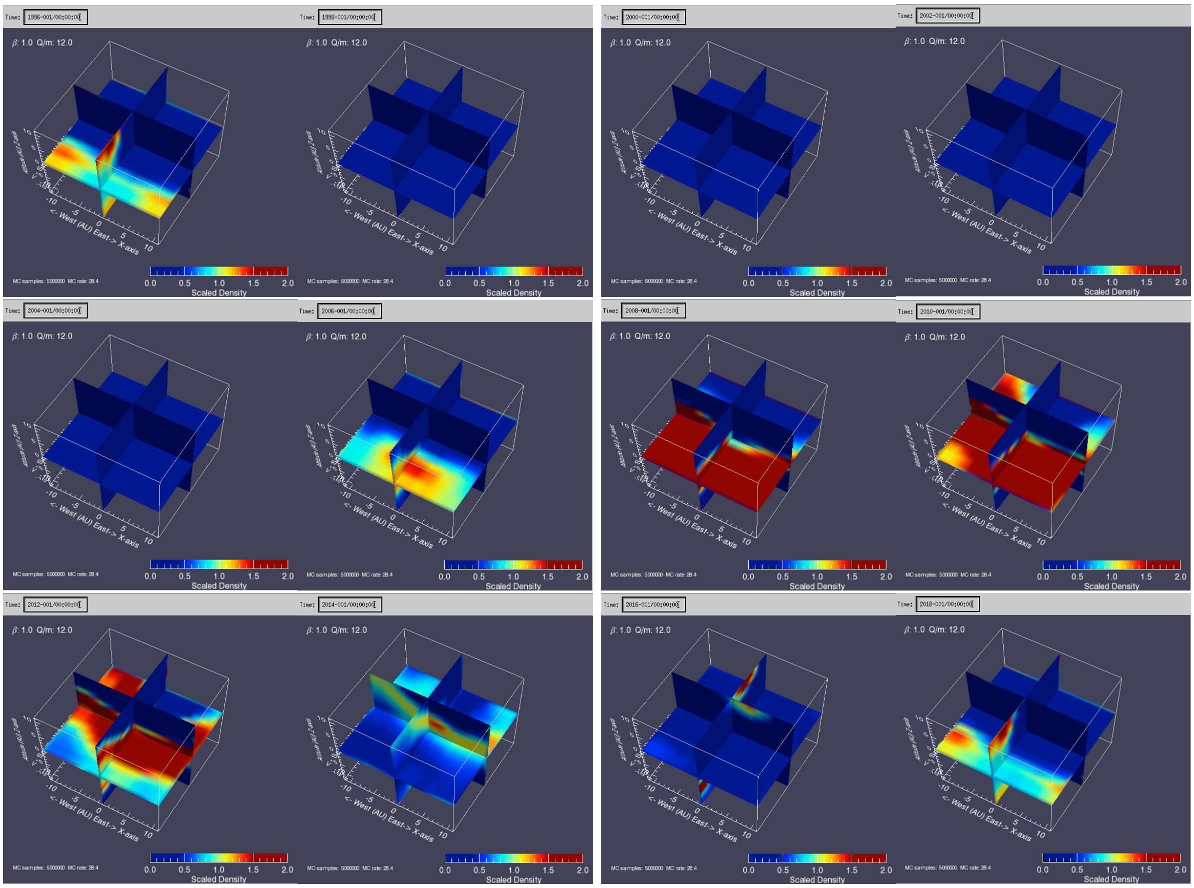

Figure 3.14: Variation in relative densities in the solar system, due to the Lorentz force ($\beta = 1$, $\frac{Q}{m} =$ 12 C/kg). Observing times are from left to right and top to bottom: 1996, 1998, 2000, 2002, 2004, 2006, 2008, 2010, 2012, 2014, 2016, 2018. The solar minimum of the defocusing cycle is in mid-1996 and of the focusing cycle is in mid-2007. The maximum effect of this on the density is about 3 years later. Solar maximum is in 2002, and the solar minimum of the focusing cycle is in mid-2007. Solar maximum is in 2013, and the solar minimum of the next defocusing cycle is in mid-2018.

Particle radius (μm)	β (...)	Q/m (C/kg)
0.5	0.5	0.2
0.3	1	0.5
0.2	1.5	1.5
0.06	1	12

Table 3.1: β and Q/m values for nominal interstellar particles close to the hypothetical β-curve for astronomical silicates with $\beta_{max} = 1.6$.

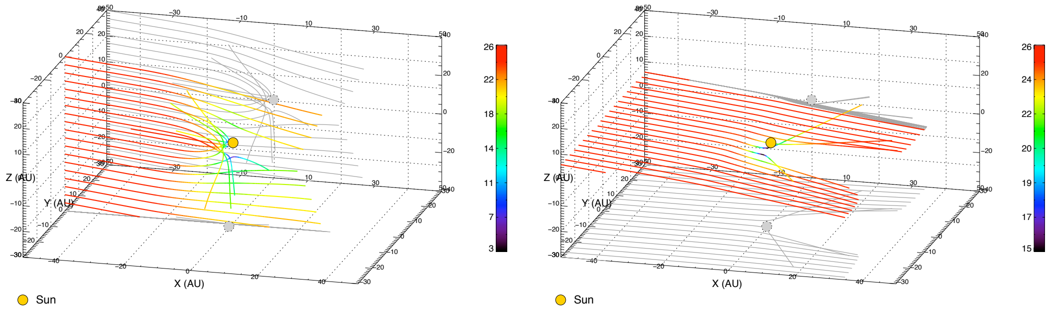

Figure 3.15: $\beta = 1.5$, Q/m = 1.5 C/kg. Start year 2000, at -50 AU from the Sun. The particles are focused towards the solar equatorial plane and for low-impact parameters they are reflected upstream of the Sun (left plot). The effect is a bit stronger than without radiation pressure force (compare with Fig. 3.9). On the right, it is visible that the particles are focused towards the solar equatorial plane, but a void region downstream of the Sun is visible that resembles the a β-cone. Fig. 3.17 (right) completes this picture.

3.1.2 Flow of nominal ISD particles ($\beta = 1.5$, Q/m = 1.5 C/kg)

In the previous sections we studied the trajectories for hypothetical particles with radiation pressure alone (Section 2.1.1) and Lorentz force ‘only’ (Section 3.1.1). However, some of these discussions apply to the flow of real interstellar grains. In Table 3.1, the β and Q/m values are given for nominal interstellar particles close to a hypothetical β-curve for astronomical silicates with $\beta_{max} = 1.6$.

For 0.5 μm particles (Q/m = 0.2 C/kg), the Lorentz force effects are considered to be small, so the case discussed in Section 2.1.1 ($\beta = 0.5$ and Q/m = 0 C/kg) is close to these big particles. Here we only consider the case for 0.2 μm particles ($\beta = 1.5$, Q/m = 1.5 C/kg) in order to see what the additional radiation pressure effects are. In Section 3.1.1 we discussed the case of particles with $\beta = 1$ and Q/m = 1.5 C/kg. Now we want to see what the additional radiation pressure effect is ($\beta = 1.5$). Comparing Fig. 3.9 ($\beta = 1$) with Fig. 3.15 ($\beta = 1.5$) we see that the additional deceleration by radiation pressure causes a stronger deflection upstream of the Sun. Downstream from the Sun, only particles with large impact parameters are found. The exclusion zone (Fig. 3.15, right) of the horizontal trajectory sheet resembles the exclusion zone of the radiation-pressure-only case (Fig. 2.2, right). During the defocusing cycle the exclusion zone becomes even wider (Fig. 3.16), and the particles are moderately accelerated.

The scatter plots (Fig. 3.17) at different slices along the beam resemble the Lorentz-force-only cases (Figs. 3.10) except for the shape of the central hole around the beam axis (cf. Fig. 2.5 for the radiation-pressure-only case). During the focusing period, higher concentrations of particles are found close to the equatorial plane but outside the exclusion zone. During the defocusing period particles are strongly concentrated at high latitudes above the solar poles.

The ISD densities during the defocusing period are strongly reduced in the inner planetary system

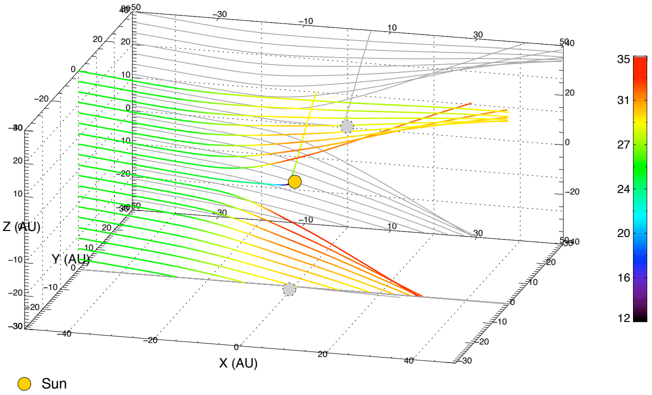

Figure 3.16: $\beta = 1.5$, Q/m = 1.5 C/kg. Start year 1990, at -50 AU from the Sun. The particles are defocused from the solar equatorial plane

(Fig. 3.18). During focusing periods, density enhancements of up to a factor 2 or more are found close to the ecliptic plane except in the exclusion zone, which is void of particles.

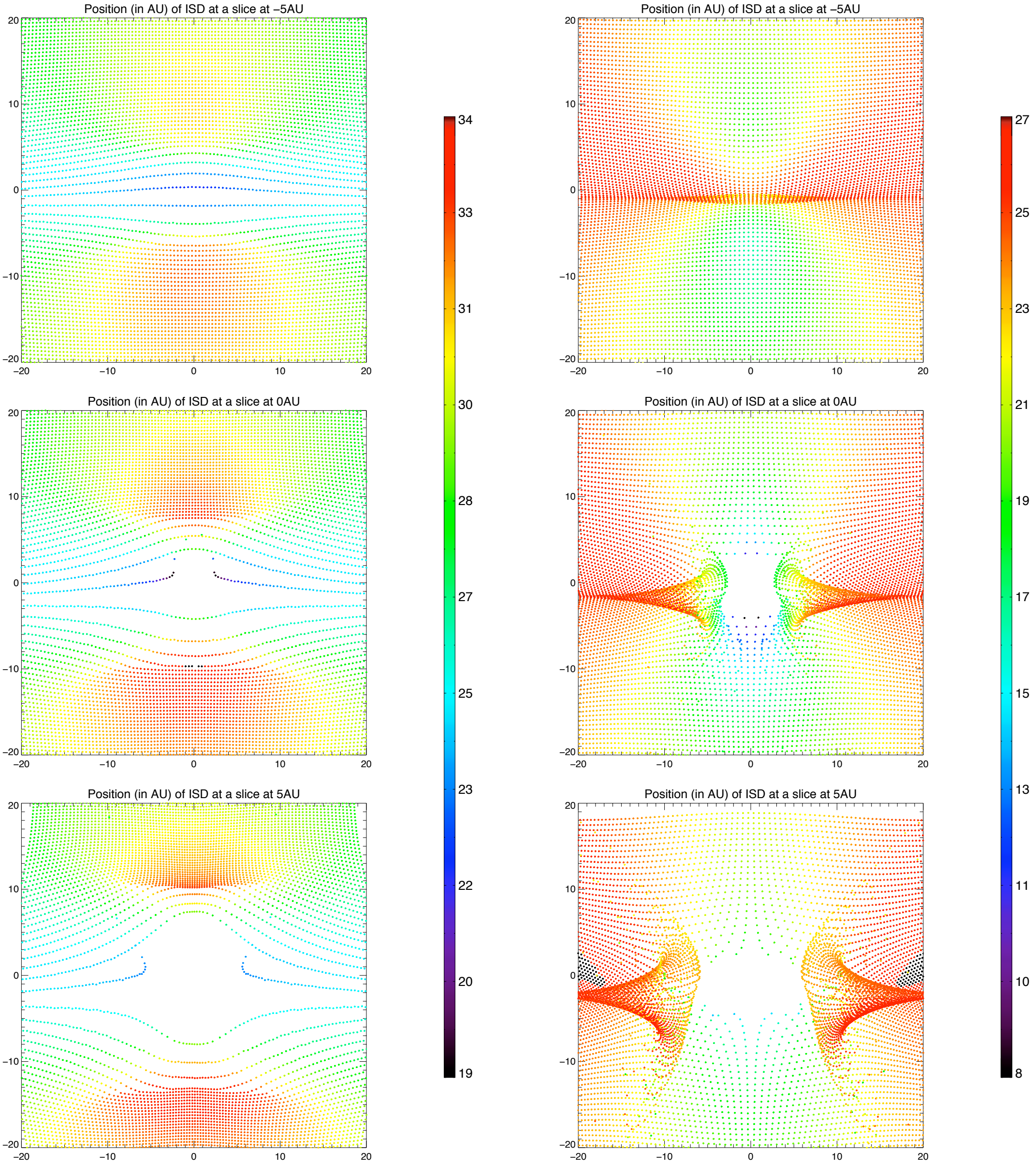

Figure 3.17: Cross-section of the trajectories during the defocusing phase of the solar cycle (left) and the focusing phase of the solar cycle (right). Start year was 1990 (left) and 2000 (right), $\beta = 1.5$, Q/m = 1.5 C/kg. The void region downstream from the Sun is enhanced by the Lorentz force in comparison with the β-only case, and high dust concentrations are visible at higher latitudes (left plot). A β-cone-like structure is visible (right), but its cross-section is not circular anymore (compare to Fig. 2.5).

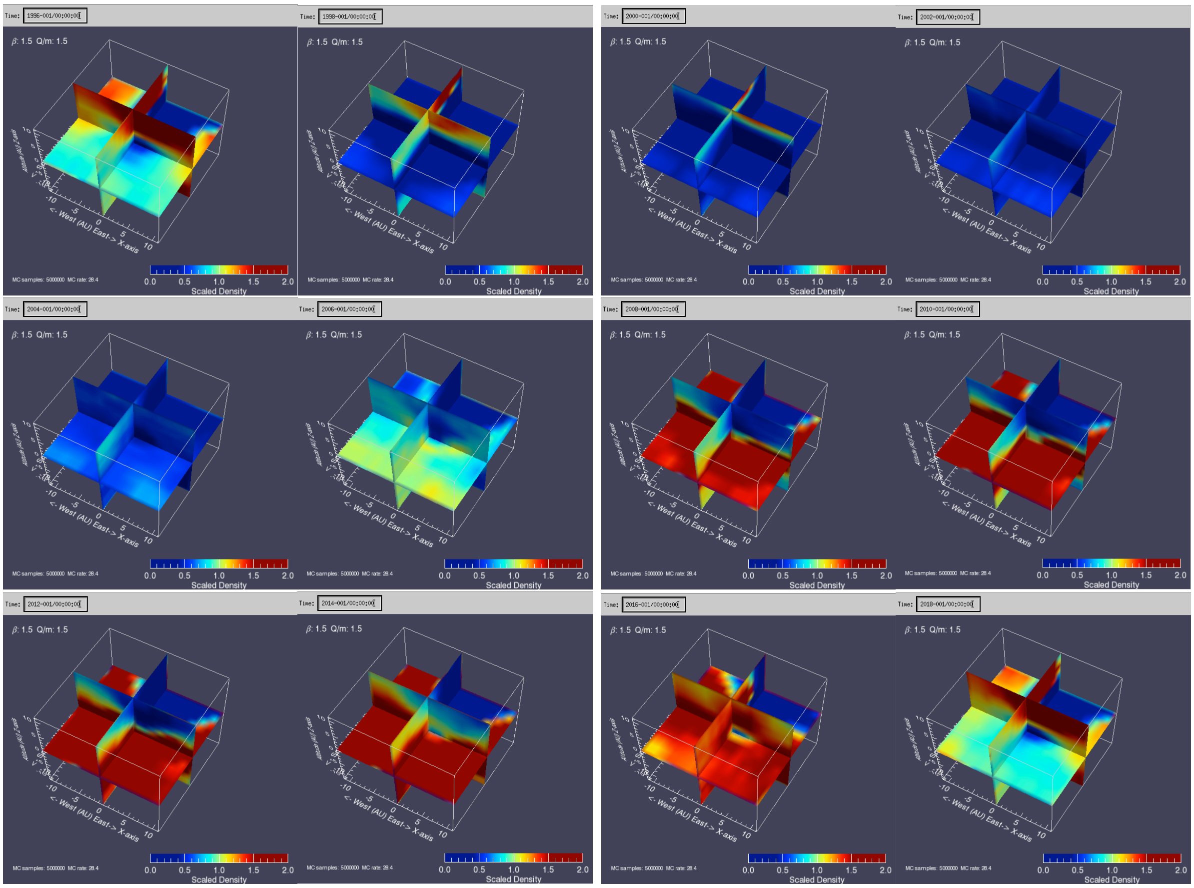

Figure 3.18: Variation in relative densities in the solar system, due to the Lorentz force ($\beta = 1.5$, Q/m = 1.5 C/kg). Observing times are from left to right and top to bottom: 1996, 1998, 2000, 2002, 2004, 2006, 2008, 2010, 2012, 2014, 2016, 2018. The solar minimum of the defocusing cycle is in mid-1996. The solar minimum of the focusing cycle is in mid-2007. The maximum effect of this on the density is about 3 years later. Solar maximum is in 2002, and the solar minimum of the focusing cycle is in mid-2007. Solar maximum is in 2013, and the solar minimum of the next defocusing cycle is in mid-2018.

3.2 Filtering of ISD at the heliopause

When interstellar dust grains enter the solar system, they pass several transition regions where magnetic field and plasma properties - and thus grain charging and Lorentz forces - change. First, the grains "encounter" the bow shock at about 250 AU where the gas of the LIC slows down to subsonic speeds. After the bow shock, the magnetic field strength increases but is still governed by the magnetic field of the LIC. Then, the grains encounter the zone where the LIC gas and the solar wind stagnate: the heliopause. Inside the heliopause (probably about 120 AU from the Sun), the solar wind dominates but is still subsonic. At about 80 AU from the Sun, the solar wind becomes supersonic at the termination shock. The region between the heliopause and the termination shock is called the heliosheath. Its magnetic field is influenced by the magnetic field of the solar wind, but it is now also known to be filled with turbulent plasma (Opher et al., 2011).

The grains in the undisturbed LIC are typically charged to have an equilibrium potential of 0.5 V (Grün and Svestka, 1996). When entering the transition region to the heliosphere, they get charged to equilibrium potentials of up to ten times higher (Linde and Gombosi, 2000) and experience the increased magnetic field strengths. The smallest grains (highest charge to mass ratio) get filtered out and are carried around the heliosphere. Linde and Gombosi (2000) have modeled this filtering between the bow shock and the termination shock and found that grains get filtered between sizes of 0.1-0.2 μm, including the recharging. Slavin et al. (2010) modeled the exclusion of small grains from the heliosphere, using full magnetohydrodynamics modeling, and concluded that 0.1 μm grains are strongly filtered but some particles can still get into the inner heliosphere, whereas 0.01 μm grains seem to be totally filtered out. For these results, the findings of (Opher et al., 2011) have not yet been included, only silicates were assumed which get higher charges (Kimura and Mann, 1998), plasma temperatures in the heliosheath are lower than expected (Richardson et al., 2008; Slavin et al., 2010) and thus charging could be milder. Both Linde and Gombosi (2000) and Slavin et al. (2010) calculated the deviation of the grains for a "defocusing" configuration of the interplanetary magnetic field in the heliosheath (positive magnetic field polarity at the north ecliptic pole). It is well possible that during other periods of the solar cycle, smaller grains get better through than presented here, due to focusing at the heliosphere boundary (Slavin, 2012, pers. communication). More research is needed to get this clear. The filtering at the heliospheric boundary is hereafter referred to as "primary filtering". The ISD grains that do pass the heliopause may still be filtered out from the inner solar system by solar radiation pressure force and Lorentz forces. This kind of filtering is referred to hereafter as "secondary filtering" and is described in Section 3.4 after introducing the ISD size distribution in the LIC in the next section.

3.3 The ISD size distribution in the LIC

Our current knowledge of the LIC comes mainly from astronomical observations. Information on the size distribution and composition of interstellar dust is obtained from the wavelength-dependent extinction and polarization of starlight, and from astronomical observations of absorption features from UV to infrared wavelengths; light scattering in the visible and ultraviolet, small-angle scattering of X-rays, thermal emission from infrared to sub-mm wavelengths, and microwave radiation from spinning dust.

The extinction curve was reproduced very well by the two component size distribution of Mathis, Rumpl and Nordsieck (Mathis et al., 1977). This MRN size distribution ranges from 5 to about 1000 nm in size (corresponding to masses of about 10^{-21} to 10^{-14} kg assuming a density of 2 g/cm^3). The observed interstellar extinction over the UV to near-IR wavelength was fitted with a very general particle size distribution of graphite and amorphous silicates. The size distribution is a power law with an exponent of -3.5. The size distribution for graphite is about 5 to 1000 nm, the silicate distribution is narrower: 25 to 250 nm. The number of large particles is not well constrained by extinction measurements because they do not contribute much to the visible extinction as they are gray.

Each one of the clouds in the Local Bubble has its own density and temperature, and it is not unthinkable that they have different dust compositions and size distributions. Since our current knowledge of the LIC comes mainly from astronomical observations averaged over several kiloparsecs, care needs to be taken about the assumption whether the MRN distribution is fully representative for all dust in the LIC.

Although there are more modern and more detailed size distributions of interstellar dust in the diffuse interstellar medium (e.g. Weingartner and Draine (2001), and Zubko et al. (2004)) we will use the MRN size distribution as a simple representation of dust in the LIC.

The MRN size distribution of grains in the diffuse interstellar medium is given by a power law

$$dn = An_H a^{-\alpha}\, da \tag{3.1}$$

with the number of grains dn within the size interval da, slope $\alpha = 3.5$, and A = 7.76 10^{-26} $\mathrm{cm}^{-2.5}$ per H nucleus (Mathis et al., 1977). In this thesis, we will assume $n_H = 0.3\ \mathrm{cm}^{-3}$, a typical value for the local interstellar medium (Frisch et al., 1999). The grain sizes, a, range from 5 to 250 nm (m = 1.7 10^{-21} kg to 2.2 10^{-16} kg). For size distributions covering a wide mass range, it is convenient to use the logarithmic differential distribution.

The differential number (n), mass number (n_m) and cross-sectional number distributions (n_A) with respect to grain size a can be calculated from Eq. 3.1:

$$\frac{dn}{d(log\ a)} = \ln 10\ An_H a^{1-\alpha} \tag{3.2}$$

$$\frac{dn_m}{d(log\ a)} = \ln 10\ An_H \frac{4\rho\pi}{3} a^{4-\alpha} \tag{3.3}$$

$$\frac{dn_A}{d(log\ a)} = \ln 10\ An_H \pi a^{3-\alpha} \tag{3.4}$$

The logarithmic mass number distribution as function of mass is then given by

$$dn = C_{MRN} \times m^{\frac{1-\alpha}{3}} d(log\ m) \tag{3.5}$$

with the constant

$$C_{MRN} = An_H \left(\frac{3}{4\pi\rho}\right)^{\frac{1-\alpha}{3}} \frac{1}{3} \ln 10 \tag{3.6}$$

The logarithmic differential (number) distribution shows the amount of grains per logarithmic mass interval (see Fig. 3.19, left). The smaller grains are more abundant than the larger ones. In order to know how the mass is distributed amongst the grain sizes, we multiply the logarithmic differential number distribution with the mass of the grains to get the logarithmic differential mass distribution:

$$dn_m = C_{MRN} \times m^{\frac{4-\alpha}{3}} d(log\ m) \tag{3.7}$$

Although the smaller ISD grains are more abundant in number, the largest part of the mass resides in larger grains (see Fig. 3.19, middle). The total mass thus depends on the largest of the grains that are present. The logarithmic differential cross-section distribution is important because of emission, scattering and absorption of light which depends on the grain cross-section. It is derived by multiplying the differential number distribution with the cross-sectional area of the grains:

$$dn_A = C_{MRN}\ \pi \left(\frac{3}{4\pi\rho}\right)^{2/3} \times m^{\frac{3-\alpha}{3}} d(log\ m) \tag{3.8}$$

The logarithmic differential cross-section distribution is shown in Fig. 3.19 on the right and it shows that the smallest grains are dominating the total "cross-section" of the grains (thus making them dominate astronomical observations), but their slope is less steep than for the logarithmic differential number density.

In-situ dust instruments (e.g. like the Ulysses dust detector) count particles above a given mass threshold, therefore cumulative distributions are important. The slope of these cumulative distributions is the same as the corresponding differential logarithmic distribution. The cumulative distributions (number of grains above a threshold mass) can be calculated using:

$$N = \int_{m_1}^{m_2} \frac{1}{\ln 10} C_{MRN} m^{\frac{-2-\alpha}{3}} dm \tag{3.9}$$

$$= \frac{3}{\ln 10\,(1-\alpha)} C_{MRN} (-m_1^{\frac{1-\alpha}{3}}) \tag{3.10}$$

$$\tag{3.11}$$

	d(log m)	d(log a)	N(m)
dn	$\frac{1-\alpha}{3}$	$1-\alpha$	$\frac{1-\alpha}{3}$
dn$_m$	$\frac{4-\alpha}{3}$	$4-\alpha$	$\frac{4-\alpha}{3}$
dn$_A$	$\frac{3-\alpha}{3}$	$3-\alpha$	$\frac{3-\alpha}{3}$

Table 3.2: The slopes of the logarithmic differential densities; they are the same as the cumulative density distributions. For the MRN-distribution, $\alpha = 3.5$

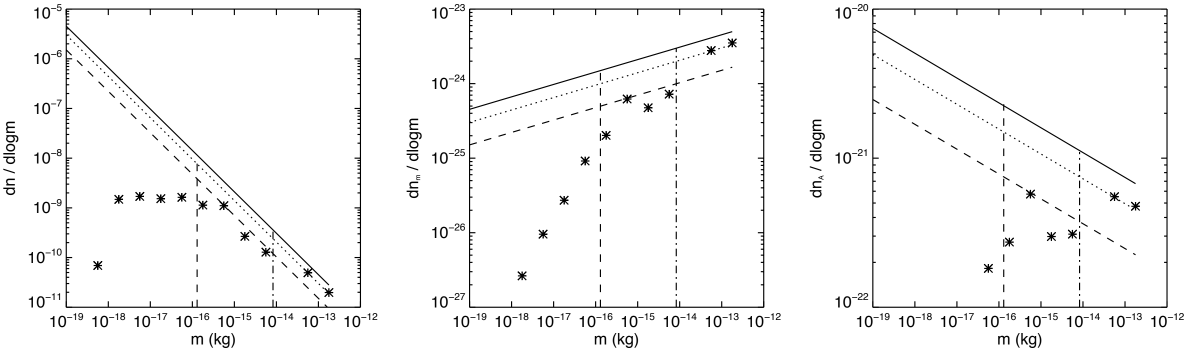

Figure 3.19: The MRN distributions for a Hydrogen density of 0.1, 0.2 and 0.3 cm^{-3} (dashed, dotted and continuous line) and the ISD distributions from Ulysses data (stars). The left plot shows the number density, the middle plot the mass number density and the right plot the cross section number density. The cut-off for silicate grains in the MRN-distribution is indicated with a vertical dashed line at 0.25 μm ($1.3 \cdot 10^{-16}$ kg) and for carbon grains at 1 μm ($8.4 \cdot 10^{-15}$ kg).

3.4 The size distribution of ISD in the inner solar system

Chapters 2 and 3.1 describe quantitatively the mechanism as well as the effects of it on the flow of ISD grains in the solar system. Here, we go one step further and investigate the effect of this filtering on the size distribution of the dust. We start with the simple case of solar radiation pressure and solar gravity only (Section 3.4.1), and expand then to include the Lorentz force (Section 3.4.2).

3.4.1 Gravity and radiation pressure only

In Sectionsec:radpressure the dynamics by solar gravity and radiation pressure alone of ISD grains is described. Fig. 2.11 shows some examples of β-curves for different materials. Generally, β increases with decreasing particle size or mass until the size is comparable to the effective wavelength of sunlight below which β decreases again. While particles with $\beta < 1$ are attracted and focused behind the Sun, particles with $\beta > 1$ are repelled by the Sun and an exclusion zone forms around and behind the Sun (Fig. 2.2, Section 2.1.1). Particles with $\beta < 1$ are also accelerated closer to the Sun whereas particles with $\beta > 1$ are slower when they come closer to β-cones. This different behavior of particles of different sizes (β-values) has as consequence that the size distribution of ISD inside the heliosphere varies from the size distribution outside the heliosphere just from the effect of radiation pressure alone.

In order to demonstrate this effect we have evaluated the relative ISD density (Eqn. 2.15, Section 2.1.1) in a plane along the flow axis of the incoming ISD as function of the particle mass, assuming the adapted astronomical silicates β-curve (Section 2.1.4). This variation of the relative mass distribution is shown in Fig. 3.20 from E. Grün. Well in front of the Sun, the density variation as function of particle mass is small, i.e similar to the density at the heliospheric boundary. However, it becomes significant around and behind the Sun. Particles with $\beta > 1$ become depleted in the paraboloid-shaped exclusion zone around and behind the Sun while particles with $\beta < 1$ are focused behind the Sun. Such a bite-out feature in the mass distribution has been observed in the Ulysses data (Landgraf et al., 1999a) and was used to get information of the β-values of interstellar grains. The enhancement of particles smaller than 10^{-17} kg will be reduced or enhanced due to electromagnetic interactions (see below).

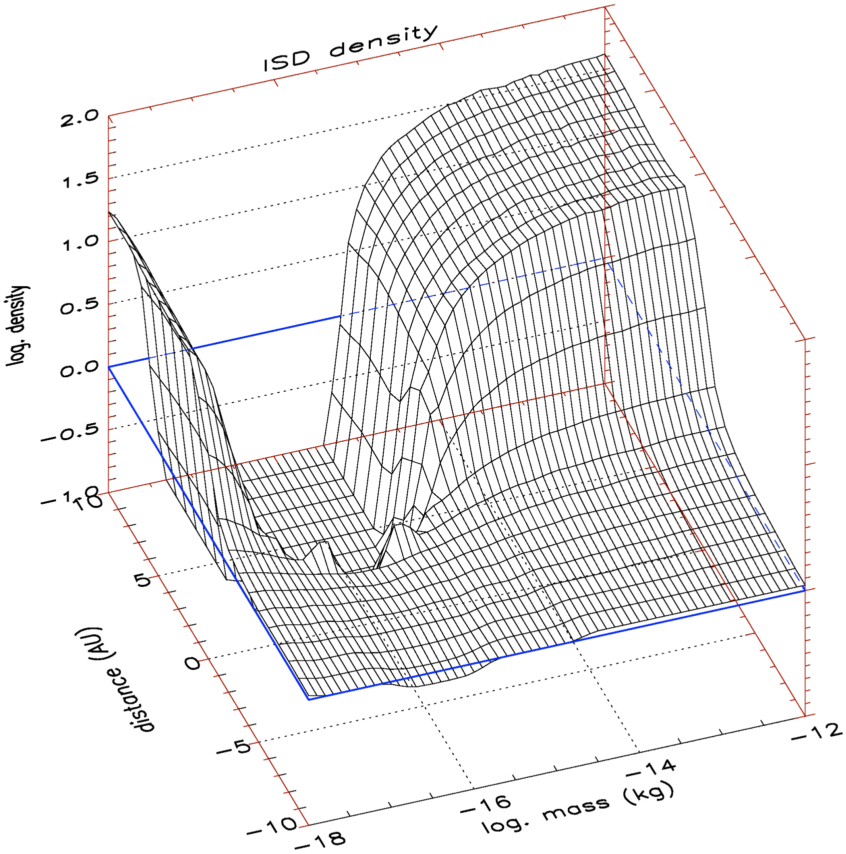

Figure 3.20: Variation of the interstellar dust density in a 1 AU column around the axis of the interstellar dust flow as a function of particle mass and distance from the Sun. Density 0 was set to the bottom of the diagram at 0.1. The blue lines denote the plane of density level of 1. The adapted β-curve for astronomical silicates was assumed. Source: E. Grün

3.4.2 Effects along the interstellar flow axis including Lorentz forces

In Section 2.1.2 we explain in some detail the dynamical interaction of charged dust particles with the interplanetary magnetic field. In the following we will display smoothed values of the interstellar relative dust flux (relative to the flux value at the outer boundary of the simulation) and speed for different points in space and time covering roughly the Q/m and β ranges shown in Fig. 2.11.

We illustrate the combined effect of the Lorentz force, solar gravity and solar radiation pressure force on the dust size distribution along the flow-axis of the dust towards the Sun, in analogy with Section 3.4.1. We plot the relative flux and relative velocity in color-scale as a function of β and Q/m on the vertical and horizontal axes (Figs. 3.21 – 3.24). The β-Q/m plots are constructed from a matrix of 70 simulations, as shown in Fig. 2.11, where the simulation results are interpolated (in 2D) to fill the whole β-Q/m space. The solid line in Figs. 3.21 – 3.24 shows the β-curve for the nominal (adapted) astronomical silicates. We do this for the locations of -10 AU (upstream), -5 AU, -3 AU and 3 AU (downstream) at a specific time. In order to show the effect of the solar cycle, we selected a time in the year 2000 (max. effect of the defocusing phase) and 2011 (max. effect of the focusing phase). This is about 3 years after the optimum focusing/defocusing field conditions (Table 2.1) because interstellar grains need that time in order to display an enhanced density near the ecliptic plane.

At 10 AU upstream (-10 AU, Fig. 3.21) the flux of big particles (Q/m < 1) is little affected by the Lorentz-force. Only the flux of small particles is reduced during the defocusing phase around year 2000. Eleven years later the flux of small particles ($1 <$ Q/m < 5) is enhanced especially for high β values. The speed of $\beta \leq 1$ particles has increased in comparison of that at the heliospheric boundary whereas that of $\beta \geq 1$ particles has decreased. For the grains with Q/m > 8 C/kg in the defocusing phase, no velocity is drawn where the flux is zero. Closer to the Sun (-5 AU, Fig. 3.22) these effects become more pronounced except that during the focusing phase the flux of very small grains (Q/m > 8) is enhanced because these particles are deflected from higher latitudes to the ecliptic plane.

At 3 AU upstream (-3 AU, Fig. 3.23) the effect of the β-cone becomes obvious in the flux of large β (> 2.5) particles, which is strongly reduced. In addition the flux of small particles (Q/m > 1) becomes strongly modulated by the electromagnetic interaction during the focusing and defocusing phases. Downstream from the Sun close to the interstellar flow axis (3 AU, Fig. 3.24) only particles with $\beta < 1$ can be found, the biggest of which (Q/m < 2) show an enhanced flux due to gravitational focusing. Again the flux of small particles (Q/m > 2) is strongly modulated by the electromagnetic interaction. The further downstream, the more abrupt the β-cone appears in terms of enhancement (gravitational focusing) and depletion (β-cone) of dust.

In the following paragraph we analyze how the size distribution of the nominal astronomical silicate particles (solid line in the preceding diagrams) is changing along the flow axis of interstellar dust. For all sizes given in Table 2.2 we obtain the relative flux values at the corresponding β and Q/m positions (cf. Figs. 3.21 – 3.24) and multiply them with the reference MRN size distribution. In Figure 3.25 we display the resulting size distribution at different epochs during the solar cycle for each of the positions along the flow axis of the dust (-10, -5, -3, and 3 AU). We show for an initial MRN size distribution the number density and the plain enhancement or reduction factor that can be applied to any size distribution we choose. The filtering at the heliopause is ignored. The dotted straight line is the original MRN distribution (and extrapolation) for $n_H = 0.3$ cm^{-3}. The black straight line is the MRN-distribution range for which simulations were done.The crosses in Fig. 3.25 are not interpolated like in Figs. 3.21 – 3.24, but are the exact simulation results for 7 different Q/m-values. The density of the grains assumed is 2 g/cm^3 and the assumed interstellar density of H atoms is 0.3 cm^{-3}.

Far upstream at -10 AU, the number density is reduced at the defocusing phase of the solar cycle for all grain sizes (year 2000: red line top row of Fig. 3.25). During the focusing phase, it is enhanced and because of the complexity of the interplay of β-cone with Lorentz force, the enhancements occur at different sizes in the size distribution, for different positions in the solar system (compare in Fig. 3.25 the position of the peak of the blue line of -10 AU (top row) with the peak of the blue line of -5 AU (second row)). During the defocusing phase, the smallest grains get filtered out (e.g. the most left point of the red line).

Upstream (-10 to -3 AU in Fig. 3.25), the size distribution for the largest grains (mass $= 3 \cdot 10^{-15}$ kg) follow more or less the MRN distribution. However, downstream (+3 AU in Fig. 3.25) these large grains are focused by gravitational focusing (low β) and hence, the fluxes are enhanced by a factor of up to 10.

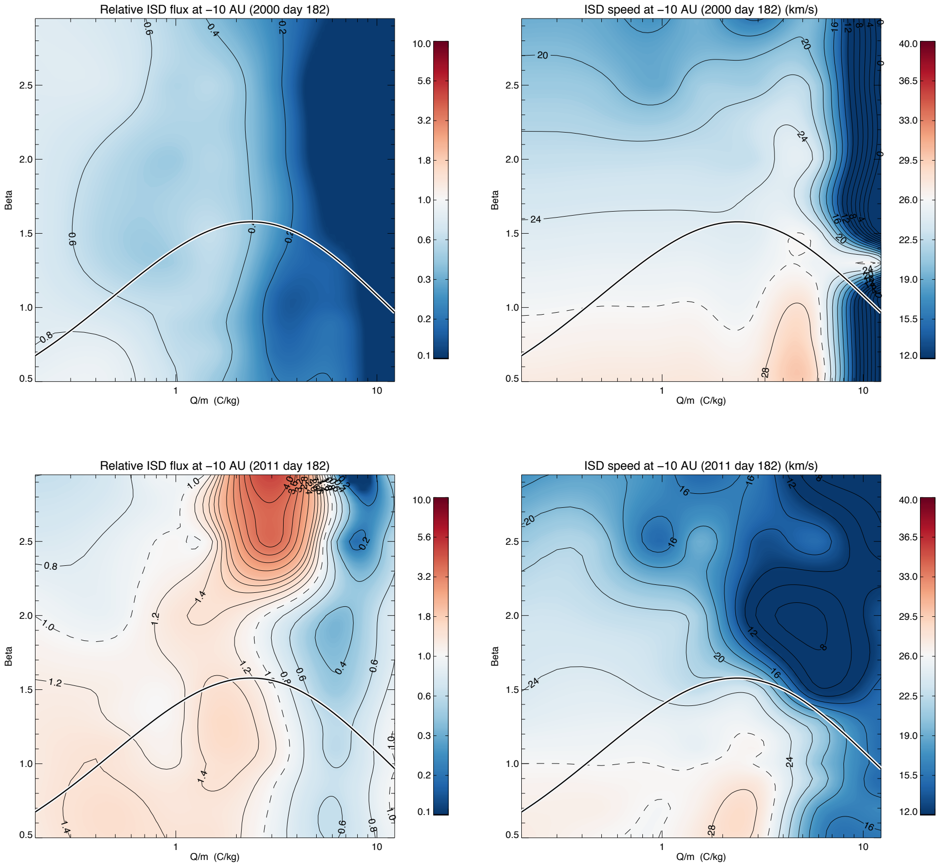

Figure 3.21: The relative flux (left) and relative velocity (right) at -10 AU (upstream) from the Sun for the defocusing phase (2000, day 182, top figures) and the focusing phase (2011, day 182, bottom figures). The adapted astronomical silicates curve is shown as a black/white line.

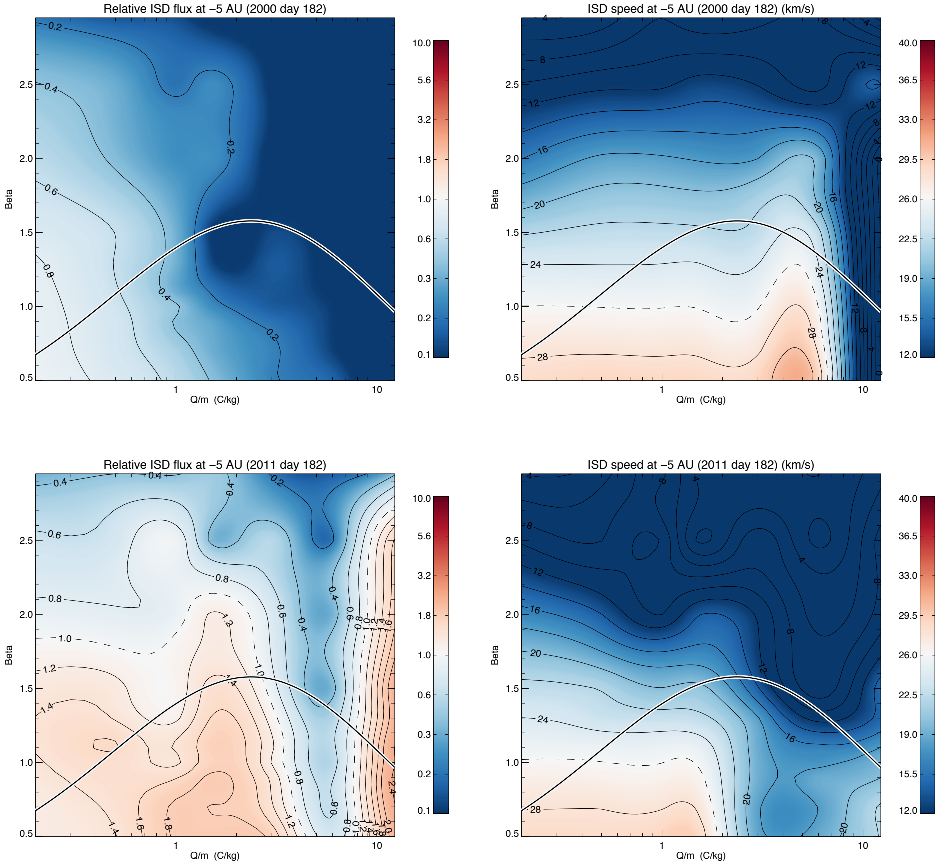

Figure 3.22: The relative flux (left) and relative velocity (right) at -5 AU (upstream) from the Sun for the defocusing phase (2000, day 182, top figures) and the focusing phase (2011, day 182, bottom figures). The adapted astronomical silicates curve is shown as a black/white line.

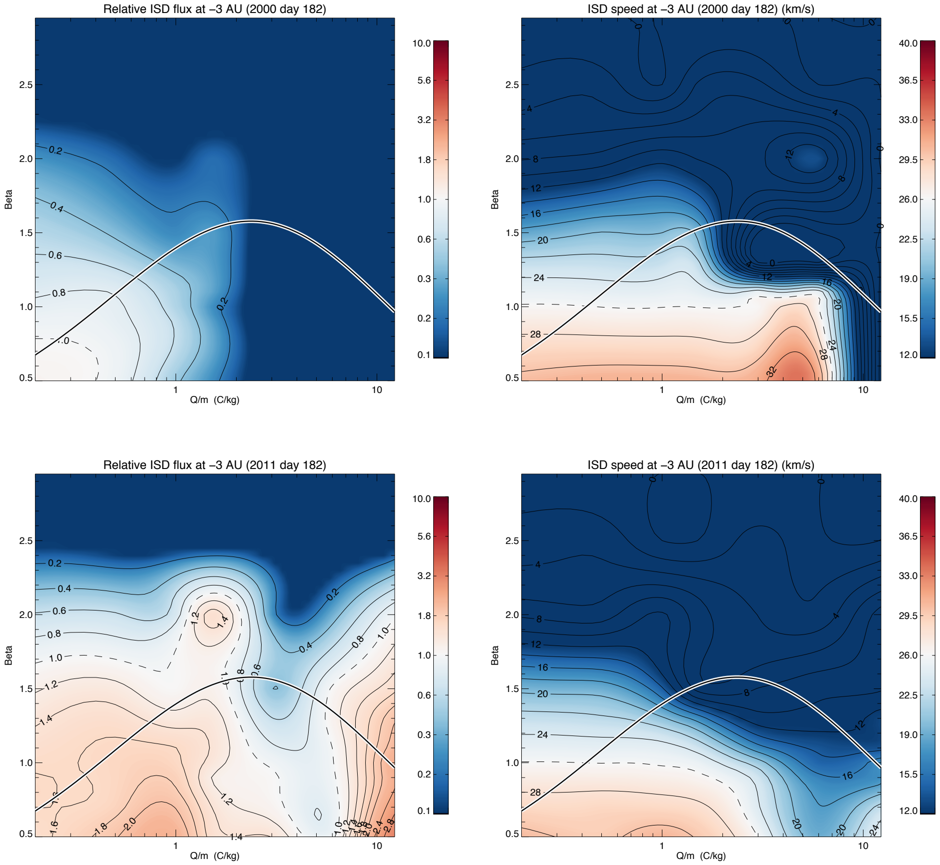

Figure 3.23: The relative flux (left) and relative velocity (right) at -3 AU (upstream) from the Sun for the defocusing phase (2000, day 182, top figures) and the focusing phase (2011, day 182, bottom figures). The adapted astronomical silicates curve is shown as a black/white line.

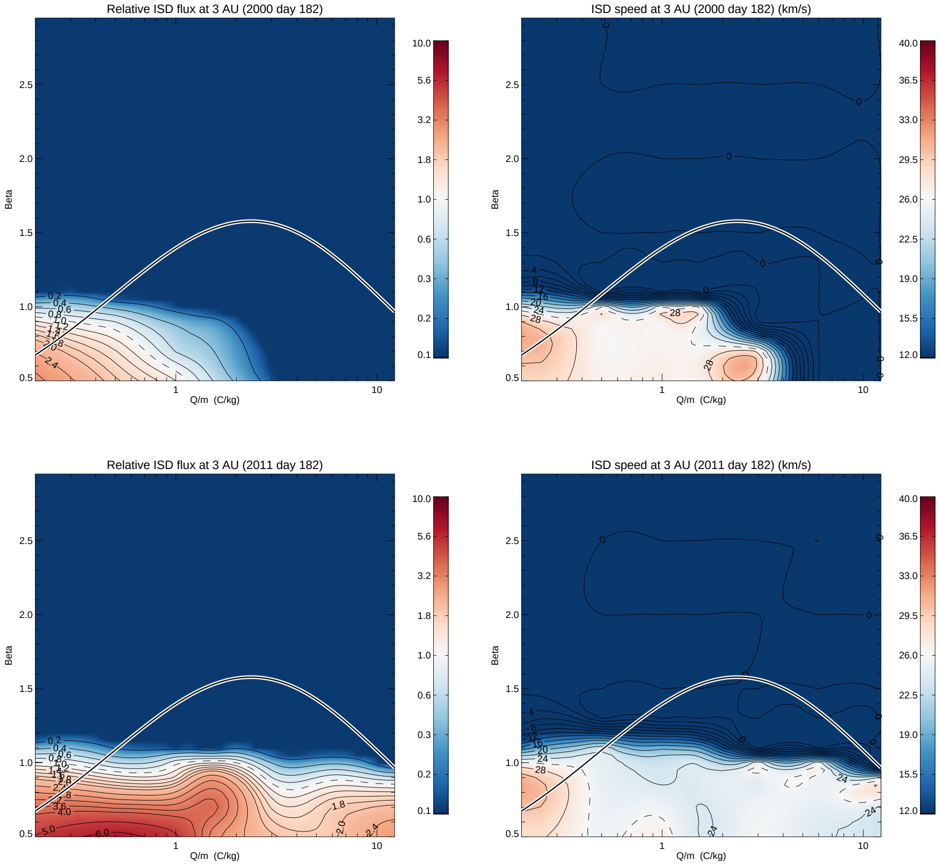

Figure 3.24: The relative flux (left) and relative velocity (right) at 3 AU (downstream) from the Sun for the defocusing phase (2000, day 182, top figures) and the focusing phase (2011, day 182, bottom figures). The adapted astronomical silicates curve is shown as a black/white line.

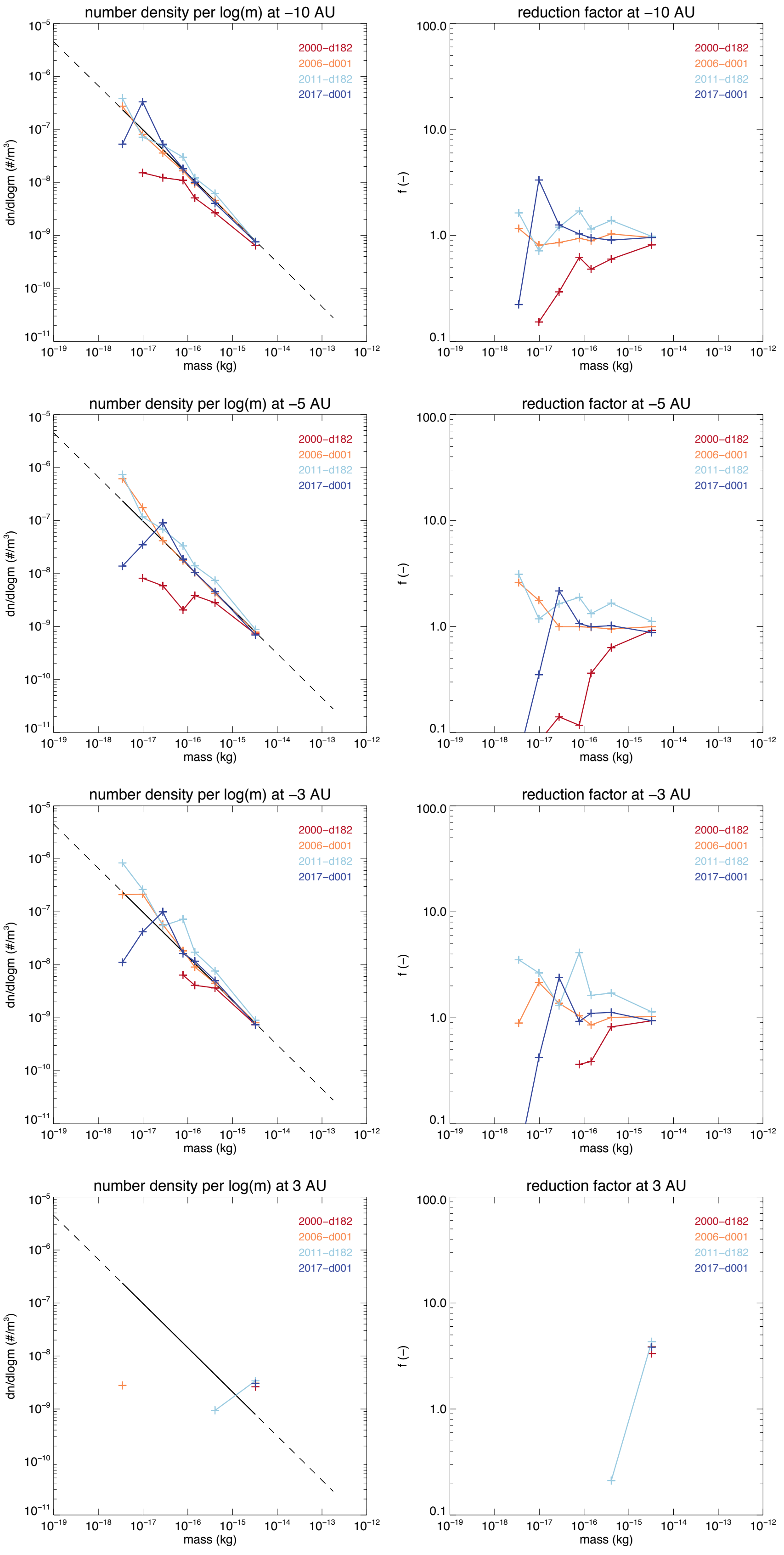

Figure 3.25: Size distributions for different times in the solar cycle (colors) and positions upstream and downstream from the Sun along the flow-axis: -10 AU (upstream), -5 AU, -3 AU and +3 AU (see text).

4

Discussion: applications of the modeling

After having explained the modeling, flow and filtering of the ISD in the first three chapters of this thesis, we apply the simulations to three different places in the solar system. Section 4.1 discusses the ISD flux and filtering at Saturn, and then focuses on its implications for the Cassini mission as an application. Section 4.2 discusses the ISD flux and filtering at Jupiter for two different Jupiter orbits and illustrates the optimal conditions for the future JUICE mission to observe ISD. This is also compared to the past Galileo mission (1996-2003). Finally, Section 4.3 discusses the ISD flux and filtering in the asteroid belt and goes deeper into interstellar dust simulations that were made for analyzing the preliminary Stardust sample-return results.

4.1 Interstellar dust at Saturn

We apply the modeling of Chapters 2 and 3 to the case of Saturn and discuss the results in the context of ISD measurements with Cassini during the orbital phase of the mission. Fig. 4.1 shows the orbit of Saturn between 1991 and 2020 with respect to the β-cones. Its orbital period (29.5 years) is longer than the 22 years full solar cycle. We look at the relative fluxes and filtered size distribution at Saturn during one orbit between 1991 and 2020 and choose 8 positions along its orbit relative to the ISD flux: upstream, downstream, sidestreams and four positions in between. The flux variations in time and location in the solar system are correlated through the orbit of Saturn.

In the appendix B.1 we discuss the relative fluxes and size distributions along the orbit of Saturn for all β and Q/m values (Figs. B.1 and B.2). Here we only summarize the main findings of this analysis for 7 grain sizes along the adapted astronomical silicates curve.

The relative fluxes with respect to Saturn throughout the solar cycle are shown in Fig. 4.2 for 7 particle sizes (Table 2.2) representing β and Q/m values of the nominal material (cf. solid line in Figs. B.1 and B.2). The biggest particles (0.7 μm) display a strongly enhanced flux (factor 4) around 2003 when Saturn is in the gravitational focusing region downstream from the Sun. Their enhanced fluxes (factor 2) around 2010 are due to the motion of Saturn against the interstellar dust flow. Conversely the flux is reduced around 1996 when Saturn moves parallel to the interstellar flow. To see the effect of the motion of Saturn alone, we refer to the $\beta = 1$ and Q/m ≈ 0 C/kg curve in Appendix B.1, Fig. B.4. In 2003 Saturn is in the β-cone for smaller particles ($\beta > 1$, between 0.1 and 0.4 μm) and hence no such interstellar grains can reach Saturn then. The flux enhancements around 2010 become even more pronounced for smaller grains (0.2 μm, factor 8) due to the Lorentz forces of the focusing phase of the solar cycle. The enhancements for grains of 0.15 μm reach values of factors up to 10 and the maximum flux shifts to later years (2013). For the smallest particles considered (~ 0.1 μm) the flux is still enhanced in the period 2007 to 2012 but no longer as much as for the somewhat bigger particles. Sharp peaks in the small particle flux appear around 2017 when Saturn is in the upstream region of the interstellar dust flow. Between

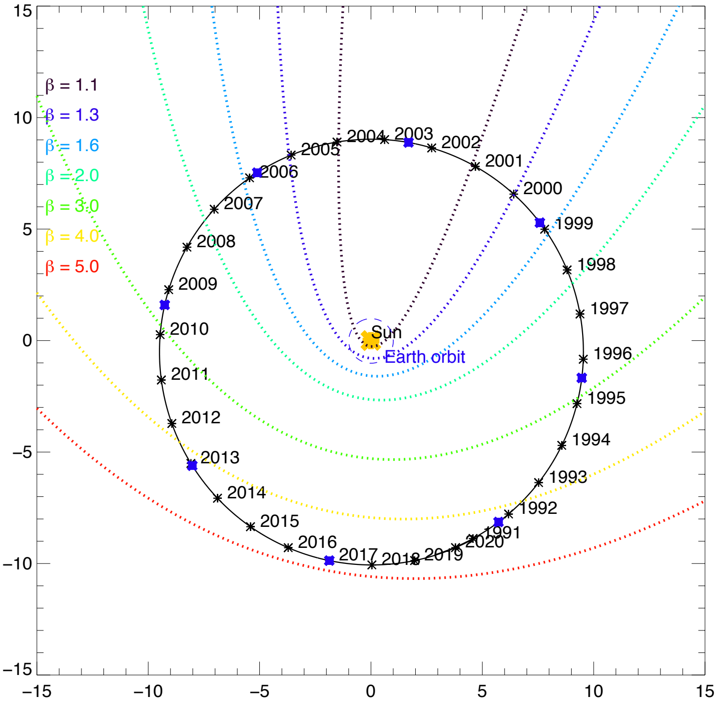

Figure 4.1: The orbit of Saturn around the Sun in the heliocentric ecliptic frame with the β-cones shown in colored dotted lines. The 8 positions for which the size distributions and β-Q/m plots are shown in this chapter and in Appendix B.1 are indicated as blue dots.

2007 and 2017, mid-sized and smaller grains ($\sim< 0.3\mu$m) experience very strong flux enhancements at different times. This has to do with the complicated focusing mechanism upstream from the Sun for grains with higher Q/m values (cf. Fig. 3.12: the grains are reflected upstream from the Sun, which we refer to as *mirroring*).

The enhancements or reductions in the size distributions (ignoring the heliopause filtering) follow again the solar cycle and β-cones. The left plot of Fig. 4.3 shows the filtered ISD size distribution at 8 different times during Saturns orbit and the right plot shows the filtering factor (i.e. the relative flux, also called "reduction factor" in this thesis). The modulation of the size dependent flux ranges from total disappearance of some particle sizes to enhancements of up to factor 10. Particles with sizes of about 0.2 μm ($5 \cdot 10^{-17}$ kg) are absent when Saturn is within the respective β-cone. This is visible around the year 2002 when only the biggest particles (0.7 μm) reach Saturn at an enhanced flux (gravitational focusing). In the period from 2009 to 2013, the flux of $>\sim 0.2$ μm sized particles is strongly enhanced due to the increased relative speed between Saturn and the interstellar flow and due to the focusing effect of the interplanetary magnetic field.

Except for the downstream region, the filtered *number flux* is highest for the smallest particles (~ 0.15 μm ($3 \cdot 10^{-17}$ kg); if they can traverse the heliopause). At favorable times (2009 to 2013) the filtered *mass flux* will be highest - not for the biggest particles, as for the undisturbed MRN distribution - but for the mid-sized grains around 0.2 μm. In 2017 the small grains contribute very clearly to the number flux if they are not filtered out at the heliopause. Depending on that filtering, a final number on the small grains can be given. In 2013, 1991 and 1995 (later in the focusing phase, and in even in the onset of the defocusing phase) there are high fluxes for small grains (e.g. 0.15 μm), due to mirroring and focusing upstream from the Sun.

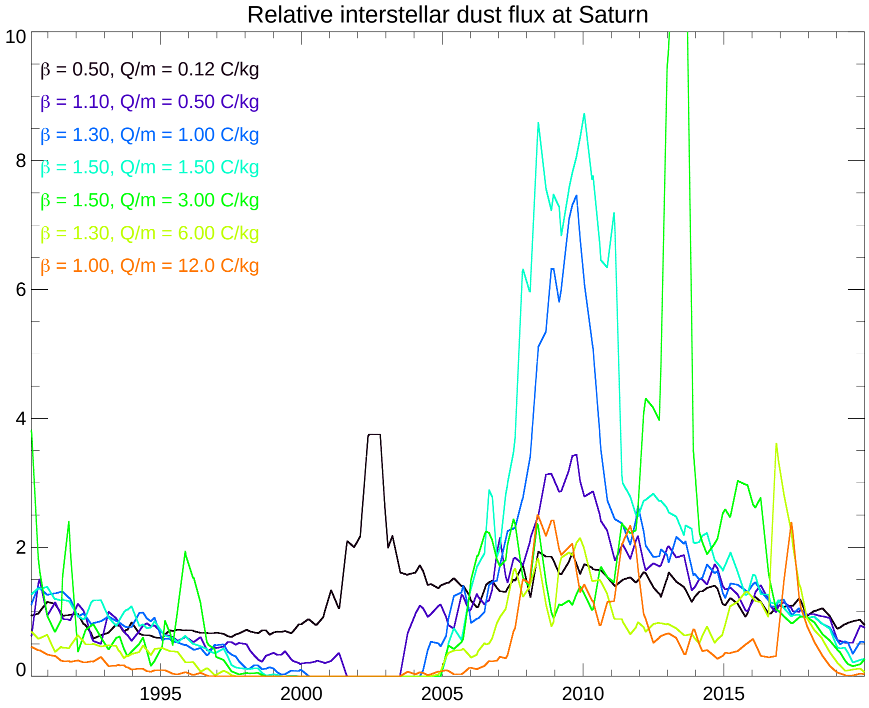

Figure 4.2: The relative fluxes with respect to Saturn throughout the solar cycle for 7 particle sizes of the nominal material (*adapted astrosilicates*), see Table 2.2. For clarity, the curves for each grain size apart are drawn in Appendix B.1, Fig. B.3.

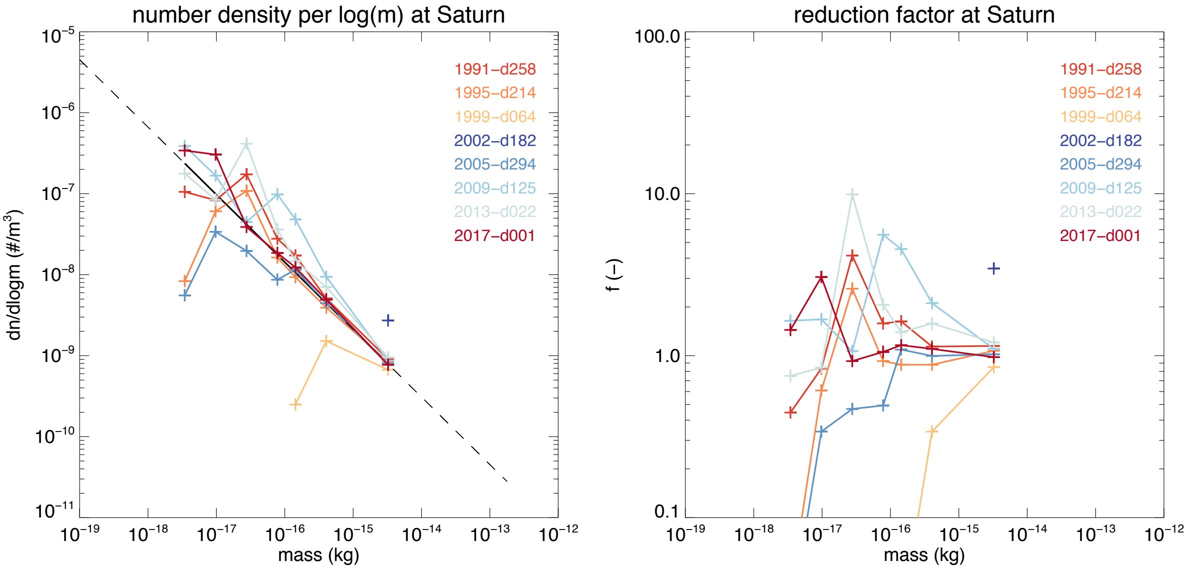

Figure 4.3: Size distributions of the ISD at Saturn for the 8 positions along its orbit. The left plot shows the number density, the right plot shows the relative flux ("reduction factor" or filtering factor). The gravitational focusing in 2002 is clear for the largest particles ($3 \cdot 10^{-15}$) as well as the strong influence of the solar cycle on the size distributions, especially for the smaller grains (cf. Fig. 3.25).

4.1.1 Predictions for Cassini

The fluxes and size distributions at Saturn were discussed in Section 4.1 and also apply to the Cassini mission. The Cassini spacecraft reached Saturn in 2004 and will orbit this planet until 2017 when the mission will be terminated. This period is especially interesting because it includes periods of high fluxes of all sizes of interstellar grains. During its cruise phase, some grains of $\sim$0.4 μm that could be ISD, were already identified in the Cassini Cosmic Dust Analyzer data (Altobelli et al., 2003). During the orbital phase of the mission, Cassini has dedicated ISD observation times where the pointing of the instrument is optimized. The interstellar dust measurements are mostly done outside of 25 Saturnian radii, outside of the Saturnian magnetosphere. We first summarize briefly why the period from about 2007 until 2017 is such a good ISD observation time for Cassini and then move on to discuss the directionality of the flux. We ignore in this discussion the influence of the Saturnian magnetosphere and gravitational focusing on the grain trajectories, because we expect this effect on the Cassini observations to be small.

The fluxes of interstellar dust are firstly enhanced by the movement of Saturn (and thus Cassini) against the ISD stream. Secondly, around 2010, the grains are focused because of the focusing phase of the solar cycle. Third, Cassini gets out of the β-cone for $\beta = 3$ in 2010 meaning that for most materials, no β-gap in the size distribution will exist and hence, the total accumulated flux will be largest. Fourth, small grains of different sizes (0.15, 0.2 and 0.25 μm) experience strong focusing at different times (2010, 2010 and 2013 respectively) due to the complex flow patterns for high Lorentz forces ("mirroring"). Also small grains are more abundant than the big grains in the original size distribution, therefore, if these are not filtered at the termination shock, then these enhancements may result in a higher observed number of small ISD grains by Cassini.

Hence, a very interesting era starts for finding ISD in Cassini data, not only for the high fluxes, but also because all sizes of all materials are theoretically able to reach the Cassini spacecraft location (outside the $\beta = 3$ cone) and thus the detector. This is interersting especially since Cassini carries a time-of-flight mass spectrometer on board to alanyze the grain composition.

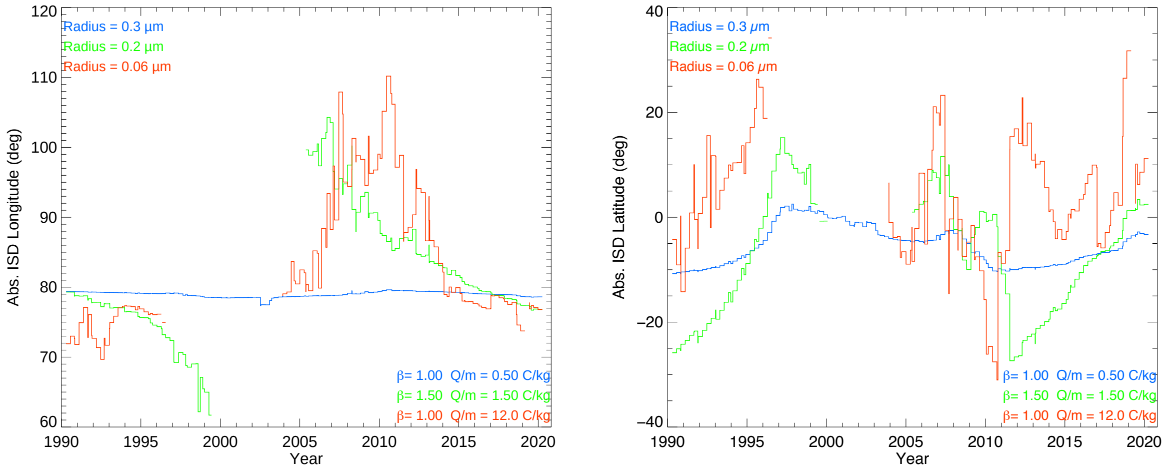

Figure 4.4: Absolute directionality of the ISD in the ecliptic frame (left plot: longitude, right plot: latitude), with time, at Saturn location, for three different ISD populations close to the adapted astrosilicates β-curve (0.3 μm, 0.2 μm, and 0.06 μm, see Table 3.1).

Apart from the fluxes, we also predict and show the evolution of the ISD directionality (in the heliocentric ecliptic frame) with time in Fig. 4.4 for three grain sizes: 0.3, 0.2 and 0.06 μm. The direction of 0.3 μm particles is determined by the Lorentz force, since $\beta = 1$. There is a variation of about 15° in latitude and 4° in longitude over 30 years of time. The directionality of the 0.2 μm particles shows a clear influence

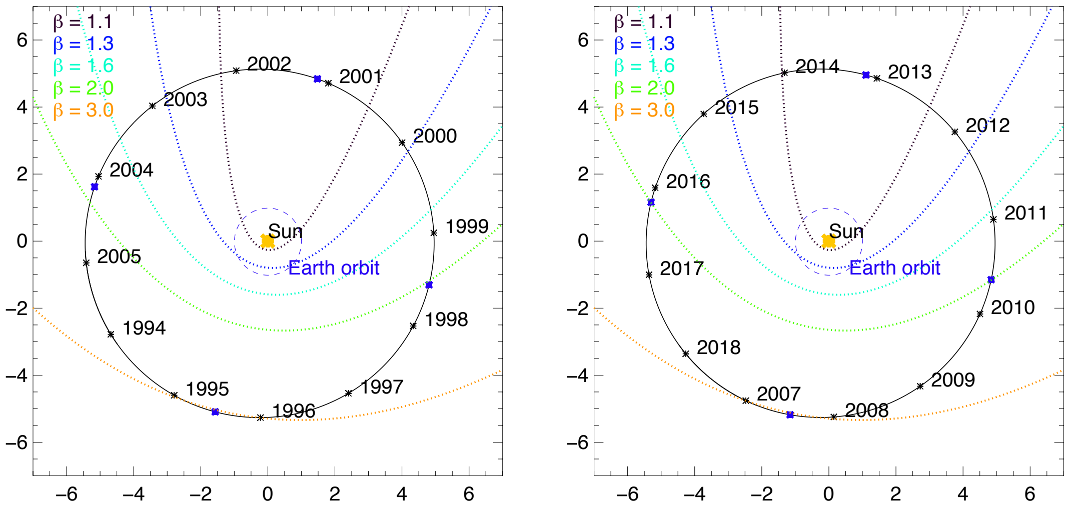

Figure 4.5: The orbit of Jupiter around the Sun with the β-cones shown in colored dotted lines. X and Y are the heliocentric ecliptic coordinates. The 4 positions (per orbit) for which we show the β-Q/m plots (Appendix B.2) and size distributions are indicated as blue dots. The left plot corresponds to the defocusing phase and the right plot corresponds to the focusing phase of the solar cycle. Note that Galileo was flying from 1996 until 2003 and was thus in large parts of its orbit in the β-cones, as well as moving in the same direction of the dust flow. For the JUICE mission, the positions of Jupiter for 2029, 2030 and 2031 correspond more or less with 2017, 2018 and 2007 in the right plot.

of the β-cone: just before Saturn enters the β-cone in 1998, the (downstream) latitude increases because Saturn (at the entrance of the cone) is in the northern part of the β-cone, where particles are deflected slightly northwards. The (downstream) longitude will decrease, because ISD particles are deflected towards the vernal equinox at the entrance side (the vernal equinox side) of the cone. In contrast, when Saturn leaves the β-cone, the longitude will be higher, and will decrease again to the undisturbed value (79° longitude, downstream direction), while the latitude will also be higher (as at entrance of the cone), and then decrease to the undisturbed latitude (-8°), in the ideal case without Lorentz force. However, the change in longitude and latitude is for 0.2 μm-particles already strongly influenced by the Lorentz force, with a total spread of about 50° in longitude and 40° in latitude. For very small particles (0.06 μm), the latitudes and longitudes are governed by Lorentz forces ($\beta = 1$) and show a spread of 40° in longitude and 80° degrees in latitude.

Such predictions as shown in this section can be used to optimize Cassini observation time or to find interstellar particles in the existing dataset.

4.2 Interstellar dust at Jupiter

Jupiter's orbital period (12 years) is only half of the full solar cycle period. Therefore we apply the simulated dust flux to the case of Jupiter for two orbital periods from 1994 until 2018 (Fig. 4.5), spanning not only the orbit of Jupiter but also both the focusing and defocusing phase of the solar cycle. We discuss the results in the frame of the ISD measurements with the Galileo mission, as well as future prospects for the JUpiter ICy moons Explorer (JUICE) mission. Jupiter is at 5 AU from the Sun, meaning that 'upstream' from the Sun, it reaches the $\beta = 3$ cone, i.e no interstellar grains with $\beta > 3$ ever reach Jupiter.

Again, the relative fluxes and velocities for the whole β-Q/m parameter space are shown and discussed in Appendix B.2 and here we summarize the results for 7 grain sizes along the adapted astronomical silicates

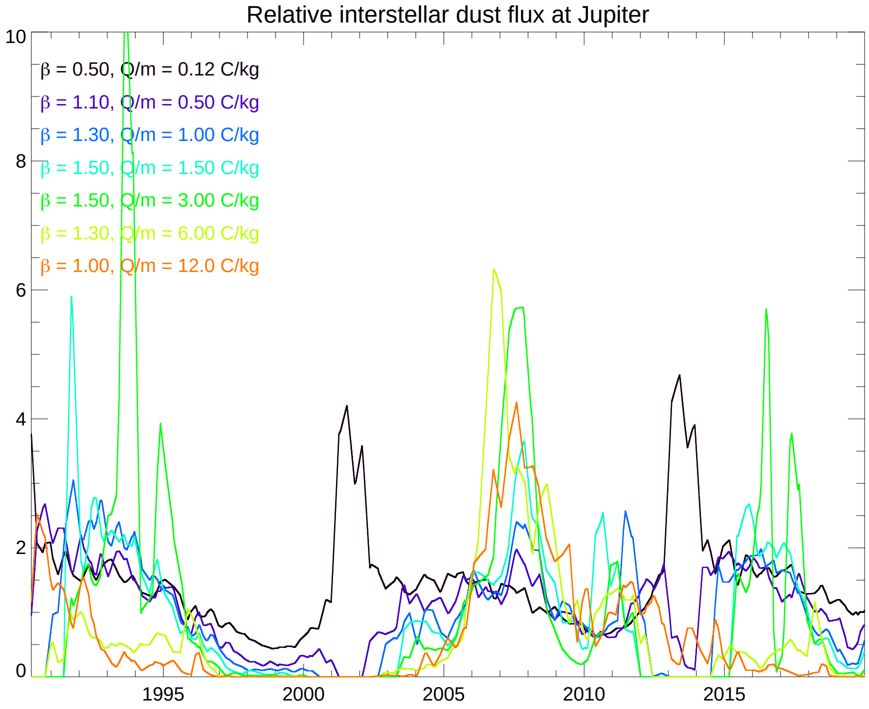

Figure 4.6: The relative fluxes with respect to Jupiter throughout the solar cycle for 7 particle sizes of the nominal material (*adapted astrosilicates*), see Table 2.2. For clarity, the curves for each grain size apart are drawn in Appendix B.2, Fig. B.9.

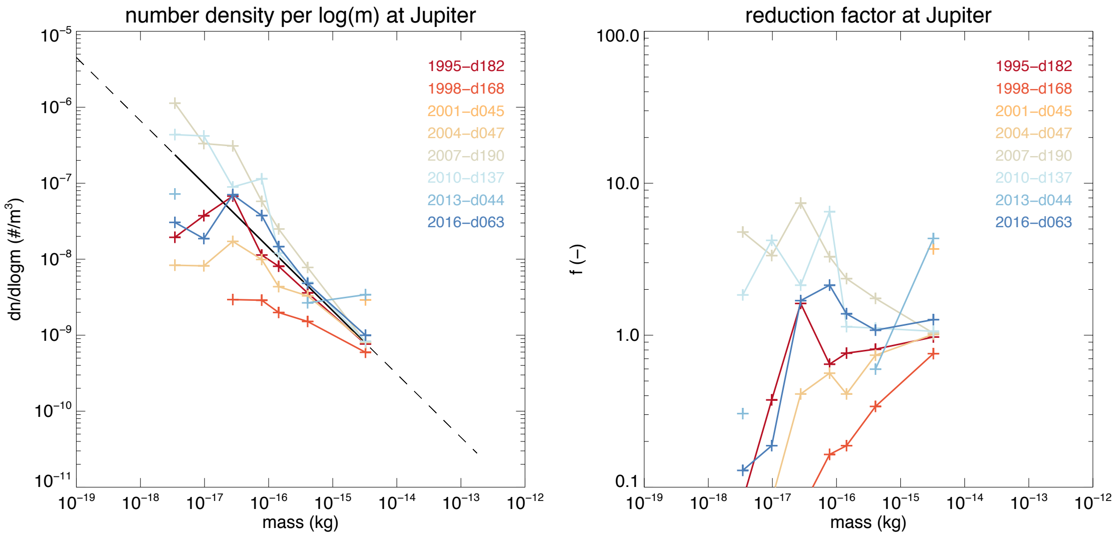

Figure 4.7: Size distributions of the ISD at Jupiter for the 4 positions per orbit. The gravitational focusing in 2001 as well as 2013 is clear for the largest particles.The influence of the solar cycle on the size distributions is visible, especially for the smaller grains (cf. Fig. 3.25).

curve. Fig. 4.6 shows the simulated time-variation of the relative flux of interstellar grains of nominal composition between 1990 and 2020 at and relative to Jupiter. For $\beta = 0.5$ and Q/m = 0.125 C/kg (0.7 μm), two peaks up to 4 times the unfiltered flux are visible in 2001 and 2013. This is because Jupiter is at the gravitational focusing region downstream of the Sun. For $\beta > 1$ and Q/m > 0.5 C/kg (grains < 0.3 μm), two gaps in the flux are visible corresponding to the β-cones when Jupiter is downstream from the Sun (2001, 2013). Between these peaks and gaps, there is a cyclic variation that doubles or halves the relative flux depending on whether Jupiter moves with or against the stream of ISD. Also, just before entering the β-cone and just after leaving it, a very small increase in relative flux is visible as explained in Section 3.4.1 (the density slightly increases in front of the exclusion zone). For higher Q/m-ratio (smaller grains), the influence of the solar cycle becomes clearer. For grains with $\beta > 1$ and very small grains (i.e. large Q/m values), the flux during the defocusing periods is zero (e.g. 1997–2003) whereas the flux at focusing periods, which are not in the β-gap, is enhanced (e.g. around 2007).

Fig. 4.7 shows the derived size distributions of the ISD at Jupiter, at different epochs corresponding to the 8 positions of Jupiter indicated in Fig. 4.5 (cf., B.7, and B.8 in Appendix B.2). These distributions are - like in Section 4.1 - for the nominal material (compact astrosilicates with density of $\rho = 2$ g/cm^3). Very clear is that the size distributions vary by large factors with the phase of the solar cycle and the orbital position of Jupiter. As was the case for Saturn, also here, the β-gap for relatively small to intermediate grains and the gravitational focusing of large grains is visible downstream from the Sun: the size distribution for 2001 shows only one point for the largest grains (0.7 μm or $3 \cdot 10^{-15}$ kg) as the smaller ones are filtered out by the β-gap as well as the Lorentz forces. The size distribution for 2013 shows two points for the larger grains (0.3–0.7 μm) and one point for the very small grains (0.07 μm). This is in the focusing phase of the solar cycle, when the smallest grains may still come through as they have $\beta < 1$ and are focused by Lorentz forces (assuming they get through the heliosphere). The highest flux enhancements (> factor 5 for 0.15 and 0.21 μm particles (masses between 10^{-17} and 10^{-16} kg)) occur during the focusing period of the solar cycle (2007 and 2010). During the defocusing periods the fluxes are at least a factor 3 lower.

4.2.1 Predictions for the Galileo mission and the JUpiter ICy moons Explorer, JUICE

Galileo was launched in 1989 and reached Jupiter in 1996, which it orbited until 2003. During its interplanetary cruise it measured interplanetary and interstellar grains (Baguhl et al., 1995a; Altobelli et al., 2005). During the orbital tour of the Galileo mission (1996-2003) the conditions for measuring interstellar dust were quite unfavorable because the solar cycle was in the defocusing condition and Jupiter moved approximately parallel with the interstellar dust flow, reducing both the relative speed and the flux of interstellar grains (Fig. 4.5). Also large parts of Jupiters orbit were downstream from the Sun in the β-cones. Besides, there were also pointing issues: the antenna was directed towards the earth, and the dust counter was thus pointing in the opposite direction from the ISD stream, at least in the downstream part of the orbit. Except for the 6 years of interplanetary cruise to Jupiter (Altobelli et al., 2005) no interstellar dust detections have been reported.

The JUpiter ICy moons Explorer (JUICE) is an ESA L-class mission candidate that would investigate the Jovian system and, in particular, the Galilean satellites Ganymede, Callisto and Europa. The spacecraft shall be launched in June 2022 and enter orbit around Jupiter in January 2030. The end of the mission is planned for June 2033. The model payload of the ESA assessment study does not include a dust detector, of which a possible instrument candidate is described in Kempf et al. (2012). However, such an instrument has been proven to be a very effective means of remotely characterizing the surface and subsurface compositions of icy moons (Postberg et al., 2011, 2009; Kempf, 2009). This would contribute greatly to the science goals of JUICE.

The situation in 2017 is comparable to the situation at arrival of the planned JUICE mission at Jupiter in 2029 except that the solar cycle is different. The spacecraft is upstream from the Sun resulting in the fact that we can see almost all small (high-β) grains. Besides, the mission is planned for the focusing phase of the solar cycle so the conditions are very favorable for measuring interstellar grains on top of Jupiter system dust. While interstellar dust (ISD) is not included in the JUICE science goals, information on this dust component will improve our understanding of the origins of the Solar System. A dust detector on JUICE would thus provide a unique opportunity for additional scientific return, especially during the last part of the cruise phase. This opportunity would provide ISD mass spectra of unprecedented precision. Now we go deeper into the ISD flux and velocity simulation results for JUICE and predict absolute fluxes based on the Ulysses measurements.

Figure 4.5 shows the orbit of Jupiter with respect to these β-cones. The positions of Jupiter in 2029, 2030 and 2031 correspond to 2017, 2018 and 2007 in the right plot of this Figure. JUICE is outside of the $\beta = 2$-cone during the last part of the cruis phase and during the orbital phase, and thus all sizes of silicate grains can reach JUICE. A gap in the observed size distribution of the ISD grains may still be visible as a result of higher β-values (such as carbonaceous materials) due to solar radiation pressure force. However, this will be minimal since JUICE skims the $\beta = 3$-cone in 2031. For JUICE this means that the optimum conditions for observing ISD are near 2031, close to Jupiter orbit insertion, so that the β-gap is as small as possible. In addition, the relative flux of grains will also be higher when Jupiter is moving towards the dust stream. This occurs between 2028 and 2031. The relative motion of the spacecraft with respect to the dust stream, and the position of JUICE with respect to the β-cones make the last phase of the cruise phase an ideal period for ISD observations.

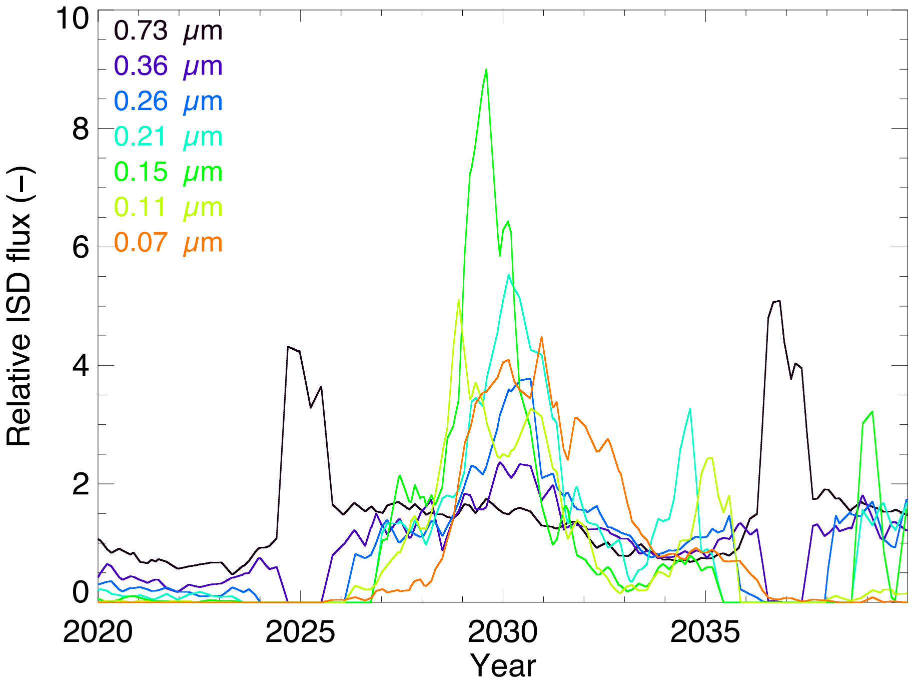

Figure 4.8: *The (smoothed) relative flux at Jupiter during the years of the JUICE mission, for several particle radii assuming the adapted astrosilicates β-curve. The β and Q/m values corresponding to these grain radii are summarised in Table 2.2.*

The solar magnetic field is expected to have a ‘focusing’ phase of the solar cycle in mid-2029. Figure 4.8

shows the relative flux with respect to the undisturbed incoming ISD flow at Jupiter for the same 7 grain sizes as in Fig. 4.6. The sudden increase in flux for smaller grains around 2030 is mainly due to the Lorentz force. The variations for the largest grains (0.73 μm radius, black line in Figure 4.8) are mainly due to the relative motion of Jupiter with respect to the flow direction of the ISD stream. The highest peak for 0.15 μm grains reaches a factor of 9, higher than the peak that was seen in 2007 in Fig. 4.6.

Figure 4.9 (right) shows the filtering factor (i.e. relative flux) from the simulations for one day during the Galileo mission (1997, day 21) and one day during the JUICE mission (2032, day 220). Since the position of Jupiter with respect to the ISD flow is very similar on both dates, most of the differences in the filtering factor are due to the Lorentz force. Figure 4.9 (left) shows the resulting number distribution of ISD grains at Jupiter. The difference between the ISD number flux for Galileo and JUICE is in the order of a factor 2, 5 and 20 for large ($\sim 4 \cdot 10^{-16}$ kg), mid-size ($\sim 1.5 \cdot 10^{-16}$ kg) and smaller grains ($\sim 3 \cdot 10^{-17}$ kg) respectively, at this position in the Solar System.

Finally, the simulated relative flux and velocity for ISD grains is shown for the whole β and Q/m parameter space (Figure 4.10) for 2029, day 186. This is shortly before arrival of JUICE at Jupiter, where the magnetic field of the planet does not yet interact with the charged grains. The black line in the plot is the β-curve for adapted astrosilicates. Figure 4.10 provides an idea of the grain sizes for which there is the most enhancement or filtering. The relative velocities depend mostly on the β-values of the grains (vertical axis) and the direction of motion of Jupiter with respect to the ISD flow: they are high at Jupiter orbit insertion (26–36 kms^{-1}) and low at the end of the mission in 2033 (minimum $\sim$ 13 kms^{-1}). The high relative flux shown in Figure 4.10 is because:

1. JUICE moves towards the nominal dust stream direction.
2. JUICE is at the edge of the $\beta = 3$ cone. Thus there is no β-gap for particles composed of most materials and therefore the flux of small to moderately-sized grains (10^{-16} – 10^{-17} kg) at JUICE will be higher than if the spacecraft was deeper within the β-cones.

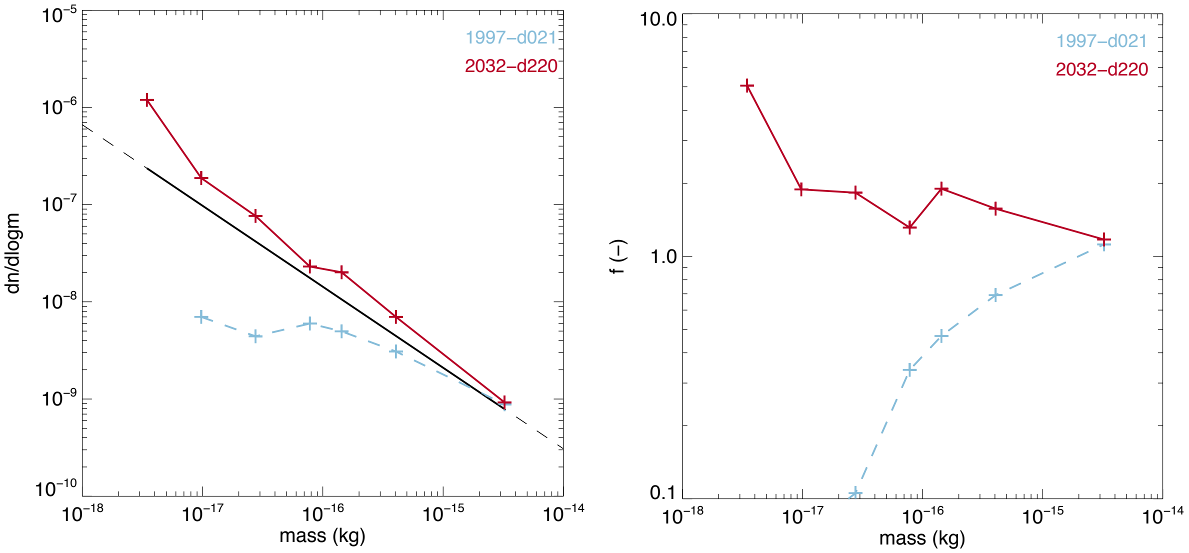

Figure 4.9: *The local ISD number distribution (left) and filtering (right) at Jupiter for one day in the Galileo mission (1997, day 21) and one day in the JUICE mission (2032, day 220). JUICE and Galileo had almost the same position in the Solar System with respect to the ISD flow. The differences are thus mainly due to variations in the Lorentz force with the solar cycle.* f (-) *is the ratio of the ISD flux at JUICE respectively Galileo, to the ISD flux before filtering in the inner Solar System. The grain radii corresponding to the masses in this Figure are given in Table 2.2. Assumptions include the astrosilicates β-curve and an initial MRN-size distribution (Mathis et al., 1977).*

3. The dust grains are strongly focused with respect to the solar equatorial plane due to the interaction of charged grains with the interplanetary magnetic field. The maximum of this effect occurs around Jupiter orbit insertion.

Effects from the Jovian magnetic and gravitational fields are also taken into account. The Jovian gravitational field is expected to increase the ISD flux by less than a factor of two. The electromagnetic effects are uncertain for ISD grains between 0.2 and 2 μm but are small for ISD velocities of 13 kms^{-2} (Colwell and Horányi, 1996; Soja et al., 2012). Grains smaller than 0.1 μm will be ejected from the Jovian system and larger grains will not be affected (Colwell and Horányi, 1996).

Predictions of absolute ISD numbers for the JUICE mission around Jupiter are based on Ulysses data: first the 'unfiltered' Ulysses size distribution is calculated according to the filtering that occurred during the Ulysses mission, and then this distribution is 'filtered' again according to the conditions at the time of JUICE. In this way the unknown filtering at the heliopause is omitted, although this is only valid if the heliopause filtering is independent of time. Approximate cumulative fluxes for JUICE are summarized in Table 4.1. For comparison to the JUICE cumulative numbers, the Ulysses cumulative numbers are added in this table. Taking into account that grains smaller than 0.1–0.2 μm will be affected by the Jovian magnetic field, the impact rate of ISD on a possible dust detector for JUICE (Kempf et al., 2012) with a surface of 225 cm^2 is estimated to be in the order of maximum 3 grains per day averaged over the orbital phase of the mission and in the order of 10 grains per day for the last part of the cruise phase. Besides the higher fluxes, the JUICE dust detector would be much more sensitive to smaller grains than the Ulysses dust detector.

It is concluded that - in the size range considered here - the flux of interstellar dust at JUICE will be in the order of 2, 5 or 20 times higher than for Galileo, depending on the size of the grains. This is because the velocity of JUICE is opposite to the direction of the interstellar dust stream; because there are few or no β-gaps in the size distribution around 2031-2032; and because the optimal focusing phase of the solar cycle also occurs around this time. This offers a unique opportunity for some extra add-on science during the last part of the cruise phase of JUICE, where the Jovian magnetic field does not yet play a significant role.

Mass (kg)	β	Q/m (C/kg)	Radius (μm)	Cum. numb. flux JUICE (m^{-2}s^{-1})	Cum. numb. flux ULYSSES (m^{-2}s^{-1})
$3.2 \cdot 10^{-15}$	0.5	0.125	0.73		
$4.1 \cdot 10^{-16}$	1.1	0.5	0.36	$7.8 \cdot 10^{-6}$	$6.69 \cdot 10^{-6}$
$1.4 \cdot 10^{-16}$	1.3	1.	0.26	$7.69 \cdot 10^{-5}$	$3.57 \cdot 10^{-5}$
$7.8 \cdot 10^{-17}$	1.5	1.5	0.21	$1.96 \cdot 10^{-4}$	$5.79 \cdot 10^{-5}$
$2.8 \cdot 10^{-17}$	1.5	3.	0.15	$5.58 \cdot 10^{-4}$	$8.4 \cdot 10^{-5}$
$9.6 \cdot 10^{-18}$	1.3	6.	0.11	$1.75 \cdot 10^{-3}$	$1.1 \cdot 10^{-4}$
$3.5 \cdot 10^{-18}$	1.0	12	0.07	$4.76 \cdot 10^{-3}$	$1.43 \cdot 10^{-4}$

Table 4.1: *The mass, β, Q/m and radius used for the filtering calculations and absolute predictions, and the cumulative fluxes of ISD grains at Jupiter orbit averaged over the JUICE and Ulysses missions. Assumptions include a density of $\rho = 2$ g/cm^3, constant grain surface potential $U = +5$ V and the adapted astrosilicates β-curve is assumed.*

4.3 Interstellar dust in the asteroid belt

In this section we discuss the variation of the size dependent interstellar dust flux in the main asteroid belt. First we chose Ceres, the biggest main belt asteroid as an example, then we discuss predictions for the Stardust mission and compare these predictions with dynamical properties of interstellar dust candidates identified by the Stardust Team.

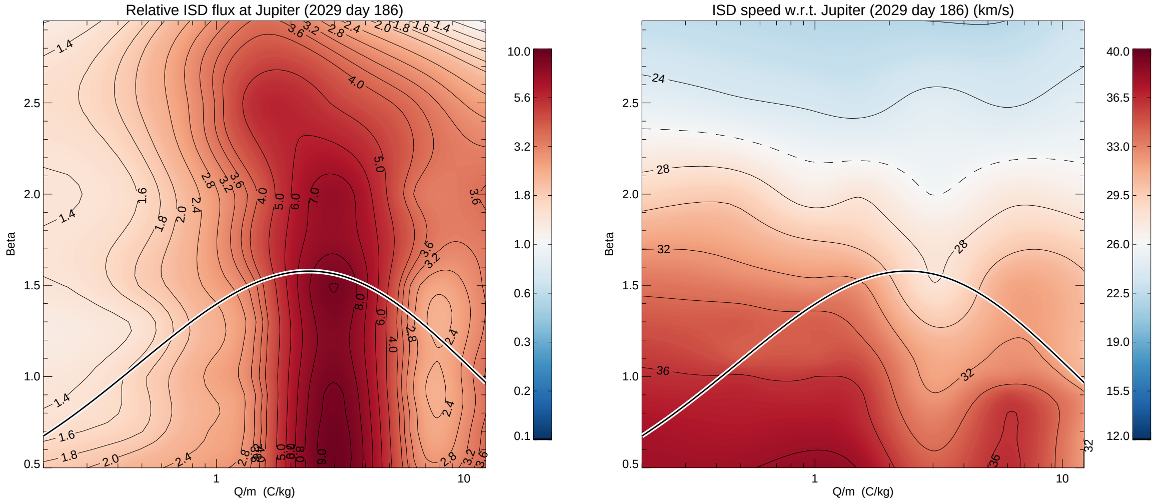

Figure 4.10: The relative flux (left) and relative velocity (right) with respect to Jupiter prior to arrival of JUICE in mid-2029 for various combinations of the parameters β and Q/m. The black line is the β-curve for astrosilicates from Gustafson (1994), adapted to have a maximum $\beta = 1.6$ according to the outcome of Landgraf (2000). Some grain masses and radii corresponding to the Q/m-values in this Figure are given in Table 2.2. The last part of the cruise phase is perfectly suited for some add-on science: the ISD flux is high due to the focusing phase of the solar cycle, and Jupiter is moving into the stream of ISD grains.

Ceres has a semi-major axis of 2.8 AU and an orbital period of 4.8 years. Fig. 4.11 shows two orbits of Ceres in two different periods of the solar cycle (defocusing: 1999-2002 and focusing: 2010-2014). Most of the asteroid's orbit lies within the $\beta = 3$ cone, therefore, only particles with smaller β values will reach the asteroid.

The fluxes onto Ceres of interstellar grains of nominal composition are shown in Fig. 4.12 throughout time from 1990 until 2020. All grain sizes from Table 2.2 are included in this plot but for clarity, the curves per grain size are again repeated in separate graphs in Appendix B.3. The gravitational focusing of large (0.7 μm) grains is visible as regular sharp peaks in relative flux. There is also a modulation due to the motion of Ceres parallel to or against the stream, resulting in flux enhancements or reductions by factors of 2 and 0.5 respectively throughout its orbit. When Ceres moves in the same direction as the ISD flow, relative speeds are low (about 10 km/s) which is optimal for in-situ sample return. On the part of the orbit where Ceres moves against the stream of ISD, measurements with an impact ionization detector are better suited because relative velocities are higher and therefore also the fluxes. A small influence of the solar cycle is already visible, as the peaks of the relative fluxes are larger around 2010 and reduced around 2000.

The same periodicity is present for 0.36 μm grains. The β-cones are visible as small gaps in the flux. The "entry"-side of the cone has a lower relative flux than when Ceres is going out of the β-cone, because of the apparent motion of Ceres with respect to the flux direction. However, both show the slight enhancement in dust flux at the boundary of the β-cones. Also here, a slight variation in the peaks of the flux is visible, which depends on the phase of the solar cycle. For even smaller grains, the influence of the solar cycle becomes more pronounced. the gravitational focusing is counterworked partially in 2000, and is enhanced in 2010. For small particles < 0.2 μm the effect of the Lorentz force gets stronger with increasing Q/m. The flux for the smallest particles becomes zero between roughly 1993 and 2004 but in 2010, even the smallest grains may be able to reach the asteroid at even enhanced fluxes provided that they make it through the termination shock.

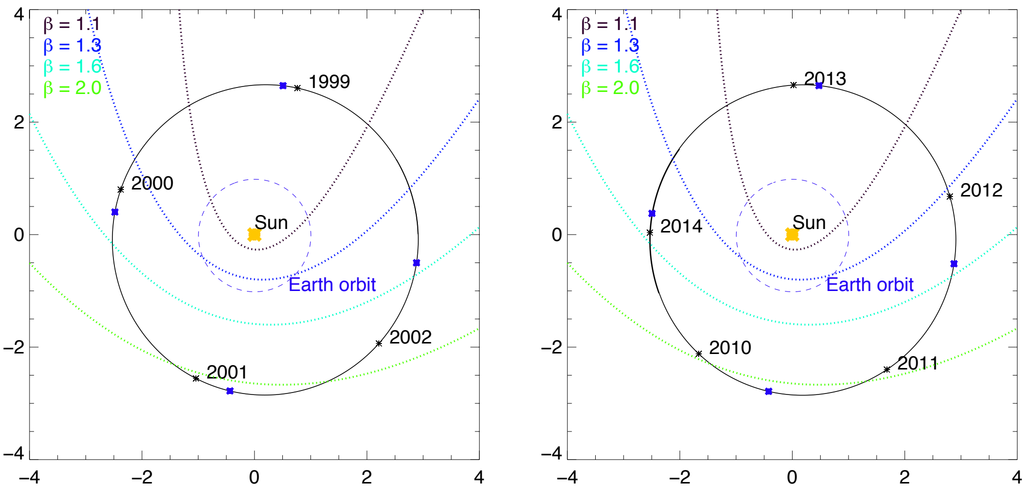

Figure 4.11: The orbit of main-belt asteroid Ceres in the heliocentric ecliptic frame, with the β-cones shown in colored dotted lines. The 4 positions (per orbit) for which we show the β-Q/m plots in Appendix B.3 and size distributions in this section are indicated as blue dots. The left plot corresponds to the defocusing phase and the right plot corresponds to the focusing phase of the solar cycle.

Fig. 4.13 shows the derived size distributions of the ISD at the four positions of Ceres during the two orbits of Fig. 4.11. The first orbit from 1999 to 2002 is during the defocusing phase of the solar cycle and the second orbit from 2010 to 2014 is during the focusing phase of the solar cycle. These distributions are for the nominal material. Again, like in the Jupiter case the size distributions vary by large factors with the phase of the solar cycle and the orbital position of the asteroid. During the defocusing phase only the biggest grains (0.7 μm or $3 \cdot 10^{-15}$ kg) display enhanced flux in the downstream region (1999). The size distribution for 2001 shows only one point for the largest grains as the smaller ones are filtered out by the β-gap as well as the Lorentz forces. The fluxes of all other (smaller) grains are strongly reduced by the combined radiation pressure and electromagnetic interactions. During the focusing phase (around 2010), almost all particles have enhanced fluxes except in the downstream region where only the biggest particles display enhanced fluxes. The size distribution for 2012 - day 323 shows two points for the larger grains and one point for the very small grains. The highest flux enhancements ($>$ factor 5 for 0.11 and 0.21 μm particles (masses between 10^{-17} and 10^{-16} kg)) occur during the focusing period of the solar cycle (2010). During the defocusing periods the fluxes are at least an order of magnitude lower.

4.3.1 ISD simulations for the Stardust mission

The Stardust mission was launched in 1999 with as main goals to return material from the coma of Comet 81P/Wild2 and to return material from the interstellar dust stream (Tsou et al., 2003). For this purpose, one side of a collector was used that consisted of 132 tiles of aerogel, with a surface of 1039 cm^2. There were also 153 cm^2 of Aluminum foils, totalling with the aerogel tiles in a collector size of 0.12 m^2 (Tsou et al., 2003). The cometary grains have been the subject of extensive analyses since the return of the mission in 2006 (Brownlee et al., 2006). A preliminary examination of the aerogel tiles on the interstellar side of the collector led to an identification of three candidate ISD grains (Westphal and et al., 2012b), and the examination of the aluminum foils resulted in four possible ISD impact craters (Stroud and et al., 2012). Calibration tests for the aerogel and foils were made at the Heidelberg Dust Accelerator and are described in (Postberg et al., 2012), whereas Westphal and et al. (2012a) discusses the unlikeliness of the ISD candidates to be of an alternative origin.

Earlier predictions of statistics of ISD captured by Stardust were made by Landgraf et al. (1999b). These authors used two ISD populations: one with radiation pressure constant $\beta = 1$ ("small grains")

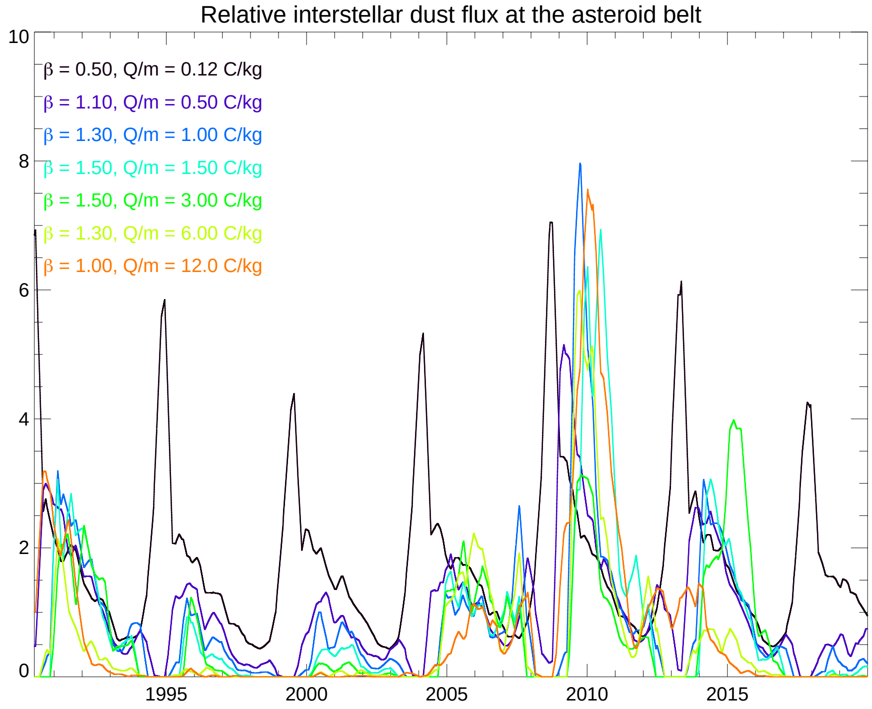

Figure 4.12: The relative ISD flux in the asteroid belt on asteroid Ceres for different grain sizes of the nominal material (*adapted astrosilicates*). Each grain size curve is also shown apart in Appendix B.3, Fig. B.12 for clarity and better comparison. Even for the largest grains of 0.7 μm with only Q/m = 0.12 C/kg, there is a small influence of the solar cycle visible.

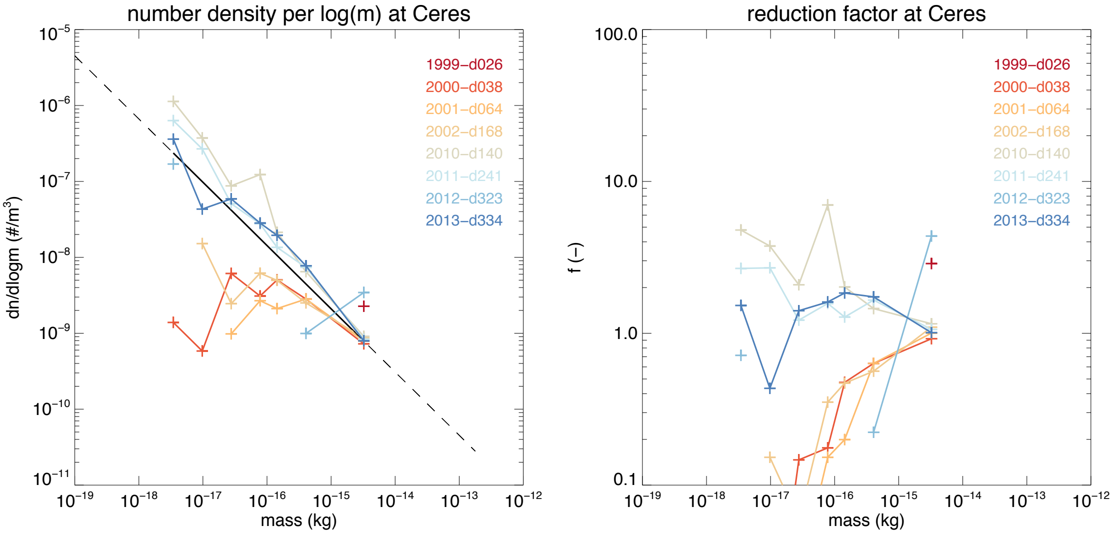

Figure 4.13: Size distributions of the ISD at the main-belt asteroid Ceres for the 4 positions per orbit (cf. Fig. 3.25).

and one with $\beta = 0.1$ and charge-to-mass ratio Q/m = 0 C/kg ("large grains"). The total duration of the collection period was assumed to be 290 days, and 80 respectively 40 grains were predicted to be captured in total for the small and large grains. However, the actual total duration of exposure was shorter. In contrast to these authors we assume a continuum of β-values rather than only two different populations (small/large). We provide an update of the estimated amount of grains that should have been captured, using updated information of the collection periods, a larger parameter space of grain properties and using the Ulysses measurements in combination with dust trajectory simulations as a starting point of the absolute number predictions.

The orbit of Stardust with respect to the β-cones is shown in Fig. 4.14. The red thick lines in the plot correspond to the collection periods (22 February 2000 – 1 May 2000, and 5 August 2002 – 9 December 2002 (Stardust@Home, 2012), totalling in 195 days). During about half of the collection time, particles with β between 1.5 and 1.6 are missing, especially towards the middle and the end of the first collection period, and towards the end of the second collection period. This means that Stardust will not capture particles of radius roughly between 0.12 and 0.25 μm during these parts of the collection period (assuming adapted astrosilicates with density of $\rho = 2$ g cm^{-3}).

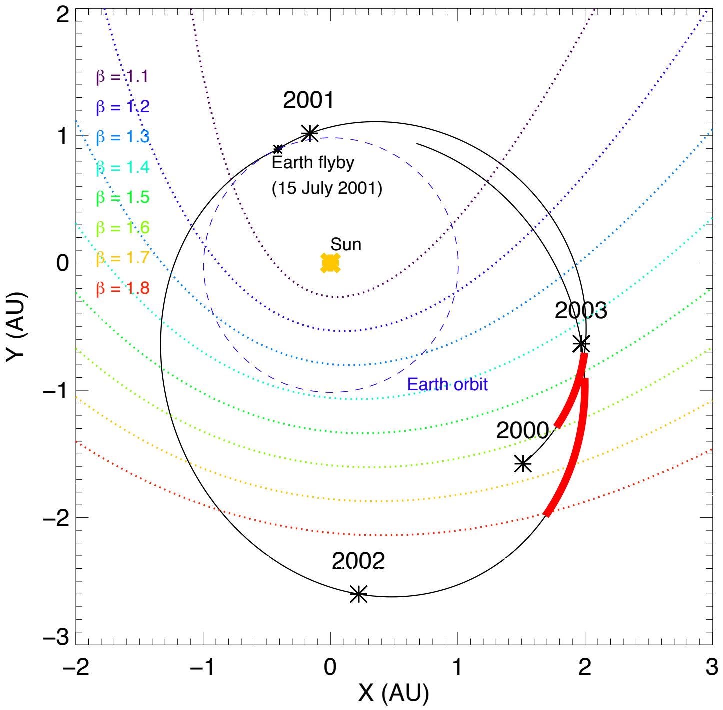

Figure 4.14: The orbit of Stardust with respect to the β-cones in the heliocentric ecliptic frame. The red thick lines are the two ISD capture periods.

During the collection periods, the Stardust collector was pointed into the nominal interstellar dust stream for which was assumed that the grains have $\beta = 1$ and are coming from an ecliptic longitude of 259° and ecliptic latitude of $+7.7°$ (JPL, 2012). The relative speed of the ISD grains with respect to the spacecraft was taken into account for the pointing direction of the collector. However, the real pointing of the collector varied from this nominal direction. Fig. 4.15 shows the ideal pointing direction of the cometary side of the collector in the heliocentric ecliptic frame as a smooth curve and the real (commanded) pointing as a wiggely curve around the ideal pointing direction. The longitude is shown as a solid line and the latitude is shown as a dashed line. Such excursions in pointing as shown in Fig. 4.15 lead to an uncertainty of about 15° in the impact direction derived from the tracks.

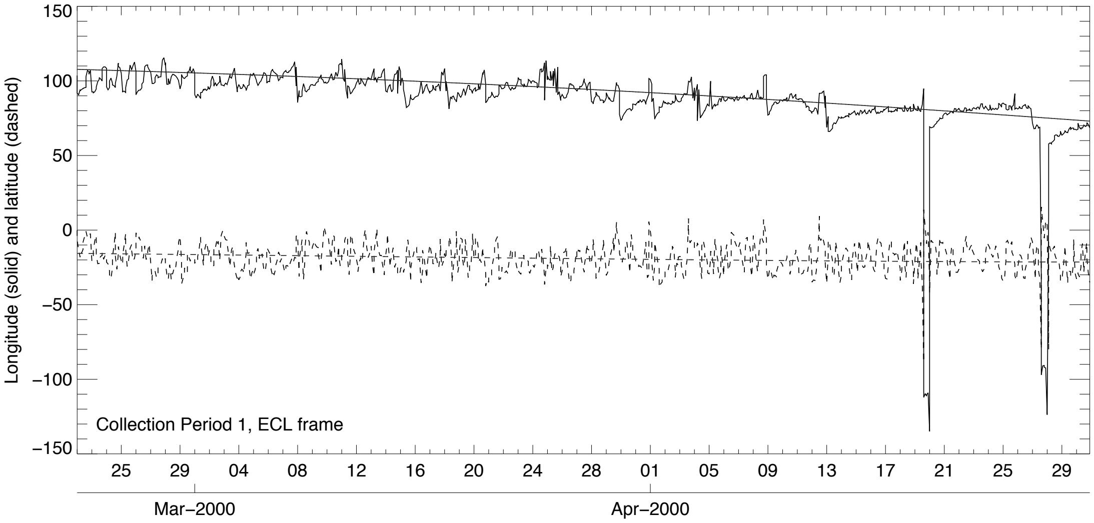

Figure 4.15: The ideal pointing and commanded pointing of the Stardust collector in the first collection period. The solid line shows the longitude and the dashed line shows the latitude in the heliocentric ecliptic frame. This pointing profile was obtained using SPICE (JPL, 2012).

The collection period occurred a few years after the solar minimum of the defocusing cycle. Therefore the grains were defocused from the solar equatorial plane by Lorentz forces and thus most of the grains on the "smaller" side of the β-curve (i.e. $\sim< 0.15$ μm or $3 \cdot 10^{-17}$ kg) will most probably not make it to the inner solar system or are strongly reduced. Besides, such small grains may already be strongly filtered at the termination shock too (Linde and Gombosi, 2000; Slavin et al., 2010).

The relative flux in the inner heliosphere with respect to the incoming flux after passing the termination shock was calculated for the period between 2000 and 2003 at both the Ulysses and Stardust positions. This was done for the 7 grain masses from Table 2.2, with β-values along the adapted astrosilicates β-curve and with density of $\rho = 2$ g cm^{-3}. Smaller grain densities would enhance the electromagnetic interaction. Fig. 4.16 shows on the left the relative flux in the inner solar system with respect to the incoming flux for both Ulysses (between 2000 and 2003) and Stardust (2000 & 2002). In Fig. 4.16, grains with $m < 3 \cdot 10^{-17}$ kg (0.15 μm or Q/m $>$ 3 C/kg), respectively $m < 1 \cdot 10^{-17}$ kg (0.1 μm or Q/m $>$ 6 C/kg) are totally filtered out or strongly reduced to less than $1/10^{\text{th}}$ of the original flux depending on the collection period.

The red line in Figure 4.16 (right) show the Ulysses measured number distribution per log(m), from Krüger (2012) between 2000 and begin 2003 and interpolated to the 7 masses from Table 2.2. From these observations the ISD number distribution at the heliospheric boundary (inside the termination shock) is calculated by inverse filtering (blue line in Fig. 4.16, right hand side). The final *forward*-filtered ISD number distribution for the Stardust mission is shown by the black line in this figure. The expected number distribution for Stardust is thus made consistent with the Ulysses measurements, taking into account the different positions of the two spacecraft. For a comparison to these measurements and derivations, an extrapolation of the MRN size distribution (Mathis et al., 1977) to the grain sizes of the simulations is shown as a straight line for a hydrogen number density $n_H = 0.3$ cm^{-3} and dust grain density of 2 g cm^{-3}.

Based on the number distributions and by taking into account the effective instrument surface of Stardust respectively Ulysses and their respective "observation times", the total estimated number of grains is about 40 (about 15 in the first collection period and 25 in the second). So far only 3 candidates of interstellar grains have been identified.

Simulations were also made for different combinations of β and Q/m to study the sensitivity of the relative flux, impact velocity and ISD flow direction on the selected grain parameters. The outcome was:

- The relative flux decreases strongly with increasing Q/m (thus with decreasing mass) as is also indicated in Fig. 4.16. Moreover, the flux also becomes zero for grains with β-value larger than the β-cone where Stardust is located. Therefore, the estimate of the flux of grains on Stardust is made by using a simulation program that includes Lorentz forces, however, at the cost of model precision (the simulations have a grid size of 1.5 AU around the Sun, and 'only' 7 masses are simulated because of limited computation time). For this reason, the simulations that include Lorentz forces are only used to make a first rough estimate of the expected amount of collected grains.

- The impact speeds vary only little with increasing Q/m within the collection time and position of Stardust: for the same β-value but different Q/m, the velocity difference is maximum 4 km/s (within the collection periods). For further investigation of the impact speeds, we use simulations with solar radiation pressure force and gravity only, but with a precision of 0.1 AU from Stardust.

- The absolute ISD latitude at Stardust varies only slightly (maximum 10°) and depends more on Q/m than on β, whereas the longitude varies more (up to 30°) and depends mostly on the β-value of the grains. The absolute longitude of the (downstream pointing) ISD velocity vector decreases as the β-value of the grain approaches the β-value of the β-cone where Stardust is located. This is as expected since the closer to the β-cone, the more the grain trajectory will deviate from its original path due to solar radiation pressure force. Because the direction does not change dramatically with Q/m, we investigate further the directions of the grains using only solar radiation pressure force and gravity, but with a precision of 0.1 AU from Stardust.

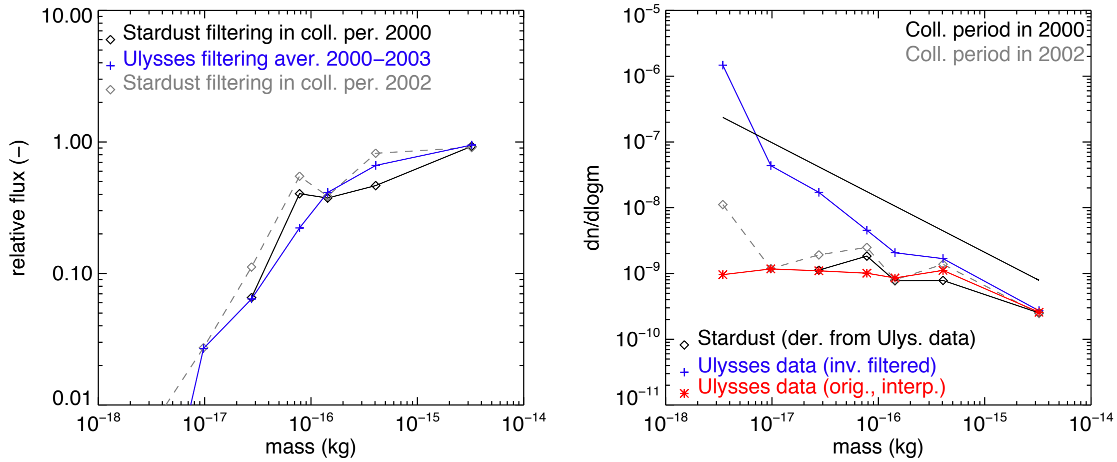

Figure 4.16: The left plot shows the relative flux of ISD grains with mass due to the filtering in the inner heliosphere for the Ulysses mission and the two collection periods of the Stardust mission. The right plot shows number density of grains for Ulysses (red stars) between 2000 and 2003 (Krüger, 2012), the *backward*-filtered Ulysses data (blue crosses), and the derived number distribution for Stardust (black diamonds). The straight black line is an extrapolation of an ISD size distribution (Mathis et al., 1977) in the LIC, in the range of simulated masses. The adapted astronomical silicates β-curve is used and the grain density ρ is assumed to be 2 g/cm^3. For the MRN-distribution a hydrogen number density of $n_H = 0.3$ cm^{-3} is used.

4.3.2 Comparison of modeling with dynamical properties of ISD candidates

Preliminary examination of the Stardust aerogel collector identified three candidate ISD grains (Westphal and et al., 2012b), and the examination of the aluminum foils resulted in four possible ISD impact craters (Stroud and et al., 2012). For these candidate ISD grains, both impact speed and impact direction (zenith and azimuth angle) are estimated from the aerogel tracks (Postberg et al., 2012; Westphal and et al., 2012b) and compared to simulations in this section. The zenith angle of the ISD impact direction on the collector is defined as the angle of the relative ISD velocity vector to the collector normal on the cometary side. The zenith angle is thus zero for grains impacting along the collector normal and $> 90°$ for grains impacting on the cometary side of the collector. The azimuthal angle is the angle on the collector surface and is 0° towards the spacecraft body in a right hand system and 180° in the anti-spacecraft direction (generally pointing towards the sun).

The impact directions of the 3 preliminary ISD grains (Westphal and et al., 2012b) were zenith angles of 28°, 41°, and 51° and azimuthal angles within 20° from the Sun direction (180° azimuth). A zenith angle uncertainty due to the spacecraft pointing is estimated to be ±15°. The (average) 15° wiggle in the spacecraft pointing does not translate in a similar excursion in zenith angle. A better error analysis could be done but is beyond the scope of this work. The impact speeds of the grains were estimated from the track sizes and shapes (Postberg et al., 2012; Westphal and et al., 2012b): grains of tracks 30 and 34 have probable impact speeds below 10 km/s and the grain of track 40 had an impact velocity above 15 km/s.

We studied the variation of the impact speeds with the grain size for 6 different times during the collection periods, namely at the beginning, middle and end of each period. The collection speeds of ISD grains are calculated from the trajectory simulations where only solar radiation pressure force and gravity are taken into account. Figure 4.17 shows the dependency of the simulated impact speeds of the grains on β, at the 6 times indicated. The ISD velocity at a fixed location decreases with increasing β-value. Note that the *relative* velocity for the ISD grains increases again for the largest β-values. As a consequence Stardust may be moving "faster" than the ISD grains and ISD grains may impact on the cometary side of the collector. This was found for some epochs by calculations of the impact directions (cf. discussion on Figure 4.19 in this section). In the last part of the two collection periods (orange curves), grains with $\beta > 1.5$ and 1.6 respectively, are missing because Stardust is inside the β-cones for these values. Note that the *relative* velocity of the grains depends on the *absolute* ISD velocity as well as on the spacecraft velocity vector which is different at different epochs of the collection period. Therefore, grains with equal β-value (e.g. $\beta = 1$) have different impact speeds at different times.

The relation between impact speed and grain size (radius) is shown in Fig. 4.18. The left-hand side of the plot is hatched for grains smaller than 0.2 μm to indicate the filtering at the heliosphere boundary. Based on our assumptions, ISD grains between 0.25 and 0.4 μm have impact speeds between 3 and 14 km/s, depending on when during the collection period they are captured. Grains between 0.4 and 0.7 μm have impact speeds between 10 and 20 km/s and grains larger than 0.7 μm have impact speeds of $14 - 25$ km/s. The gaps in the speed curves (Figure 4.18) around grain radius 0.16 μm (from roughly 0.12 μm $-$ 0.23 μm) are consequences of the β-cone for $\beta = 1.5$.

Also the ISD impact directions on the Stardust collector change depending on β and thus on grain size. The largest shift in directionality occurs for particles with β close to the maximum β-value that can reach Stardust, i.e. around $\beta = 1.5$ to $\beta = 1.6$. The absolute ISD latitudes change by only a few degrees, whereas the absolute longitudes change by up to 30° for particles of about 0.25 μm. This has a large influence on the zenith and azimuth angle of the ISD impact direction on the collector. In the simulations discussed in this Section, we do not consider the effects of the 15° spacecraft attitude deadband, which adds to the uncertainty, but we assume a perfect pointing in the *relative* ISD grain velocity direction for grains with $\beta = 1$ (259° ecliptic longitude and +8° ecliptic latitude (Landgraf, 2000)).

Fig. 4.19 shows the simulated impact zenith angles on the collector and assumes an initial dust direction (79° ecl. longit.,−8° ecl. latit.) and *perfect* spacecraft pointing as explained in the previous

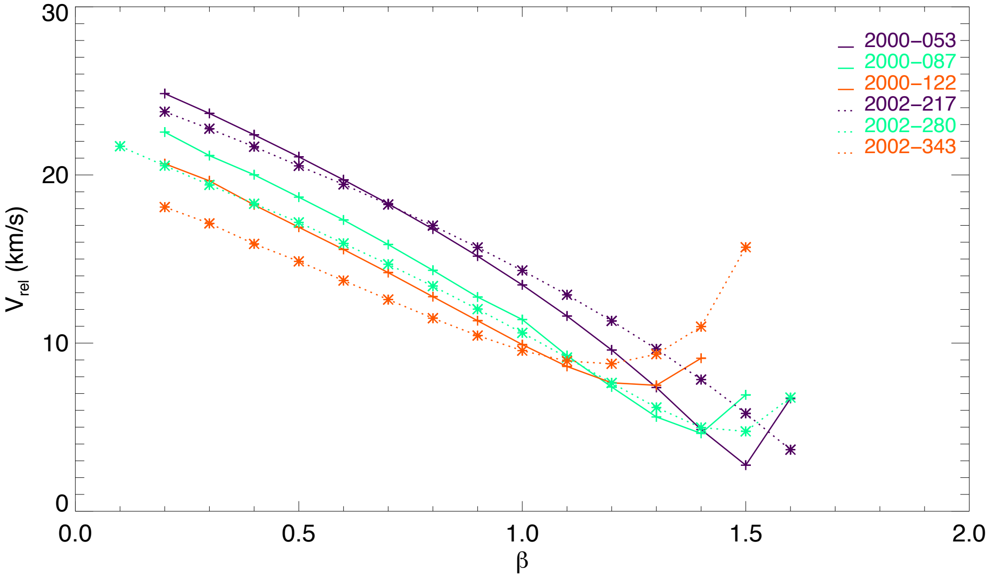

Figure 4.17: The simulated impact speeds with β-values of the grains at 6 times during the 2 collection periods of the Stardust mission. Lorentz forces are not taken into account in this plot.

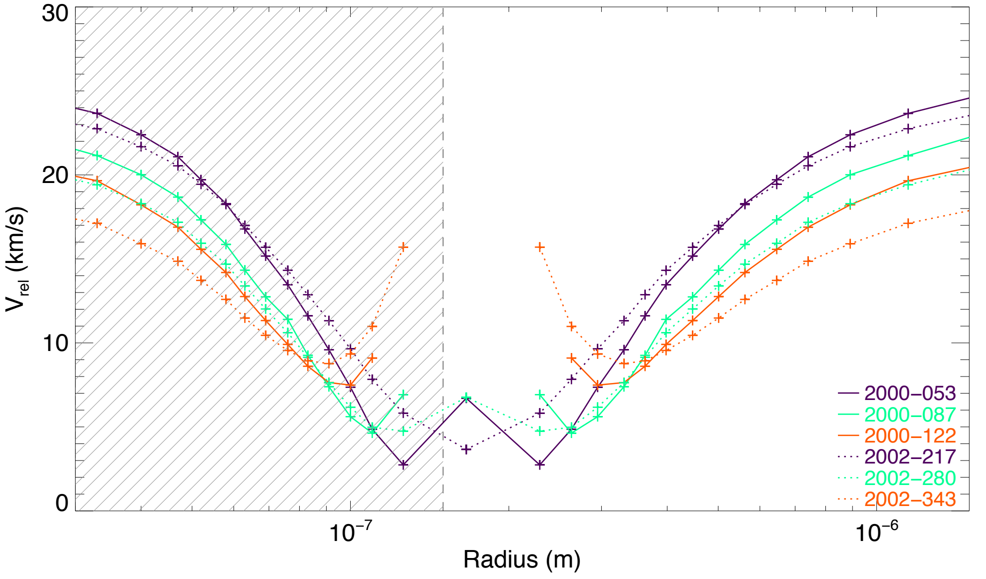

Figure 4.18: The calculated impact velocities for different particle sizes (radii, in meter) and for 6 different times during the collection periods of the Stardust mission. Assumed was the adapted astrosilicates β-curve and density of $\rho = 2$ g cm^{-3}. Lorentz forces are not taken into account in this plot. The larger particles will be fast, but may be less abundant in absolute number. Very small particles are filtered out by Lorentz forces.

paragraph. In the beginning of the second collection period (2002-d217), Stardust is still far away from the $\beta = 1.6$ cone and the zenith angle on the collector remains close to the collector normal. For higher β-values and later times in the collection periods, the zenith angle deviation increases as Stardust is closer to the cones. Grains with $\beta = 1$ move on straight trajectories through the solar system at all times, so if assuming an "ideal" spacecraft pointing, these grains have about 0° impact zenith angles on the collector (see Fig. 4.19). Grains with zenith angle larger than 90° will impact on the cometary side of the collector. This is not only because the (absolute) longitude of the ISD changes when Stardust is closer to the β-cones, but also because the absolute velocity of the grains with β close to 1.5 and 1.6 gets lower and approaches the spacecraft velocity. Hence, Stardust "overtakes" some of the interstellar dust grains which then impact on the cometary side of the collector. This plot is independent of grain density or β-curve assumed.

The range of impact speeds and zenith angles that were found from track size, shape and direction are also shown in Figure 4.19 (with a 30° wide box to indicate roughly the uncertainty in track direction due to spacecraft pointing uncertainty) and they overlap the speeds and zenith angles from the simulations very well.

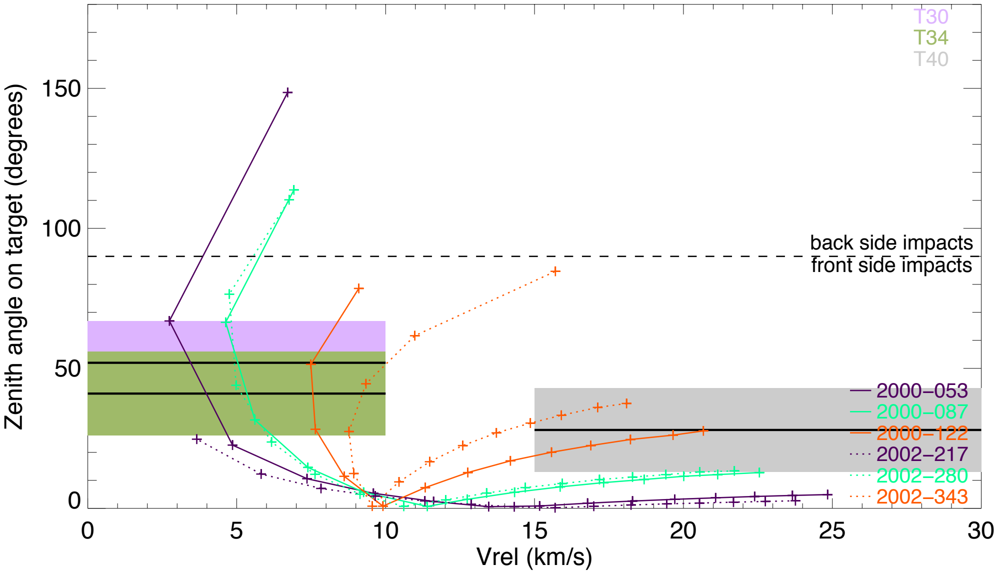

Figure 4.19: The zenith angle of the ISD impact direction on the Stardust collector with increasing impact speed is shown for 6 epochs during the two collection periods. A zenith angle larger than 90° indicates that the grains are impacting on the cometary side of the collector. The zenith angles of the 3 ISD candidates found in the aerogel (Westphal2012) and a 15° deadband are indicated (colored regions).

Figure 4.20 shows the simulated azimuthal angles on the Stardust collector with impact speed. The grains with the highest speeds correspond to $\beta < 1$ grains and they impact in the direction towards the Sun (180° azimuth). The grains with $\beta = 1$ have undetermined azimuthal angles since their impact velocity vector is close to the collector normal, i.e. they have a zenith angle of 0°. Also in Figure 4.20 we plot the azimuthal angles from the 3 tracks, including 15° to illustrate the spacecraft pointing error. Here, only for Track 40, there is much overlap between the velocities and azimuthal angle from the track and the simulations. Again, this is independent from the grain density or β-curve assumed, but it does depend strongly on the initial ISD direction of 259° longitude and ideal spacecraft pointing assumed, as will be discussed in the following.

Most interstellar dust impacts occur close to a plane through the collector normal in the 0°–180° azimuth direction. We can project the impact direction onto that plane and define a "capture zenith angle" which is the zenith angle, multiplied by the negative cosine of the azimuthal angle. Figure 4.21 from Andrew Westphal shows this "capture zenith angle" for 3 different initial directions of the incoming dust with the relative speed. Values below zero indicate azimuthal angles in the spacecraft direction (0° azimuth) whereas positive values indicate azimuthal angles towards the Sun direction (180° azimuth). The zenith angles extracted from the tracks of the 3 preliminary ISD grains in the collector (Westphal and et al., 2012b) are indicated in the plot as horizontal lines surrounded by coloured error boxes. A first brief look at the Stardust results with respect to the modeling revealed that for the average inflow direction of 259°, only one grain fits the simulations (Track 40, previous paragraph). If all 3 grains are of interstellar origin, then the 274° inflow direction fits better. However, because of the large statistical uncertainty (only 3 ISD impacts) and the uncertainties in the determination of the exact impact direction and uncertainties in the modeling assumptions we do not place much significance to this result yet.

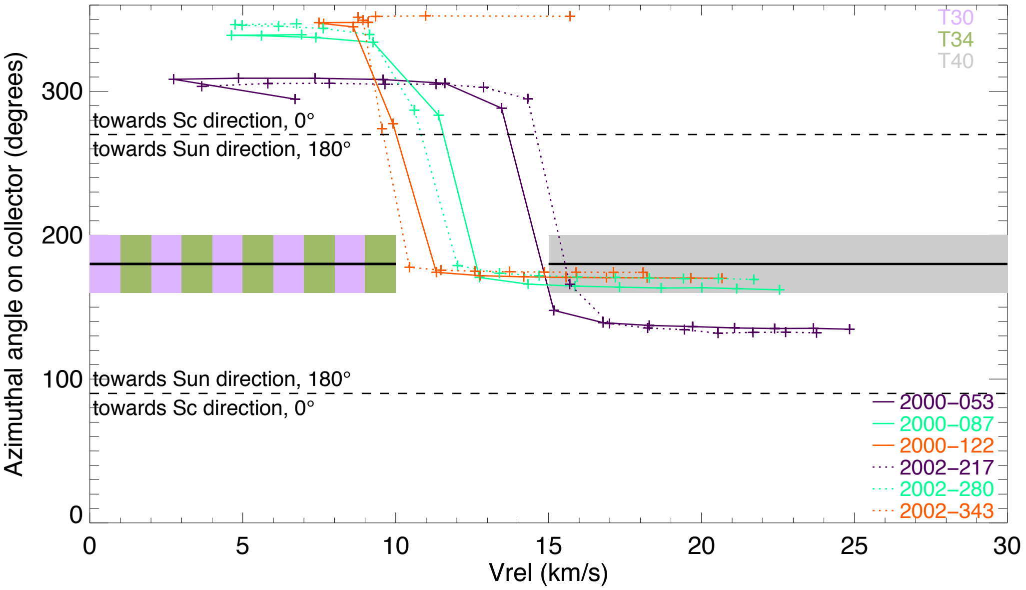

Figure 4.20: The azimuth angle of the ISD impact direction on the Stardust collector with increasing impact speed is shown for 6 epochs during the two collection periods and inflow direction 259°. The azimuth angles of the 4 ISD candidates found in the aerogel (Westphal2012) and a 15° deadband are indicated (colored regions).

The results from the calculations by Andrew Westphal (Fig. 4.21) were confirmed for one direction of the initial dust (269° ecliptic longitude) and are shown in Fig. 4.22. There, also speeds between 5 and 10 km/s have azimuthal angles around 180° (and higher) instead of around 0°, in contrary to Fig. 4.20.

When a β-curve and material density are assumed, the size range of collected grains can be estimated. Figure 4.23 shows the simulated zenith angle with grain radius assuming the astrosilicates β-curve and a density of 2 g/cm^3. From this curve, it can be concluded that grains with radius smaller than about 0.25 μm will not be captured by Stardust: either they are not present because of the position of Stardust with respect to the β-cones (orange curves), or they will impact on the cometary side of the dust collector (zenith angles $> 90°$), or they are filtered out by Lorentz forces (hatched region in Fig. 4.23 and earlier discussions). The only period in which also the smallest grains (if not filtered by Lorentz forces) could

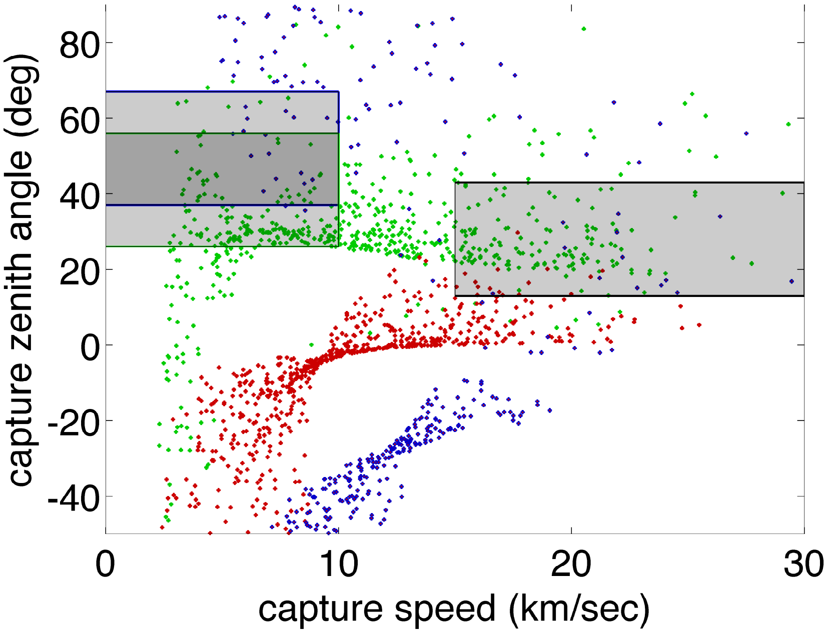

Figure 4.21: This scatter plot shows the "capture zenith angle" (the zenith angle multiplied by the negative cosine of the azimuthal angle) for 3 different directions of the incoming dust: 244° (blue), 259° (red) and 274° (green) with the impact velocity. Also the capture zenith angles of the 3 found ISD candidates are indicated as grey boxes. Source: A.Westphal.

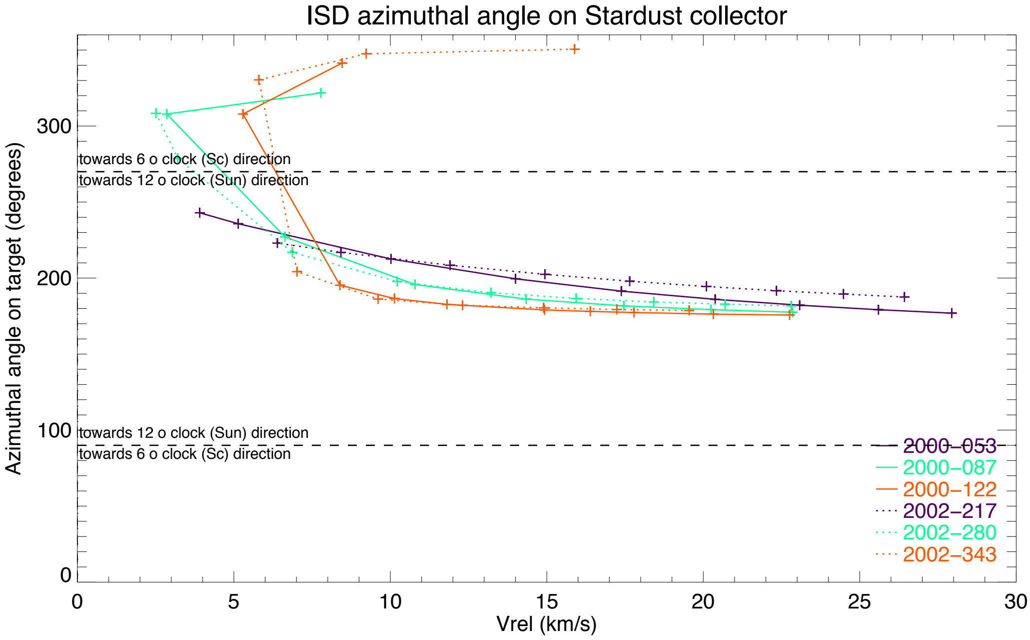

Figure 4.22: The azimuth angle of the ISD impact direction on the Stardust collector with increasing impact speed for 6 epochs during the two collection periods and inflow direction 269° instead of the nominal 259°.

have been captured with the ISD-side of the collector is the beginning of the second collection period (cf. the purple dotted line in Fig. 4.23), at least if we assume an initial incoming dust direction of 259° longitude. The boxes in Fig. 4.23 indicate the range of sizes of 3 particles given by Westphal and et al. (2012b).

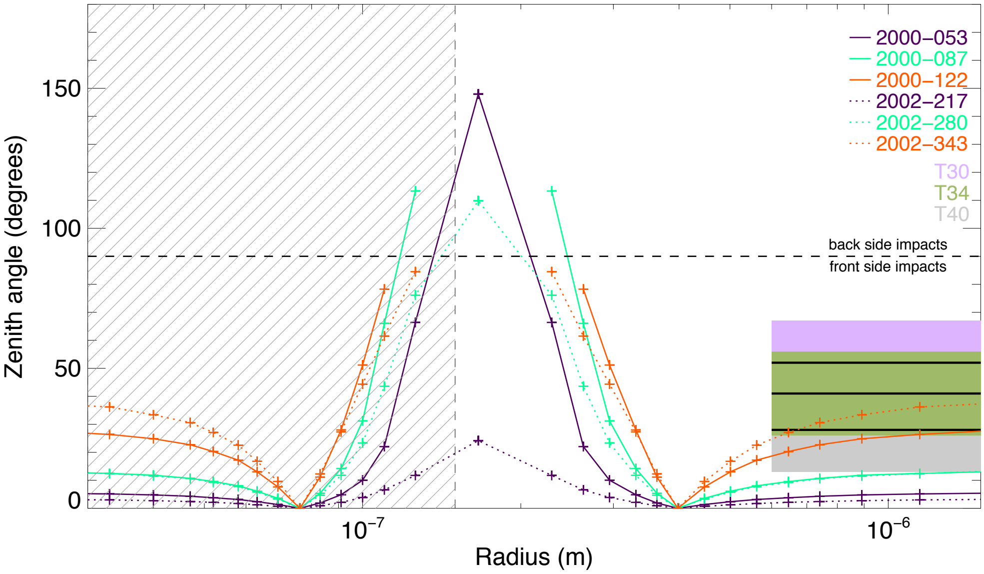

Figure 4.23: The zenith angle of the ISD impact direction on the Stardust collector with increasing grain radius a is shown for 6 epochs during the two collection periods. For this graph, the astrosilicates β-curve and a grain density of 2 g/cm^3 was assumed. The boxes indicate the range of sizes of 2 particles given by Westphal and et al. (2012b).

By comparing the velocity and impact direction of the three ISD candidates to the simulations, the β-values can be constrained to a range of 1.15–1.6 for tracks 30 and 34 and between 0–1 for track 40. Fig. 4.23 showed the impact zenith angle with grain radius assuming the adapted astrosilicates β-curve and a density of 2 g cm^{-3}. However, the three interstellar dust candidates have densities that were surprisingly low (Westphal and et al., 2012b). Grains that are porous or fluffy will have a different β-curve than assumed here, and thus the lower and upper size limit of simulated grains that could be captured (like shown in Fig. 4.23) will differ.

Concluding, the measured zenith angles and speeds of the 3 ISD candidates correspond well to the calculated impact speeds and zenith angles of dust with β-value between 1.1 and 1.5 (tracks 30 and 34) and the grain of track 40 must have had $\beta < 0.9$. The azimuth angle of one candidate particle is compatible with the simulated azimuth angle but for two others the measured angle deviates significantly from the predicted angles for ISD particles with the assumed dynamical parameters. However, by tuning these assumptions, a compatible solution can be found to match the observed grains with the simulations: another grain density and a shifted initial dust direction (274°) could probably make all three grains to correspond to the observed azimuth angles, zenith angles, impact speeds and grain sizes. An initial dust direction of 274° is still within the statistical uncertainty limits for the initial dust direction found by Landgraf (1998).

As a consequence there are too many uncertainties in the assumptions to conclude uniquely from this dynamical study whether the particle candidates are truly of interstellar origin or not but within the uncertainties in the simulations (e.g. initial dust direction), it is also not disproven. The main uncertainties are spacecraft pointing, grain density, grain material (β-curve), initial ISD speed and direction, and uncertainties in measured speed and direction of the extracted grain candidates. Another uncertainty comes from not knowing "when" the grain has impacted and thus what the relative velocity of the grain with respect to the spacecraft was.

The small number of the identified grains and the uncertainties of the dynamical characteristics prevent constraining dynamical interstellar dust properties at the present time. When more interstellar grains will be identified on the Stardust collector the ISD dynamical properties and the ISD flow may be further constraint. However, the method of comparing simulations to the grain impact parameters from tracks in the aerogel seems a good approach when statistics get better and more grains are found. An even better approach would be a sample return mission with an active dust collector where the time of impact is recorded as well as the dust trajectory through a grid in front of the collector (Grün et al., 2012).

5

Summary

This thesis describes the modulation of the ISD flow through the solar system using simulations of ISD trajectories. The interaction with the heliosphere, the resulting flow, and the filtering of ISD size distribution in the inner solar system are studied. After gaining insight in the flow and filtering of ISD, the simulations are applied to specific locations in the solar system and to specific space missions like Cassini, JUICE and Stardust. The methods used in this thesis open up doors for future ISD research.

The solar system moves through the local Interstellar Medium (ISM) filled with gas and dust with a relative velocity of 26 km/s. The gas and dust appear to come frome one direction of 259° ecliptic longitude and 8° ecliptic latitude with an uncertainty of ±15° (Frisch et al., 1999). The interstellar dust (ISD) is first filtered and modulated at the termination shock of the heliosphere and then in the inner solar system by three main forces: solar gravity, solar radiation pressure force and Lorentz force resulting from the motion of the charged grains through the interplanetary magnetic field (IMF). This causes a modulation in ISD flux and size distribution that was observed by Ulysses to be a factor of 3 between 1992 and 2008. The grain parameters determining the trajectories of the grains are β and Q/m. β is the ratio of solar radiation pressure force to gravity and depends on the grain size, material and morphology. It is a constant for one grain moving through the heliosphere. Q/m is the charge to mass ratio of a compact spherical grain assuming a constant potential of +5V with respect to infinity. Q/m is larger for smaller grains. The relation between β and grain size is defined in a so-called β-curve. In this thesis, an adapted astronomical silicates β-curve of Gustafson (1994) was assumed for calculating the size distributions, which was modified to the outcome of the study of Landgraf et al. (1999a) to have $\beta_{max} = 1.6$.

Monte Carlo simulations of dust trajectories in the inner solar system were performed where the starting position and time of the ISD grains was varied. From these simulations, trajectories, velocities, fluxes, densities and directions of the ISD flow were derived.

The dust trajectories affected by solar gravity and radiation pressure force only are axi-symmetric, time-invariable and can be determined analytically. The radiation pressure reduces the effects of the solar gravity. The trajectories are attractive or repulsive hyperbola ($\beta <$ or > 1) or straight line trajectories for $\beta = 1$. In case of the repulsive hyperbola ($\beta > 1$), the grains do not enter the region close to and downstream from the Sun which is called the β-cone. For instance, $\beta = 1.3$ grains will not get closer to the Sun than 1 AU. The solar radiation pressure force and gravity lead to a gap in the size distribution (β-gap) for middle-sized grains ($\beta > 1$, around 0.2 μm) or a concentration of ISD downstream from the Sun for very small and very large grains ($\beta < 1$). Very close to the β-cone, there is a local increase of relative density.

The ISD grains are charged and therefore experience electromagnetic forces when moving through the IMF that is frozen in the solar wind plasma. The IMF is modeled by a Parker spiral (Parker, 1958) and the solar wind speed is assumed constant at 400 km/s. The azimuthal component of the IMF causes the grains to deflect towards or away from the solar equatorial plane depending on the polarity of the IMF. The mean magnetic dipole field over one solar rotation was used for the simulations in this thesis, which is valid for simulations down to about 2 AU from the Sun. The closer to the Sun, the larger the influence of the Lorentz force although the relative strength of the Lorentz force to the (effective) gravity generally decreases. The non-averaged magnetic field value is also implemented in the model but requires much longer computation times. When Lorentz forces act, the flow pattern becomes more complicated and makes the stream non-stationary: there is a focusing and defocusing with respect to the solar equatorial plane in a 22-year cycle and the effect is larger for smaller grains (high Q/m). This was predicted by Levy and Jokipii (1976); Gustafson and Misconi (1979); Morfill and Grün (1979), observed by Ulysses (Landgraf, 1998) and is confirmed by the simulations in this study. The variations in relative flux lead to temporal enhancements or depletions of ISD grains in the planetary region of about factor 5 for grains $< 0.1\mu$m, 3 for grains of abour 0.3 μm and 1.5 for grains of about 0.7 μm assuming compact astrosilicates. Very small grains (< 0.15 μm) are even reflected upstream from the Sun during the focusing phase of the solar cycle, which was called 'mirroring' in this thesis. Smaller grains (< 0.1 μm) will not even make it to the inner solar system because they are filtered out at the termination shock of the heliosphere (Linde and Gombosi, 2000; Slavin et al., 2010). The Lorentz force expands the β-cones during the defocusing phase of the solar cycle and causes a concentration of accelerated ISD grains north and south out of the ecliptic plane at about 10-20 AU above the poles of the Sun. As a result, small grains stream out of the solar system at high latitudes and velocities. In the focusing phase, the β-cone is smaller mainly in the direction perpendicular to the ecliptic plane and grains are focused and accelerated in the ecliptic plane just outside of the β-cones. The Lorentz force enhances or reduces the small end of the size distribution depending on the phase of the solar cycle and the location in the solar system.

In the upstream direction at large distances ($\geq$10 AU) the differences between the straight-line trajectories and the trajectories for other β and Q/m values are small. For grains of 0.1 μm the electromagnetic forces are dominant. At 0.2 μm the solar radiation pressure force is strongest (but outside of 1 AU the magnetic forces still prevail) and as from 1 μm, Lorentz forces hardly have an effect. The speeds are typically modulated from the original speed of 26 km/s at long distances down to 0 km/s and up to 50 km/s and even more.

The size distributions in the inner solar system are strongly modified from the incoming ISD size distribution and vary with grain properties, location in the solar system and time in the solar cycle. Big particles are influenced most by solar radiation pressure force and gravity whereas small grains are most of the time diverted to higher latitudes and thus depleted inside of 10 AU. However, for the relative fluxes on planets or spacecraft missions in the solar system, also their motion with respect to the ISD flow plays a role: when the planet moves towards the ISD flow, the relative velocity and thus flux increases which is good for in-situ detection of ISD. When the planet moves parallel to the stream of ISD then the relative velocity (and flux) is lower which is more suited for sample return missions where it is important to bring back the grains intact, even if the flux is lower. This contrast in flux due to the motion of the planet is higher for planets close to the Sun. Three specific cases were studied of the flux and size distribution: at Saturn, at Jupiter and at the main-belt asteroid Ceres in order to get an idea of what a spacecraft in these orbits would observe of ISD. ISD measurements at planet orbits like of Jupiter, Mars, Venus or an asteroid are well suited for characterizing the ISD size distribution and grain composition with time. These planets cover all the β-cone regions in relatively short time span, and provide a higher flux when moving against the stream of ISD, due to their high orbital velocity.

For each of these locations the ISD flux for a specific mission was analyzed: Cassini at Saturn, JUpiter ICy moons Explorer (JUICE) at Jupiter and Stardust between 1 and 2.5 AU from the Sun. The ISD simulations for Cassini are a helpful tool for optimizing the pointing of the instrument for future observations until 2017 as well as to extract the ISD impacts from the data, based on the expected impact directions and velocities. Around 2010 Saturn and Cassini are moving against the stream of ISD and thus higher fluxes are expected for all sizes. Also in 2010, Saturn left the β-cone for $\beta = 3$ allowing even the most absorbing ISD grains to be observed if present. In addition, there is a focusing phase of the solar cycle in mid-2007 (in the model) and with a time-lag of a few years, this results in a maximal focusing of most of the grains between 2008 and 2011 depending on their size (one exception: Q/m = 3 C/kg in 2014). There is a variation of 15° in latitude and 4° in longitude over 30 years of measurement time at Saturn for 0.3 μm grains for astronomical compact silicates. However, this can be more for fluffy aggregates. For smaller grains, this variation increases to up to 50° latitude and 40° longitude and the flux can reach 10 times the incoming ISD flux. Dedicated ISD measurement campaigns were done in 2010 and will continue until 2017.

The ISD analysis for the JUICE mission, that is scheduled to arrive at Jupiter in 2029, lead to the conclusion that JUICE provides an ideal opportunity to do extra add-on research on ISD, especially during the last part of the cruise phase. In the size range considered (10^{-18}–10^{-15} kg), the flux of ISD at JUICE is 2, 5 or 20 times the flux present at Galileo (1989-2003). This is because the direction of motion of Jupiter is opposite to the ISD stream in 2029, there are only few β-gaps in the size distribution and in 2029, the focusing phase of the solar cycle is expected to focus the grains in the planetary regions. For the Cassini and JUICE analyses no gravitational focusing or magnetic field effects of Saturn or Jupiter were taken into account.

For the Stardust sample-return mission, the ISD fluxes, impact directions and impact speeds were analyzed during the two ISD capturing periods in 2000 and 2002 and they were compared to the impact angles and speeds of the 3 candidate ISD grains found during the InterStellar Preliminary Examination (ISPE). The information on the impact angles and velocities of these grains was collected from the track directions and shapes that were calibrated with a dust accelerator. The impact directions and speeds were calculated for solar radiation pressure force and gravity alone, while the fluxes were derived from Monte Carlo simulations including Lorentz forces. In 2000 and 2002, Stardust was moving in the same direction of the ISD flow leading to very low fluxes and impact velocities. The low impact velocities were needed to keep the grains intact upon capture. However, the low fluxes were even reduced by the defocusing of grains due to electromagnetic forces since the collection periods were close after the maximum effect occurred for the defocusing phase of the solar cycle.

The Lorentz force filters almost or all grains below about 0.15 μm radius (assuming compact astrosilicates) depending on the collection period, and reduces the flux for grains below 0.25 μm. The simulated impact velocities were between 3 and 14 km/s for the smallest simulated grains (0.25-0.3 μm) and between 14 and 25 km/s for grains with radius between 0.4 and 0.7 μm. The simulated zenith angles are mostly $< 40°$ of the collector normal for impact velocities above 10 km/s. For impact velocities larger than 10 km/s, the impact zenith angles even increased to above 90° meaning that the very slow grains impact on the cometary side of the collector, i.e. Stardust is overtaking the ISD grains on their trajectories. The zenith angles of the 3 ISD candidates correspond well to the zenith angles and impact speeds of the simulated grains. The simulated azimuth angles concentrate around 180° for the largest grains with high impact speeds, and around 0° for the slow grains (impact speeds < 10 km/s). However, the azimuthal angles found by the ISPE were all three in the 180° direction for nominal grains with initial incoming direction of 259° longitude. However, by changing the initial incoming ISD dust direction to 269° or even 274° degrees (which is still within statistical uncertainty limits of the initial ISD direction (Landgraf, 1998)), and assuming grains with lower density, allows to make a fit between the zenith angle, azimuthal angle, grain size and impact speed of the 3 ISD candidates and the simulations.

The expected number of impacts was calculated based on the flux from Ulysses and adapted to the filtering at the time and location of Stardust. Assuming compact astrosilicates with a grain density of 2 g cm^{-3}, a total of 40 grains were estimated during the collection periods.

Comparing the zenith angle and impact velocity of Track 30 and 34 to the simulations suggests that these found ISD candidates have β-values between 1.1 and 1.5 and for Track 40, $\beta < 0.9$. However, the azimuthal angles of Track 30 and 34 did not correspond to these results and there is a large margin depending on uncertainties like spacecraft pointing and assumed initial ISD direction. Therefore, only if more grains are found and a statistically significant dataset is available, then one can constrain grain properties by comparing the simulations to the impact parameters of the grains in the aerogel. For now, by tuning the assumptions like initial inflow direction within the accepted limits (±15°), the results of the simulations could possibly correspond to the impact parameters of the three found ISD candidates but an interstellar origin is not uniquely proven. Also the grain density and the β-curve assumed have an impact on the results.

6

Outlook

With this thesis I have contributed to opening doors for future ISD research. The techniques shown in this work to analyze the ISD flow for specific missions and for different grain parameters shall be combined with the existing ISD data from for instance the Ulysses mission. As such, possible causes of the shift of dust observed in 2005 can be explored more in depth and ISD grain properties may be constrained by comparing piecewise the simulations to the measurements per orbit segment.

This outlook illustrates briefly how the techniques presented in this thesis can be applied for future ISD research. Also, the role of the techniques used in this thesis are discussed in the context of several other research examples like constraining the dust parameters, understanding the filtering at the heliopause and understanding the differences in size distribution between the simulations, astronomical observations and measurements made by spacecraft.

6.1 Improved analysis of Ulysses data

The 17 years of ISD observations by the Ulysses spacecraft comprises the most comprehensive data set of ISD covering almost one full (magnetic) solar cycle of about 22 years. Because of its special orbit perpendicular to the interstellar flow interstellar dust could be uniquely distinguished from interplanetary dust during most of its orbit. Ulysses measured the flux, the direction, and the size distribution of interstellar grains as a function of position and time during 3 complete orbits around the sun.

Of special interest are spatial and temporal variations of flux, the direction, and the size distribution which are indicative specific dynamical grain parameters beta and Q/m. (Landgraf et al., 1999a) recognized a gap in the size distribution between $1 \cdot 10^{-17}$ and $3 \cdot 10^{-16}$ kg that was seen in data of 2-4 AU from the Sun in comparison with data outside 4 AU. This indicated that the grains have a maximum β-value of 1.6 for astronomical silicates with density of 2 g cm^{-3}. However, only the flux and no directions were used to compare the data to the simulations, and the dataset covered only data from 1992 until 1996. Another example is a shift in ISD direction of 30° in rotation angle that was measured by Ulysses in 2005 (Krüger et al., 2007) and even 50° were reported in an analysis by Strub et al. (2011).

Future research on interpreting Ulysses data will be done in cooperation with the Ulysses DUST PI and his team. The goal will be to find an explanation of the shift in ISD direction, to improve the model of the ISD flux, direction and size distributions and as such also to constrain the grain material properties. In order to reach these goals, the flux variations, size distributions and ISD directions from simulations will be compared to the Ulysses data per orbit segment and thus also per time segment, provided that these segments contain statistically significant numbers of ISD grain. This task is referred to as "β-spectroscopy" (Altobelli, 2004).

The ISD grain properties are not fully determined, therefore, it is useful to consider the whole β-Q/m space when comparing data to simulations. In this manner the dependency of the ISD flux, directionality and size distributions (the 3 *observables* of Ulysses) on β and Q/m constrain and direct us towards one β-curve or a combination of them.

Preliminary analysis of the shift in ISD direction observed in 2005 is shown in Figure 6.1. It shows the β-Q/m parameter space for the relative flux and latitude of the ISD grains on November 15th 2005 with respect to Ulysses. This figure suggests that a shift of dust of up to 44° in latitude can be explained by particles of sizes 0.15-0.2 μm (Q/m = 2–3 C/kg) which is much smaller than the bulk particle size of 0.3 μm found by Landgraf (1998). Earlier in 2005, grains as small as 0.1 μm (Q/m = 6 C/kg) display also a shift in the simulations of similar magnitude. These β-Q/m plots may help to find the grain parameters that are needed to fit the observations. However, for proving that the heliospheric interaction is truly the cause of the shift of dust in 2005, also absolute fluxes, directionalities depending on different grain sizes and time-dependent size distributions should be compared to the data and fit at the same time of the whole dataset. A first glance at the simulation results and fluxes and directions from measurements (Landgraf et al., 2003; Krüger et al., 2007; Strub et al., 2011) look positive but much more work is needed to find a good fit.

There may be other implications when we find that other materials than compact silicates (e.g. fluffy grains or a combination of grains with different compositions) give a better fit to the Ulysses data. This may have an effect on the interpretation of the Ulysses measurements themselves. So far calibration measurements with compact silicates, iron or quartz particles were used. A re-analysis of the calibration data may be needed that includes new information and insights:

- The effect of fluffy grains on the grain charging: fluffy or porous grains have higher charges. This would affect the simulation results.
- The effect of fluffy grains on the impact signal: fluffy or porous grains would 'mimic' the impacts of larger grains, especially on the large end of the size distribution. This could be with one order of magnitude (Hornung, 2012, pers. comm.).

Such a re-analysis would lead to new measured size distributions and simulated velocities, fluxes and directions per orbit segment and the comparison between data and simulations has then to be repeated over (iteration).

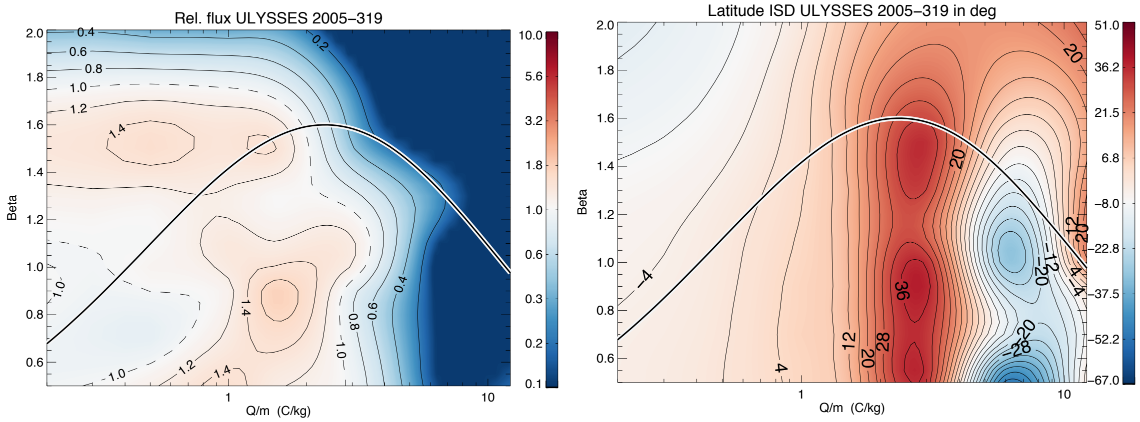

Figure 6.1: The relative flux and latitude of the ISD with respect to Ulysses on November 15th 2005.

Other possibilities of scenarios to explain the shift of dust are local dust inhomogeneities in the ISM (Grün and Landgraf, 1997) over 1 kpc (variability in local environment, modifications outside of heliosphere). From (Linde and Gombosi, 2000; Slavin, 2012) it is known that for a positive magnetic polarity at the north ecliptic pole, grains $< 0.2\mu$m will be partially filtered at the termination shock and grains $< 0.1\mu$m will be completely filtered out. It is possible (Slavin, 2012) that for a the negative magnetic polarity at the north ecliptic pole, such small grains do pass and modify the fluxes and directionalities at the termination shock besides the known modulation in the inner solar system. Up to now, the Ulysses data and simulations have not been compared in sufficient depth to prove or disprove that the shift of dust can be explained by the solar system modulation alone. Results from missions like Voyager and IBEX will provide more clarity in the structure of the outer heliosphere.

6.2 Other applications of the ISD model

ISD modelling taking into account the special conditions of current and future space mission will support science planning of dedicated ISD measurement campaigns. E.g. the Cassini spacecraft is the 3-axis stabilized platform; therefore, careful planning of the spacecraft attitude i.e. pointing of the dust instrument CDA is necessary to optimize ISD measurements. After successful implementing such observations ISD modelling will be necessary for the interpretation of the obtained data. Preliminary analysis (this thesis) demonstrates that Cassini is expected to get more data at maximum ISD flux. For the first time Cassini CDA will provide composition measurements of ISD grains.

Even earlier ISD modelling can help the mission design of a future space mission. An example is the outer planet missions JUICE for which ISD modelling can support orbit design and science planning. Even the selection of a science instrument may be affected once the added value of ISD science is recognized.

A similar analysis of ISD data as for Ulysses may be applied to data of current missions to the outer solar system like New horizons, or re-analysis of data of older missions (Galileo). For Stardust it is expected that more grains will be found such that there will be better statistics. When more ISD grains are identified then the model can be updated with better compositional information and better constraints on the dynamical grain parameters.

6.3 Improvements to the current model

The assumed solar wind speed (400 km/s) may have little effect since the azimuthal component of the IMF is inversely proportional to this and thus the largest part of the Lorentz force is independent of solar wind speed. Similarly, it is not expected that more detailed UV flux data will change a lot. However, the IMF model needs some refinement for application to the inner solar system. Although the current ISD model works well for applications to the outer solar system at 1 AU the averaging of the IMF over a solar rotation (25 days) is no longer applicable but a rotating magnetic field model needs to be used. The solar magnetic field was adapted in our model to use the Solar Wilcox Observatory data instead of an IMF that rotates at a constant rate, but the simulations ran used the averaged magnetic field for computation time reasons.

The current simulations used a grid size of 1.5 AU which is too coarse for applications inside about 2 AU. Therefore, a refinement to a smaller gridsize is necessary for applications closer to the Sun. Fine grid simulations will help for mission design like SARIM+, DUNE, future proposals for S-class missions close to Earth. It will also help for data analysis of current missions close to the Sun like STEREO and GORID.

All in all modelling of the interstellar dust flow through the solar system holds promise for exciting new discoveries for quite some time in the future.

A

The flow of ISD in the solar system: graphical overview

This appendix gives a graphical overview of the characteristics of the ISD flow in the solar system. The plots that we collect here are:

- Trajectory plots (introduced in Section 3.1)
- Plots showing the closest approach of the grains to the Sun (introduced in Section 2.1)
- Cross sections of the dust flow at three distances from the Sun along the interstellar flow axis (introduced in Section 2.1)
- Densities across the solar system from -11 to 11 AU (introduced in Section 2.1)
- Relative fluxes and velocities for all β and Q/m combinations at four distances from the Sun along the interstellar flow axis are not repeated here, but they complete the overview. We refer to Section 3.4.2 for the plots and the discussion.
- The size distribution derived from applying the relative fluxes along the adapted astronomical silicates curve to the MRN-distribution (ignoring filtering at the termination shock), and the relative flux along this β-curve (introduced in Section 3.4) are also not repeted. Again, we refer to Section 3.4.2 for the plots and the discussion.

A.1 Trajectories

A.1.1 Radiation pressure and gravity only

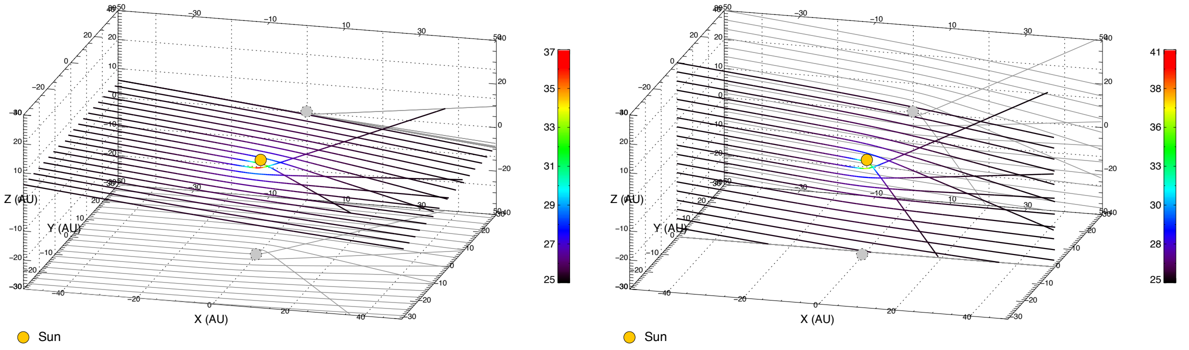

Figure A.1: $\beta = 0.5$, Q/m = 0 C/kg

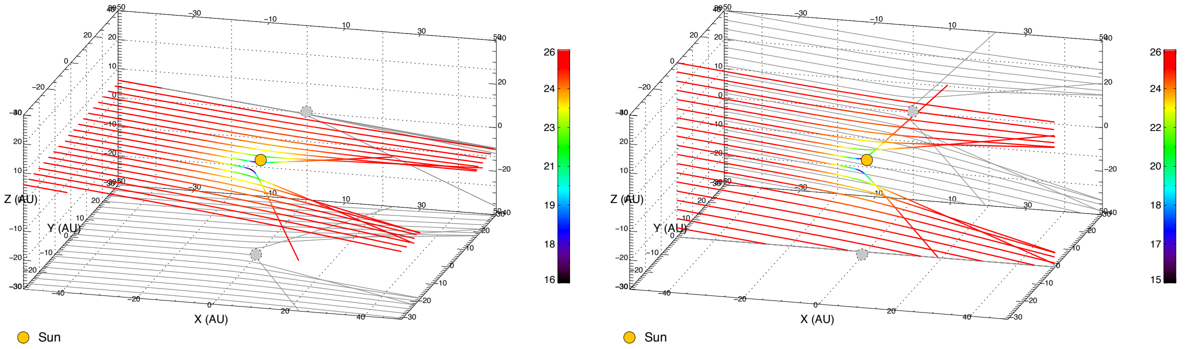

Figure A.2: $\beta = 1.6$, Q/m = 0 C/kg

A.1.2 Lorentz forces only

Focusing phase of the solar cycle

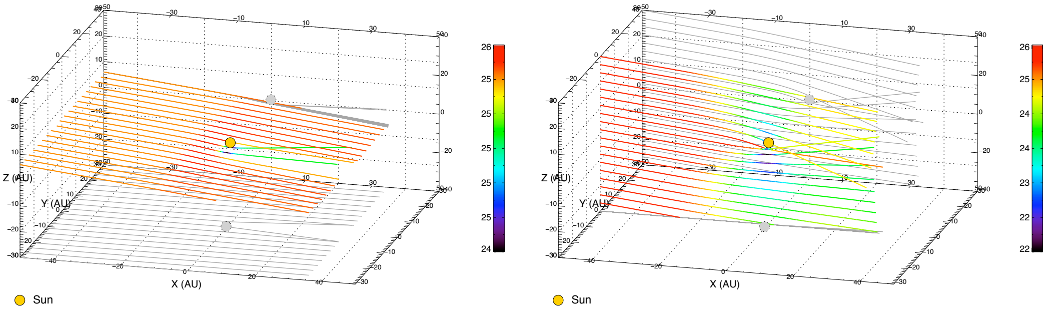

Figure A.3: $\beta = 1.0$, Q/m = 0.5 C/kg

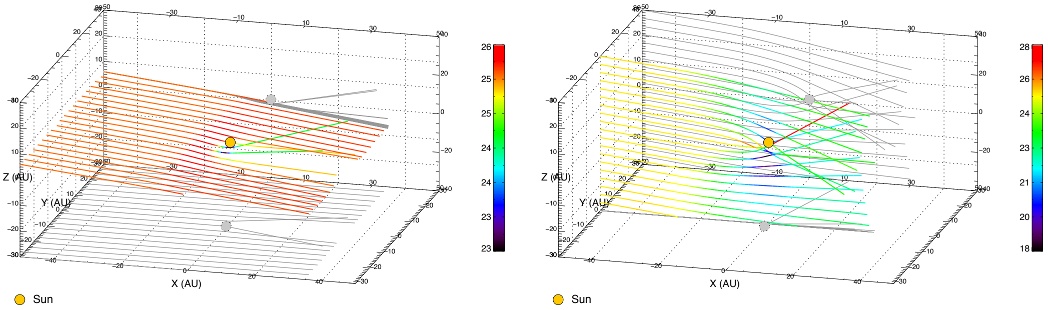

Figure A.4: $\beta = 1.0$, Q/m = 1.0 C/kg

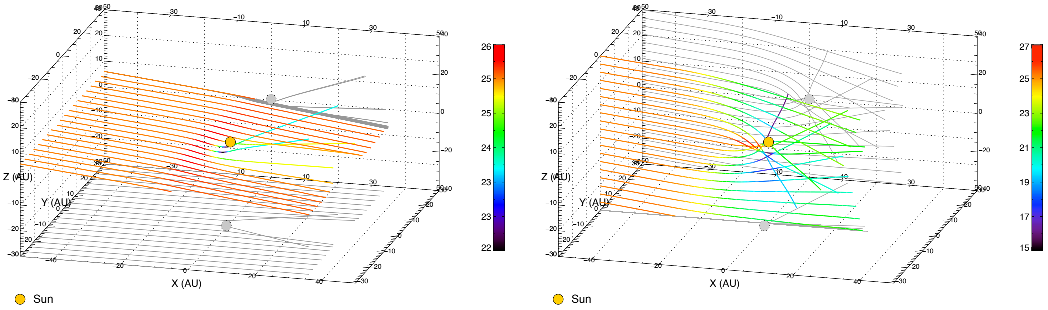

Figure A.5: $\beta = 1.0$, Q/m = 1.5 C/kg

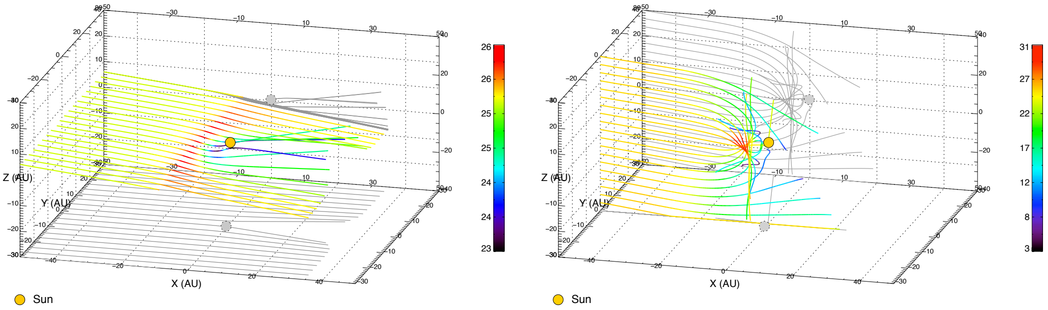

Figure A.6: $\beta = 1.0$, Q/m = 3.0 C/kg

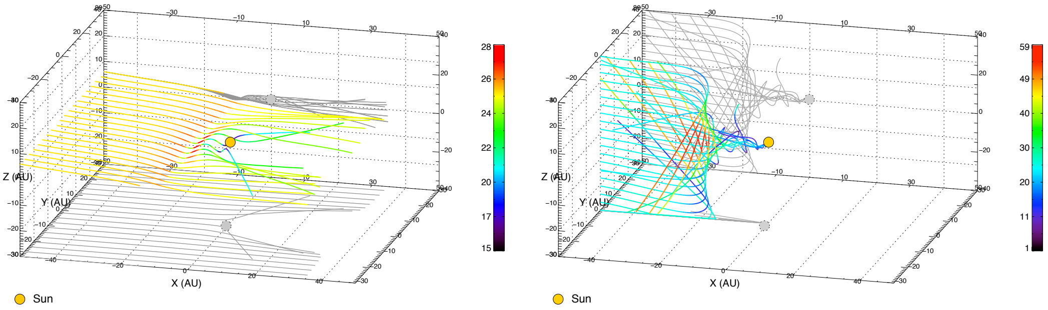

Figure A.7: $\beta = 1.0$, Q/m = 12.0 C/kg

Defocusing phase of the solar cycle

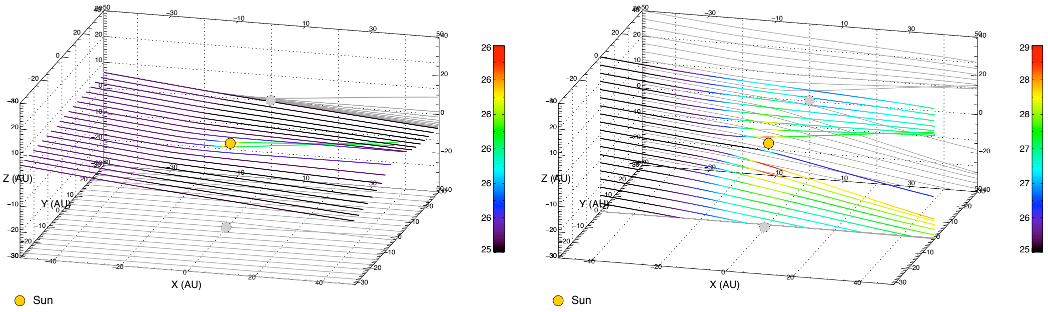

Figure A.8: $\beta = 1.0$, Q/m = 0.5 C/kg

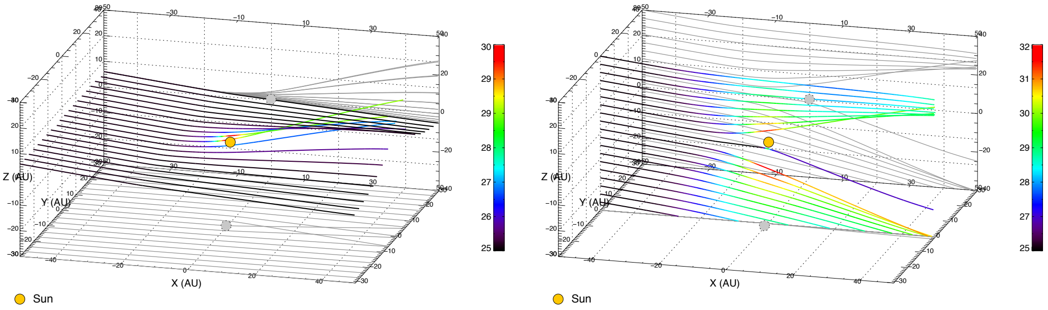

Figure A.9: $\beta = 1.0$, Q/m = 1.0 C/kg

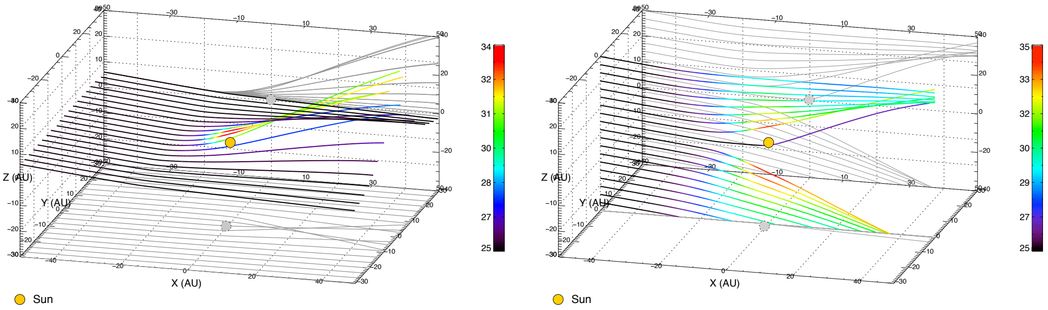

Figure A.10: $\beta = 1.0$, Q/m = 1.5 C/kg

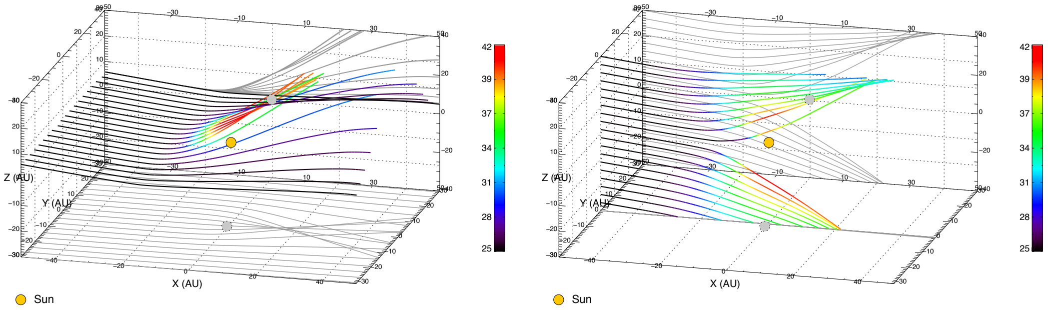

Figure A.11: $\beta = 1.0$, Q/m = 3.0 C/kg

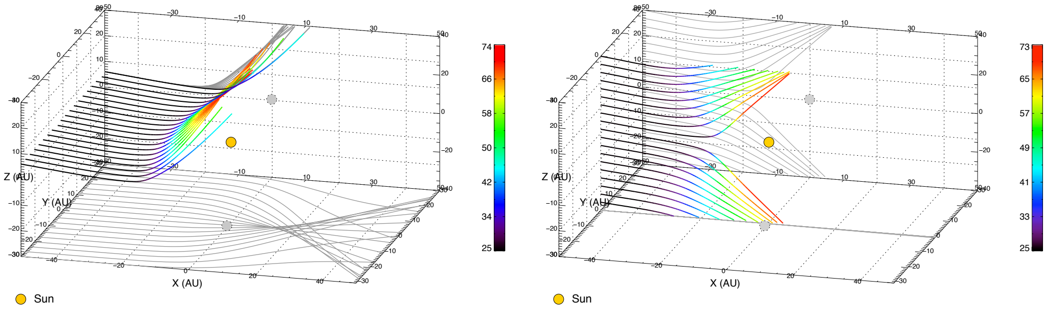

Figure A.12: $\beta = 1.0$, Q/m = 12.0 C/kg

A.1.3 Radiation pressure, gravity and Lorentz forces

Focusing phase of the solar cycle

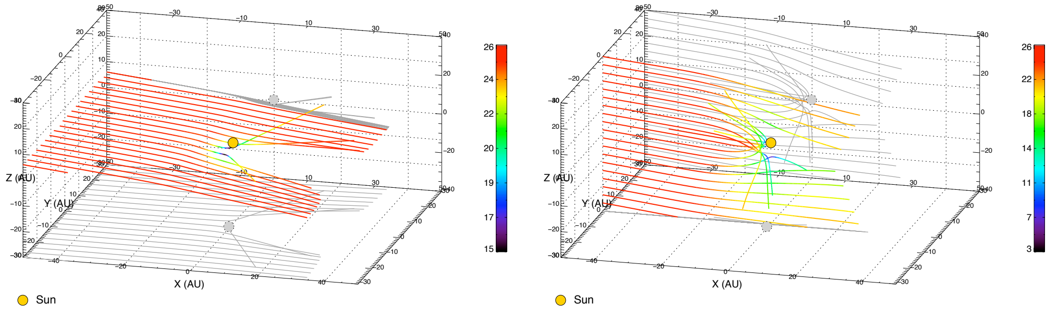

Figure A.13: $\beta = 1.5$, Q/m = 1.5 C/kg

Focusing phase of the solar cycle

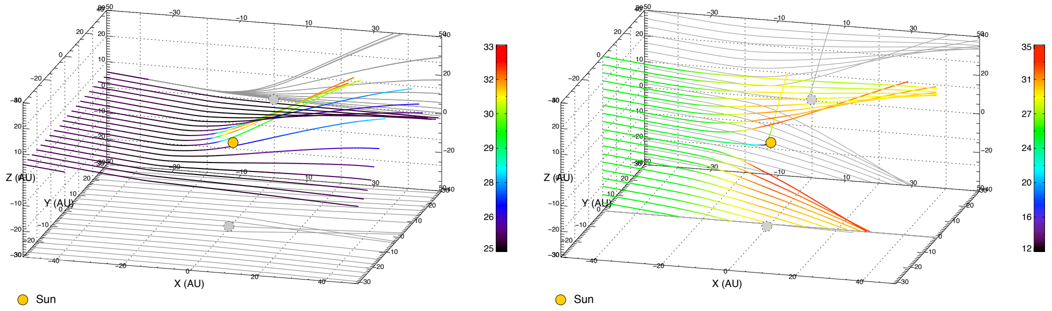

Figure A.14: $\beta = 1.5$, Q/m = 1.5 C/kg

A.2 Closest approaches

A.2.1 Radiation pressure and gravity only

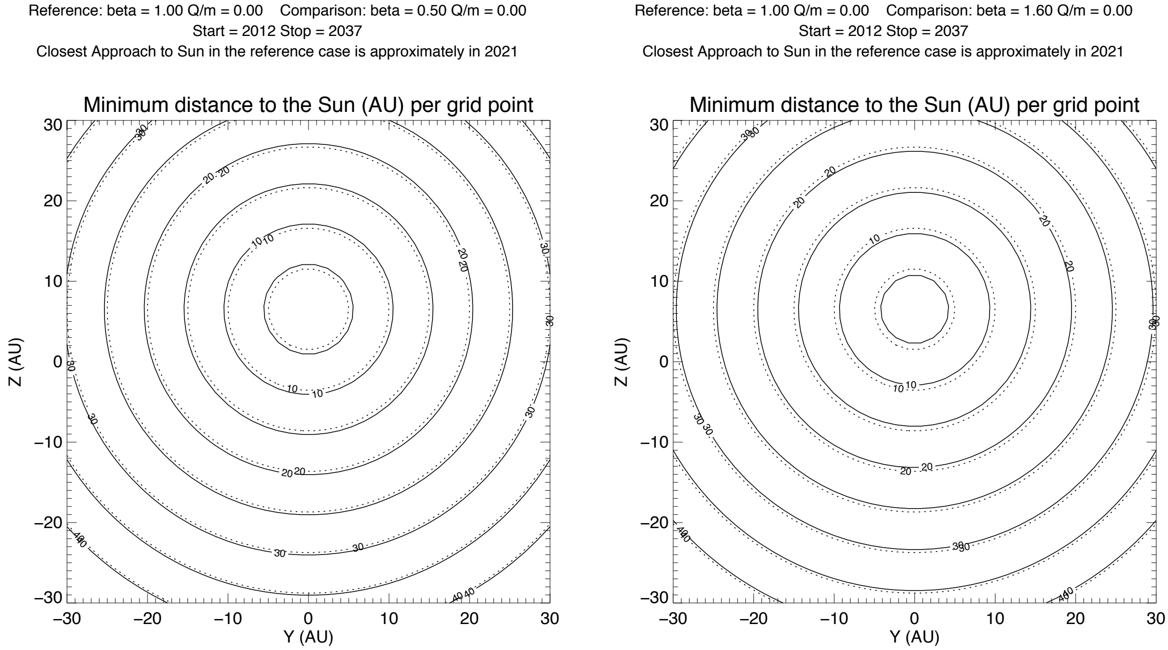

Figure A.15: $\beta = 0.5$, Q/m = 0 C/kg (left) and $\beta = 1.6$, Q/m = 0 C/kg (right)

A.2.2 Lorentz forces only

Focusing phase of the solar cycle

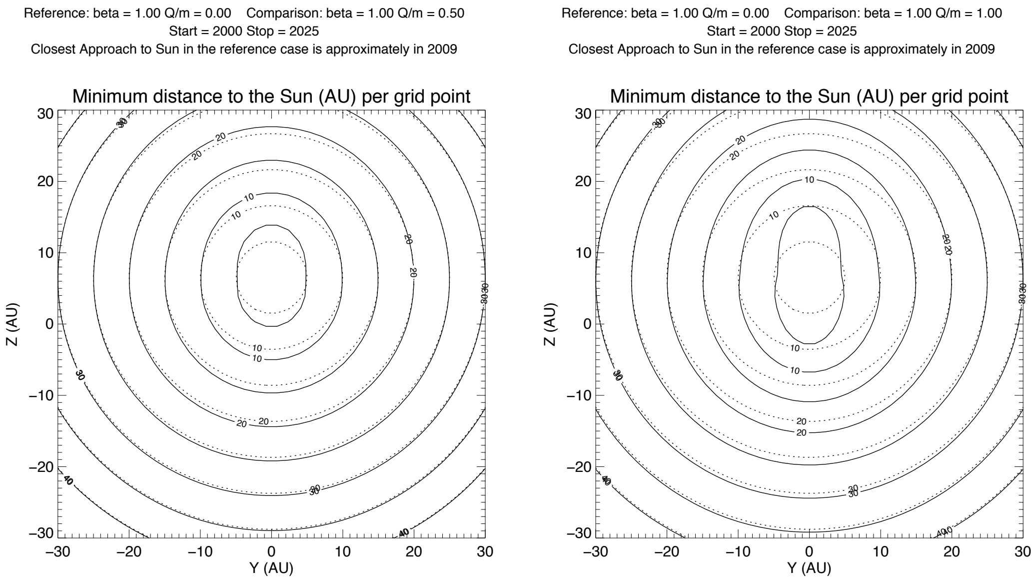

Figure A.16: $\beta = 1.0$, Q/m = 0.5 C/kg (left) $\beta = 1.0$, Q/m = 1.0 C/kg (right)

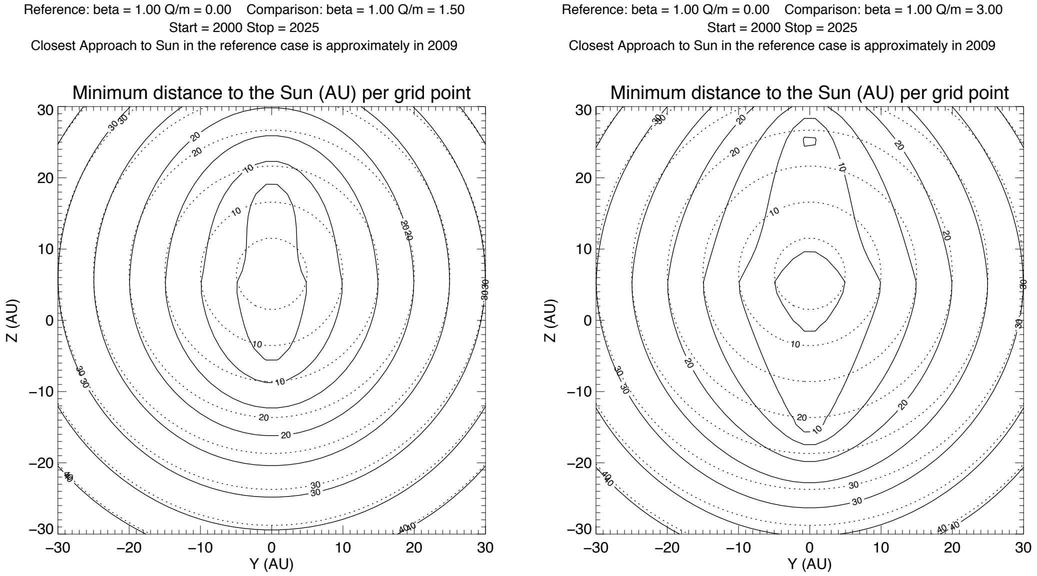

Figure A.17: $\beta = 1.0$, Q/m = 1.5 C/kg (left) $\beta = 1.0$, Q/m = 3.0 C/kg (right)

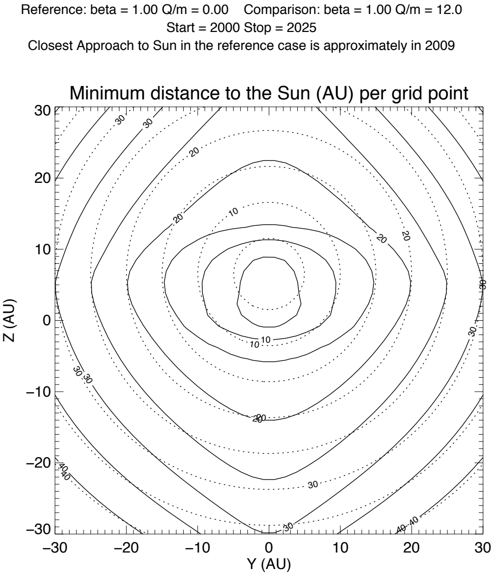

Figure A.18: $\beta = 1.0$, Q/m = 12.0 C/kg

Defocusing phase of the solar cycle

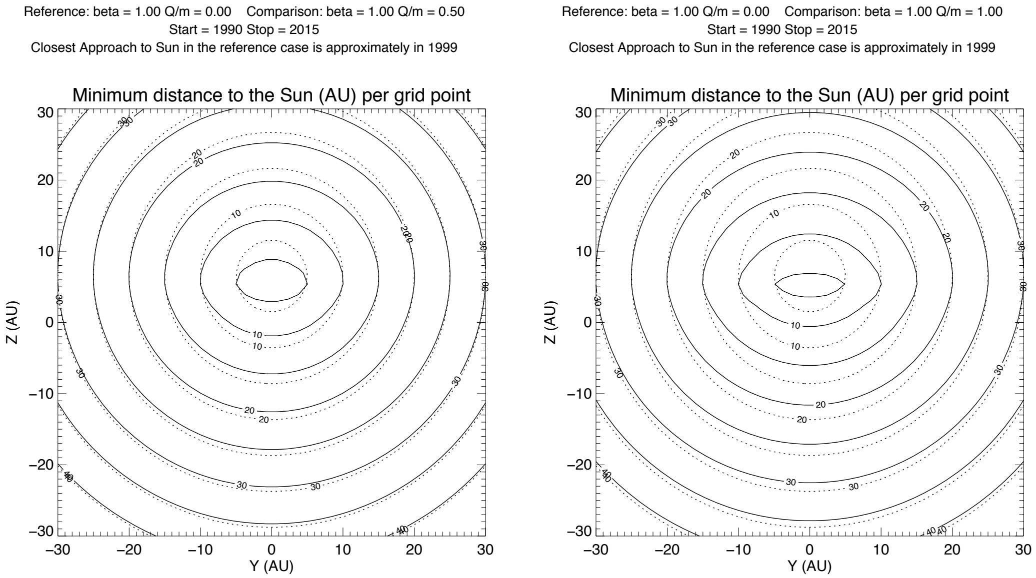

Figure A.19: $\beta = 1.0$, Q/m = 0.5 C/kg (left) and $\beta = 1.0$, Q/m = 1.0 C/kg (right)

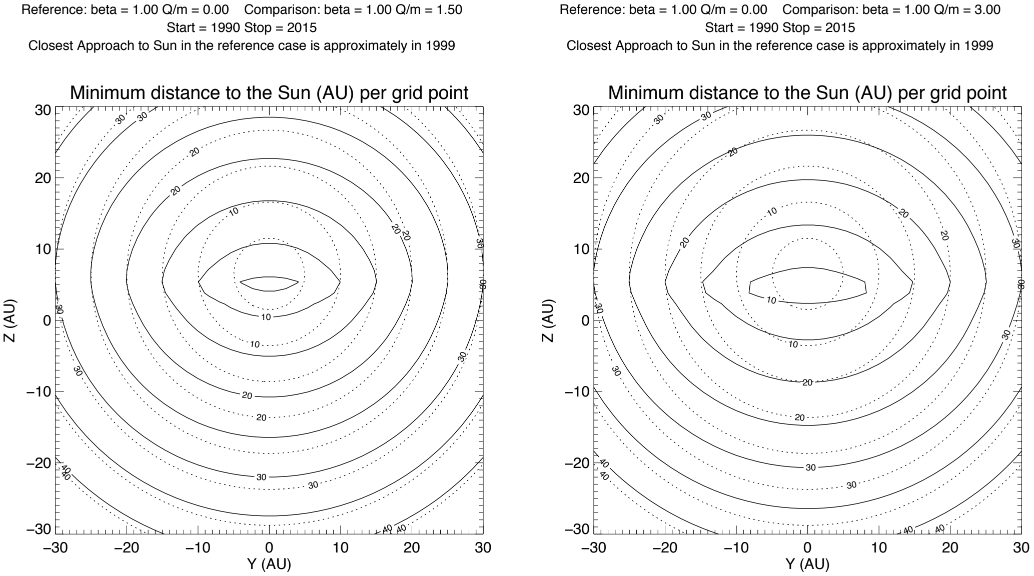

Figure A.20: $\beta = 1.0$, Q/m = 1.5 C/kg (left) and $\beta = 1.0$, Q/m = 3.0 C/kg (right)

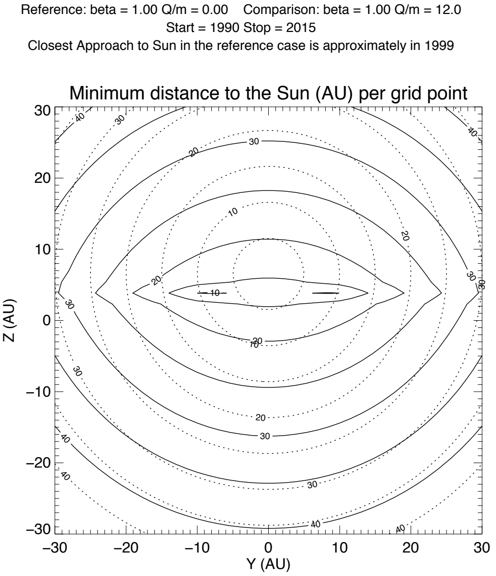

Figure A.21: $\beta = 1.0$, Q/m = 12.0 C/kg

A.2.3 Radiation pressure, gravity and Lorentz forces

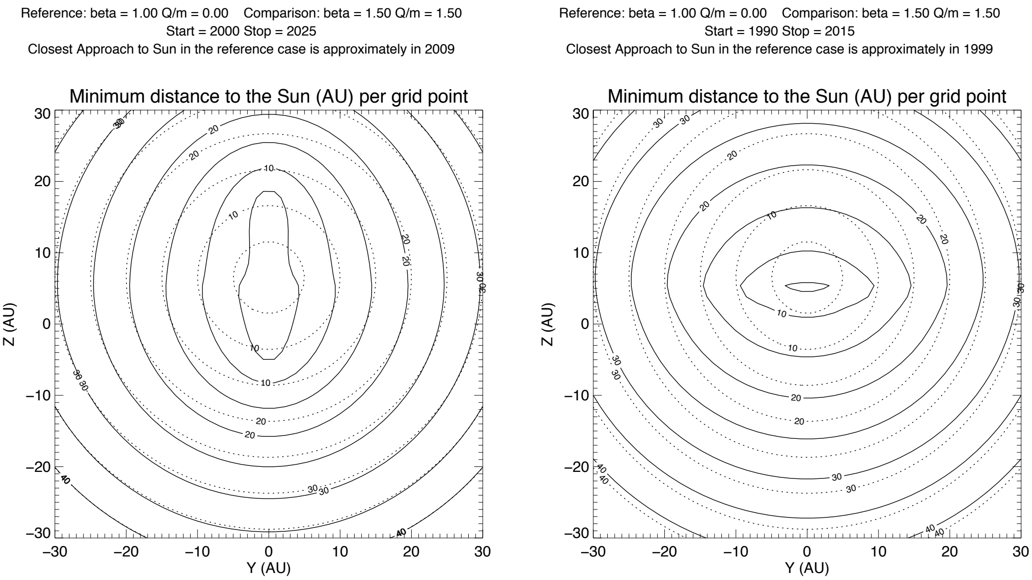

Figure A.22: β = 1.5, Q/m = 1.5 C/kg focusing phase (left), defocusing phase (right)

A.3 Cross sections

A.3.1 Radiation pressure and gravity only

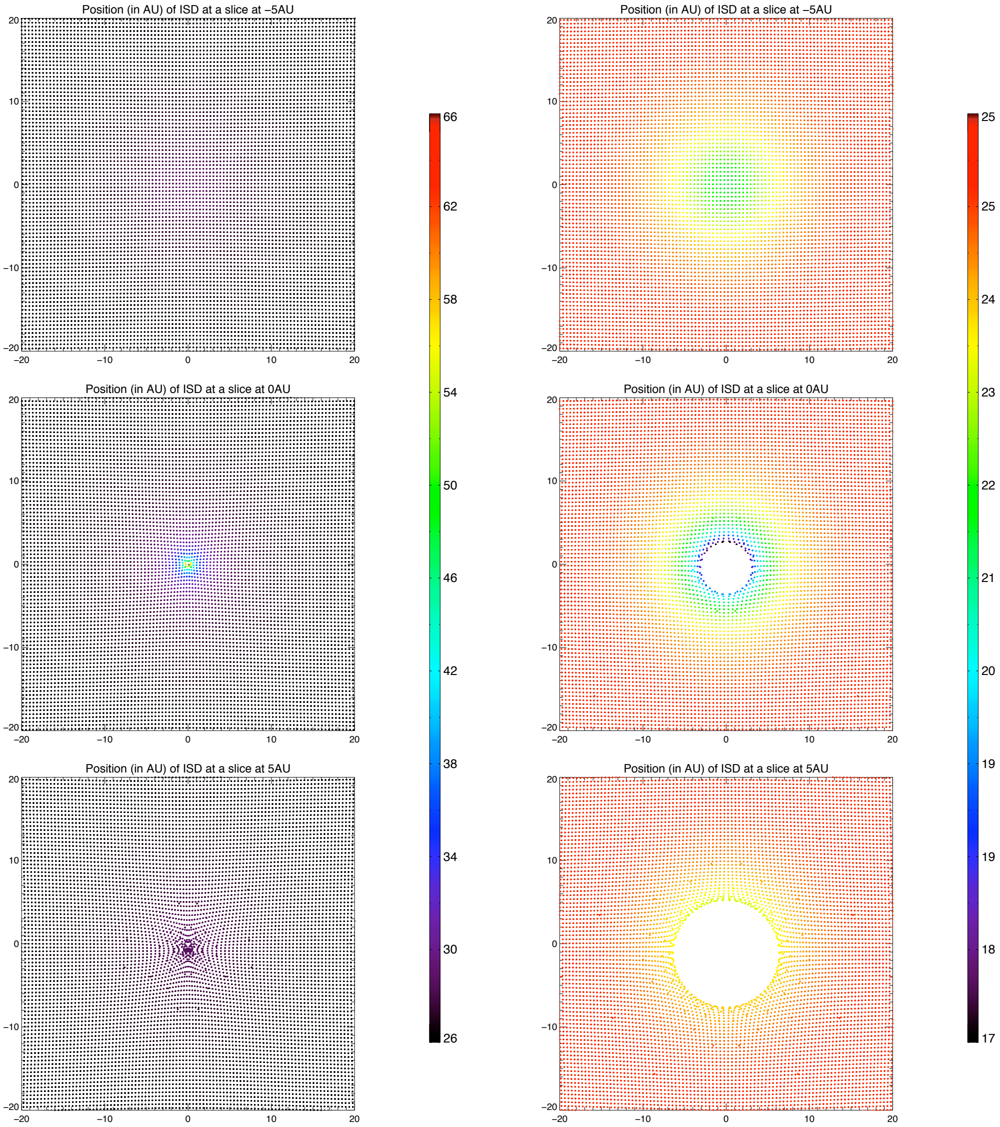

Figure A.23: $\beta = 0.5$, Q/m = 0 C/kg (left) and $\beta = 1.6$, Q/m = 0 C/kg (right)

A.3.2 Lorentz forces only

Focusing and defocusing phase of the solar cycle

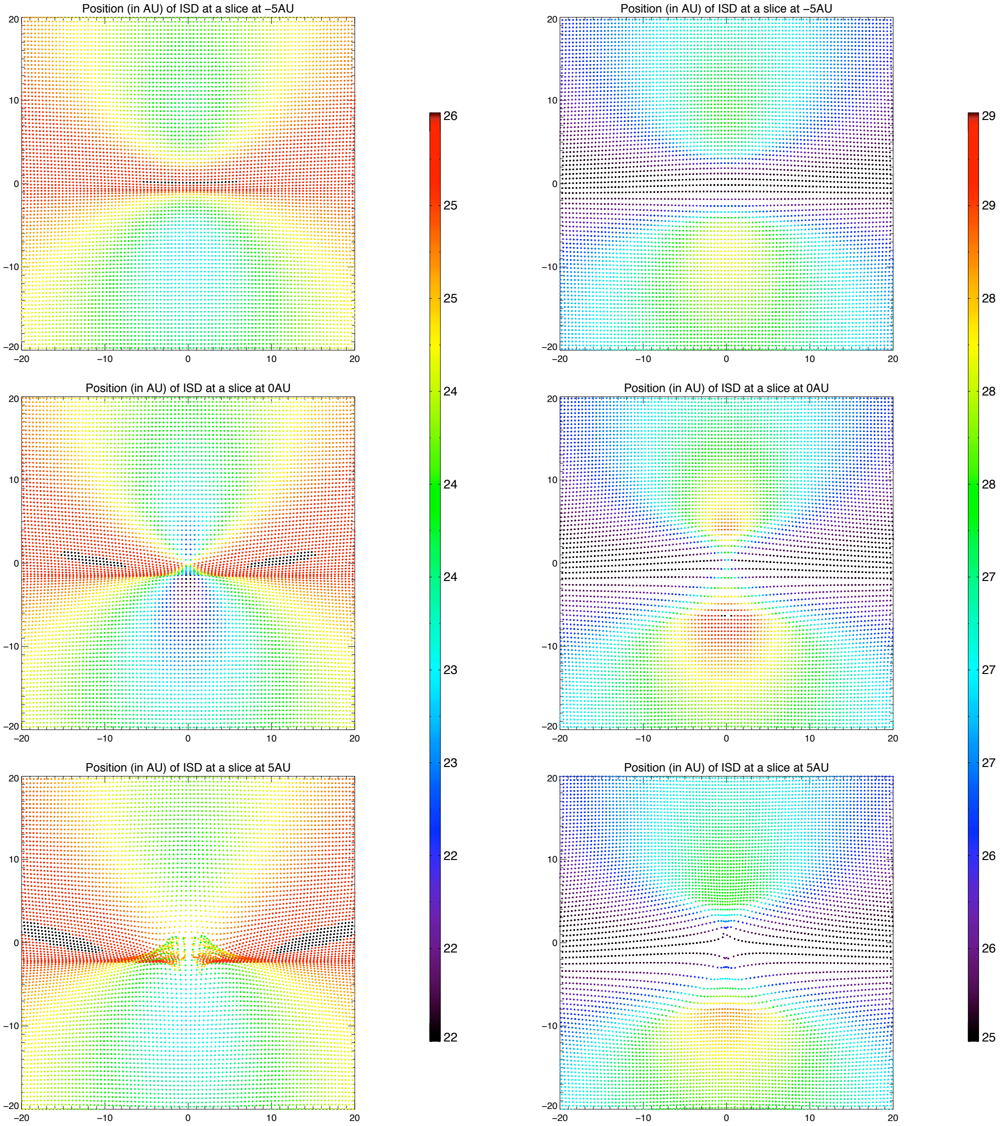

Figure A.24: $\beta = 1.0$, Q/m = 0.5 C/kg, focusing (left), defocusing (right)

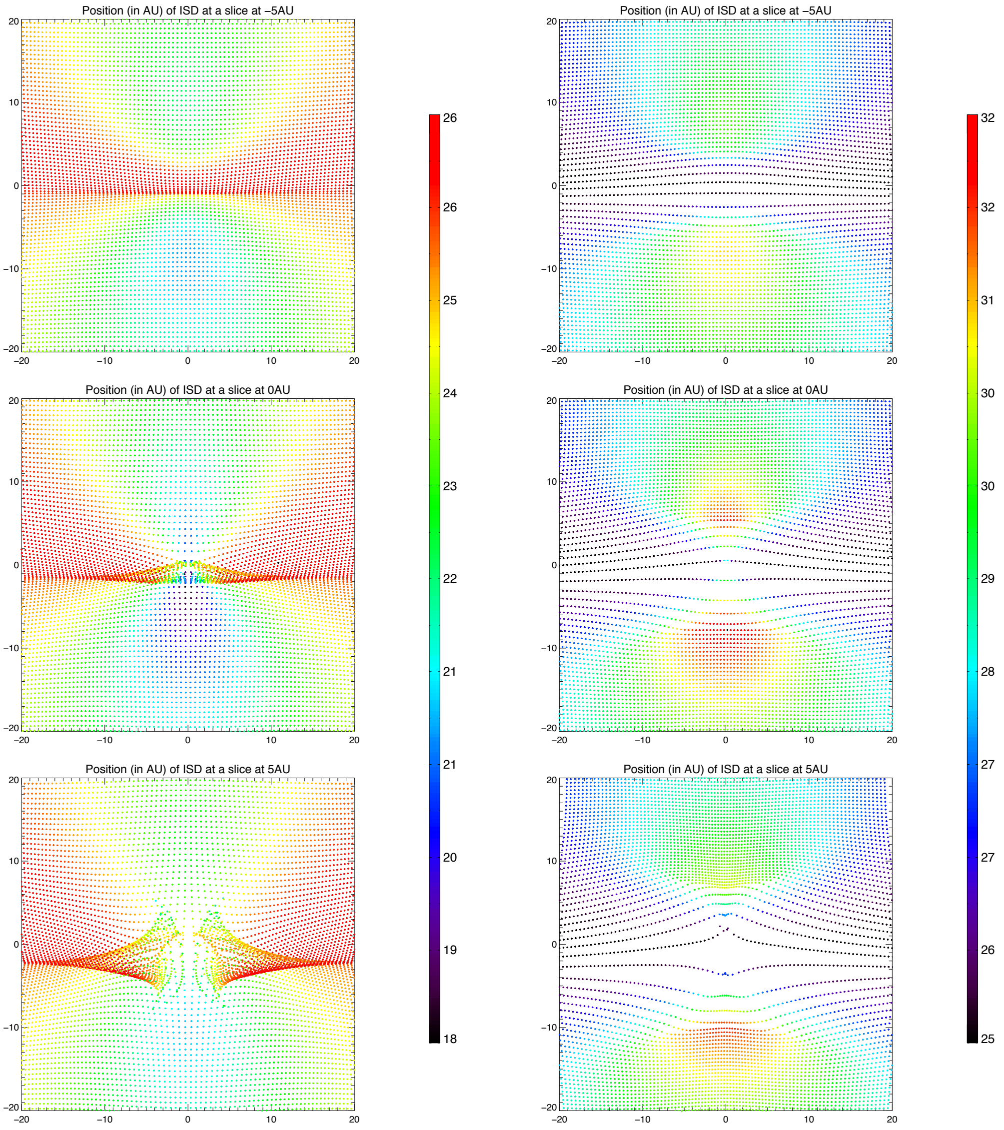

Figure A.25: $\beta = 1.0$, Q/m = 1.0 C/kg, focusing (left), defocusing (right)

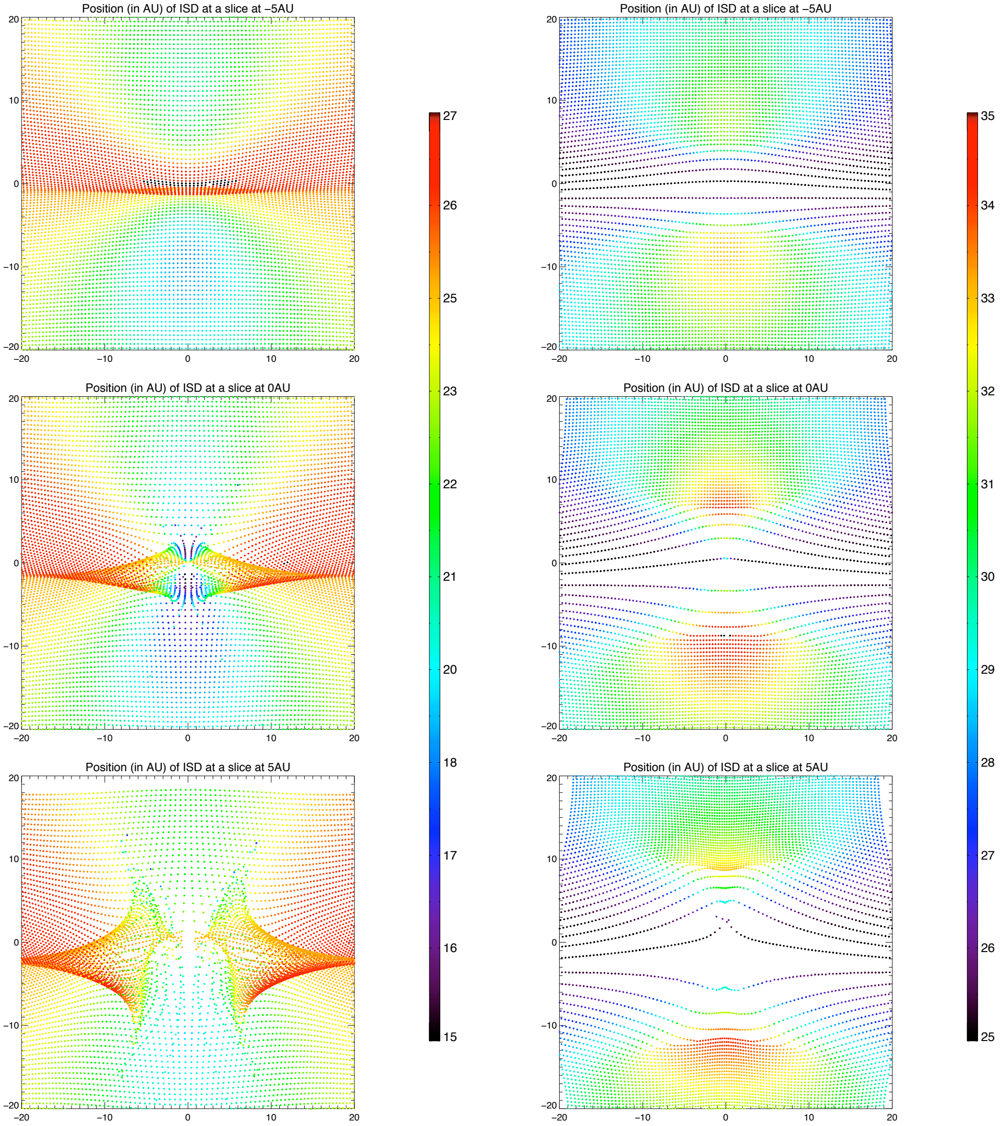
Position (in AU) of ISD at a slice at −5AU

Position (in AU) of ISD at a slice at −5AU

Position (in AU) of ISD at a slice at 0AU

Position (in AU) of ISD at a slice at 0AU

Position (in AU) of ISD at a slice at 5AU

Position (in AU) of ISD at a slice at 5AU

Figure A.26: $\beta = 1.0$, Q/m = 1.5 C/kg, focusing (left), defocusing (right)

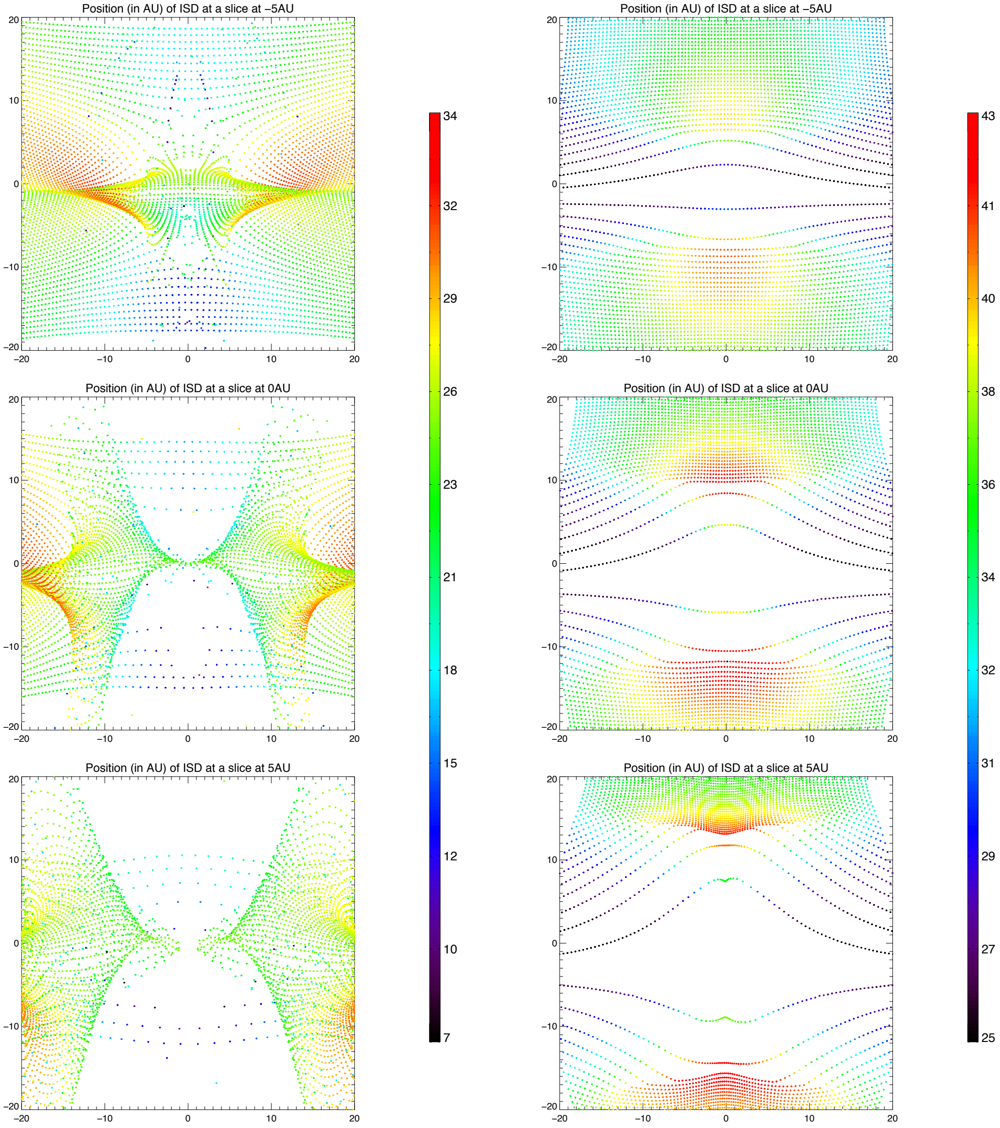

Position (in AU) of ISD at a slice at −5AU

Position (in AU) of ISD at a slice at −5AU

Position (in AU) of ISD at a slice at 0AU

Position (in AU) of ISD at a slice at 0AU

Position (in AU) of ISD at a slice at 5AU

Position (in AU) of ISD at a slice at 5AU

Figure A.27: $\beta = 1.0$, Q/m = 3.0 C/kg, focusing (left), defocusing (right). A small amount of grains reach velocities up to 400 km/s (not shown here) in the focusing phase.

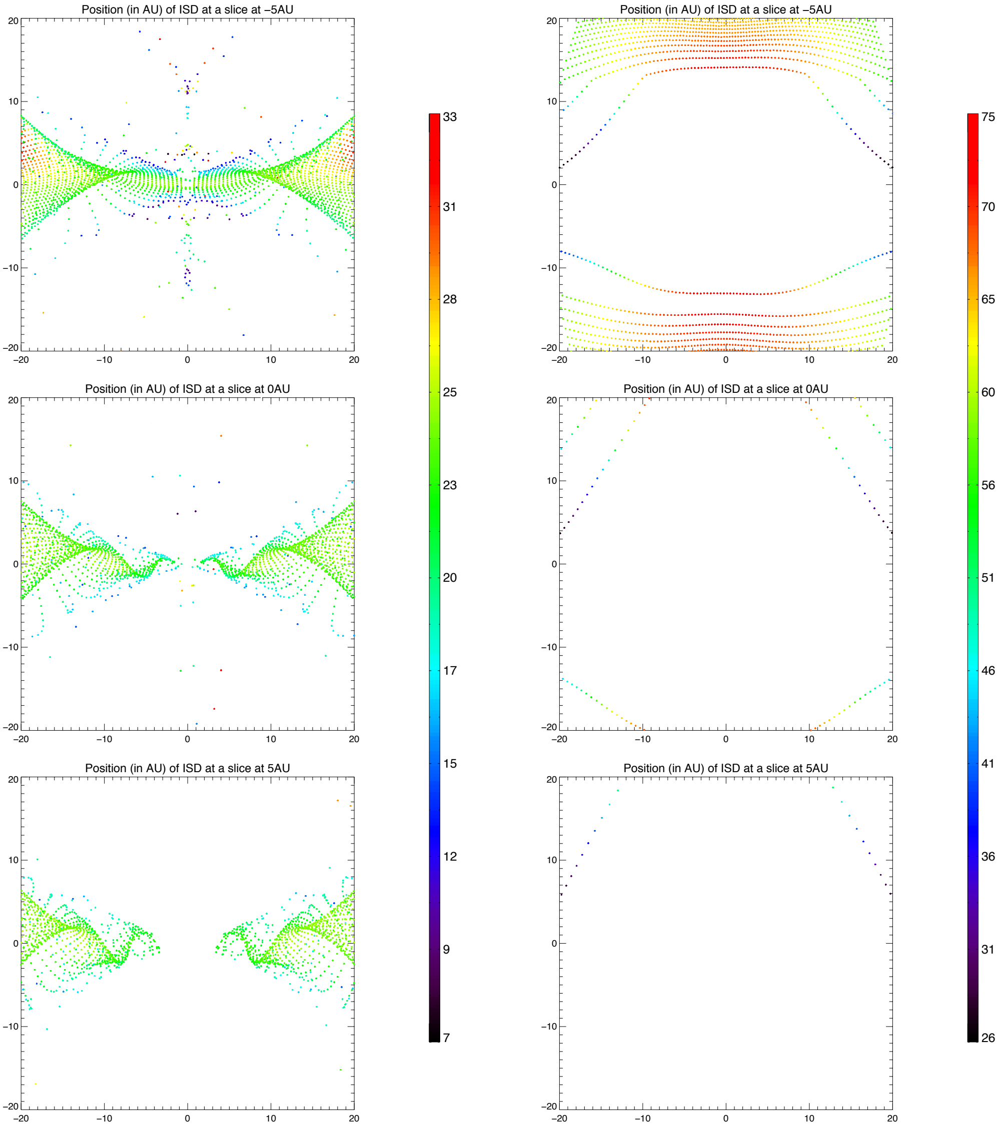

Figure A.28: $\beta = 1.0$, Q/m = 12.0 C/kg, focusing (left), defocusing (right). A small amount of grains reach velocities up to 900 km/s north and south from the Sun in the focusing phase (not shown here).

A.3.3 Radiation pressure, gravity and Lorentz forces

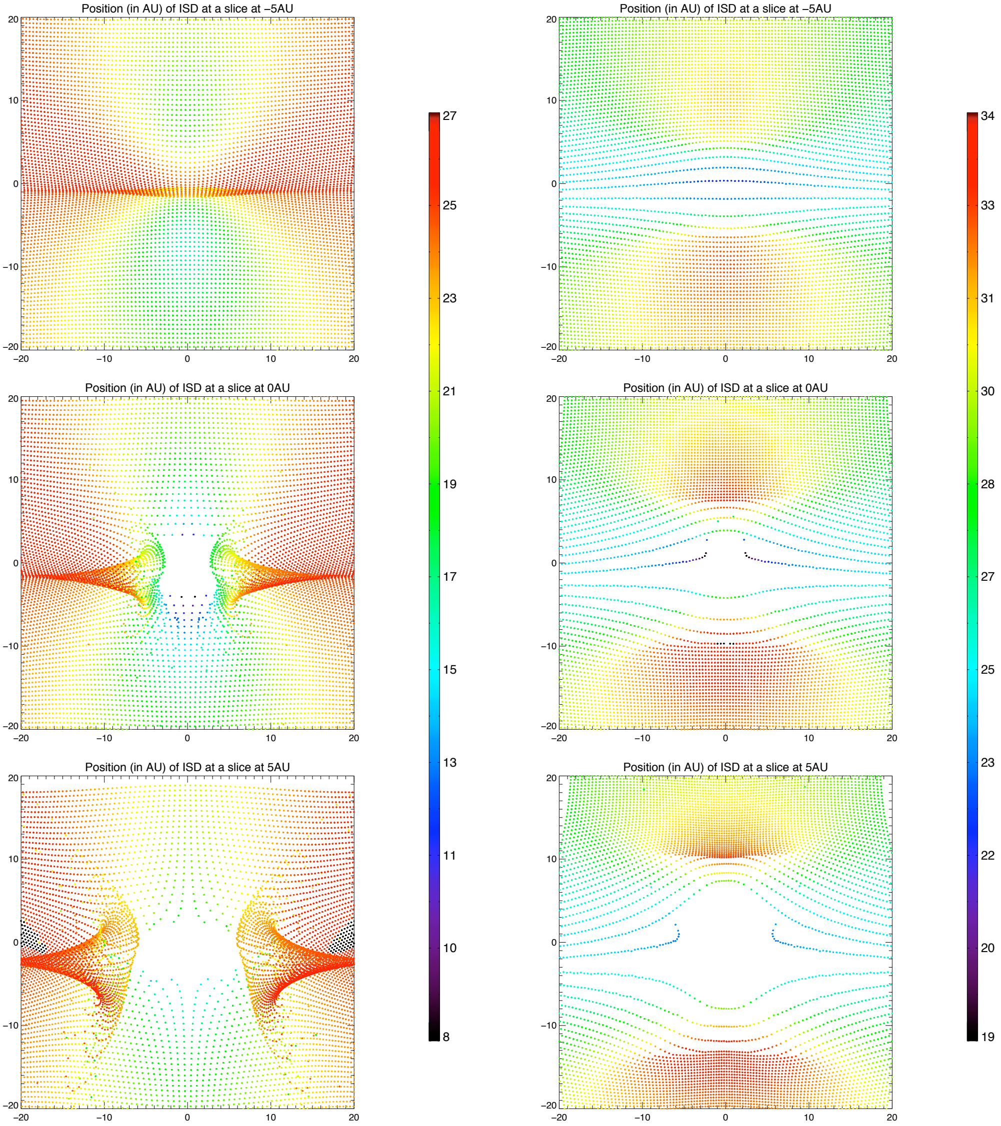

Figure A.29: $\beta = 1.5$, Q/m = 1.5 C/kg focusing phase (left), defocusing phase (right)

A.4 Densities

A.4.1 Radiation pressure and gravity only

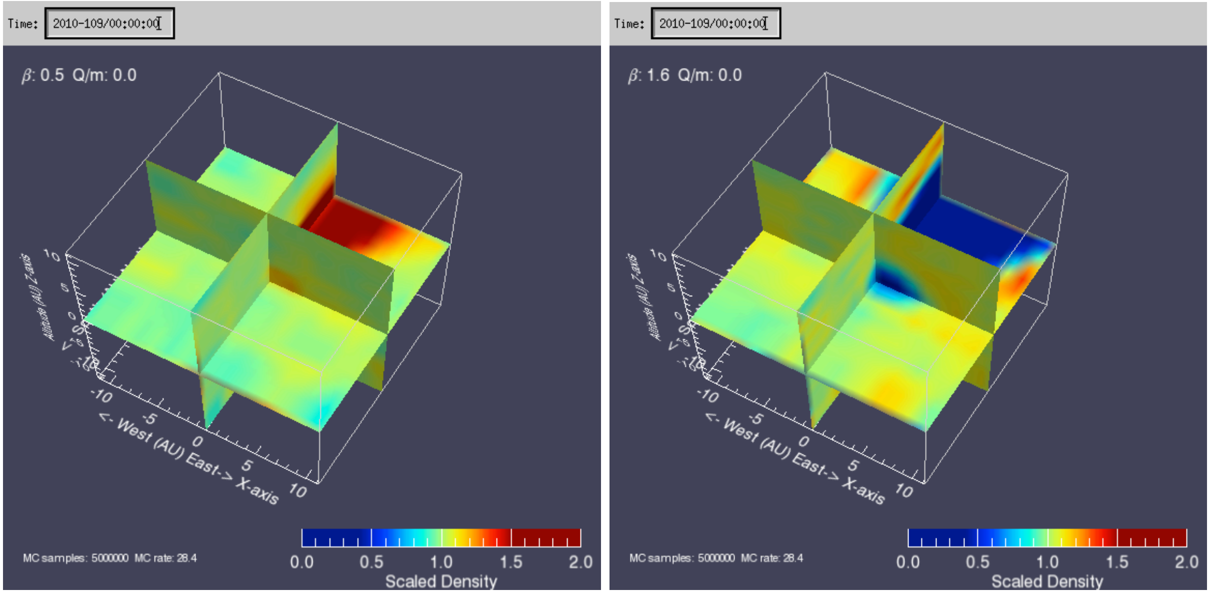

Figure A.30: Relative density map of ISD in the solar system up to 11 AU from the Sun, for particles with $\beta = 0.5$ (left) and $\beta = 1.6$ (right). The density is shown with respect to the undisturbed ISD density at infinity, and the color scale is limited to an upper relative density of 2. For grains with $\beta = 0.5$, the relative density downstream of the Sun is enhanced due to the gravitational focusing (left). The β-cone for $\beta = 1.6$ is visible as a conically-shaped volume of depletion (right).

A.4.2 Lorentz forces only

Focusing and defocusing phase of the solar cycle

Variation in relative densities in the solar system due to the Lorentz force. Observing times are from left to right and top to bottom: 1996, 1998, 2000, 2002, 2004, 2006, 2008, 2010, 2012, 2014, 2016, 2018. The solar minimum of the defocusing cycle is in mid-1996 and the solar minimum of the focusing cycle is in mid-2007. The maximum effect of this on the density is about 3 years later. Solar maximum is in 2002 and 2013, and the solar minimum of the focusing cycle is in mid-2007 and mid-2018.

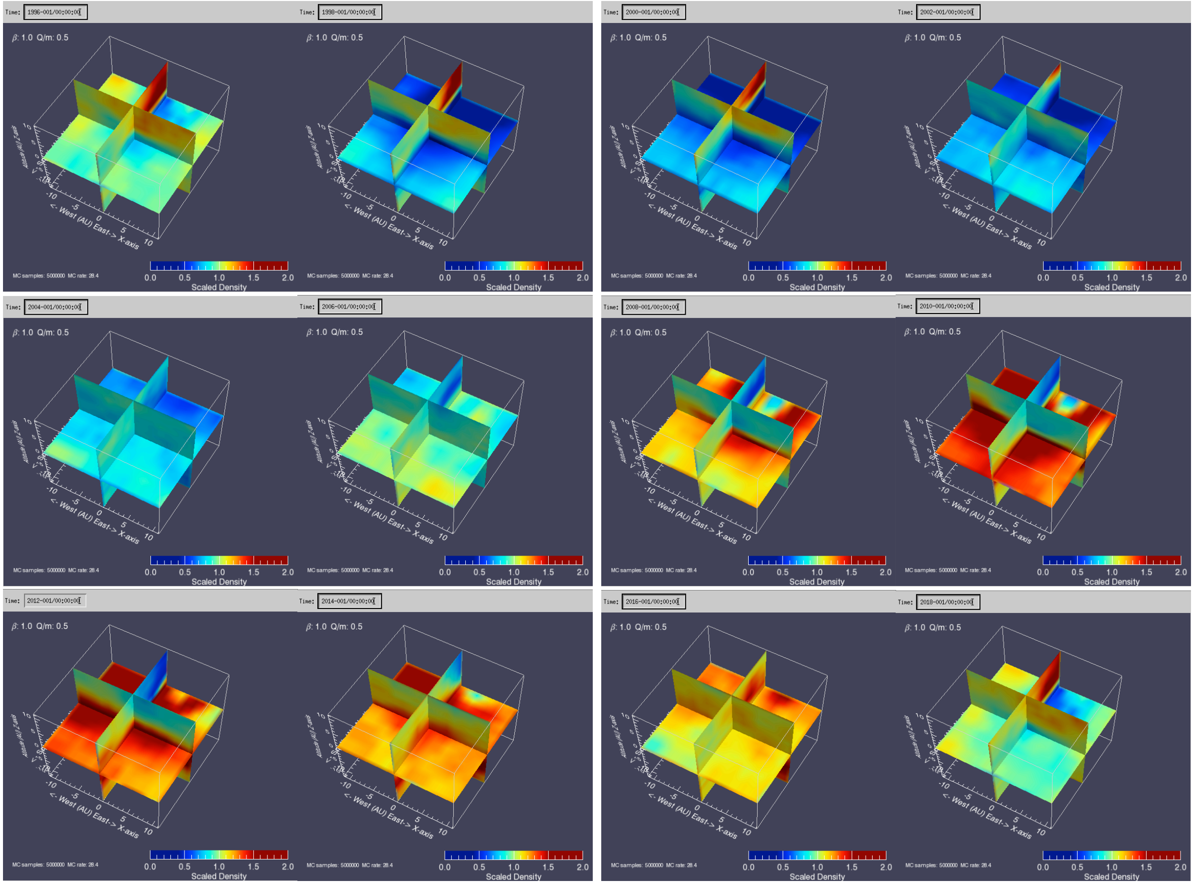

Figure A.31: $\beta = 1$, Q/m = 0.5 C/kg

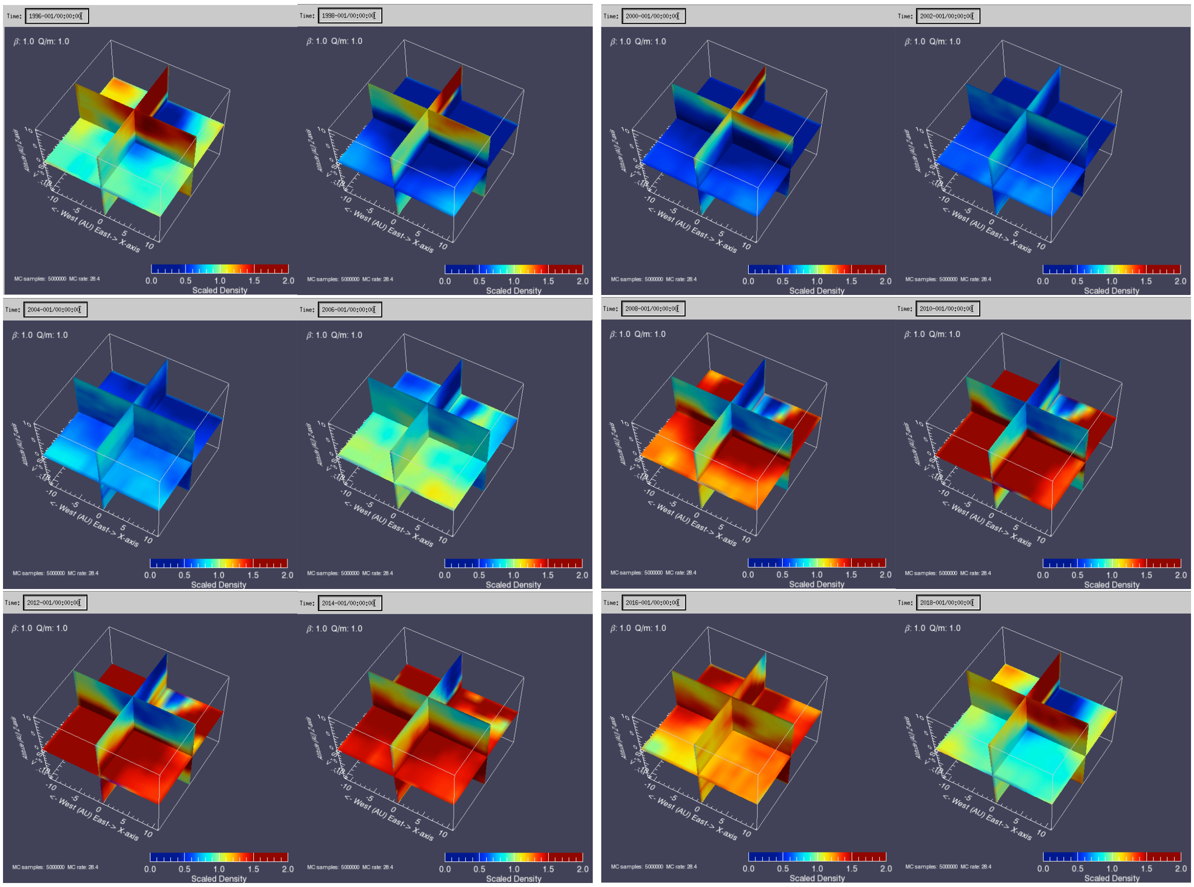

Figure A.32: $\beta = 1$, Q/m = 1.0 C/kg

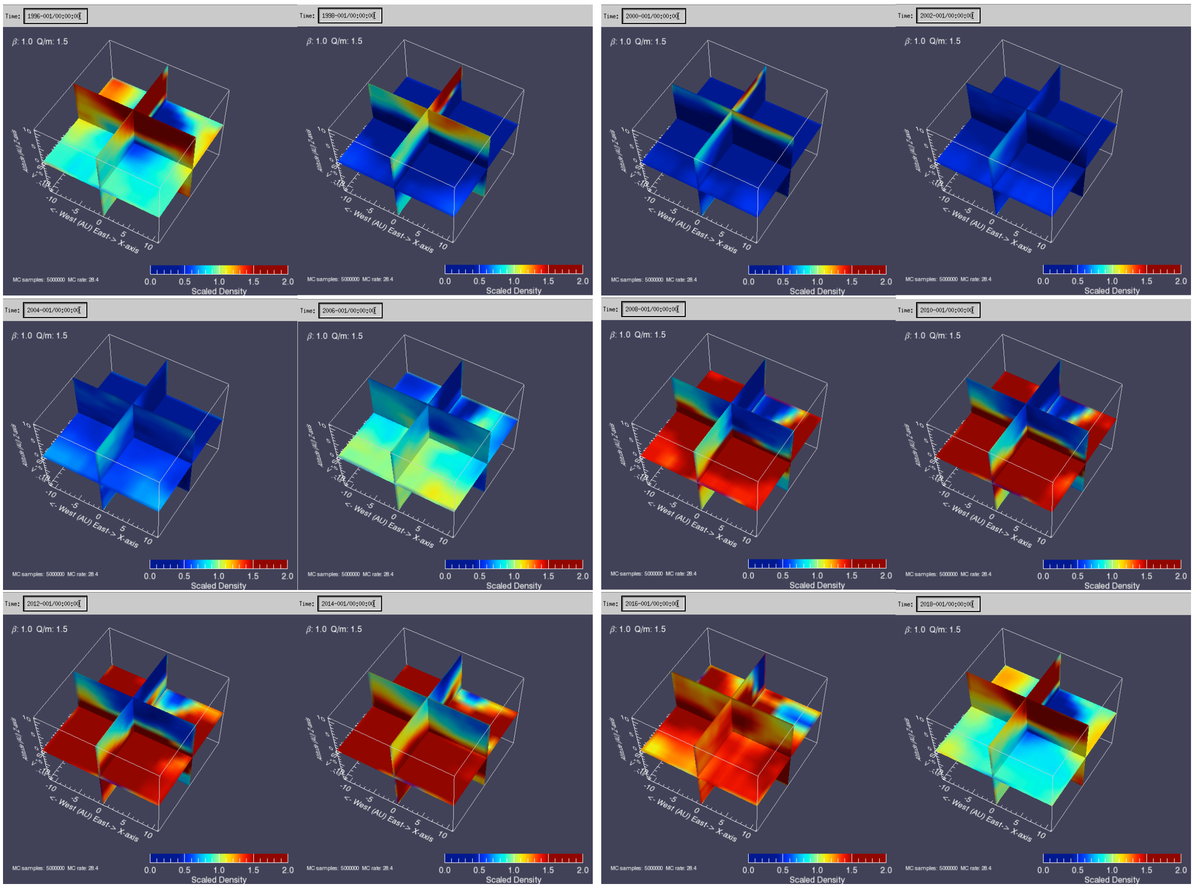

Figure A.33: $\beta = 1$, Q/m = 1.5 C/kg

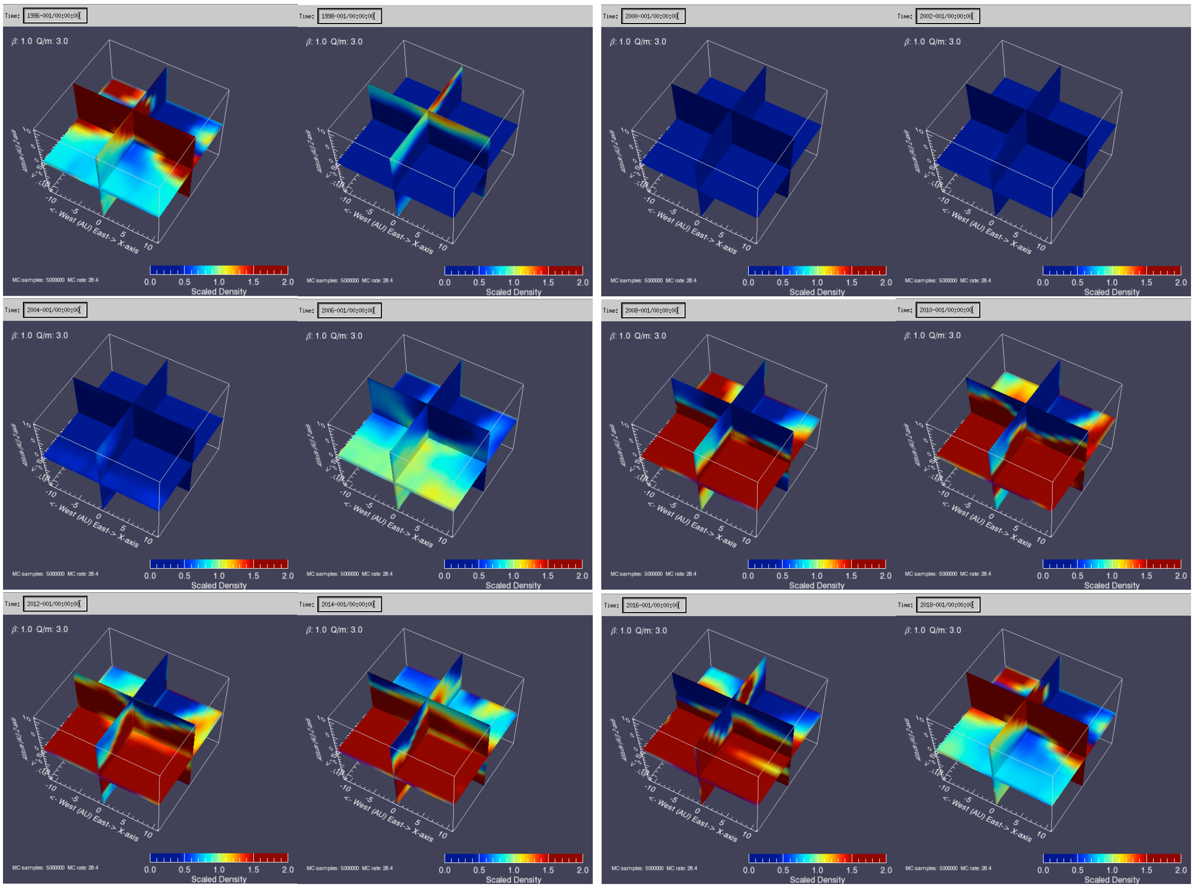

Figure A.34: $\beta = 1$, Q/m = 3.0 C/kg

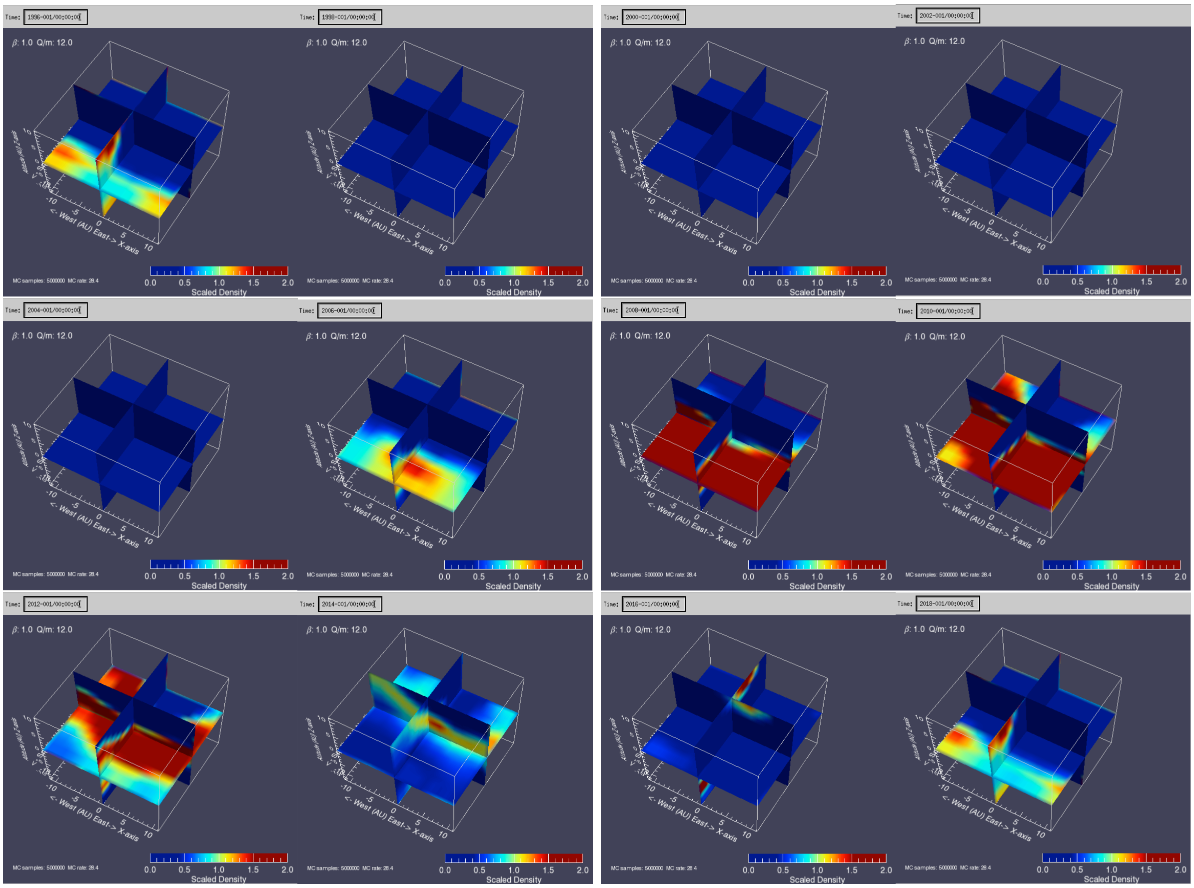

Figure A.35: $\beta = 1$, Q/m = 12.0 C/kg

A.4.3 Radiation pressure, gravity and Lorentz forces

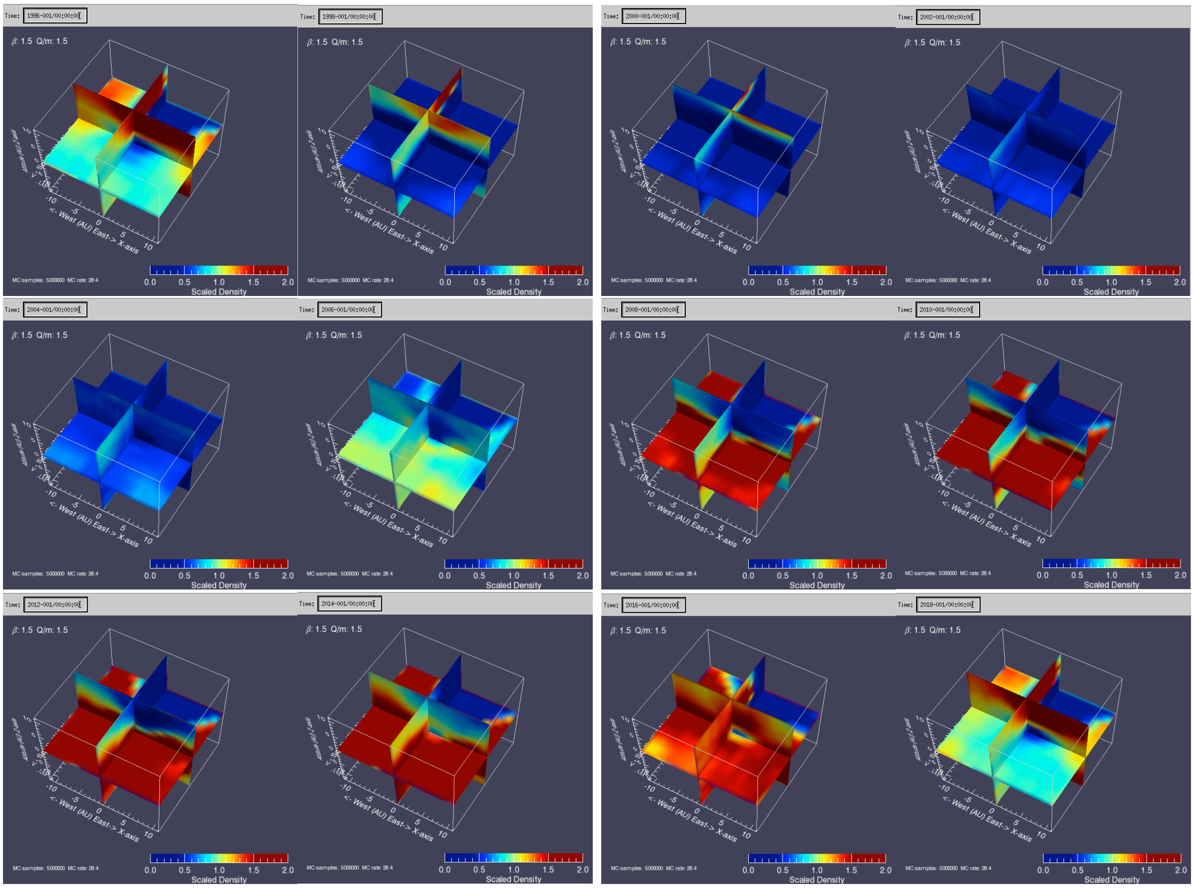

Figure A.36: $\beta = 1.5$, Q/m = 1.5 C/kg

$\mathcal{B}$

Applications of the modeling: the filtering at Saturn, Jupiter and Asteroid belt

B.1 ISD filtering at Saturn

In Section 4.1 the relative fluxes were studied for 7 grain sizes along the β-curve, at Saturn's orbit. Here, we discuss in analogy with Section 3.4.2, the β-Q/m graphs from which these relative fluxes were derived, by following the relative fluxes and velocities along the β-curve in the β-Q/m graphs. Figures B.1 and B.2 show these for the 8 positions throughout the solar cycle and Saturn's orbit. The adapted astronomical silicates β-curve is shown as a black/white line. In 1991, between the focusing and defocusing period (Table 2.1) Saturn is in the upstream portion of the interstellar flow. The flux of particles with $2 <$ Q/m < 4 and β-values > 1.3 is still enhanced more than a factor 2 while the flux of particles with Q/m > 6 is significantly reduced (Fig. B.1). This flux enhancement shifts to smaller β values in 1995. In 1999 the interstellar flux is strongly reduced for all particles except for big particles (Q/m < 0.1 and $\beta < 1.5$). In 2002, Saturn is in the downstream portion of the interstellar flow inside the β-cone for all small particles ($\beta > 1$) and in the focusing region of big particles ($\beta < 1$). However, electromagnetic interactions diffuse the focusing effect for Q/m > 1. In the whole period from 1991 to 1999 the relative speed between Saturn and interstellar grains is below the V_{inf} (26 km/s) because Saturn is moving parallel to the interstellar dust flow and hence the relative speed is reduced by Saturn's orbital speed (9.7 km/s). Only in 2002 the relative speed of big interstellar particles ($\beta < 1$) exceeds V_{inf} because the speed vector of interstellar dust and Saturn are no longer close to parallel.

The relative fluxes and velocities in 2005 to 2017 are much higher (Fig. B.2) than in the preceding period because Saturn is moving into the dust direction (increasing both flux and relative velocity) as well as because of the focusing phase of the solar cycle (2009 to 2013). By 2009, Saturn is at the edge of the $\beta = 3$ cone as well as moving against the dust stream and in the midst of the focusing phase of the solar cycle. In 2013, Lorentz forces change the shape of the β-Q/m plot but still very high fluxes can be found for small grains with Q/m between 3 and 6 C/kg, presumed they can traverse the termination shock. Impact velocities get reduced because of the direction of motion of Saturn.

Fig. B.3 represents the relative flux for 7 grain sizes along the adapted astronomical silicates curve. The last colored plot is a combination of the first 7. As the grain size decreases, the influence of the solar cycle becomes more dominant. Filtering at the termination shock is not taken into account.

Figs. B.4 and B.5 show the relative fluxes for all β and Q/m values, at Saturn. This overview gives a good insight in the influence of both parameters in the resulting flux patterns. The left column contains $\beta < 1$, the right column contains values of $\beta > 1$ and Q/m of the grains increases from top to bottom according to the 7 grain sizes from Table 2.2.

Fig. B.6 is added to this appendix to illustrate the influence of the β-cone on the relative flux, for moderately charged grains like the charge on grains of 0.3 to 0.4 μm (but with varying β-values). For $\beta < 1$, there is an increase in relative flux in 2002 when Saturn is "downstream" of the Sun. For $\beta = 1$ and Q/m $= 0.5$, there is a reduction in the relative flux because of the Lorentz force, and for $\beta > 1$, the influence of the β-cone is clearly visible when comparing the curve with the one of $\beta = 1$. This figure clearly illustrates that for lower β-values, the gravitational focusing compensates the reduced flux due to the Lorentz forces between 2001 and 2003. β varied between 0.7 and 1.5 while keeping the charge-to-mass ratio constant at 0.5 C/kg.

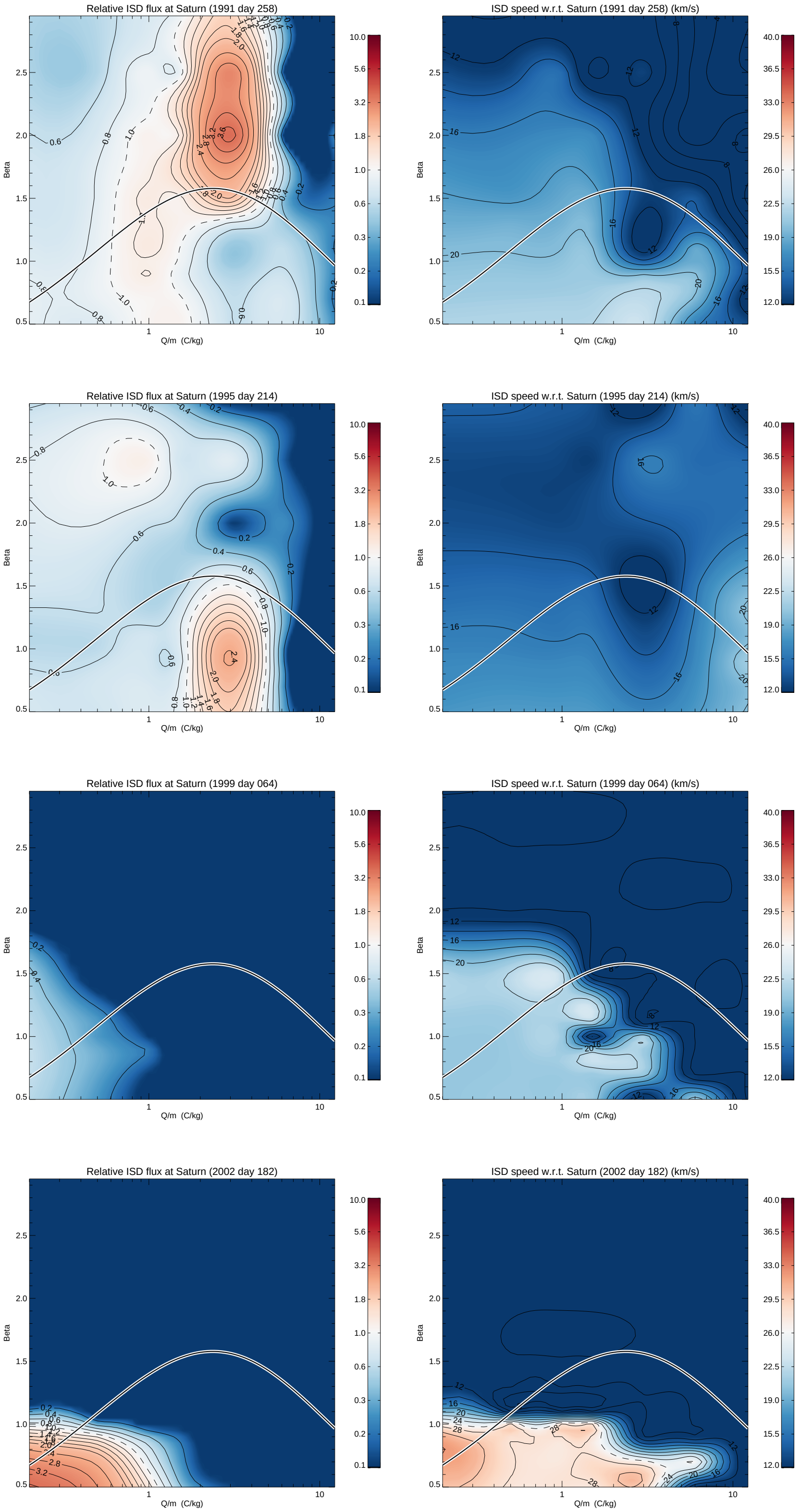

Relative ISD flux at Saturn (1991 day 258)

ISD speed w.r.t. Saturn (1991 day 258) (km/s)

Relative ISD flux at Saturn (1995 day 214)

ISD speed w.r.t. Saturn (1995 day 214) (km/s)

Relative ISD flux at Saturn (1999 day 064)

ISD speed w.r.t. Saturn (1999 day 064) (km/s)

Relative ISD flux at Saturn (2002 day 182)

ISD speed w.r.t. Saturn (2002 day 182) (km/s)

Figure B.1: The relative flux (left) and relative velocity (right) with respect to Saturn for approximately the defocusing phase (1991 – 1992) of the solar cycle. Saturn is moving mainly in the same direction of the dust flow and is downstream from the Sun in 2002 (inside all β-cones).

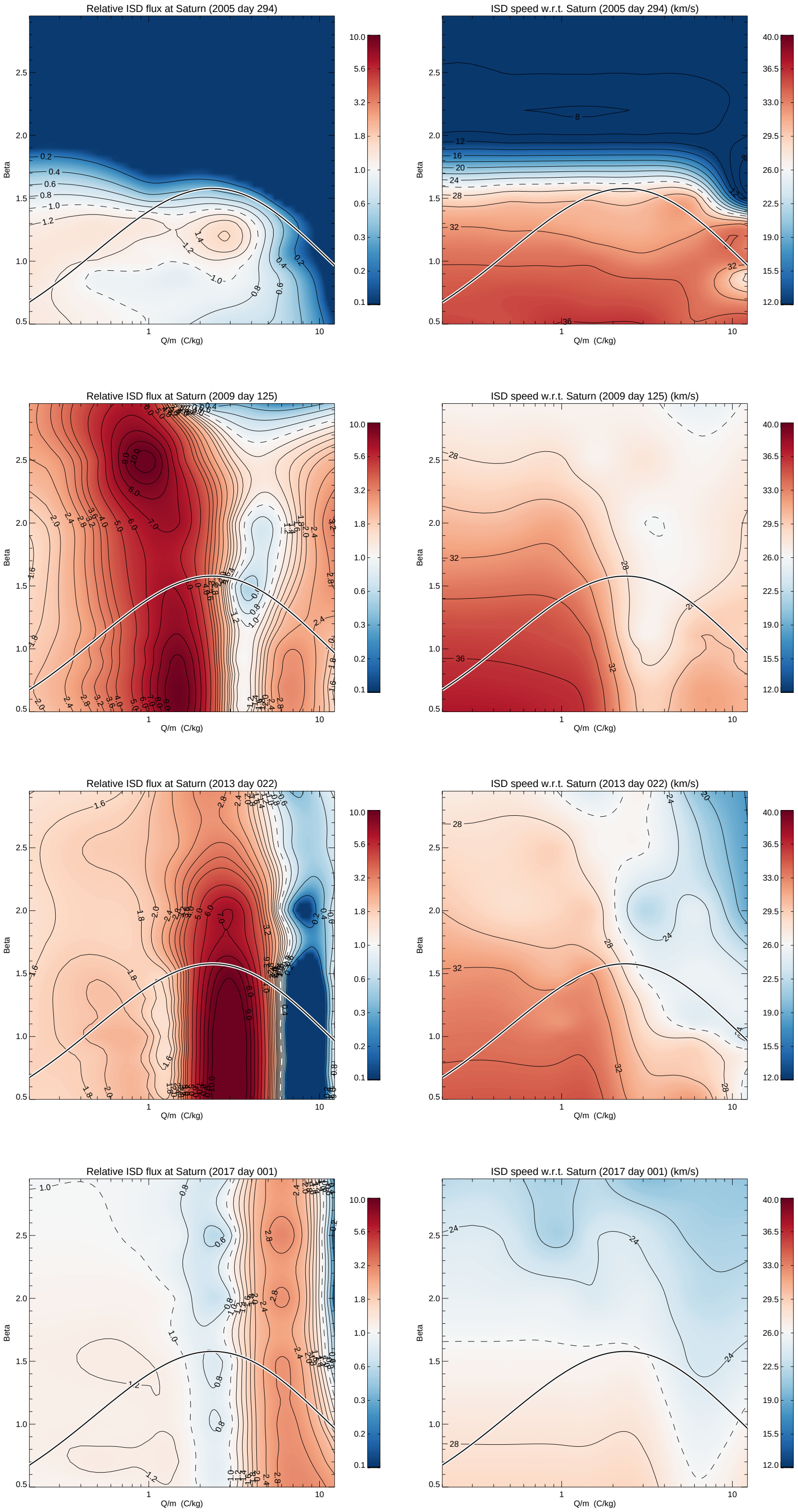

Figure B.2: The relative flux (left) and relative velocity (right) with respect to Saturn for approximately the focusing phase (2005 – 2017) of the solar cycle. Saturn is moving mainly into the dust flow and is upstream from the Sun in 2017.

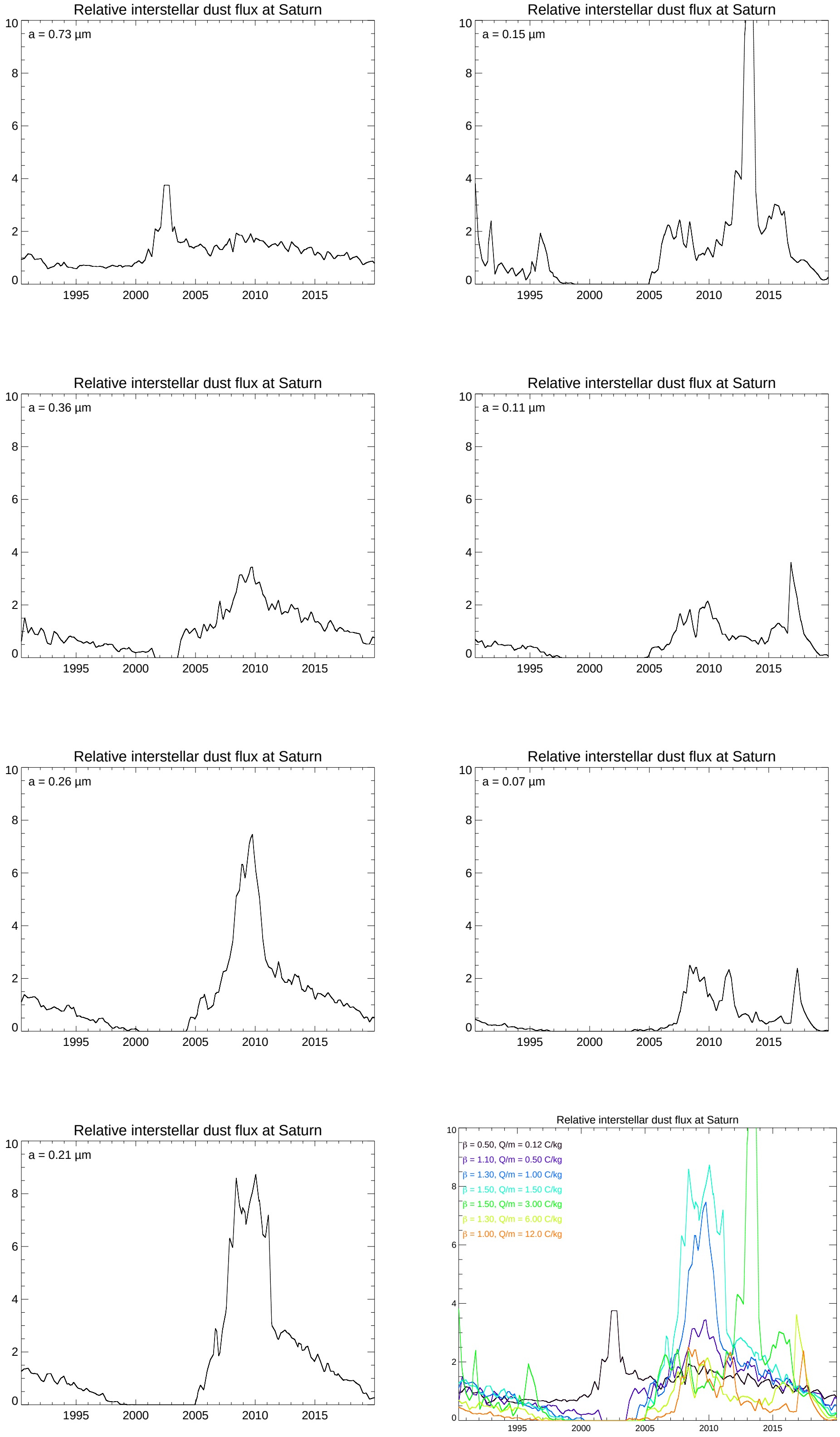

Figure B.3: Time-series of relative fluxes with respect to Saturn for different grain sizes (0.73, 0.36, 0.26, 0.21, 0.15, 0.11 and 0.07 μm).

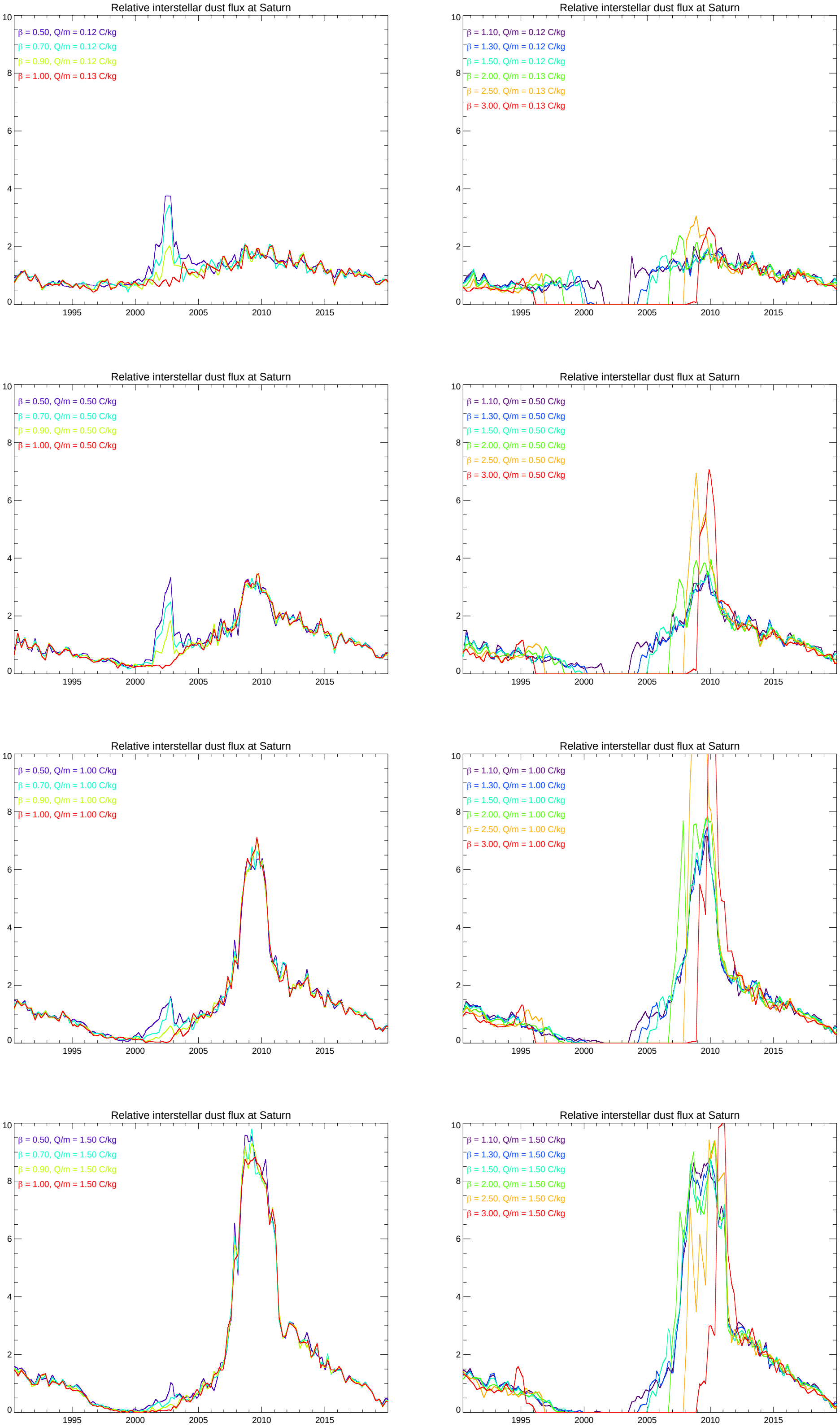

Figure B.4: Overview of relative fluxes at Saturn for all combinations of β and Q/m (from top to bottom: 0.12, 0.5, 1 and 1.5 C/kg), with time. Left: $\beta < 1$, right: $\beta > 1$.

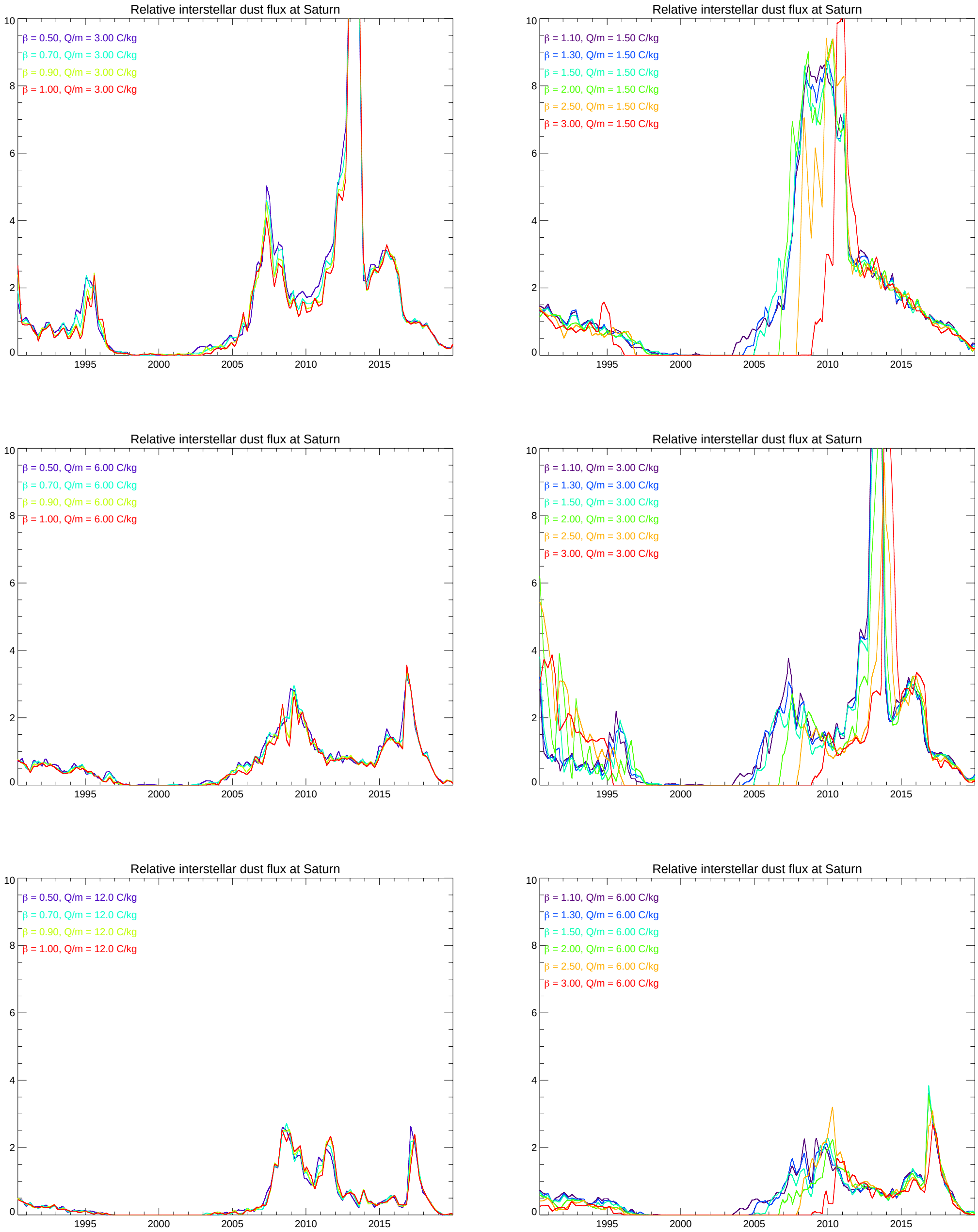

Figure B.5: Overview of relative fluxes at Saturn for all combinations of β and Q/m (from top to bottom 3, 6 and 12 C/kg), with time. Left: $\beta < 1$, right: $\beta > 1$.

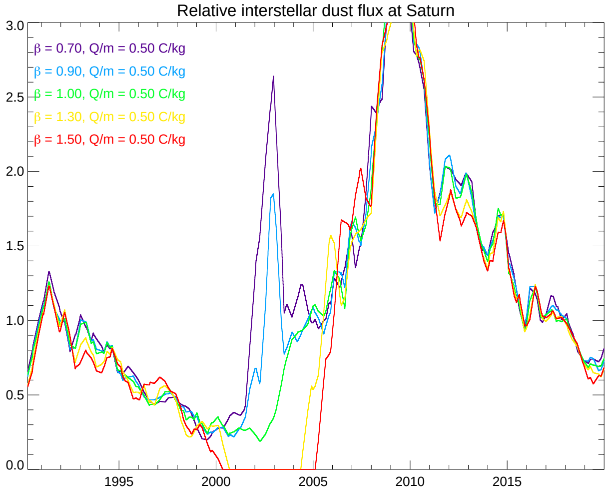

Figure B.6: Relative flux with respect to Saturn (smoothed with a width of 200 days), and scaled to the incoming flux. Five different β-values are shown, and Q/m is fixed at 0.5 C/kg. This is to illustrate the effect of β for a moderate Q/m corresponding to the charge on compact grains of 0.3 to 0.4 μm.

B.2 ISD filtering at Jupiter

Again, we discuss here the β-Q/m graphs from which the relative fluxes were studied along the β-curve in Section 4.2. A first look at the β-Q/m plots for Jupiter (Figs. B.7 and B.8) reveals immediately that there is a strong effect of the focusing and defocusing phase of the solar cycle: fluxes are strongly reduced in Fig. B.7, whereas they are enhanced in Fig. B.8. The locations in the plots for 1995, 1998, 2001 and 2004 are equal to the locations in the plots of 2007, 2010, 2013 and 2016, but the period in the solar cycle is different (defocusing in Fig. B.7 versus focusing in Fig. B.8). From top to bottom, Jupiter is upstream, sidestream (moving with the flow of ISD), downstream and again sidestream (against the flow of ISD). The adapted astronomical silicates β-curve is shown as a black/white line.

Upstream, the relative flux is moderate for 1995 whereas it is high for the focusing phase (2007). The relative velocities vary from high velocities at low β, and lower velocities for higher β-values (as grains get slower near the β-cone for $\beta > 1$ and get faster for lower β-values). The variation in velocities with different β is larger than in the case of Saturn, because we are closer to the Sun and Jupiter's orbital speed is faster (cf. also Fig. 3.22 in section 3.4.2 for the flux and velocity at a fixed position of 5 AU upstream from the Sun). On the sidestream side there is a very low flux in 1998 because of both the defocusing phase of the solar cycle and the relative movement of Jupiter with respect to the dust flow direction. In the focusing phase, the flux is somewhat higher. Both show very low relative velocities since the orbital speed of Jupiter is about 13 km/s and the nominal dust speed is 26 km/s. In 2001 and 2013, Jupiter is downstream from the Sun. The β-cone is visible through having no flux above $\beta = 1$ and the gravitational focusing is visible for small β-values through a strong enhancement of relative flux. During the focusing phase of the solar cycle (Fig. B.8), this enhancement is stronger for certain combinations of β and Q/m. During the defocusing phase (Fig. B.7), also downstream the grains are filtered out as from a certain size (Q/m > 2 C/kg). The Lorentz forces seem to slow down the grains slightly during the focusing phase (Fig. B.8). When in the sidestream position against the ISD flow, the flux in the focusing phase (2016 in Fig. B.8) is clearly higher than in the defocusing case (2004 in Fig. B.7). The defocusing flux is higher in 2004 than in 1998 (Figs. B.7) because we are further in the solar cycle as well as moving into the stream of ISD grains. This is clearly visible in the relative velocities which become very high.

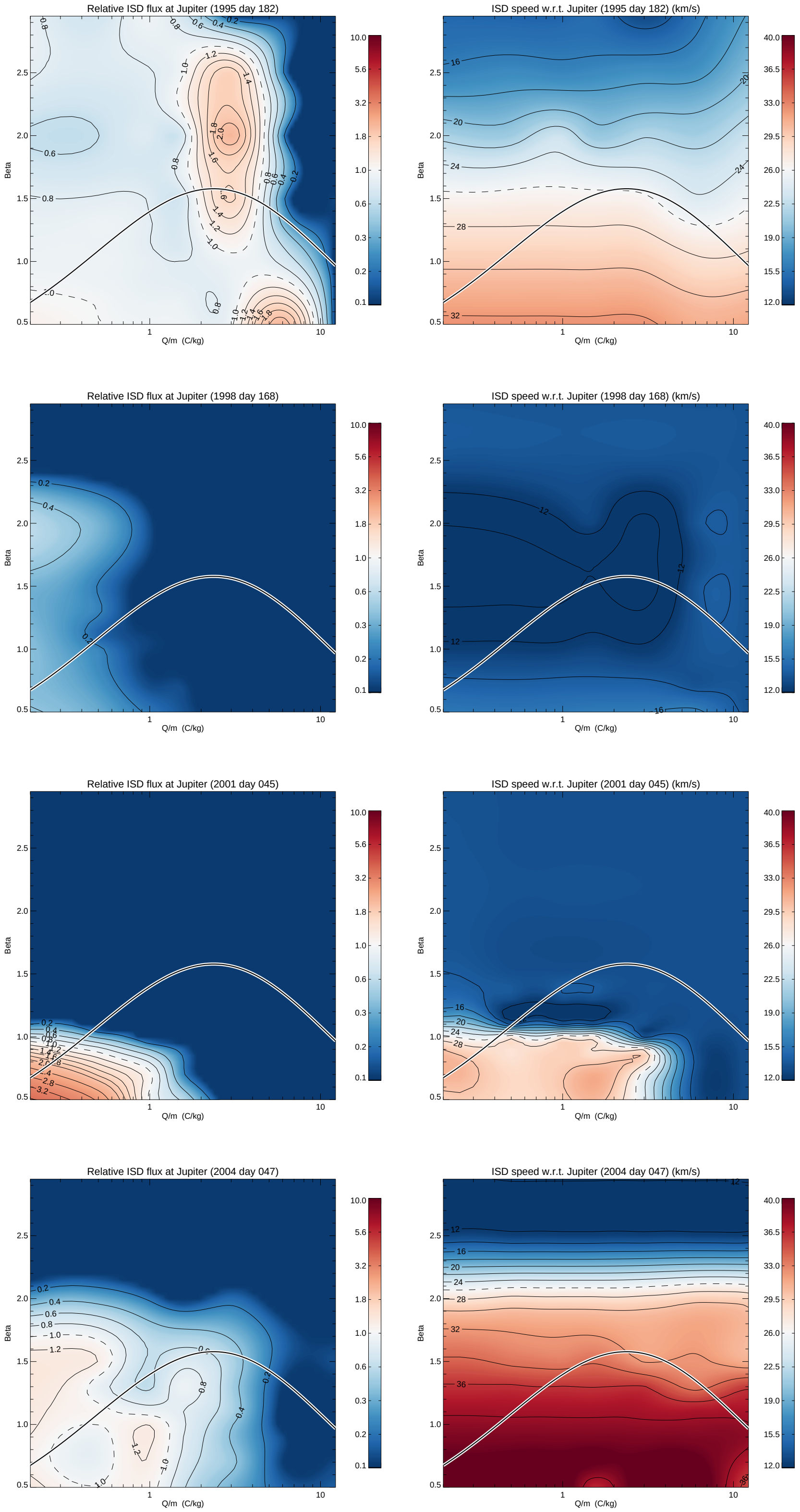

Relative ISD flux at Jupiter (1995 day 182)

ISD speed w.r.t. Jupiter (1995 day 182) (km/s)

Relative ISD flux at Jupiter (1998 day 168)

ISD speed w.r.t. Jupiter (1998 day 168) (km/s)

Relative ISD flux at Jupiter (2001 day 045)

ISD speed w.r.t. Jupiter (2001 day 045) (km/s)

Relative ISD flux at Jupiter (2004 day 047)

ISD speed w.r.t. Jupiter (2004 day 047) (km/s)

Figure B.7: The relative flux (left) and relative velocity (right) with respect to Jupiter for approximately the defocusing phase (1995 – 2004) of the solar cycle for the 4 positions indicated in 4.5 (left).

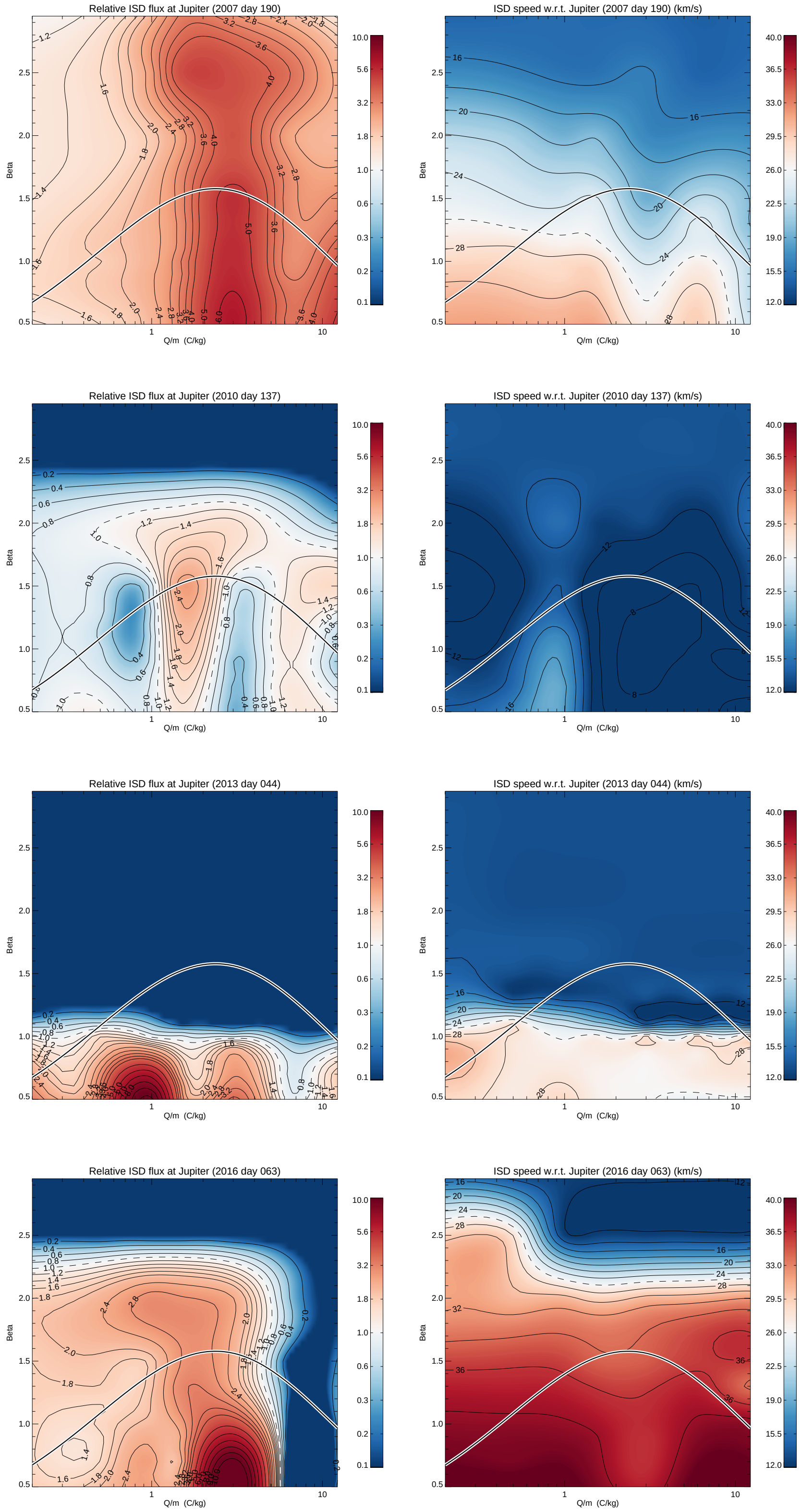

Figure B.8: The relative flux (left) and relative velocity (right) with respect to Jupiter for approximately the focusing phase (2007 – 2016) of the solar cycle for the 4 positions indicated in 4.5 (right).

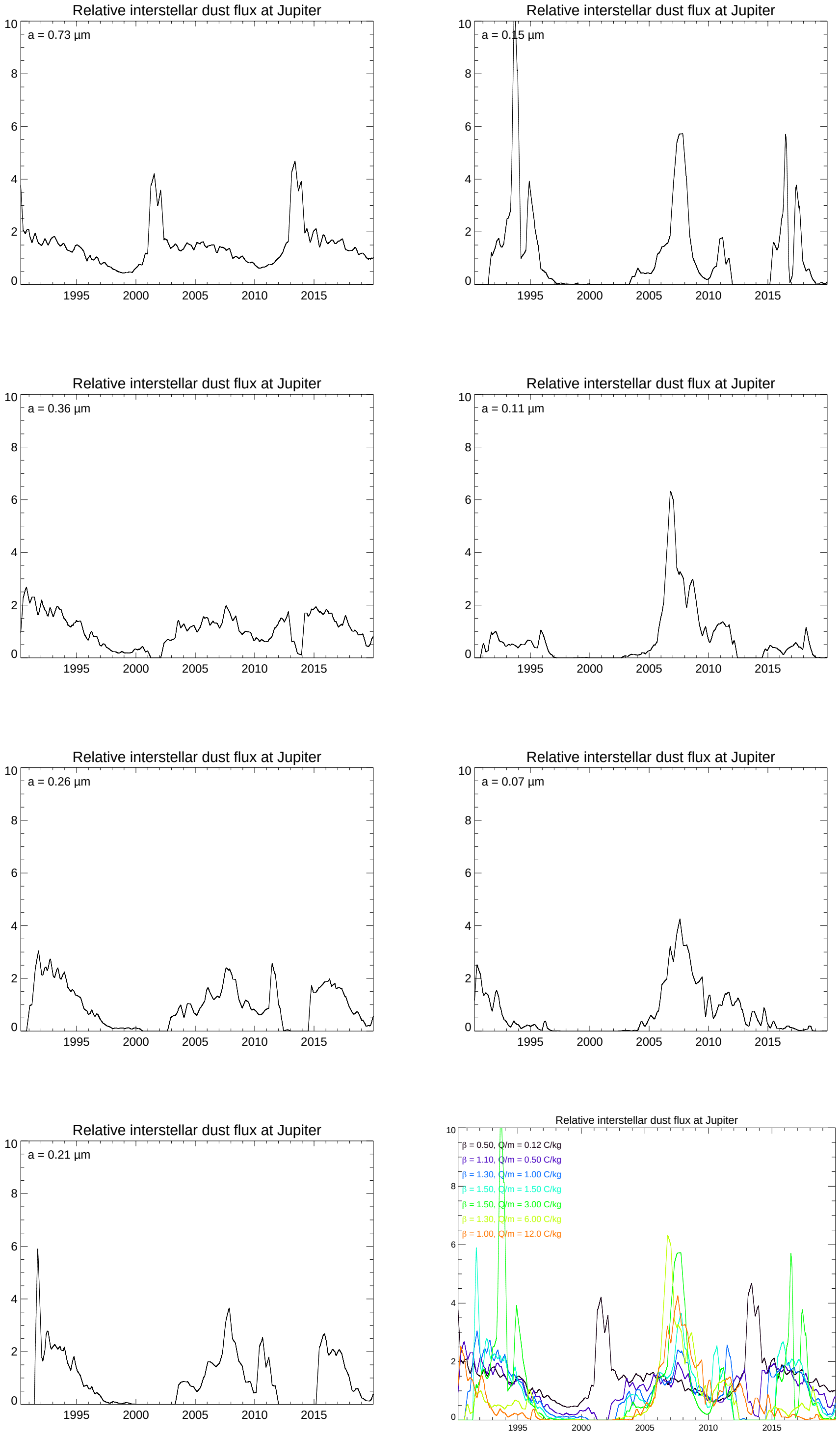

Figure B.9: Time-series of relative fluxes with respect to Jupiter for different grain sizes (0.73, 0.36, 0.26, 0.21, 0.15, 0.11 and 0.07 μm (cf. Fig. B.3)). As the grain size decreases, the influence of the solar cycle becomes more dominant. Filtering at the heliopause is not taken into account.

B.3 ISD filtering in the asteroid belt

In analogy with the previous appendices (B.1,B.2) we discuss the β-Q/m plots for the relative flux and velocity in the asteroid belt. Again, the adapted astronomical silicates β-curve is shown as a black/white line. During the defocusing period only bigger particles (Q/m < 1 and $\beta < 1$) reach the asteroid at somewhat enhanced fluxes (Fig. B.10). The relative speeds of interstellar grains are generally higher than their initial speed of 26 km/s because of the significant orbital speed of the asteroid (18 km/s). Only in 2002 when the asteroid moves approximately parallel with the interstellar flow the relative speed becomes as low as 10 km/s. At this and similar periods interstellar material may be collected at the asteroid surface.

For about half of the asteroid's orbit no particles with $\beta \geq 2$ will reach the asteroid (Fig. B.11). However, their fluxes are generally enhanced except for 2011 when the asteroid's motion subtracts from the interstellar flow speed and, hence, also the fluxes are reduced. Only the flux of particles with Q/m ~ 2 are enhanced even there. Downstream of the interstellar flow (end of 2012) the fluxes of all particles of $\beta < 1$ are strongly enhanced (gravitational focusing and Lorentz forces).

Fig. B.12 shows again the time evolution of the relative flux for the 7 grain sizes apart, and then (colored plot) for all of them in one graph.

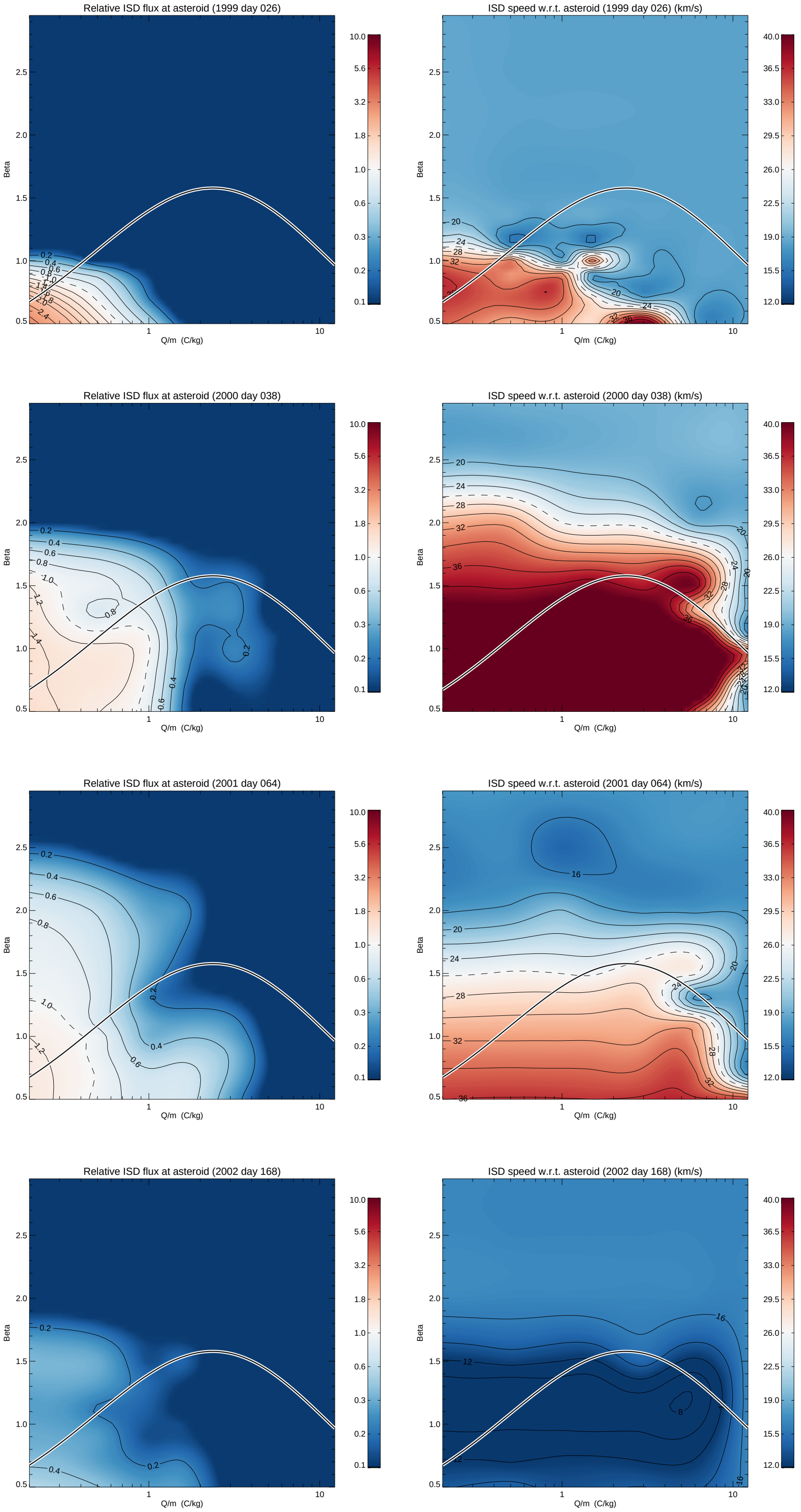

Relative ISD flux at asteroid (1999 day 026)

ISD speed w.r.t. asteroid (1999 day 026) (km/s)

Relative ISD flux at asteroid (2000 day 038)

ISD speed w.r.t. asteroid (2000 day 038) (km/s)

Relative ISD flux at asteroid (2001 day 064)

ISD speed w.r.t. asteroid (2001 day 064) (km/s)

Relative ISD flux at asteroid (2002 day 168)

ISD speed w.r.t. asteroid (2002 day 168) (km/s)

Figure B.10: The relative flux (left) and relative velocity (right) with respect to main-belt asteroid Ceres for approximately the defocusing phase (1999 – 2002) of the solar cycle for the 4 positions indicated in 4.11 (left). The variation in velocity is mainly due to the direction in which Ceres moves with respect to the ISD flow direction.

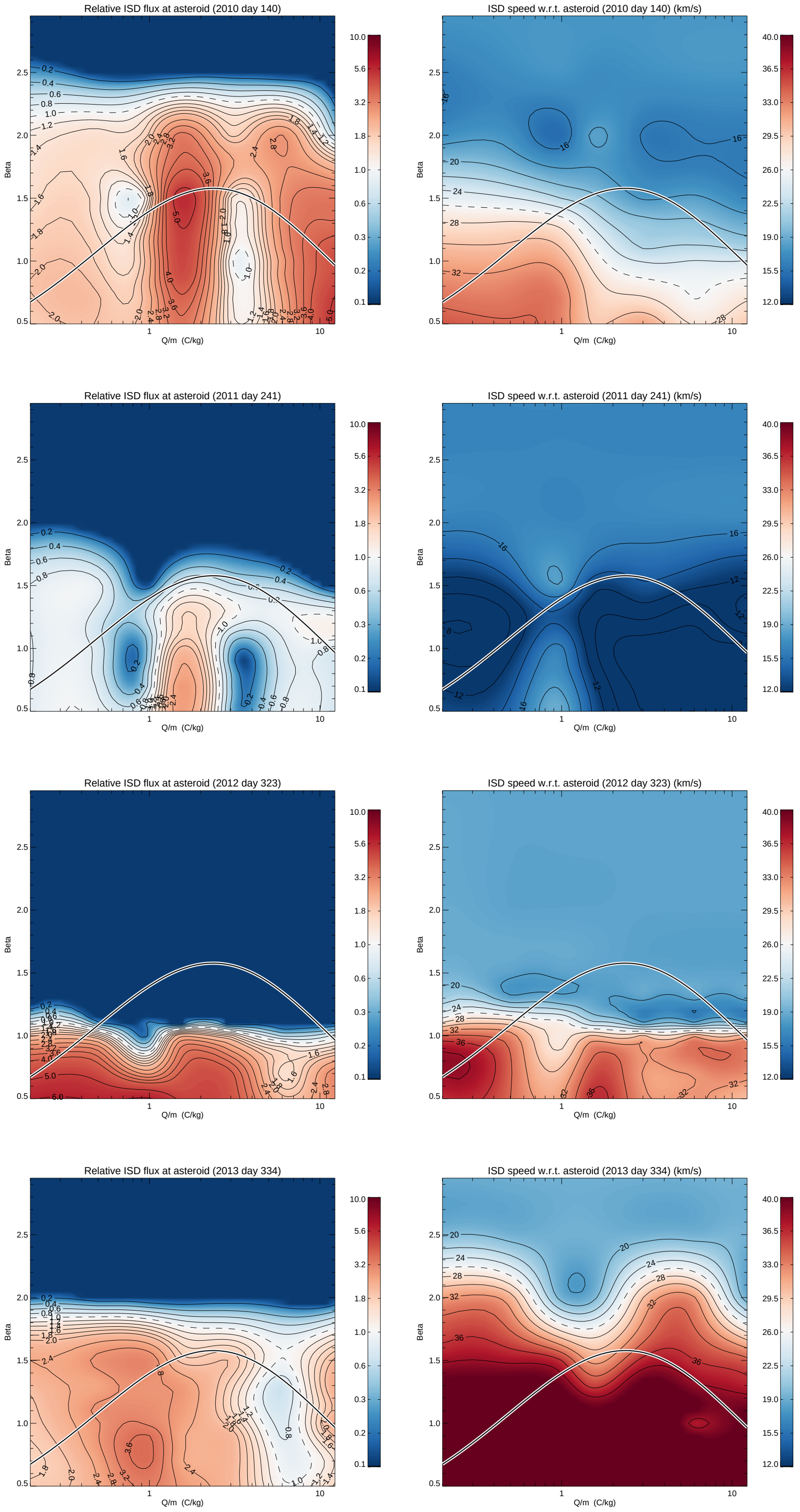

Figure B.11: The relative flux (left) and relative velocity (right) with respect to main-belt asteroid Ceres for approximately the focusing phase (2010 – 2013) of the solar cycle for the 4 positions indicated in 4.11 (right). The variation in velocity is mainly due to the direction in which Ceres moves with respect to the ISD flow direction.

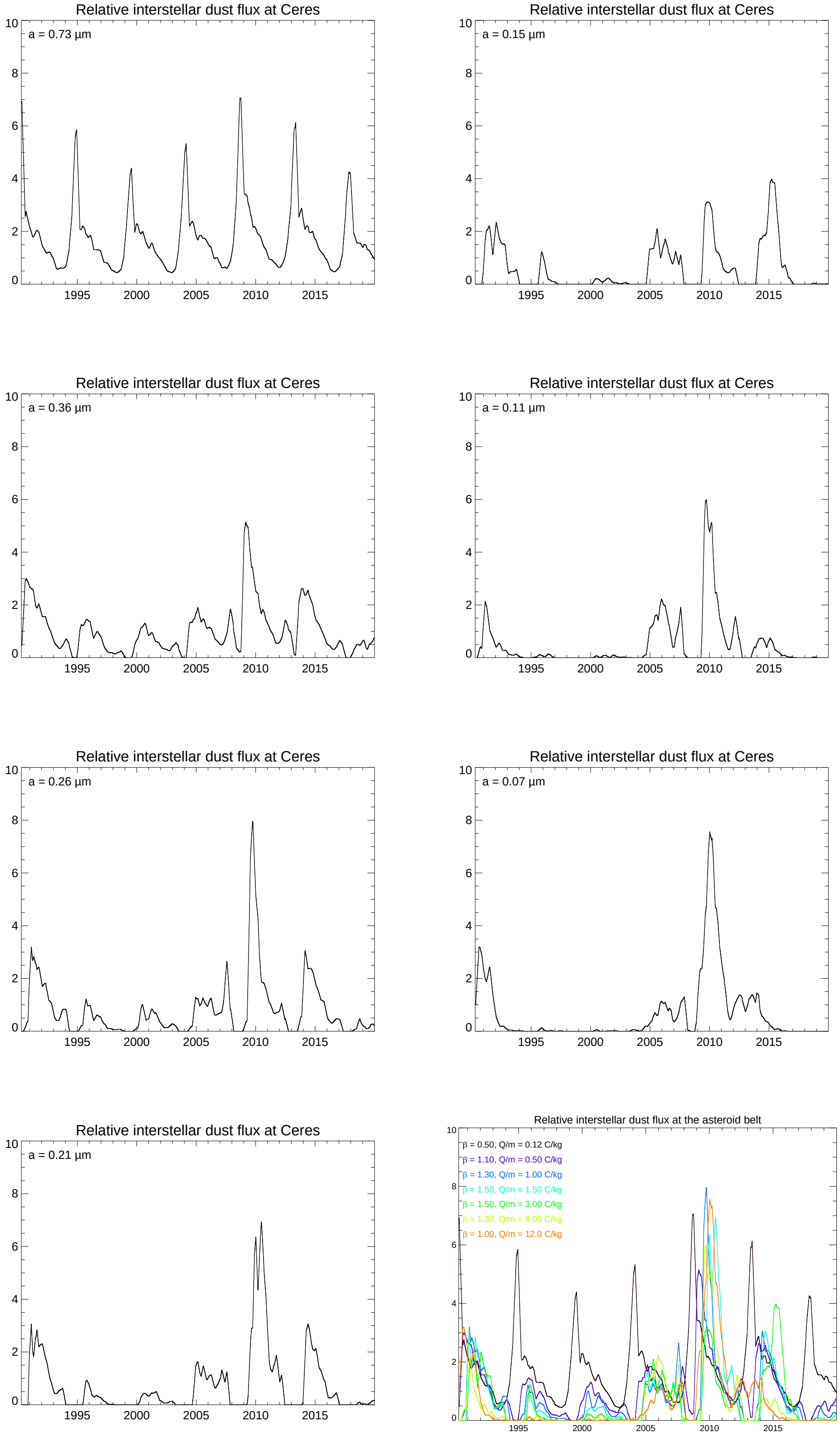
Relative interstellar dust flux at Ceres

Relative interstellar dust flux at the asteroid belt

Figure B.12: Time-series of relative fluxes with respect to main-belt asteroid Ceres for different grain sizes (0.73, 0.36, 0.26, 0.21, 0.15, 0.11 and 0.07 μm

Bibliography

N. Altobelli. *Monitoring of the Interstellar Dust Stream in the Inner Solar System Using Data of Different Spacecraft.* PhD thesis, Ruprecht-Karls-Universität Heidelberg, 05 2004.

N. Altobelli, S. Kempf, M. Landgraf, R. Srama, V. Dikarev, H. Krüger, G. Moragas-Klostermeyer, and E. Grün. Cassini between Venus and Earth: Detection of interstellar dust. *Journal of Geophysical Research (Space Physics)*, 108:8032–+, Aug. 2003. doi: 10.1029/2003JA009874.

N. Altobelli, S. Kempf, H. Krüger, M. Landgraf, M. Roy, and E. Grün. Interstellar dust flux measurements by the Galileo dust instrument between the orbits of Venus and Mars. *Journal of Geophysical Research (Space Physics)*, 110:7102–+, July 2005. doi: 10.1029/2004JA010772.

N. Altobelli, E. Grün, and M. Landgraf. A new look into the Helios dust experiment data: presence of interstellar dust inside the Earth's orbit. *A&A* , 448:243–252, Mar. 2006. doi: 10.1051/0004-6361:20053909.

S. Auer, S. Kempf, and E. Gruen. Computed Electric Charges of Grains with Highly Irregular Shapes. *Dust in Planetary Systems*, 643:177–180, Jan. 2007.

M. Baguhl, E. Grün, D. P. Hamilton, G. Linkert, R. Riemann, and P. Staubach. The flux of interstellar dust observed by Ulysses and Galileo. *Space Sci. Rev.*, 72:471–476, 1995a.

M. Baguhl, D. P. Hamilton, E. Grün, S. F. Dermott, H. Fechtig, M. S. Hanner, J. Kissel, B. A. Lindblad, D. Linkert, G. Linkert, I. Mann, J. A. M. McDonnell, G. E. Morfill, C. Polanskey, R. Riemann, G. Schwehm, P. Staubach, and H. A. Zook. Dust Measurements at High Ecliptic Latitudes. *Science*, 268:1016–+, 1995b.

M. Baguhl, E. Grün, and M. Landgraf. In Situ Measurements of Interstellar Dust with the ULYSSES and Galileo Spaceprobes. *Space Science Reviews, v. 78, Issue 1/2, p. 165-172.*, 78:165–172, 1996.

D. Brownlee, P. Tsou, J. Aléon, C. M. O. . Alexander, T. Araki, S. Bajt, G. A. Baratta, R. Bastien, P. Bland, P. Bleuet, J. Borg, J. P. Bradley, A. Brearley, F. Brenker, S. Brennan, J. C. Bridges, N. D. Browning, J. R. Brucato, E. Bullock, M. J. Burchell, H. Busemann, A. Butterworth, M. Chaussidon, A. Cheuvront, M. Chi, M. J. Cintala, B. C. Clark, S. J. Clemett, G. Cody, L. Colangeli, G. Cooper, P. Cordier, C. Daghlian, Z. Dai, L. D'Hendecourt, Z. Djouadi, G. Dominguez, T. Duxbury, J. P. Dworkin, D. S. Ebel, T. E. Economou, S. Fakra, S. A. J. Fairey, S. Fallon, G. Ferrini, T. Ferroir, H. Fleckenstein, C. Floss, G. Flynn, I. A. Franchi, M. Fries, Z. Gainsforth, J.-P. Gallien, M. Genge, M. K. Gilles, P. Gillet, J. Gilmour, D. P. Glavin, M. Gounelle, M. M. Grady, G. A. Graham, P. G. Grant, S. F. Green, F. Grossemy, L. Grossman, J. N. Grossman, Y. Guan, K. Hagiya, R. Harvey, P. Heck, G. F. Herzog, P. Hoppe, F. Hörz, J. Huth, I. D. Hutcheon, K. Ignatyev, H. Ishii, M. Ito, D. Jacob, C. Jacobsen, S. Jacobsen, S. Jones, D. Joswiak, A. Jurewicz, A. T. Kearsley, L. P. Keller,

H. Khodja, A. L. D. Kilcoyne, J. Kissel, A. Krot, F. Langenhorst, A. Lanzirotti, L. Le, L. A. Leshin, J. Leitner, L. Lemelle, H. Leroux, M.-C. Liu, K. Luening, I. Lyon, G. MacPherson, M. A. Marcus, K. Marhas, B. Marty, G. Matrajt, K. McKeegan, A. Meibom, V. Mennella, K. Messenger, S. Messenger, T. Mikouchi, S. Mostefaoui, T. Nakamura, T. Nakano, M. Newville, L. R. Nittler, I. Ohnishi, K. Ohsumi, K. Okudaira, D. A. Papanastassiou, R. Palma, M. E. Palumbo, R. O. Pepin, D. Perkins, M. Perronnet, P. Pianetta, W. Rao, F. J. M. Rietmeijer, F. Robert, D. Rost, A. Rotundi, R. Ryan, S. A. Sandford, C. S. Schwandt, T. H. See, D. Schlutter, J. Sheffield-Parker, A. Simionovici, S. Simon, I. Sitnitsky, C. J. Snead, M. K. Spencer, F. J. Stadermann, A. Steele, T. Stephan, R. Stroud, J. Susini, S. R. Sutton, Y. Suzuki, M. Taheri, S. Taylor, N. Teslich, K. Tomeoka, N. Tomioka, A. Toppani, J. M. Trigo-Rodríguez, D. Troadec, A. Tsuchiyama, A. J. Tuzzolino, T. Tyliszczak, K. Uesugi, M. Velbel, J. Vellenga, E. Vicenzi, L. Vincze, J. Warren, I. Weber, M. Weisberg, A. J. Westphal, S. Wirick, D. Wooden, B. Wopenka, P. Wozniakiewicz, I. Wright, H. Yabuta, H. Yano, E. D. Young, R. N. Zare, T. Zega, K. Ziegler, L. Zimmerman, E. Zinner, and M. Zolensky. Comet 81P/Wild 2 Under a Microscope. *Science*, 314:1711–, Dec. 2006. doi: 10.1126/science.1135840.

D. E. Brownlee, D. A. Tomandl, and E. Olszewski. Interplanetary Dust; A New Source of Extraterrestrial Material for Laboratory Studies. In *Lunar and Planetary Institute Science Conference Abstracts*, volume 8 of *Lunar and Planetary Inst. Technical Report*, page 145, Mar. 1977.

J. A. Burns, P. L. Lamy, and S. Soter. Radiation forces on small particles in the solar system. *Icarus* , 40:1–48, Oct. 1979. doi: 10.1016/0019-1035(79)90050-2.

J. E. Colwell and M. Horányi. Magnetospheric effects on micrometeoroid fluxes. *JGR* , 101:2169–2176, 1996. doi: 10.1029/95JE03103.

B. T. Draine. Interstellar Dust Models and Evolutionary Implications. In T. Henning, E. Grün, & J. Steinacker, editor, *Cosmic Dust - Near and Far*, volume 414 of *Astronomical Society of the Pacific Conference Series*, pages 453–+, Dec. 2009.

B. Feuerbacher and B. Fitton. Experimental investigation of photoemission from satellite surface materials. *J. Appl. Phys.*, 43(4):1563–1572, April 1972.

P. C. Frisch, J. M. Dorschner, J. Geiss, J. M. Greenberg, E. Grün, M. Landgraf, P. Hoppe, A. P. Jones, W. Krätschmer, T. J. Linde, G. E. Morfill, W. Reach, J. D. Slavin, J. Svestka, A. N. Witt, and G. P. Zank. Dust in the local interstellar wind. *Astrophys. J.*, 525:492–516, Nov. 1999.

P. C. Frisch, M. Bzowski, E. Grün, V. Izmodenov, H. Krüger, J. L. Linsky, D. J. McComas, E. Möbius, S. Redfield, N. Schwadron, R. Shelton, J. D. Slavin, and B. E. Wood. The Galactic Environment of the Sun: Interstellar Material Inside and Outside of the Heliosphere. *Space Science Reviews*, 146:235–273, Aug. 2009. doi: 10.1007/s11214-009-9502-0.

E. Grün and M. Landgraf. Collisional Consequences of Big Interstellar Grains. In *Bulletin of the American Astronomical Society*, volume 29, page 1045, 1997.

E. Grün and J. Svestka. Physics of Interplanetary and Interstellar Dust. *Space Science Reviews, v. 78, Issue 1/2, p. 347-360.*, 78:347–360, 1996.

E. Grün, H. Fechtig, M. Hanner, J. Kissel, B.-A. Lindblad, D. Linkert, D. Maas, G. Morfill, and H. Zook. The Galileo dust detector. *Space Sci. Rev.*, 60:317–340, 1992.

E. Grün, H. Zook, M. Baguhl, A. Balogh, S. Bame, H. Fechtig, R. Forsyth, M. Hanner, M. Horanyi, J. Kissel, B.-A. Lindblad, D. Linkert, G. Linkert, I. Mann, J. McDonnel, G. Morfill, J. Phillips, C. Polanskey, G. Schwehm, N. Siddique, P. Staubach, J. Svestka, and A. Taylor. Discovery of Jovian dust streams and interstellar grains by the Ulysses spacecraft. *Nature*, 362:428–430, 1993.

E. Grün, B. Gustafson, I. Mann, M. Baguhl, G. E. Morfill, P. Staubach, A. Taylor, and H. A. Zook. Interstellar dust in the heliosphere. *Astron. Astrophys.*, 286:915–924, 1994.

E. Grün, M. Baguhl, D. P. Hamilton, J. Kissel, D. Linkert, G. Linkert, and R. Riemann. Reduction of Galileo and Ulysses dust data. *Planetary and Space Sci.*, 43:941–951, 1995.

E. Grün, Z. Sternovsky, M. Horanyi, V. Hoxie, S. Robertson, J. Xi, S. Auer, M. Landgraf, F. Postberg, M. C. Price, R. Srama, N. A. Starkey, J. K. Hillier, I. A. Franchi, P. Tsou, A. Westphal, and Z. Gainsforth. Active Cosmic Dust Collector. *Planet. Space Sci.* , 60:261–273, Jan. 2012. doi: 10.1016/j.pss.2011.09.006.

B. S. Gustafson. Physics of zodiacal dust. *Ann. Rev. Earth Planet. Sci.*, 22:553–595, 1994.

B. S. Gustafson and N. Misconi. Streaming of Interstellar Grains in the Solar System. *Nature*, 282: 276–278, 1979.

B. S. Gustafson, J. Greenberg, L. Kolokolova, Y. Xu, and R. Stognienko. *Interplanetary Dust*, chapter Interactions with Electromagnetic Radiation: Theory and Laboratory Simulations, pages 509–569. Springer-Verlag, Berlin Heidelberg New York, 2001.

J. R. Hill and D. A. Mendis. Electrostatic disruption of a charged conducting spheroid. *Canadian Journal of Physics*, 59:897–901, July 1981.

J. Hoeksema. Wilcox solar observatory, http://wso.stanford.edu, Apr. 2011. URL `http://wso.stanford.edu`.

M. Horányi. Charged dust dynamics in the solar system. *Annu. Rev. Astrophys.*, 34:383–418, 1996.

K. Hornung. Pers. comm., 2012.

J. Jones and L. M. G. Poole. Gravitational focusing and shielding of meteoroid streams. *MNRAS* , 375: 925–930, Mar. 2007. doi: 10.1111/j.1365-2966.2006.11349.x.

N. JPL. Stardust spice kernels, 2012. http://naif.jpl.nasa.gov/naif/.

S. Kempf. Dust Spectroscopy of Jovian Satellite Surface Composition. In *European Planetary Science Congress 2009*, page 472, Sept. 2009.

S. Kempf, R. Srama, N. Altobelli, S. Auer, V. Tschernjawski, J. Bradley, M. Burton, S. Helfert, T. Johnson, H. Krüger, G. Moragas-Klostermeyer, and E. Grün. Cassini between Earth and asteroid belt: First in-situ charge measurements of interplanetary grains. *Icarus*, 171:317–335, 2004.

S. Kempf, R. Srama, E. Grün, A. Mocker, F. Postberg, J. K. Hillier, M. Horányi, Z. Sternovsky, B. Abel, A. Beinsen, R. Thissen, J. Schmidt, F. Spahn, and N. Altobelli. Linear high resolution dust mass spectrometer for a mission to the Galilean satellites. *Planet. Space Sci.* , 65:10–20, May 2012. doi: 10.1016/j.pss.2011.12.019.

H. Kimura and I. Mann. The electric charging of interstellar dust in the solar system and consequences for its dynamics. *Astrophys. J.*, 499:454–+, May 1998.

H. Kimura and I. Mann. Radiation pressure on porous micrometeoroids. In W. J. Baggaley & V. Porubcan, editor, *Meteroids 1998*, pages 283–+, 1999.

F. Krüger, W. Werther, J. Kissel, and E. Schmid. Assignment of quinone derivatives as the main compound class composing 'interstellar' grains based on both polarity ions detected by the 'cometary and interstellar dust analyser' (cida) onboard the spacecraft stardust. *Rapid Commun. Mass Spectrom.*, 18:103–111, Aug. 2004.

H. Krüger. Pers. communication, 2012.

H. Krüger, M. Landgraf, N. Altobelli, and E. Grün. Interstellar Dust in the Solar System. *Space Science Reviews*, 130:401–408, June 2007. doi: 10.1007/s11214-007-9181-7.

M. Landgraf. Modeling the motion and distribution of interstellar dust inside the heliosphere. *J. Geophys. Res.*, 105:10303–10316, 2000. URL `http://adsabs.harvard.edu/cgi-bin/nph-bib_query?bibcode=2000JGR...10510303L&db_key=AST`.

M. Landgraf. *Modellierung der Dynamik und Interpretation der In-Situ-Messung interstellaren Staubs in der lokalen Umgebung des Sonnensystems.* PhD thesis, Ruprecht-Karls-Universität Heidelberg, 1998.

M. Landgraf, K. Augustsson, E. Grün, and B. A. S. Gustafson. Deflection of the local interstellar dust flow by solar radiation pressure. *Science*, 286:2319–2322, 1999a.

M. Landgraf, M. Müller, and E. Grün. Prediction of the in-situ dust measurements of the stardust mission to comet 81P/Wild 2. *Planet. Space Sci.* , 47:1029–1050, Aug. 1999b.

M. Landgraf, W. J. Baggaley, E. Grün, H. Krüger, and G. Linkert. Aspects of the mass distribution of interstellar dust grains in the solar system from in situ measurements. *J. Geophys. Res.*, 105: 10343–10352, 2000.

M. Landgraf, H. Krüger, N. Altobelli, and E. Grün. Penetration of the heliosphere by the interstellar dust stream during solar maximum. *J. Geophys. Res.*, 108:5–1, Aug. 2003.

E. H. Levy and J. R. Jokipii. Penetration of interstellar dust into the Solar System. *Nature*, 264:423–424, 1976.

T. J. Linde and T. I. Gombosi. Interstellar dust filtration at the heliospheric interface. *J. Geophys. Res.*, 105:10411–10418, 2000. URL `http://adsabs.harvard.edu/cgi-bin/nph-bib_query?bibcode=2000JGR...10510411L&db_key=AST`.

I. Mann. Interstellar Dust in the Solar System. *ARAA* , 48:173–203, Sept. 2010. doi: 10.1146/annurev-astro-081309-130846.

J. S. Mathis, W. Rumpl, and K. H. Nordsieck. The size distribution of interstellar grains. *Astrophys. J.*, 217:425–433, 1977.

G. E. Morfill and E. Grün. The motion of charged dust particles in interplanetary space-II. Interstellar grains. *Planet. Space Sci.* , 27:1283–1292, Oct. 1979. doi: 10.1016/0032-0633(79)90106-5.

T. Mukai. On the charge distribution of interplanetary grains. *A&A* , 99:1–6, June 1981.

M. Opher, J. F. Drake, M. Swisdak, K. M. Schoeffler, J. D. Richardson, R. B. Decker, and G. Toth. Is the Magnetic Field in the Heliosheath Laminar or a Turbulent Sea of Bubbles? *ApJ* , 734:71, June 2011. doi: 10.1088/0004-637X/734/1/71.

E. N. Parker. Dynamics of the interplanetary gas and magnetic fields. *Astrophys. J.*, 128:664–+, Nov. 1958.

F. Postberg, S. Kempf, J. Schmidt, N. Brilliantov, A. Beinsen, B. Abel, U. Buck, and R. Srama. Sodium salts in E-ring ice grains from an ocean below the surface of Enceladus. *Nature* , 459:1098–1101, June 2009. doi: 10.1038/nature08046.

F. Postberg, E. Grün, M. Horanyi, S. Kempf, H. Krüger, J. Schmidt, F. Spahn, R. Srama, Z. Sternovsky, and M. Trieloff. Compositional mapping of planetary moons by mass spectrometry of dust ejecta. *Planet. Space Sci.* , 59:1815–1825, Nov. 2011. doi: 10.1016/j.pss.2011.05.001.

F. Postberg, J. K. Hillier, S. Armes, S. Bugiel, A. Butterworth, Z. Gainsforth, E. Grün, Y. W. Li, R. Srama, V. J. Sterken, J. Stodolna, M. Trieloff, and A. Westphal. High speed interstellar dust analogue capture in stardust flight-spare aerogel. *Meteoritics and Planetary Science*, 2012. submitted.

S. Redfield and J. L. Linsky. The Structure of the Local Interstellar Medium. IV. Dynamics, Morphology, Physical Properties, and Implications of Cloud-Cloud Interactions, Jan. 2008.

J. D. Richardson, J. C. Kasper, C. Wang, J. W. Belcher, and A. J. Lazarus. Cool heliosheath plasma and deceleration of the upstream solar wind at the termination shock. *Nature* , 454:63–66, July 2008. doi: 10.1038/nature07024.

G. Schwehm. Radiation pressure on interplanetary dust particles. In H. Elsaesser & H. Fechtig, editor, *Interplanetary Dust and Zodiacal Light*, volume 48 of *Lecture Notes in Physics, Berlin Springer Verlag*, pages 459–463, 1976. doi: 10.1007/3-540-07615-8_526.

J. D. Slavin, 2012. Personal communication.

J. D. Slavin, P. C. Frisch, J. Heerikhuisen, N. V. Pogorelov, H.-R. Mueller, W. T. Reach, G. P. Zank, B. Dasgupta, and K. Avinash. Exclusion of Tiny Interstellar Dust Grains From the Heliosphere. *Twelfth International Solar Wind Conference*, 1216:497–501, Mar. 2010. doi: 10.1063/1.3396301.

R. Soja, N. Altobelli, H. Krüger, and V. J. Sterken. Dust environment predictions for the ESA L-class mission candidate JUICE, 2012. Planet. Space Sci., in prep.

R. Srama, T. J. Ahrens, N. Altobelli, S. Auer, J. G. Bradley, M. Burton, V. V. Dikarev, T. Economou, H. Fechtig, M. Görlich, M. Grande, A. Graps, E. Grün, O. Havnes, S. Helfert, M. Horanyi, E. Igenbergs, E. K. Jessberger, T. V. Johnson, S. Kempf, A. V. Krivov, H. Krüger, A. Mocker-Ahlreep, G. Moragas-Klostermeyer, P. Lamy, M. Landgraf, D. Linkert, G. Linkert, F. Lura, J. A. M. McDonnell, D. Möhlmann, G. E. Morfill, M. Müller, M. Roy, G. Schäfer, G. Schlotzhauer, G. H. Schwehm, F. Spahn, M. Stübig, J. Svestka, V. Tschernjawski, A. J. Tuzzolino, R. Wäsch, and H. A. Zook. The Cassini Cosmic Dust Analyzer. *Space Science Reviews*, 114:465–518, Sept. 2004a. doi: 10.1007/s11214-004-1435-z.

R. Srama, A. Srowig, M. Rachev, E. Grün, S. Auer, T. Conlon, A. Glasmachers, D. Harris, S. Helfert, S. Kempf, H. Linnemann, G. Moragas-Klostermeyer, and V. Tschernjawski. Development of an Advanced Dust Telescope. *Earth Moon and Planets*, 95:211–220, Dec. 2004b. doi: 10.1007/s11038-005-9040-z.

R. Srama, N. Altobelli, J. de Kam, S. Kempf, H. Krüger, S. Lera, G. Moragas-Klostermeyer, M. Rachev, A. Srowig, M. Landgraf, Q. Vo, and E. Grün. DUNE-eXpress Dust astronomy with ConeXpress. *Advances in Space Research*, 38:2093–2101, Jan. 2006. doi: 10.1016/j.asr.2005.09.009.

R. Srama, T. Stephan, E. Grün, N. Pailer, A. Kearsley, A. Graps, R. Laufer, P. Ehrenfreund, N. Altobelli, K. Altwegg, S. Auer, J. Baggaley, M. J. Burchell, J. Carpenter, L. Colangeli, F. Esposito, S. F. Green, H. Henkel, M. Horanyi, A. Jäckel, S. Kempf, N. McBride, G. Moragas-Klostermeyer, H. Krüger, P. Palumbo, A. Srowig, M. Trieloff, P. Tsou, Z. Sternovsky, O. Zeile, and H.-P. Röser. Sample return of interstellar matter (SARIM). *Experimental Astronomy*, 23:303–328, Mar. 2009. doi: 10.1007/s10686-008-9088-7.

R. Srama, H. Krüger, T. Yamaguchi, T. Stephan, M. Burchell, A. T. Kearsley, V. Sterken, F. Postberg, S. Kempf, E. Grün, N. Altobelli, P. Ehrenfreund, V. Dikarev, M. Horanyi, Z. Sternovsky, J. D. Carpenter, A. Westphal, Z. Gainsforth, A. Krabbe, J. Agarwal, H. Yano, J. Blum, H. Henkel, J. Hillier, P. Hoppe, M. Trieloff, S. Hsu, A. Mocker, K. Fiege, S. F. Green, A. Bischoff, F. Esposito, R. Laufer, T. W. Hyde, G. Herdrich, S. Fasoulas, A. Jäckel, G. Jones, P. Jenniskens, E. Khalisi, G. Moragas-Klostermeyer, F. Spahn, H. U. Keller, P. Frisch, A. C. Levasseur-Regourd, N. Pailer, K. Altwegg, C. Engrand, S. Auer, J. Silen, S. Sasaki, M. Kobayashi, J. Schmidt, J. Kissel, B. Marty, P. Michel, P. Palumbo, O. Vaisberg, J. Baggaley, A. Rotundi, and H. P. Röser. SARIM PLUS - sample return of comet 67P/CG and of interstellar matter. *Experimental Astronomy*, 33:723–751, Apr. 2012. doi: 10.1007/s10686-011-9285-7.

Stardust@Home. Stardust at home website http://stardustathome.ssl.berkeley.edu/, 2012.

P. Staubach, E. Grün, and R. Jehn. The meteoroid environment near earth. *Adv. Space Res.*, 19:301–308, 1997.

V. J. Sterken, N. Altobelli, S. Kempf, H. Krüger, F. Postberg, R. H. Soja, R. Srama, and E. Grün. An optimum opportunity for interstellar dust measurements by the JUICE mission. *Planetary and Space Science*, 2012a. in Press.

V. J. Sterken, N. Altobelli, S. Kempf, H. Krüger, R. Srama, P. Strub, and E. Grün. The filtering of interstellar dust in the solar system, 2012b. Submitted.

V. J. Sterken, N. Altobelli, S. Kempf, G. Schwehm, R. Srama, and E. Grün. The flow of interstellar dust into the solar system. *A&A* , 538:A102, Feb. 2012c. doi: 10.1051/0004-6361/201117119.

V. J. Sterken, A. J. Westphal, and >30,000 co-authors. Impact speeds and directions of interstellar grains on the stardust dust collector. *Meteoritics and Planetary Science*, in prep., 2012d.

Z. Sternovsky, E. Grün, K. Drake, J. Xie, M. Horanyi, R. Srama, S. Kempf, F. Postberg, A. Mocker, S. Auer, and H. KrÃijger. Novel instrument for dust astronomy: Dust telescope. In *IEEEAC*, number 1291, 2010.

R. Stroud and et al. Tbd. *Meteoritics and Planetary Science*, 2012. submitted.

P. Strub, V. J. Sterken, H. Krüger, E. Grün, and M. Horanyi. Interstellar dust flow through the solar system. In *AIP conference proceedings - 6th International Conference on the Physics of Dusty Plasmas Garmisch-Partenkirchen, Germany - Dusty/Complex plasmas: basic and interdisciplinary research*, volume 1397, 2011.

P. Tsou, D. E. Brownlee, S. A. Sandford, F. Hörz, and M. E. Zolensky. Wild 2 and interstellar sample collection and Earth return. *Journal of Geophysical Research (Planets)*, 108:8113, Oct. 2003.

J. C. Weingartner and B. T. Draine. Dust Grain-Size Distributions and Extinction in the Milky Way, Large Magellanic Cloud, and Small Magellanic Cloud. *ApJ* , 548:296–309, Feb. 2001. doi: 10.1086/318651.

A. Westphal and et al. Stardust interstellar preliminary examination ii: Optical ob- servations and backgrounds. *Meteoritics and Planetary Science*, 2012a. submitted.

A. Westphal and et al. Three interstellar dust candidates returned by the stardust spacecraft. *Science*, 2012b. in preparation.

M. Witte, H. Rosenbauer, M. Banaszkiewicz, and H. Fahr. The ULYSSES neutral gas experiment - Determination of the velocity and temperature of the interstellar neutral helium. *Advances in Space Research*, 13:121–130, 1993.

V. Zubko, E. Dwek, and R. G. Arendt. Interstellar Dust Models Consistent with Extinction, Emission, and Abundance Constraints. *ApJS* , 152:211–249, June 2004. doi: 10.1086/382351.

Curriculum Vitae

Veerle Jasmin Sterken
Born on 22.06.1980 in Ghent, Belgium

Education

1998 – 2005:	Faculty of Aerospace Engineering, TU Delft (The Netherlands). Master's degree received in the research group "Astrodynamics and satellite systems" on 19.05.2005
1992 – 1998:	Secondary school: Sint-Bavohumaniora - Ghent (Belgium). Option "Mathematics-Sciences"
1986 – 1992:	Primary school: Sint-Jozefinstituut - Ghent (Belgium)

Work experience

2009 – 2012:	PhD student at IGEP (TU Braunschweig), in cooperation with MPIK and ESA. Space research, focused on the dynamics of interstellar dust in the heliosphere
April – May 2009:	Faculty visitor at ESA – ESAC, Madrid, Spain for the PhD project
2006 – 2008:	Study of disturbances on Darwin optical path at TUDelft in cooperation with Thales Alenia Space and ESA
Sept. 2006:	Consultant of Science and Technology, Delft, working for TNO: Survey of possible Belgian-Dutch cooperation in the space market
2005 – 2006:	Young Graduate Trainee at ESA – ESTEC (The Netherlands) Support of the Geosail and the Cross-Scale technology reference studies
2000 – 2002	Assistant in the Engineering Mechanics courses (Aerospace engineering – TU Delft)

Other work and study related activities

2007:	Participation to the Kiruna winter school on Aurora Borealis and cold weather related phenomena
2003, 2005, 2006	Participation to the ESA Student IAF Programme
2004/2005:	Graduation project in cooperation with TNO – Science and Industry (Delft, the Netherlands) about the impact of the space and satellite environment on the optical path differences of Darwin
2003:	Traineeship at ESOC (Darmstadt, Germany): Mission Analysis: working on the use of FEEPs propulsion for the GAIA mission
2002:	Participation to the Alpbach Summer School on Space Weather: Physics, Impacts and Predictions
2000:	Participated and selected for the 3rd ESA Parabolic Flight Campaign: Fluid research with main focus on the technical design of the equipment used

Awards/Fellowships

2012:	LPI Career Development Award
2007:	Amelia Earhart Fellowship

Related Reports/Publications

2007:	V.J. Sterken: Sir Hermann Bondi, a journey through his life and the early endeavours of Europe into space. Acta astronautica, Vol. 61, p. 514-525, and IAC 2006 Conf. Proc. IAC-06-E4.1.05.
2005:	V.J. Sterken: Master's thesis at the Delft University of Technology: Impact of the space and satellite environment on the optical path differences of Darwin, (TNO report no. 050006), and IAC 2005 Conf. Proc. IAC-05-C.2.5.
2003:	V.J. Sterken, M. Hechler: ESOC Mission Analysis Section Working Paper No. 458, GAIA Mission Analysis: Use of FEEPs for orbit maintenance.
2002:	Co-author of the Alpbach Summer School report: GLOTEC: Global real-time TEC-map Satellite Navigation System Reliability Forecast.
2000:	Co-Author of the report on the Parabolic Flight Campaign experiment: Technical Description and Strength Calculations of the Test Set-up for Micro-gravity Experiments in the 2000 ESA Parabolic Flight Campaign for Group 1023. Delft University of Technology report no. FM&P-00.011 cat.h.

Acknowledgements

I am thankful to the many people and institutions who have greatly supported me in the process of writing this thesis and growing slowly into a scientist.

In the very first place I sincerely wish to thank my daily supervisor Prof. Dr. Eberhard Grün, under whose wings it was a true privilege to write a PhD thesis. Eberhard, thank you very very much for your supervision, integrity, dedication, enthusiasm and drive for science, for your visions, patience, understanding and humor which made working with you on a daily basis a very pleasant experience!

I owe special thanks to Markus Landgraf. Not only has his scientific work been the starting point and a solid basis for my thesis, also his good advice and sound opinions have helped me further in life. Together with Prof. Eberhard Grün, Markus is a true inspiration for my future career and life.

Many thanks also to the dust group, where I've had the chance to develop myself as a beginning scientist in a very exciting field! I'd like to thank Ralf Srama for the practical support throughout the thesis and for giving me the opportunity to start with this work within the dust group. Special thanks go to Sascha Kempf who was my daily supervisor in the first year, for all the help with setting up the Monte Carlo simulation and for the object oriented programming. I also thank Sean Hsu for always being open to discuss scientific issues as well as whenever I had a question about IDL. I am grateful to Frank Postberg for involving me into the Stardust project.

It was a great pleasure and honor to be involved in the Interstellar Preliminary Examination of the Stardust project and I have very much enjoyed the fruitful discussions with the team. Many special thanks to Andrew Westphal for the very nice cooperation and discussions and for the financial support which made it possible to attend the LPSC in 2012. All those who still want to search for dust can surf to *http://stardustathome.ssl.berkeley.edu*

I am grateful to Harald Krüger and Peter Strub for the many exchanges and cooperation on the Ulysses data and simulations, and for the contributions to the papers and proposals we wrote and still write.

I'd like to thank ESA and in specific Gerhard Schwehm for providing financial support for my thesis, which is embedded in a project of the TU Braunschweig. I am also thankful for the faculty funding during my 2-months stay in the premises of ESAC, Madrid in 2009. In those two months I was guided by Dr. Nicolas Altobelli to whom I owe much gratitude for the scientific guidance and collaboration throughout the whole PhD period and for making it possible for me to start my PhD with him as an extra advisor/collaborator. Many thanks also to Rachel Soja for being my compagnon while writing the JUICE papers and IMEX proposal. I also want to thank Åsa Ericson for helping me in my stay in Madrid and Sergio Suarez for his friendship and covoiturage during those two months.

I am grateful to the University of Braunschweig, IGEP department for being the host of the ESA contract. A special thanks to Jurgen Blum and Nicole Mund for all the support I received, for thinking along when problems appeared and for reading and correcting this thesis. I also cordially thank Prof. Karl-Heinz Glassmeier for joining and leading the exam committee. I thank the University of Stuttgart, to where the dust group has moved, for providing me with a contract for allowing me to finish my PhD.

I thank the Max Planck Institute for Nuclear Physics (MPIK) for welcoming me as a guest in the institute as well as for the financial support in March 2012. I have seldomly met so many excellent scientists as in this institute and the many conversations with my colleague-“doktoranden” as well as the senior scientsts have been very instructive and a true motivation. In special, I owe the people of the Ullrich Gruppe many thanks for the nice atmosphere under colleagues, for the fun together and for all the support in daily PhD-life. Especially, I would like to thank Selim, Andy & Indy, Lutz, Helga, Renate, Alexander EBIT, Christian Dorn, Julian, the table football players and the group of keen runners. If there is one commonality between long distance running and science, it is perseverance and the will to bite through. Then comes the joy.

I acknowledge the financial support from the LPI career development award, the scholarship to attend the ICPDP, COSPAR travel support and MetSoc travel grant which have allowed me to participate in these conferences and exchange with scientists from overseas.

I’d like to take the opportunity to thank all the people who have played an important role in overcoming the difficulties that I came across during the PhD. In Germany, I absolutely owe a special thanks to Tingting & Huabai and again Prof. Eberhard Grün for their support in 2010 and many thanks to Ruth & José for their support in 2011. I’d also like to thank the Belgians Alwyn & Roos, Klaas, Pieter T., Sabine & Maarten for all the extra support and for our nice adventures outdoor. I got addicted. I’m also very grateful for my true friendship with Pieter and Jeroen which felt like “home” and which stood for much integrity, humor and fun: an important aspect when moving alone into a foreign country. Besides my Belgian friends, I also have enjoyed a lot and felt supported a lot by my closest friends in Germany: Kilian, Janine, Marc, Joice, Gregor, Heidi, Kai, Tingting, Huabai: thank you for supporting all the ups and downs of (PhD) life. I’ve enjoyed the times in the band “die Brenner” and I’ve truly enjoyed the brunches and parties together. You know how to drum the beat.

During my PhD-time I was very active in “fun sports” which were not only a hold on during stressful times and a balance for hard work, but through which I also learned other aspects of life: the world and myself. I owe many thanks to the Excentriques through which I truly enjoyed the team work in the caves and the many nice evenings together outdoors. Especially many thanks to Chris and Wera for all the skills - including human skills - that you have taught me! I’d also like to thank the support of the skydiving club in Walldorf, in particular Rüdiger & Isolde. It is good to have a completely different and often stunning environment and hence put my mind on something else but the PhD thesis. I’ve seen very beautiful things up and down there of which most people cannot imagine they exist.

Thanks also to many others like Mihaela & Christian, Sytze, Martin, Cedric, Filippo and numerous people who I did not mention but who contributed through support in any form!

Finally, I would like to conclude with some very special thanks to my family in Belgium for all the support during the many stressful days. Especially, I’d like to thank my parents and my twin sister Mieke for always supporting me and giving me the feeling of “home sweet home”. Yes, I do often miss Belgium and when living abroad, it is good to have a supportive base at home. When bad luck struck, you’ve undoubtedly been the most important support. Thanks also for motivating me for doing what I wanted to do (no matter whether it is a PhD in Germany or rather skydiving...) and for all the good moments together. A special last word to express my joy to see my niece Elise whenever I come home.